

Spreading Processes

in Complex Networks of Cultured Neurons and Society

Dissertation

for the award of the degree

“Doctor rerum naturalium”

of the Georg-August University Göttingen

within the doctoral program

Physics of Biological and Complex Systems

of the Georg-August University School of Science (GAUSS)

submitted by

Franz Paul Spitzner

from Leipzig, Germany

Göttingen, 2023

Thesis committee and members of the examination board

First referee and supervisor

Prof. Dr. Viola Priesemann

Max Planck Institute for Dynamics and Self-Organization, Göttingen

Second referee

Dr. Andreas Neef

Göttingen Campus Institute for Dynamics of Biological Networks

Prof. Dr. Peter Sollich

Institute for Theoretical Physics, Georg-August University Göttingen

Further members of the examination board

Prof. Dr. Jörg Enderlein

Third Institute of Physics, Georg-August University Göttingen

Prof. Dr. Michael Wilczek

Theoretical Physics I, University of Bayreuth

Prof. Dr. Theo Geisel

Max Planck Institute for Dynamics and Self-Organization, Göttingen

Date of the oral examination: 19 September 2023

“There was a button,” Holden said. *“I pushed it.”*

— James S.A. Corey, *Nemesis Games*

Dedicated to my late stepfather who planted a seed of curiosity.

Acknowledgements

As I am getting closer to the finishing line of the Ph.D., I find myself sampling emotion-space with a bigger step size than before. On the one hand, I feel sentimental to see this chapter coming to an end, and about having to part ways with many people who I have grown very fond of. On the other hand, I am excited about the things to come, and I am happy about the subtle reminder to stop every now and then, catch a breath, and appreciate all the good things that came my way. Looking back, they were more than anyone could ask for. And almost always they came with kind people attached to them: people who gave me a chance, who believed in me, who supported me — all without asking for anything in return. The next few paragraphs, and the implied hug (imagine me with a wide smile), are for all those people. Thank you!

I mentioned chances. One incredible and crucial chance was given to me by Viola. Without her, and without that chance some five years ago, I would not be here. Thank you Viola, for inviting me to become part of your group, for providing patient guidance, for indulging my often naive point of view, and for teaching me to focus on the things that matter. It has been my honest pleasure to work with you.

Viola has a knack for gathering amazing people around her — which becomes clear instantaneously when you meet her group. I fondly remember my first day, when I met a student who proficiently explained the project I would work on. I judged him to be a senior Ph.D.; Jonas was indeed close to graduating, and handed in his *Master's thesis* soon after. Over the years to come, we would share a multitude of projects, and dinners, every one of which was a treat. Thank you, Jonas, for always being around, for being my trusted coauthor on several papers, and for helping out every time I got stuck. Then there is of course João, who I want to thank for discussions on a nerd-level I can have with no one else, and in particular, for standing with me through the longest review process of all. Thanks to Jens, who taught me that all (well most) scientific problems are solvable, and to Annika of the timescales team, for spotting oh-so-many bugs in my code and providing the kindest of feedback. I also want to thank Lucas and Fabian, my next-door theoreticians, for countless discussions, frequent advice, and the occasional rant, all of which I enjoyed deeply. Thanks to Sebastian who joined me on various coding sessions that well exceeded standard

working hours, and to Seba, with his overwhelmingly positive attitude. I know no other person who radiates good vibes like you do, and you have been a great inspiration for me.

From all my colleagues, I want to especially thank Johannes. I owe you a huge chunk of gratitude, for help in more ways than I can count. Over the past decade (!) you have been a mentor, counselor, and inspiration, and you have become one of my dearest friends. This thesis would not have been possible without your relentless support. Even if I turn my back on academia in the end, I hope for any excuse to work (or to procrastinate) with you.

I was repeatedly asked why I am writing the thesis in the *we*-form. *Are you not confident enough?* I am. *Don't you see it as your work?* Yes, I do. Some consider this choice a matter of preference, but for me, there is a bit more to it: The thesis has been a great effort, which I could not have managed alone. Every little detail has been discussed (directly or indirectly) with a colleague, a friend, or family. The *we* is my way to acknowledge that.

For instance, none of the publications would have been possible without my incredible collaborators over the years. Thank you for putting our heads together to solve interesting puzzles, and for keeping your smiles up during the countless hours in meetings. Special thanks to Jordi, who welcomed me into his lab in Barcelona and, together with Hideaki, significantly shaped the neuro-part of this thesis.

I would also like to thank all the other people who made this thesis possible: My thesis advisory committee, the members of the examination board, and the referees. My colleagues at the Max Planck Institute, who created such a welcoming work environment. Barbara, who helped me file my first (and every following) travel application and always had an open ear for issues both, of bureaucratic nature and not. Antje and Frauke, the coordinators of my graduate school, who helped always kindly and resourcefully with the formalities, which I severely underestimated.

Unsurprisingly for an undertaking of such duration, the extent of people who contributed goes beyond the work environment. I want to thank my family, foremost my parents and grandparents, who were there from the very beginning, long before a “*work environment*” was even a graspable concept for me. Thank you for supporting all my ideas and plans, no matter how futile. You laid the founding stones to make me the person I am today, and you taught me to love that person. Someone who also contributed greatly in that regard is my brother, Johannes. Growing up with you has shaped me in more ways than anything else, all of which I remember fondly and value greatly. Thank you!

I also want to thank all my dear friends, who joined me on my path, sometimes just a few miles, sometimes a lifetime. Thank you Nico and Max, and Kalli and Maik, whom I visit far too seldom but can always count on. Thank you to all the Goldis, who stand me even caffeine-deprived and who make our flat my home.

Finally, I want to express my deepest gratitude to my partner, Caro. Thank you for your love and patience, and for accepting me despite all my flaws. I am so lucky to have found a person who passionately enjoys as much as I do the joint moments of outrage about the flawed academic system — and all the rest. You are always there when I need you, and especially in those past months, you have been an immense support, helping me to see the silver lining when it was faint, and to enjoy the precious times with our little fur-nose. You make it all make sense.

I gratefully acknowledge support from the Max-Planck-Society, and funding by SMARTSTART, the joint training program in computational neuroscience by the VolkswagenStiftung and the Bernstein Network. I was further funded by the German Research Foundation (Deutsche Forschungsgemeinschaft, DFG), SFB-1528 — Cognition of Interaction.

Contents

Acknowledgements	6
List of publications	12
1 Introduction	15
1.1 Thesis outline	17
1.2 Background	18
1.2.1 Phase transitions in neuronal systems	18
1.2.2 Emergent dynamics shaped by network structure	20
1.2.3 Cultures of dissociated neurons	21
1.2.4 Human interaction networks	23
1.2.5 Non-Markovian dynamics	24
2 MR. Estimator, a toolbox to determine intrinsic timescales from subsampled spiking activity	25
2.1 Introduction	27
2.2 Workflow	28
2.3 Interpretation in a neuroscience context	32
2.4 Technical details	33
2.5 Discussion	40
References	45
3 Sampling effects and measurement overlap can bias the inference of neuronal avalanches	49
3.1 Introduction	52
3.2 Results	52
3.3 Discussion	62
3.4 Methods	63
References	68
Supplementary material, in appendix A	133

4	Modular architecture facilitates noise-driven control of synchrony in neuronal networks	73
4.1	Introduction	75
4.2	Results	76
4.3	Discussion	81
4.4	Materials and methods	82
	References and notes	85
	Supplementary material, in appendix B	149
5	How contact patterns destabilize and modulate epidemic outbreaks	87
5.1	Introduction	89
5.2	Results	90
5.3	Discussion	94
5.4	Methods	95
	References	98
	Comparison with real-world dispersion	100
	Supplementary material, in appendix C	183
6	Discussion	103
6.1	A question of perspective	104
6.1.1	The micro-macro problem	104
6.1.2	Inference and causal modeling	105
6.2	Dispersion, an example for the role of non-Markovian dynamics	106
6.2.1	Contact patterns cause dispersion	106
6.2.2	Encounter-trains: a powerful representation of contact networks	107
6.2.3	Next steps	109
6.3	Sampling bias	109
6.4	Revisiting the working point of neuronal systems	110
6.4.1	A unified picture of neuronal avalanches	110
6.4.2	Next steps	111
6.5	Conclusion and outlook	112
	Bibliography	115
	Appendices A–C: Supplementary material	133

List of publications

Publications [Ps1–Ps3] and [Ps5] constitute chapters of this thesis.

* Asterisks mark publications as first author or with equal contribution.

- Ps1* H. Yamamoto, **F. P. Spitzner**, T. Takemuro, V. Buendía, H. Murota, C. Morante, T. Konno, S. Sato, A. Hirano-Iwata, A. Levina, V. Priesemann, M. A. Muñoz, J. Zierenberg, and J. Soriano. “Modular Architecture Facilitates Noise-Driven Control of Synchrony in Neuronal Networks”. *Science Advances* 9 (2023): eade1755. DOI: [10.1126/sciadv.ade1755](https://doi.org/10.1126/sciadv.ade1755)
- Ps2* J. Zierenberg, **F. P. Spitzner**, J. Dehning, V. Priesemann, M. Weigel, and M. Wilczek. “How Contact Patterns Destabilize and Modulate Epidemic Outbreaks”. *New Journal of Physics* 25 (2023): 053033. DOI: [10.1088/1367-2630/acd1a7](https://doi.org/10.1088/1367-2630/acd1a7)
- Ps3* J. P. Neto, **F. P. Spitzner**, and V. Priesemann. “Sampling Effects and Measurement Overlap Can Bias the Inference of Neuronal Avalanches”. *PLoS Computational Biology* 18 (2022): e1010678. DOI: [10.1371/journal.pcbi.1010678](https://doi.org/10.1371/journal.pcbi.1010678)
- Ps4 K. Leite, P. Garg, **F. P. Spitzner**, S. Guerin Darvas, M. Bähr, V. Priesemann, and S. Kügler. “ α -Synuclein Impacts on Intrinsic Neuronal Network Activity Through Reduced Levels of Cyclic AMP and Diminished Numbers of Active Presynaptic Terminals”. *Frontiers in Molecular Neuroscience* 15 (2022): 868790. DOI: [10.3389/fnmol.2022.868790](https://doi.org/10.3389/fnmol.2022.868790)
- Ps5* **F. P. Spitzner**, J. Dehning, J. Wilting, A. Hagemann, J. P. Neto, J. Zierenberg, and V. Priesemann. “MR. Estimator, a Toolbox to Determine Intrinsic Timescales from Subsampled Spiking Activity”. *PLoS ONE* 16 (2021): e0249447. DOI: [10.1371/journal.pone.0249447](https://doi.org/10.1371/journal.pone.0249447)
- Ps6 S. Contreras, J. Dehning, M. Loidolt, J. Zierenberg, **F. P. Spitzner**, J. H. Urrea-Quintero, S. B. Mohr, M. Wilczek, M. Wibral, and V. Priesemann. “The Challenges of Containing SARS-CoV-2 via Test-Trace-and-Isolate”. *Nature Communications* 12 (2021): 378. DOI: [10.1038/s41467-020-20699-8](https://doi.org/10.1038/s41467-020-20699-8)

- Ps7 S. Contreras, J. Dehning, S. B. Mohr, S. Bauer, **F. P. Spitzner**, and V. Priesemann. “Low Case Numbers Enable Long-Term Stable Pandemic Control without Lockdowns”. *Science Advances* 7 (2021): eabg2243.
DOI: [10.1126/sciadv.abg2243](https://doi.org/10.1126/sciadv.abg2243)
- Ps8* J. Dehning, J. Zierenberg, **F. P. Spitzner**, M. Wibral, J. P. Neto, M. Wilczek, and V. Priesemann. “Inferring Change Points in the Spread of COVID-19 Reveals the Effectiveness of Interventions”. *Science* 369 (2020): eabb9789.
DOI: [10.1126/science.abb9789](https://doi.org/10.1126/science.abb9789)

Preprints

- Ps9 L. Rudelt, D. G. Marx, **F. P. Spitzner**, B. Cramer, J. Zierenberg, and V. Priesemann. “Signatures of Hierarchical Temporal Processing in the Mouse Visual System”. 2023.
DOI: [10.48550/arXiv.2305.13427](https://doi.org/10.48550/arXiv.2305.13427)
- Ps10 A. Hagemann, M. S. Kehl, J. Dehning, **F. P. Spitzner**, J. Niediek, M. Wibral, F. Mormann, and V. Priesemann. “Intrinsic Timescales of Spiking Activity in Humans during Wakefulness and Sleep”. 2022.
DOI: [10.48550/arXiv.2205.10308](https://doi.org/10.48550/arXiv.2205.10308)
- Ps11* J. Dehning, **F. P. Spitzner**, M. C. Linden, S. B. Mohr, J. P. Neto, J. Zierenberg, M. Wibral, M. Wilczek, and V. Priesemann. “Model-Based and Model-Free Characterization of Epidemic Outbreaks”. 2020.
DOI: [10.1101/2020.09.16.20187484](https://doi.org/10.1101/2020.09.16.20187484)

Past work

- Ps12* **F. P. Spitzner**, J. Zierenberg, and W. Janke. “The Droplet Formation-Dissolution Transition in Different Ensembles: Finite-size Scaling from Two Perspectives”. *SciPost Physics* 5 (2018): 062. DOI: [10.21468/SciPostPhys.5.6.062](https://doi.org/10.21468/SciPostPhys.5.6.062)
- Ps13 J. Zierenberg, N. Fricke, M. Marenz, **F. P. Spitzner**, V. Blavatska, and W. Janke. “Percolation Thresholds and Fractal Dimensions for Square and Cubic Lattices with Long-Range Correlated Defects”. *Physical Review E* 96 (2017): 062125.
DOI: [10.1103/PhysRevE.96.062125](https://doi.org/10.1103/PhysRevE.96.062125)
- Ps14 N. Fricke, J. Zierenberg, M. Marenz, **F. P. Spitzner**, V. Blavatska, and W. Janke. “Scaling Laws for Random Walks in Long-Range Correlated Disordered Media”. *Condensed Matter Physics* 20 (2017): 13004. DOI: [10.5488/CMP.20.13004](https://doi.org/10.5488/CMP.20.13004)

1 Introduction

Complex networks appear across various contexts of our lives. Telecommunication, transport, infrastructure and finance are candidates to come to mind, and we humans ourselves, just going about our day as usual, meeting others, create a complex network of contacts. Also in our bodies, we can find intricate complex networks, not just of metabolic and molecular interactions, but in a structural sense. As a particular example, consider the human brain, where the cortex alone is built of 16×10^9 neurons, forming far-from-random structures, which are reflected e.g. in columns and hierarchical areas, each associated with distinct functional benefits or evolutionary necessity [1].

These networks can form a backbone on which spreading processes unfold [2]. In the nervous system, action potentials propagate from one neuron to the next, potentially forming ongoing cascades as activity spreads through the underlying network. On social media, news passes from one person to the next, causing a seemingly unpredictable spread of information. The way information travels then depends on who talks to whom or, more generally, the structure of the communication network. For example, once a piece of news is shared by an influencer with millions of followers, the reach of this news increases dramatically. Such network nodes with more-than-average links are commonly referred to as *hubs*, and they can greatly affect the spread on the network [3, 4]. There are many other structural features of networks that affect spreading, such as *small-world-ness* [5], *clustering* [6, 7], or densely connected *communities* where interactions between members of the community are more likely than with outsiders [3, 8, 9]. In many cases, they imply a structural heterogeneity that alters the spreading dynamics compared to a homogeneous network [10].

In this thesis, we discuss two examples where particular structural aspects of a network interplay with a spreading process to give rise to remarkable emergent dynamics: i) As a well-controlled neuronal system, we consider *in vitro* cultures of cortical neurons that are engineered to feature a modular topology [11]. Notably, in neuronal systems, the network structure is not only the backbone of activity propagation but also represents a form of information storage, as memories are formed through long-lasting changes of the connection strength between neurons [12]. One could say *structure is knowledge*. ii) As an example of disease spread on a human contact network, we explore face-to-face contact

1 Introduction

data of university students [13] and study the interplay of contact patterns and disease progression. In both examples, our models go beyond a spreading process unfolding on a static network. We take into account that the spreading dynamics are not isolated and find that interactions with the environment can lead to unforeseen emergent dynamics.

1.1 Thesis outline

We investigate how spreading processes are modulated by the underlying structure. To that end, we develop tools to quantify the dynamics in an unbiased manner from sparse data and showcase how recording parameters can affect the inference. We then consider two examples, *in vitro* neuronal cultures and a human contact network, where rich dynamics unfold on a topological backbone.

In Chapter 2, we showcase our software package that enables an unbiased estimation of the autocorrelation time from heavily subsampled activity in various contexts. Although the implemented multistep-regression estimator derives from a simple branching process, the tool has found wide application and helped to infer the distance to criticality in several studies [Ps3, Ps9, Ps10, 14–17].

In Chapter 3, we focus on the neuroscience context and investigate how measurement overlap and recording parameters affect the observed dynamics. We find that it is not essential to record as many units (or as large a fraction) of the system as possible, but models need to be tailored to the available measurements and data; in the case of neuronal recordings, spikes are favorable over coarse measures such as local field potentials (LFP).

In Chapter 4, we investigate engineered cultures of cortical neurons that feature a modular topology. Using spiking data from optical recordings, we find that the modular architecture facilitates control of the global dynamic state through a noisy input. Due to the inhomogeneous connectivity (highly connected within modules, sparsely connected across modules), the noisy input reduces the stochastic inter-module activity propagation, while modules remain synchronized. Notably, optical recordings of *in vitro* cultures enable a nearly perfect spatial sampling at single-cell resolution, which allows us to draw the connection between single-unit and larger-scale dynamics. Here, we find that a parsimonious, effective description — where modules form the smallest units — can be sufficient to describe system-wide dynamics.

In Chapter 5, we turn to an example where perfect sampling is not possible (and hopefully never will be): Human contact networks. Similar to Chapter 4 we investigate if, and at what scale, effective descriptions of the spatio-temporal structure are sufficient to describe relevant macroscopic dynamics. In particular, this work is motivated by the question to which extent the well-mixed and Markovian assumptions underlying common compartmental models of disease spread are warranted. We develop a statistical description of human contact networks that reflects macroscopic observables relevant to disease spread, and find that generative models of human contact patterns need to be non-Markovian.

In Chapter 6, we present an overarching discussion and future perspectives.

1.2 Background

1.2.1 Phase transitions in neuronal systems

Depending on system parameters (including but not exclusive to underlying structural properties) spreading processes exhibit vastly different dynamics. For instance, the spread of an infectious disease could be stable, with case numbers relaxing to some finite value after a small perturbation occurred, or it could be unstable, with case numbers increasing until a large fraction of the population has been infected. Motivated by concepts from statistical physics, these different regimes are often called phases, and each phase comes with its own characteristic dynamic states and configurations. When the system changes from one phase to another, it is said to undergo a non-equilibrium *phase transition* [18, 19]. There are diverse types of non-equilibrium phase transitions, but the most well-known examples are from stable to unstable, synchronous to asynchronous, or absorbing to active. Often, these transitions are accompanied by emerging correlations: As the system undergoes the transition, the spatial and temporal distance for which system variables are statistically dependent diverges. For example, for absorbing-to-active transitions, when the distance to the transition becomes small, $\epsilon \rightarrow 0$, the correlation length and time diverge with respective *critical exponents* [19]:

$$\xi_{\perp} \sim |\epsilon|^{-\nu_{\perp}} \quad \text{and} \quad \xi_{\parallel} \sim |\epsilon|^{-\nu_{\parallel}}.$$

In a neuroscience context, a parsimonious model of neural activity propagation that features an absorbing-to-active transition is the driven branching network. In this case, the transition is controlled by the branching parameter m , which, in simple words, describes how many further activations a previous activation will cause; it determines if the system is in the absorbing phase with low activity ($m < m_{\text{crit}}$) or in the active phase ($m > m_{\text{crit}}$) [20]. Closely related, when the network topology and coalescence effects [21] are not of primary interest, the simpler *branching process* [22, 23] can be used, for which a similar transition occurs at $m_{\text{crit}} = 1$, where on expectation, every activation causes exactly one other activation. The branching process is of particular interest in this thesis because it serves as a minimal model also for disease spread (Chapter 5), and the *autocorrelation time*, which is in this context often denoted by τ instead of ξ_{\parallel} , can be directly linked to the branching parameter (Chapter 2).

Focusing on a single neuron, the autocorrelation time describes the duration over which the neuron's current state (e.g. its firing rate) is related to its past state, and it serves as a proxy for working memory [24, 25]. Because information storage is a central aspect of

computation [26], the large correlations that accompany many phase transitions could be considered beneficial for information processing [20, 27, 28]. However, because computational performance depends on other metrics, too, there cannot be a working point that is universally ideal — independent of context or example. Rather, depending on the task at hand, requirements often vary and oppose one another [29, 30].

Despite this intuitive conundrum (*or maybe, because of it*), the notion that neuronal systems benefit from operating near a non-equilibrium phase transition has received tremendous attention [20, 23, 29, 31–37]. Considering a neural system’s dynamics as either stable or unstable, the charm of this so-called *critical brain hypothesis* can be easily seen: In the low-activity phase, the network responds fast to perturbations such as presented stimuli, but correlations (in time and space) are low, which is undesirable. For instance, the movement of a limb easily extends over multiple seconds, requiring coordination (and thus, correlation) over a time period that is much longer than the millisecond timescale of neuronal firing. On the other hand, in the unstable phase, activity would spread uncontrollably (such as seen in epilepsy patients [36]), hindering activity-based computation. Thus, the ideal operating point would be directly at (or very near to) the transition, where correlations are large. This entails scale-free (power-law) statistics and the separation of timescales [31], precise selectivity [20], and diverse dynamics, with a maximal number of metastable states and network responses [38].

However, a critical brain also faces conceptual challenges: An increase in the variability of network responses is accompanied by a decrease in specificity [39] and reliability [40, 41]. In other words, if the space of responses is infinite, how can a particular input lead to a meaningful and deterministic response, as would be required from a reliable computing device? Further, at criticality, the time until a past stimulus is cleared or forgotten becomes infinite, which, assuming serial computation, prevents the next input from being processed. This so-called critical slowing down is a consequence of the diverging correlations and it occurs already before the transition point is reached [42]. To summarize, not all properties associated with criticality are beneficial for computing, and some already manifest in the vicinity of the transition. Thus, rather than maximizing a single property, “*sufficient performance for a given task is a more likely design principle*” [29].

An elegant concept that addresses contradictions around the critical brain hypothesis has been introduced as *dynamic adaptive computation* [29, 40]. Dynamic adaptive computation builds on the idea that instead of a single working point, there is a *regime* of operation around criticality, and that the dynamics of the system, (and, thereby, computing properties) change swiftly when a control parameter is altered. Reconsidering the branching process, the susceptibility $\chi \sim |\epsilon|^{-\gamma}$ diverges when the distance to criticality

1 Introduction

$\epsilon = m - m_{\text{crit}}$ becomes small. Note that χ is a response function, and it can be seen as the sensitivity that describes the relative impact of an external perturbation. In particular, to adapt the sensitivity according to e.g. task requirements, a small modulatory change to Δm has the greatest effect when $m \approx 1$. Avoiding $m > 1$, to allow a safety margin from instability, the ideal regime of operation would thus be slightly subcritical [29]. Such a *reverberating* regime has found experimental support *in vivo* [43, 44], but evidence from *in vitro* studies is less clear, which we discuss in detail in Chapter 3. Two open questions that remain are how adaptive tuning is biologically implemented, and which role structural heterogeneity plays.

1.2.2 Emergent dynamics shaped by network structure

Before returning to neuronal systems, let us consider a curious and relatable example from everyday life that illustrates how sensitive dynamic processes are to the network structure on which they unfold. In infrastructure networks, whose function often relies on a precisely set working point, even subtle changes in the structure can be detrimental. Contrary to intuition, an expansion of the network (creating new links to improve overall performance) can have the opposite effect — a phenomenon known as *Braess' paradox* [45]. It can be found in a variety of networks and has gained recent attention for power grid extensions [46], where the augmentation and addition of grid links are given necessities. However, these changes affect how load and flow are distributed, potentially altering preferential pathways. Due to the conservation of energy, and if no new sources are added, an increased flow through reinforced links also causes an increased flow in unchanged links [46]. Previously underused links may now become a preferred path, pushing them closer to their capacity limit. Although power grids are only loosely comparable to biological systems, this example illustrates how sensitive the dynamics unfolding on networks are to the underlying structure.

Also in neuronal systems, the underlying structure affects the resulting dynamics in countless ways, and often, distinct structural aspects can be linked to specific functions [47]. Cortical *areas* are generally associated with distinct sensory, motor, or associative functions [48, 49], whereas (horizontal) *layers* organize the cortical connectivity [50, 51], traversed by (vertical) *columns* that form the canonical processing units of the cortex [52]. These meso- and macroscopic structures form from diverse cellular types of neurons that are again structurally and functionally distinct [53, 54]. However, in general, elucidating the connection between structure, dynamics, and function remains challenging [55, 56].

In modeling studies and *in vitro*, on the other hand, the connection between structure, dynamics, and, to an extent also function, can often be rigorously established. For instance,

large-scale dynamical models revealed that the heterogeneities across areas and inter-areal connections give rise to a range of dynamic working points, where a *hierarchy of timescales* satisfies different functional requirements (fast processing for sensory information vs. long integration for motor control) [57]. On a more abstract level, modular and hierarchical organization (such as of the human connectome) has been shown to enable extended regions of criticality [58–60]. These *Griffiths phases* occur when structural inhomogeneities such as disorder or random defects produce rare regions that are only weakly coupled. The rare regions can isolate and confine activity, causing it to develop distinctly from the surrounding [59, 61–63], which, in turn, smears out and shifts the dynamic transition point — with network responses diverging all along the extended critical region [59, 63]. Thus, yielding the associated functional benefits like pattern richness and large dynamic range, this example illustrates how structure, dynamics, and function can be linked in a principled way.

1.2.3 Cultures of dissociated neurons

A principled understanding has also long been the main motivation for experiments of neuronal cultures [64, 65]. In such preparations, experimentalists can electrophysiologically probe individual neurons with relative ease: *Patch-clamping* [66, 67] enabled studies of single-neuron dynamics and the interactions between pairs of neurons, while recordings stemming from *Multi-electrode arrays* [68] or optical *fluorescence imaging* [69] yield a wider perspective at the network level.

In particular, using cultures of dissociated neurons *in vitro*, these two perspectives can be exploited together to link single-neuron properties to (functional) network structure, and emergent dynamics (see [70] for a recent example). To create such a system, neurons are first extracted and dissolved in liquid media, before being plated on suitable substrates where they reattach and grow. This procedure disrupts any network structure that might have formed before extraction, but it offers great control over the resulting system and enables bottom-up studies. For example, depending on the plated neuron density, a rich repertoire of the characteristic *network bursts* manifests [71], which also depends on development age [71–76], the extent of spatial aggregation [77–79], the formation of a percolating cluster of connections [80–82] or the interplay between topology and dynamic noise [83, 84].

On the one hand, precise control over the cultures' structure enables experimentalists to design network structures that shape certain dynamics e.g. as 1-dimensional communication channels [85], logic devices such as AND-gates or diodes [86], or increasingly complex modular assemblies [11, 87, 88] to mimic, for instance, feed-forward

layering [89]. On the other hand, under suitable conditions, cultures also self-organize into such topologies that enable rich, proposedly close-to-critical, dynamics [74, 75, 90–92]. For example, as the cultures mature, the connectivity profile changes [82, 93], with the density of synapses increasing [94, 95], and resulting dynamics reflect these changes [73, 74]. Initially, individual spikes occur sporadically (as connections are still sparse) but become more correlated over time [73]; intense network-wide bursts tend to form at around 14 days-in-vitro [73, 96], and settle to more variable dynamic states over the following weeks [71, 73–75]. In this self-organization process, two aspects stand out: i) to support dynamics beyond network-wide bursts, the structures that form are heterogeneous and modular [77, 92, 97] and ii) they develop in an activity-dependent manner [74, 98].

The activity-dependent development can be driven by various types of *plasticity* [99, 100], each describing a specific way in which properties like the connections between neurons change in response to their firing. The best-known type of plasticity is Hebbian plasticity [101] commonly quoted as “*neurons that fire together wire together*” [102]. More elaborate formulations like spike-timing-dependent plasticity (STDP) go beyond the temporal proximity between spikes and consider their order [103]. For example, the connection between two neurons could be strengthened if a post-synaptic neuron spiked shortly after the pre-synaptic neuron (although it might be weakened if the post-synaptic neuron fired first [103]). In both cases, the shorter the delay between spikes, the stronger the structural change. This implies that the characteristic *in vitro* network bursts — with rapid activations — should be a key determinant that shapes network structure.

A phenomenon that is similar to synchronized bursts can also be found *in vivo*: in the form of pre-natal, self-generated, *retinal waves* [104]. Retinal waves propagate throughout the entire visual system [105], and evidence suggests that they play a central role in the development of the visual system [104, 106]. This opens an intriguing perspective on spontaneous activity in cortex: It was recently proposed that self-generated activity before birth (in the absence of visual stimuli) could act as an effective pre-training that allows faster learning once stimuli are presented [107] — which again stresses the role of background activity. Similarly, in the developed cortex, ongoing background activity stems from the many projections from other brain areas, such as asynchronous inputs from the thalamus that proposedly modulate cortical synchronization [108–110].

Together, this leads to the question of how emergent system-wide events are controlled mechanistically by asynchronous input. We will address this question in Chapter 4, where we go beyond a heuristic description of synchrony in cultures, and, using modeling at different scales, propose an underlying adaptation mechanism that explains the transient input dependence on short timescales.

1.2.4 Human interaction networks

As another example of the pivotal role of structure in complex networks, we consider human interaction networks, because they exhibit a barrage of structural properties whose effects have motivated decades of research [3, 111]. The probably most famous property of human contact networks is that any two people know each other through six contacts or less [112]. The *small-world* effect goes back to experiments on (offline) social networks [113] and it describes that the mean path length between network nodes increases at most logarithmically with the total number of nodes [114], which can lead to very fast spreading of information or infectious diseases [5]. At the same time, not all human relations are equal. We may have hundreds of acquaintances, but only a few good friends in our closest circle or *layer* [115]. When we are introduced to new people, the introduction is often made by a mutual friend. This preferential attachment leads to the formation of *clusters* [7, 114], and in the corresponding contact network, two nodes that share a common neighbor are likely to be connected directly. Preferential attachment also leads to scale-free degree distributions and *hubs* that have a higher-than-expected number of links [116], like, for example, a salesperson who meets many clients on a daily basis. When considering disease spread on physical contact networks, such hubs can affect the spread in non-trivial ways [117, 118] as they are likely the first to become infected, but also immune. Further, because of the various contexts in which humans interact (from work to the karate club, at university, in one's family or with friends), the contact networks that span across these contexts are *modular*: Nodes form groups of high connectivity [119], which might themselves divide into groups of groups and so forth, creating a hierarchical organization [120] of overlapping communities [121, 122]. Together, all these features emphasize the rich structures we can find in human contact networks.

Crucially, the “*structure*” of contact networks is not limited to static (or spatial) aspects such as who interacts with whom. Rather, they are constantly evolving—raising the question of who interacts and *when*. This requires a more subtle perspective than a spreading process developing on a static network that acts as the topological backbone. If the timescales of the spreading process are close to those of the network changes, the spreading becomes impossible to disentangle from the dynamics of the network itself, and a holistic approach is required [10]. In that regard, the framework of *temporal networks* is useful, as it directly incorporates that links (contacts) between nodes are transient [123]. Although taking temporal information into account seems more complex than a static description, it allows to uncover community evolution [124], and can at times even simplify the picture, directly exposing features such as gatherings and social cores [125]. As we will also explore in Chapter 5, despite its complexity, much of the temporal structure follows

1 Introduction

reoccurring schedules [125, 126], or, in simple words, our memory of which day of the week it is.

1.2.5 Non-Markovian dynamics

Many processes in nature and everyday life are memoryless and can be modeled by a Markov process [127]. A simple example is a board game where moves are determined by rolling a dice. At any time step t in such a game, the potential next moves X_{t+1} only depend on the player's position i and the rolled dice, but not how the player got there (i_{t-1}, \dots, i_0):

$$P(X_{t+1} = j \mid X_t = i, X_{t-1} = i_{t-1}, \dots, X_0 = i_0) = P(X_{t+1} = j \mid X_t = i).$$

This so-called Markov property often makes it feasible to treat models analytically [127], but it is violated whenever the system described by the model has memory or history dependence.

Both, human contact networks and neural networks are examples of such systems, where dynamics are non-Markovian. In contact networks, this manifests through clustering and correlated contact times; *if you encounter the bus driver, you are also likely to encounter fellow passengers*. In neuronal networks, it manifests as memory on the network level but also for individual nodes, through plasticity or refractoriness; most neurons that just spiked are unlikely to spike again within the next few milliseconds [128]. Indeed, the non-Markovian nature is baked into most models of neuronal firing, where membrane potentials are modeled to integrate presynaptic currents over time. Conversely, models of contact networks and disease spread often assume the Markov property, for example through memoryless, Poissonian agents or well-mixed compartments (with exponentially distributed transition times). Of course, this seeming inconsistency remains purely conceptual, as long as the model can successfully reproduce the observed data. However, it raises the question under which conditions Markovian models fail, and how they compare to non-Markovian ones [129–136]. For the particular case of disease outbreaks on a human contact network, we address this question in Chapter 5.

2


MR. Estimator, a toolbox to determine intrinsic timescales from subsampled spiking activity

Published in PLoS ONE (2021)

DOI [10.1371/journal.pone.0249447](https://doi.org/10.1371/journal.pone.0249447)

Preprint [arXiv:2007.03367](https://arxiv.org/abs/2007.03367)

Source code github.com/Priesemann-Group/mrestimator

License 

Own contributions

- ✓ Conceptualization
- ✓ Methodology
- ✓ Software
- ✓ Validation
- ✓ Formal Analysis
- ✓ Investigation
- Resources
- ✓ Data Curation
- ✓ Writing — Original Draft
- ✓ Writing — Review & Editing
- ✓ Visualization
- Supervision
- Project Administration
- Funding Acquisition

I developed the software presented in this chapter, with contributions from JD. The mathematical background was developed by JW and VP, and has been previously published in [137]. I investigated the dependence on trial-length and methods for estimating correlation coefficients. I created all figures. All authors wrote the manuscript.

RESEARCH ARTICLE

MR. Estimator, a toolbox to determine intrinsic timescales from subsampled spiking activity

F. P. Spitzner^{1*}, J. Dehning¹, J. Wilting¹, A. Hagemann¹, J. P. Neto¹, J. Zierenberg¹, V. Priesemann^{1,2*}¹ Max-Planck-Institute for Dynamics and Self-Organization, Göttingen, Germany, ² Bernstein-Center for Computational Neuroscience (BCCN) Göttingen, Göttingen, Germany* paul.spitzner@ds.mpg.de (EPS); viola.priesemann@ds.mpg.de (VP)

OPEN ACCESS

Citation: Spitzner FP, Dehning J, Wilting J, Hagemann A, P. Neto J, Zierenberg J, et al. (2021) MR. Estimator, a toolbox to determine intrinsic timescales from subsampled spiking activity. PLoS ONE 16(4): e0249447. <https://doi.org/10.1371/journal.pone.0249447>

Editor: Michal Zochowski, University of Michigan, UNITED STATES

Received: October 6, 2020

Accepted: March 18, 2021

Published: April 29, 2021

Peer Review History: PLOS recognizes the benefits of transparency in the peer review process; therefore, we enable the publication of all of the content of peer review and author responses alongside final, published articles. The editorial history of this article is available here: <https://doi.org/10.1371/journal.pone.0249447>

Copyright: © 2021 Spitzner et al. This is an open access article distributed under the terms of the [Creative Commons Attribution License](https://creativecommons.org/licenses/by/4.0/), which permits unrestricted use, distribution, and reproduction in any medium, provided the original author and source are credited.

Data Availability Statement: Referenced scripts are available at <https://github.com/Priesemann-Group/mrestimator/blob/v0.1.7/examples/paper>

Abstract

Here we present our Python toolbox “MR. Estimator” to reliably estimate the intrinsic time-scale from electrophysiological recordings of heavily subsampled systems. Originally intended for the analysis of time series from neuronal spiking activity, our toolbox is applicable to a wide range of systems where subsampling—the difficulty to observe the whole system in full detail—limits our capability to record. Applications range from epidemic spreading to any system that can be represented by an autoregressive process. In the context of neuroscience, the intrinsic timescale can be thought of as the duration over which any perturbation reverberates within the network; it has been used as a key observable to investigate a functional hierarchy across the primate cortex and serves as a measure of working memory. It is also a proxy for the distance to criticality and quantifies a system’s dynamic working point.

1 Introduction

Recent discoveries in the field of computational neuroscience suggest a major role of the so-called intrinsic timescale for functional brain dynamics [1–8]. Intuitively, the intrinsic timescale characterizes the decay time of an exponentially decaying autocorrelation function (in this work and in many contexts it is synonymous to the autocorrelation time). Exponentially decaying correlations are commonly found in recurrent networks (see e.g. Refs. [5, 9]), where the intrinsic timescale can be related to information storage and transfer [10–12]. More importantly, such decaying autocorrelations are also found in the network-spiking-dynamics recorded in the brain: Here, the intrinsic timescale serves as a measure to quantify working memory [3, 4] and unravels a temporal hierarchy of processing in primates [1, 2].

Although autocorrelations and the intrinsic timescale can be derived from single neuron activity, they characterize the dynamics within the whole recurrent network. The single neuron basically serves as a readout for the local network activity. One can consider spiking activity in a recurrent network as a branching or spreading process, where each presynaptic spike triggers on average a certain number m of postsynaptic spikes [13–15]. Such a spreading process

Simulation data are available at <https://doi.org/10.12751/g-node.licm4y>.

Funding: FPS and JD were funded by the Volkswagen Foundation through the SMARTSTART Joint Training Program Computational Neuroscience. JZ is supported by the Joachim Herz Stiftung. All authors acknowledge funding by the Max Planck Society. The funders had no role in study design, data collection and analysis, decision to publish, or preparation of the manuscript.

Competing interests: The authors have declared that no competing interests exist.

typically features an exponentially decaying autocorrelation function, and the associated time constant is in principle accessible from the activity of each unit. However, approaching the single-unit level, the magnitude of the autocorrelation function can be much smaller than expected, and can be disguised by noise.

In experiments we approach this level: we typically sample only a small part of the system, sometimes only a single or a dozen of units. This subsampling problem is especially problematic in neuroscience, where even the most advanced electrode measurements can record at most a few thousand out of the billions of neurons in the brain [16, 17]. However, we recently showed that this spatial subsampling only biases the magnitude of the autocorrelation function (of autoregressive processes) and that—despite the bias—the associated intrinsic timescale can still be inferred by using multi-step regression (MR). Because the intrinsic timescale inferred by MR is invariant to spatial subsampling, one can infer it even when recording only a small set of units [5].

Here, we present our Python toolbox “MR. Estimator” that implements MR to estimate the intrinsic timescale of spiking activity, even for heavily subsampled systems. Since our method is based on spreading processes in complex systems, it is applicable beyond neuroscience, e.g. in epidemiology or social sciences such as the timescale of epidemic spreading (from subsampled infection counts) [5] or the timescale of opinion spreading (from subsampled social networks) [18].

The main advantage of using our toolbox over a custom implementation to determine intrinsic timescales is that it provides a consistent way that can now be adopted across studies. It supports trial structures and we demonstrate how multiple trials can be combined to compensate for short individual trials. Lastly, the toolbox calculates confidence intervals by default, when a trial structure is provided.

In the following, we discuss how to apply the toolbox using a code example (Sec. 2). We then briefly focus on the neuroscience context (including a real-life example, Sec. 3) before we derive the MR estimator and discuss technical details such as the impact of short trials (Sec. 4). While of general interest, this section is not required for a general understanding of the toolbox. In the discussion (Sec. 5), we present selected examples where intrinsic timescales play an important role. Lastly, an overview of parameters and toolbox functions is given in Tables 1 and 2 at the end of the document.

2 Workflow

To illustrate a typical workflow, we now discuss an example script that generates an overview panel of results, as depicted in Fig 1. The discussed script and other examples are provided online [19].

In the example, we generate a time series from a branching process with a known intrinsic timescale (Fig 1A). At the discrete time steps Δt of such a branching process, every active unit activates a random number of units (on average m units) for the next time step. As this principle holds for any unit, activity can spread like a cascade or avalanche over the system. Taking the perspective of the entire system, the current activity A_t (or number of active units) depends on the previous activity and the branching parameter m . Then, the branching parameter is directly linked to the intrinsic timescale $\tau = -\Delta t / \ln(m)$: As m becomes closer one, τ grows to infinity (for the mathematical background, see Sec. 4). Because τ corresponds to the decay time of the autocorrelation function (Fig 1C), a larger τ will cause a slower decay.

With this motivation in mind, it is the main task of the toolbox to determine the *correlation coefficients* r_k —that describe the autocorrelation function of the data—and to *fit* an analytic autocorrelation function to the determined r_k —which then yields the intrinsic time scale. In

Table 1. List of the most common parameters and functions where they are used. For a full list of each function’s possible arguments, please refer to the online documentation [43].

Symbol	Parameter description	Function	Example argument
k	Discrete time steps of correlation coefficients (shift between original and delayed time series)	<code>full_analysis()</code>	<code>kmax = 1000</code>
		<code>coefficients()</code>	<code>steps=(1, 1000)</code>
		<code>fit()</code>	<code>steps=(1, 1000)</code>
	Unit of discrete time steps	<code>full_analysis()</code>	<code>dtunit='ms'</code>
		<code>coefficients()</code>	<code>dtunit='ms'</code>
		<code>fit()</code>	<code>dtunit='ms'</code>
Δt	Size of the discrete time steps in dtunits	<code>full_analysis()</code>	<code>dt = 4</code>
		<code>coefficients()</code>	<code>dt = 4</code>
		<code>fit()</code>	<code>dt = 4</code>
r_k	Correlation coefficients	<code>fit()</code>	<code>data</code>
	Method for calculating r_k	<code>full_analysis()</code>	<code>coefficientmethod='sm'</code>
		<code>coefficients()</code>	<code>method='ts'</code>
	Selecting Fitfunctions:	<code>full_analysis()</code>	<code>fitfuncs=['exp', 'offset', 'complex']</code>
		<code>fit()</code>	<code>fitfunc='exp'</code>
α	Subsampling fraction	<code>simulate_subsampling()</code>	<code>prob</code>
		<code>simulate_branching()</code>	<code>subp</code>
$\langle A_t \rangle$	Activity (e.g. of a branching process)	<code>simulate_branching()</code>	<code>a = 1000</code>
m	Branching parameter	<code>simulate_branching()</code>	<code>m = 0.98</code>
h	External input	<code>simulate_branching()</code>	<code>h = 100</code>
		<code>full_analysis()</code>	<code>numboot = 100, seed = 101</code>
		<code>coefficients()</code>	<code>numboot = 100, seed = 102</code>
	Bootstrapping: number of samples, rng seed	<code>fit()</code>	<code>numboot = 100, seed = 103</code>

<https://doi.org/10.1371/journal.pone.0249447.t001>

the example, we determined r_k with the toolbox’s default settings (Fig 1C) and we fitted two alternative exponentially decaying functions to determine the intrinsic timescale (a plain exponential and an exponential that is shifted by an offset). The toolbox returns estimates and 75% confidence intervals for the branching parameter and the intrinsic timescale (Fig 1D); the estimates match the known values $m = 0.98$ and $\tau \approx 49.5$ that were used in the example. To demonstrate the effect of subsampling in the example, we recorded only 5% of the occurring events of the branching process.

Listing 1. Example script (Python) that creates artificial data from a branching process and performs the multistep regression. An example to import experimental data is available online, along with detailed documentation explaining all function arguments [19].

Table 2. The (lengthy) descriptions of fit-functions and coefficient-methods can be abbreviated.

Full name	Abbreviation
<code>'trialseparated'</code>	<code>'ts'</code>
<code>'stationarymean'</code>	<code>'sm'</code>
<code>'exponential'</code>	<code>'e', 'exp'</code>
<code>'exponential_offset'</code>	<code>'eo', 'exp_offset', 'exp_off'</code>
<code>'complex'</code>	<code>'c', 'cplx'</code>

<https://doi.org/10.1371/journal.pone.0249447.t002>

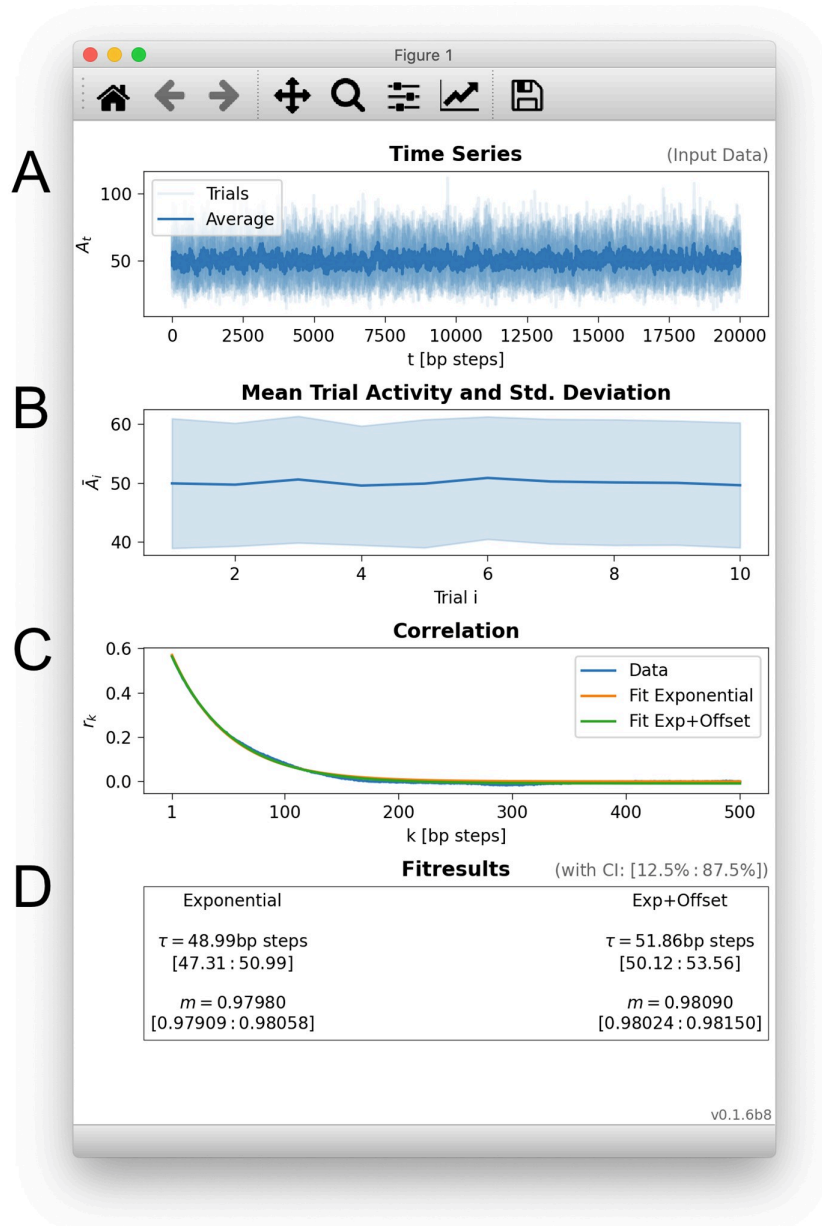


Fig 1. The toolbox provides a `full_analysis()` function that performs all required steps and produces an overview panel. A: Time series of the input data, here the activity A_t , of ten trials of a branching process with $m = 0.98$ and $\tau = \Delta t / \ln(m) \approx 49.5$ steps (Δt is the step size of the branching process). **B:** Mean activity and standard deviation of activity for each trial. This display can reveal systematic drifts or changes across trials. **C:** Correlation coefficients r_k are determined from the input data, and exponentially decaying autocorrelation functions are fitted to the r_k . Several alternative fit functions can be chosen. **D:** The decay time of the autocorrelation function corresponds to the intrinsic timescale τ , and allows to infer the corresponding branching parameter m . The shown fit results contain confidence intervals in square brackets (75% by default).

<https://doi.org/10.1371/journal.pone.0249447.g001>

```
# load the toolbox
import mrestimator as mre

# enable matplotlib interactive mode so
# figures are shown automatically
mre.plt.ion ()

# 1. -----#
# example data from branching process
bp = mre.simulate_branching (m = 0.98, a = 1000,
subp = 0.05, length = 20000, numtrials = 10, seed = 43771)
# make sure the data has the right format
src = mre.input_handler (bp)

# 2. -----#
# calculate autocorrelation coefficients,
# embed information about the time steps
rks = mre.coefficients (src, steps = (1, 500), dt = 1, dtu-
nit = 'bp steps', method = 'trialeparated')

# 3. -----#
# fit an autocorrelation function, here
# exponential (without and with offset)
fit1 = mre.fit(rks, fitfunc = 'exp')
fit2 = mre.fit(rks, fitfunc = 'exp_offset')

# 4. -----#
# create an output handler instance
out = mre.OutputHandler ([rks, fit1, fit2])
# save to disk
out.save ('~/mre_example/result')

# 5. -----#
# gives same output with other file title
out2 = mre.full_analysis (data = bp, dt = 1, kmax = 500,
dtunit = 'bp steps', coefficientmethod = 'trialeparated',
fitfuncs = ['exp', 'exp_offset'], targetdir = '~/mre_exam-
ple/')
```

1. Prepare data: After the toolbox is loaded, the input data needs to be in the right format: a 2D NumPy array [20–22]. To support a trial structure, the first index of the array corresponds to the trial (even when there is only one trial), the second index corresponds to the time (in fixed time steps). All trials need to have the same length.

We provide an optional `input_handler()` that tries to guess the passed format and convert it automatically. For instance, it can check and convert data that is already loaded (as shown in Listing 1) or load files from disk, when a file path is provided.

2. Multiple regressions: Once the data is in the right format, multiple linear regressions are initiated by calling `coefficients()` (see Sec. 4.3 for more details). The function performs linear regressions between the original time series (`src`), and the same time series after it was shifted by k time steps. It returns the slopes found by the regression—we call them correlation coefficients r_k (`rks`). Here, we specify to calculate the correlation coefficients for steps $1 \leq k \leq 500$. In Listing 1, the linear regression is performed for each trial separately. To obtain a joint estimate across all trials, the estimated r_k are averaged (`trialseparated` method). Confidence intervals are calculated using bootstrapping.

Please note that (independent from subsampling) the linear regression can be biased due to short trials [23, 24]. In case of stationary activity across trials, the issue can be circumvented by using the `stationarymean` method (see Sec. 4.3 and Fig 5).

3. Fit the autocorrelation function: Next, we fit the correlation coefficients using a desired function (`fitfunc`). In order to estimate the intrinsic timescale, this function needs to decay exponentially. Motivated by recent experimental studies [1], the default function is `exponential_offset` (other options include an `exponential` and a `complex` fit with empirical corrections).

4. Visualize and store results: Multiple correlation coefficients and fits can be exported using an instance of `OutputHandler`. The `save()` function not only exports a plot but also a text file containing the full information that is required to reproduce it.

5. Wrapping up: For convenience, the `full_analysis()` function performs all steps with default parameters and displays an overview panel as shown in Fig 1.

3 Interpretation in a neuroscience context

Timescales of neural dynamics have been analyzed in various contexts and can be interpreted as reward memory [25] or as temporal receptive windows [26]. Here, however, we focus on the timescale of the decay of the autocorrelation function [1], which is thought to be related to the duration of integration in local circuits [2] or to working memory [3, 4]. As such, the intrinsic timescale represents a measure of how long information is kept (or can be integrated) in a local circuit; it ranges between 50 to 500 ms and this diversity of timescales is believed to arise from differences in local connectivity [27, 28].

In the brain, the autocorrelation function is not only determined by the intrinsic timescale. If the spiking activity is dominated by a single timescale τ , the autocorrelation is expected to decay exponentially (see Sec. 4): $C(k) \propto \exp(-\frac{k}{\tau})$. However, often the autocorrelation is more complex, which we take into account and provide a `complex` fit function, based on an empirical analysis of autocorrelation functions by König [29]:

$$C(k) = De^{-\frac{k}{\tau_{\text{exp}}}} + Ee^{-\left(\frac{k}{\tau_{\text{osc}}}\right)^{\gamma}} \cos(2\pi vk) + Fe^{-\left(\frac{k}{\tau_{\text{gauss}}}\right)^2} + O. \quad (1)$$

In addition to the exponential decay, the `complex` fit function features three terms that account for:

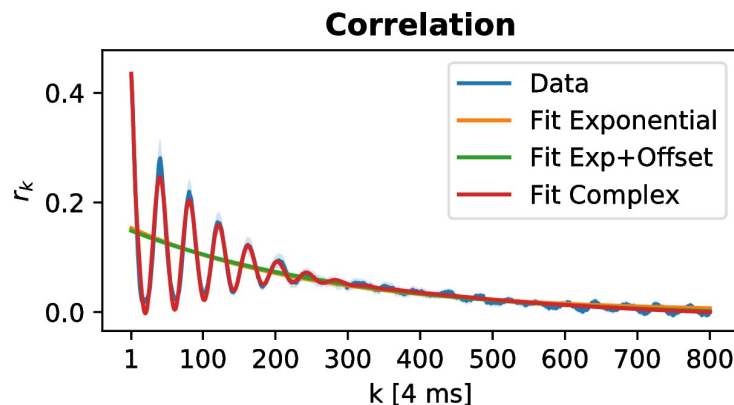


Fig 2. Example analysis of spiking activity from rat hippocampus during an open field task that demonstrates the usage of the `complex` fit function. A short example code that analyzes the data [30] and produces this figure is listed in appendix A.

<https://doi.org/10.1371/journal.pone.0249447.g002>

- Neural oscillations, reflected as an exponentially decaying cosine term: $Ee^{-\left(\frac{k}{\tau_{\text{osc}}}\right)^{\gamma}} \cos(2\pi\nu k)$.
- Short term dynamics of a neuron with a refractory period, reflected as a Gaussian decay:

$$Fe^{-\left(\frac{k}{\tau_{\text{gauss}}}\right)^2}.$$

- An offset O which arises due to the small non-stationarities of the recordings on timescales longer than a few seconds.

To illustrate the usefulness of the `complex` fit function, we analyze an openly available dataset of spiking activity in rat hippocampus [30]. We find an intrinsic timescale of around 1.5 seconds (which is similar to the timescales found in rat cortex [31]). One challenging characteristic of this dataset are theta oscillations (5–10 Hz) in the population activity, which carry over to the autocorrelation function. Because the `complex` fit function features an oscillatory term, it can capture these oscillations, and still yield a solid estimate of the autocorrelation time. (Fits from functions without the oscillatory term will deviate from the data and lead to biased estimates.) Additionally, by including this term into the fit, we also obtain an estimate of the oscillation frequency: In the shown example (Fig 2), we find $\nu = 6.1$ Hz, which is well in the range of theta oscillations. This shows that our toolbox can deal with complex neuronal dynamics of single-cell activity.

4 Technical details

4.1 Derivation of the multi-step regression estimator for autoregressive processes

The statistical properties of activity propagation in networks can be approximated by a stochastic process with an autoregressive representation [15, 18, 32], at least to leading order [14]. We will use this framework of autoregressive processes to derive the multi-step regression estimator and show that it is invariant under subsampling [5].

Here, we consider the class of stochastic processes with an autoregressive representation of first order. This process combines a stochastic, internal generation of activity with a stochastic, external input. The internal generation on average yields m new events per event, where m is

called the branching parameter (using the terminology of the driven branching process) [33–35]. The external input is assumed to be an uncorrelated Poisson process with rate h (a generalization to non-stationary input can be found in Ref. [36]). For discrete time steps Δt , we denote the number of active units at time t with A_t and obtain the autoregressive representation

$$\langle A_{t+1} | A_t \rangle = mA_t + h\Delta t, \tag{2}$$

where $\langle \cdot \rangle$ denotes the expectation value. This autoregressive representation is the basis of our subsampling invariant method and makes it applicable to the full class of first-order autoregressive processes. From Eq (2), we can also see that one could determine m from a time series of a system’s activity by using linear regression. The *linear regression* estimate of m is

$$m_{lr} = \frac{\text{Cov}[A_{t+1}, A_t]}{\text{Var}[A_t]} = \frac{\sum_{t=1}^{T-1} (A_{t+1} - \langle A_{t+1} \rangle)(A_t - \langle A_t \rangle)}{\sum_{t=1}^{T-1} (A_t - \langle A_t \rangle)^2}. \tag{3}$$

This well established approach [5, 33, 37, 38] only considers the pairs of activity that are separated by one time step—it measures the slope of the line that best describes the point cloud (A_{t+1}, A_t) . Instead, the *multi-step regression* (MR) estimator considers all the pairs of activity separated by increasing time differences k —it estimates multiple regression slopes.

Analogous to the case of $k = 1$ in Eq (3), we define the *correlation coefficients* r_k as the slope of the line that best describes the point cloud (A_{t+k}, A_t)

$$r_k \frac{\text{Cov}[A_{t+k}, A_t]}{\text{Var}[A_t]} = \frac{\langle (A_{t+k} - \langle A_{t+k} \rangle)(A_t - \langle A_t \rangle) \rangle}{\langle A_t^2 \rangle - \langle A_t \rangle^2}. \tag{4}$$

For an autoregressive process that is fully sampled, these correlation coefficients become $r_k = m^k$. To show this, we first generalize Eq (2) using the geometric series (cf. Ref. [5, 36])

$$\langle A_{t+k} | A_t \rangle = m^k A_t + h\Delta t \frac{1 - m^k}{1 - m}. \tag{5}$$

We then use the law of total expectation to obtain $\langle A_{t+k} A_t \rangle = \langle \langle A_{t+k} | A_t \rangle A_t \rangle$ and $\langle A_{t+k} \rangle = \langle \langle A_{t+k} | A_t \rangle \rangle$. This allows us to rewrite the covariance:

$$\text{Cov}[A_{t+k}, A_t] = \langle A_{t+k} A_t \rangle - \langle A_{t+k} \rangle \langle A_t \rangle \tag{6}$$

$$= \langle \langle A_{t+k} | A_t \rangle A_t \rangle - \langle \langle A_{t+k} | A_t \rangle \rangle \langle A_t \rangle \tag{7}$$

$$= m^k \langle A_t^2 \rangle + h\Delta t \frac{1 - m^k}{1 - m} \langle A_t \rangle - m^k \langle A_t \rangle^2 - h\Delta t \frac{1 - m^k}{1 - m} \langle A_t \rangle \tag{8}$$

$$= m^k (\langle A_t^2 \rangle - \langle A_t \rangle^2) = m^k \text{Var}[A_t]. \tag{9}$$

When we insert this result into Eq (4), we find that the correlation coefficients are related to the branching parameter as $r_k = m^k$, which enables the toolbox to detect the branching parameter from recordings of processes that are subcritical ($m < 1$), critical ($m = 1$) or supercritical ($m > 1$).

In the special case of stationary activity, where $\langle A_t \rangle = \langle A_{t+k} \rangle$, the correlation coefficients can be further related to an autocorrelation time. In this case, the correlation coefficients, Eq (4),

match the correlation function

$$r_k = \frac{\langle A_{t+k} A_t \rangle - \langle A_t \rangle^2}{\langle A_t^2 \rangle - \langle A_t \rangle^2} = C(A_{t+k}, A_t). \tag{10}$$

Note that we here consider the definition of the autocorrelation function normalized to the time-independent variance (other definitions are also common, e.g. a time-dependent Pearson correlation coefficient $\text{Cov}[A_{t+k}, A_t] / \text{Std}[A_t] \text{Std}[A_{t+k}]$). For stationary autoregressive processes, the correlation function decays exponentially and we can introduce an autocorrelation time τ

$$C(A_{t+k}, A_t) = e^{(-k \Delta t / \tau)} \tag{11}$$

$$= e^{(k \ln m)} = m^k. \tag{12}$$

We can thus identify a relation between the branching parameter m and the intrinsic timescale τ (or, more precisely, the autocorrelation time) via the time discretization Δt :

$$\tau = -\Delta t / \ln(m). \tag{13}$$

It is important to note that τ is an actual physical observable, whereas m offers an interpretation of how the intrinsic timescales are generated—it sets the causal relation between two consecutive generations of activity. Whereas m depends on how we chose the bin size of each time step Δt , the intrinsic timescale τ is independent of bin size.

4.2 Subsampling invariant estimation of the intrinsic timescale by multi-step regression

Subsampling describes the typical experimental constraint that often one can only observe a small fraction of the full system [5, 39, 40]. Given the full activity A_t , we denote the activity that is recorded under subsampling with a_t . We describe the amount of subsampling (the fraction of the system that is observed) through the sampling probability α , where $\alpha = 1$ recovers the case of the fully sampled system.

It can be shown that subsampling causes a bias b that only affects the amplitude of the autocorrelation function—but not the intrinsic timescale that characterizes the decay [5]. This is illustrated in Fig 3. By fitting the exponential and the amplitude, the subsampling problem boils down to an additional free parameter in the least-square fit of the correlation coefficients:

$$r_k = b m^k = b e^{-k \Delta t / \tau} \text{ with } b = \alpha^2 \frac{\text{Var}[A_t]}{\text{Var}[a_t]}, \tag{14}$$

where a_t is the (recorded) activity under subsampling and A_t is the (unknown) activity that would hypothetically be observed under full sampling. As we see above (Eq (14), Fig 3) the intrinsic timescale τ is independent of the sampling fraction α . In general, when measuring autocorrelations, Eq (10), by definition $r_0 = 1$. Under subsampling however, the amplitude for $r_k \geq 1$ decreases as fewer and fewer units of the system are observed. This can cause a severe underestimation in the single regression approach, Eq (3).

In order to formalize the estimation of correlation coefficients r_k for subsampled activity, let us denote the set of all activity observations with $x = \{a_t\}$ and the observations k time steps later with $y = \{a_{t+k}\}$. If T is the total length of the recording, then we have $T - k$ discretized

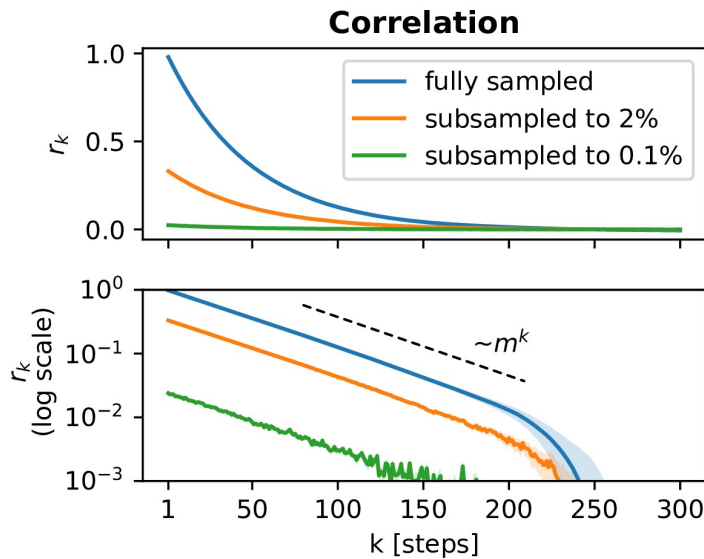


Fig 3. The amplitude of correlation coefficients decreases under subsampling, whereas the intrinsic timescale τ and the branching parameter m (characterized by the slope of the r_k on a logarithmic scale) are invariant. Coefficients were determined by the toolbox for a fully sampled and binomially subsampled branching processes [19].

<https://doi.org/10.1371/journal.pone.0249447.g003>

time steps to work with. Then

$$r_k = \frac{\text{Cov}[x, y]}{\text{Var}[x]} = \frac{\sum_{t=1}^{T-k} (x_t - \langle x \rangle)(y_t - \langle y \rangle)}{\sum_{t=1}^{T-k} (x_t - \langle x \rangle)^2}, \tag{15}$$

where we approximate the expectation values $\langle x \rangle$ and $\langle y \rangle$ using

$$\bar{x} = \frac{1}{T-k} \sum_{t=1}^{T-k} a_t \text{ and } \bar{y} = \frac{1}{T-k} \sum_{t=1}^{T-k} a_{t+k}.$$

In other words, \bar{x} is the mean of the observed time series and \bar{y} is the mean of the *shifted* time series.

4.3 Different methods to estimate correlation coefficients

The drawback of the naive implementation, Eq (11), is that it is biased if T is rather short—which is often the case if the recording time was limited (for a recent discussion of this topic see also Ref. [24]). In the case of short recordings, \bar{x} and \bar{y} are biased estimators of the expectation values $\langle a_i \rangle$ and $\langle a_{t+k} \rangle$. However, we can compensate the bias by combining multiple short recordings, if available.

In practice, multiple recordings are often available: If individual recordings are repeated several times under the same conditions, we refer to these repetitions as *trials*. One typically assumes that across these trials, the expected value of activity is stationary. However, this is not necessarily the case because trial-to-trial variability might be systematic. Since this assumption has to be justified case-by-case, the toolbox offers two methods to calculate the correlation coefficients: the `trialseparated` and `stationarymean` method.

4.3.1 Trialseparated. The `trialseparated` method makes less assumptions about the data than the `stationarymean` method. Each trial provides a separate estimate of the

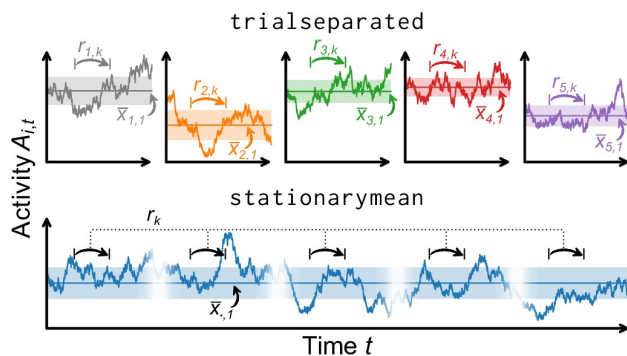


Fig 4. Illustration of the two methods for determining the correlation coefficients r_k from spiking activity A_t . Both methods assume a trial structure of the data (discontinuous time series)**Top:** The `trialseparated` method calculates one set of correlation coefficients $r_{i,k}$ for every trial i (via linear regression)**Bottom:** The `stationarymean` method combines the information of all trials to perform the linear regression on a single, but larger pool of data. This gives an estimate of r_k that is bias corrected for short trial lengths.

<https://doi.org/10.1371/journal.pone.0249447.g004>

correlation coefficients $r_{i,k}$. Let us again denote the observations before (after) the time lag with x_i (y_i), where index i denotes the i -th out of N total trials. All trials share the same number of time steps T . We can apply Eq (15) to each trial separately and thereafter average over the per-trial result:

$$r_k = \frac{1}{N} \sum_{i=1}^N \left[\frac{\sum_{t=1}^{T-k} (x_{i,t} - \bar{x}_{i,k})(y_{i,t} - \bar{y}_{i,k})}{\sum_{t=1}^{T-k} (x_{i,t} - \bar{x}_{i,k})^2} \right] = \frac{1}{N} \sum_{i=1}^N r_{i,k} \tag{16}$$

with

$$\bar{x}_{i,k} = \frac{1}{T-k} \sum_{t=1}^{T-k} a_{i,t} \quad \text{and} \quad \bar{y}_{i,k} = \frac{1}{T-k} \sum_{t=1}^{T-k} a_{i,t+k}$$

As the expected activity $\langle a_t \rangle$ is estimated within each trial separately, this method is robust against a change in the activity from trial to trial. On the other hand, the `trialseparated` method suffers from short trial lengths when $\bar{x}_{i,k}$ and $\bar{y}_{i,k}$ become biased estimates for the activity.

4.3.2 Stationarymean. The `stationarymean` method assumes the activity to be stationary across trials: Now, the expected activity $\langle a_t \rangle$ is estimated by $\bar{x}_{.,k}$ and $\bar{y}_{.,k}$ that use the full pool of recordings (containing all trials):

$$r_k = \frac{\sum_{i=1}^N \left[\frac{1}{T-k} \sum_{t=1}^{T-k} (x_{i,t} - \bar{x}_{.,k})(y_{i,t} - \bar{y}_{.,k}) \right]}{\sum_{i=1}^N \frac{1}{T} \sum_{t=1}^T (x_{i,t} - \bar{x}_{.,k})^2} \tag{17}$$

with

$$\bar{x}_{.,k} = \frac{1}{N(T-k)} \sum_{i=1}^N \sum_{t=1}^{T-k} a_{i,t} \quad \text{and} \quad \bar{y}_{.,k} = \frac{1}{N(T-k)} \sum_{i=1}^N \sum_{t=1}^{T-k} a_{i,t+k}$$

The two methods are illustrated in Fig 4 and the impact of the trial length on the estimated autocorrelation time is shown in Fig 5. For short trials (red shaded area), the `stationarymean` provides precise estimates—already for time series that are only on the order of ten

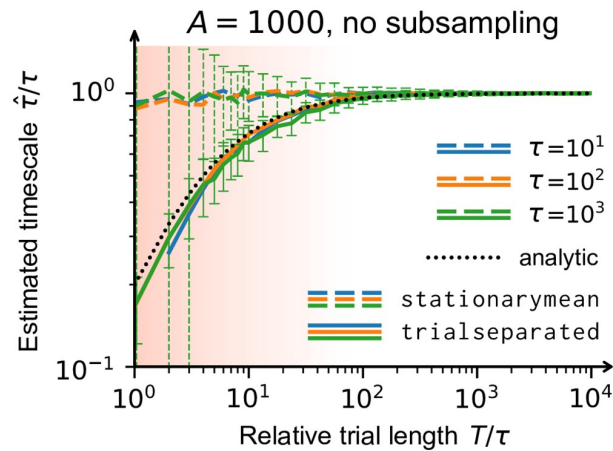


Fig 5. Independent of subsampling, correlation coefficients can be biased if trials are short. As a function of trial length, the autocorrelation time that was estimated by the toolbox ($\hat{\tau}$) is compared with the known value of a stationary, fully sampled branching process (τ). Each measurement featured 50 trials and was performed once with each method, `trialseparated` (solid lines) and `stationarymean` (dashed lines). For short time series (red shaded area), it is known analytically that the correlation coefficients are biased [23]. The bias propagates to the intrinsic timescale (black dotted line) and it is consistent with the timescale obtained from the `trialseparated` method. The `stationarymean` method can compensate the bias, if enough trials are available across which the activity is indeed stationary. However, the improvement to the estimates scales directly with the number of trials—the effective statistical information is increased with each trial. Error bars (for clarity only depicted for $\tau = 10^3$): standard deviation across 100 simulations. For more details, see appendix B.

<https://doi.org/10.1371/journal.pone.0249447.g005>

times as long as the autocorrelation time itself. The `trialseparated` method, on the other hand, is biased for short trials but it makes less strict assumptions on the data. Thus, the `trialseparated` method should be used if one is confident that trial durations are long enough.

As a rule of thumb, if an *a priori* estimate of τ exists, we advise to use trials that are at least 10 times longer than that estimate. The longer, the better. As an example, to reliably detect $\hat{\tau} \approx 200$ ms (for instance in prefrontal cortex), a time series of 2 s could suffice (when using the `stationarymean` method). Furthermore, as a consistency check, we recommend to compare estimates that derive from both methods.

4.4 Toolbox interface to estimate correlation coefficients

The correlation coefficients are calculated by calling the `coefficients()` function, with the `method` keyword.

```
# typical keyword arguments, steps from 1 to 500
rks = mre.coefficients(src, method = 'stationarymean',
steps = (1, 500))

# create custom steps as a numpy array,
# here from 1 to 750 with increment 2
my_steps = np.arange(1, 750, 2)
```

```
# specify the created steps,
# step size dt and unit of the time-step
rks = mre.coefficients(src, method = 'stationarymean',
steps = my steps, dt = 1, dtunit = 'bp steps')
```

From the code example above, it is clear that one has to choose for which k -values the coefficients are calculated. This choice needs to reflect the data: the chosen steps determine the range that can be fitted. If not enough steps are included, the tail of the exponential is overlooked, whereas if too many steps are included, fluctuations may cause overfitting. A future version of the toolbox will give a recommendation, for now it is implemented as a console warning.

The k -values can be specified with the `steps` argument, by either specifying an upper and lower threshold or by explicitly passing an array of desired values. In order to give the r_k physical meaning, the function also takes the time bin size Δt (corresponding to the step size k) and the time unit as arguments: `dt` and `dtunit`, respectively. Those properties become part of the returned data structure `CoefficientResult`, so that the subsequent fit- and plot-routines can use them.

4.5 Toolbox data structure

Recordings are often repeated with similar conditions to create a set of trials. We took this into account and built the toolbox on the assumption that we always have a trial structure, even if there is only a single recording.

The trial structure is incorporated in a two dimensional NumPy array [20–22], where the first index (i) labels the trial. The second index (t) specifies the time step of the trials activity recording $A_{i,t}$, where time is discretized and each time step has size Δt . All trials must have the same length and the same Δt (or in other words, should be recorded with the same sampling rate).

Because all further processing steps rely on this particular format, we provide the `input_handler()` that attempts convert data structures into the right one. The `input_handler()` works with nested lists, NumPy arrays or strings containing file paths. Wildcards in the file path will be expanded and all matching files are imported. If a file has multiple columns, each column is taken to be a trial. To select which of the columns to import, specify for example `usecols=(0, 1, 2)` which would import the first three columns.

4.6 Error estimation

The toolbox provides confidence intervals based on bootstrap resampling [41]. Resampling usually requires the original data to be cut into chunks (bins) that are recombined (drawing with replacement) to create new realizations, the so called bootstrap samples. Because the toolbox works on the trial structure, the input data usually does not need to be modified: each trial becomes a bin that can then be drawn with replacement to contribute to the bootstrap sample. While this is a good choice if sufficient (~ 100) trials are provided, using trials directly for resampling means that no error estimates are possible with a single trial. If no trial structure is available, such as for resting-state data, an easy workaround is to manually cut long time

series into shorter chunks to artificially create the trial structure [19]. The error estimation via bootstrapping is implemented in the `coefficients()`, `fit()` and `full_analysis()` functions. All three take the `numboot` argument to specify how many bootstrap samples are created.

4.7 Getting help

Please visit the project on GitHub [42] and see our growing online documentation [43]. You can also call `help()` on every part of the toolbox:

```
# as an example, create variables.
bp = mre.simulate branching(m = 0.98, a = 10)
# try pressing tab e.g. after typing mre.c
rks = mre.coefficients(bp)
# help() prints the documentation,
# and works for variables and functions alike
help(rks)
help(mre.full_analysis)
```

5 Discussion

Our toolbox reliably estimates the intrinsic timescale from vastly different time series, from electrophysiological recordings to case numbers of epidemic spreading to any system that can be represented by an autoregressive process. Most importantly, it relies on the multi-step regression estimator so that unbiased timescales are found even for heavily subsampled systems [5].

In this work, we also took a careful look at how a limited duration of the recordings—a common problem in all data-driven approaches—can bias our estimator [23, 24]. With extensive numeric simulations we showed that the estimator is robust if conservatively formulated guidelines are followed. We can also bolster our previous claim [5] that the estimator is very data efficient. Moreover, short time series (trials) can be compensated by increasing the number of trials.

The toolbox thereby enables a systematic study of intrinsic timescales, which are important for a variety of questions in neuroscience [44]. Using the branching process as a simple model of neuronal activity, it is intuitive to think of the intrinsic timescale as the duration over which any perturbation reverberates (or persists) within the network [13, 45]. According to this intuition, different timescales should benefit different functional aspects of cortical networks [12, 46, 47].

Experimental evidence indeed shows different timescales for different cortical networks [5, 48]. It even suggests a temporal hierarchy of brain areas [1, 2, 49]; areas responsible for sensory integration feature short timescales, while areas responsible for higher-level cognitive processes feature longer timescales. For cognitive processes (for example during task-solving), the

intrinsic timescale was further linked to working memory. In particular, working memory might be implemented through neurons with long timescales [3, 4, 50].

In general, recordings could exhibit multiple timescales simultaneously [51–53]. This can be readily realized with the toolbox by using a custom fit function (e.g. a sum of exponential functions, see Sec. 3). However, it is important to be aware of the possible pitfalls of fitting elaborate functions to empirical data [53, 54]. In our experience, most recordings exhibit a single dominant timescale.

Lastly, it was theorized that biological recurrent networks can adapt their timescale in order to optimize their processing for a particular task [46, 55, 56]. For artificial recurrent networks, such a tuning capability was already shown to be attainable by operating around the critical point (of a dynamic second order phase transition) [15, 32, 47, 57]. For instance, reducing the distance to criticality increases the information storage in these networks [10, 12]. At the same time, the observed intrinsic timescale increases. It is plausible that the mechanisms of near-critical, artificial systems also apply to cortical networks [58–60]. This and other hypothesis can now be reliably tested with our toolbox and properly designed experiments [8]. For applications of our approach and the MR. Estimator toolbox see e.g. Refs. [48, 61, 62] and Ref. [7, 36, 63], respectively.

6 Appendix

6.1 A Real-world Example

Listing 2. Minimal script that shows how to prepare real-world data [30, 64], and produces Fig 2 from the main text. Characteristic for this dataset are theta oscillations (5–10 Hz) that carry over to the autocorrelation function. We first create a time series of activity by time-binning the spike times. Then, we create an artificial trial structure to demonstrate error estimation and apply the built-in fit functions. Last, we print the frequency $\nu = 6.13$ Hz of the theta oscillations as an example to show how to access the different parameters of the `complex` fit. The full script is available on GitHub [19], and for further details, also see the online documentation [43].

```
# helper function to convert a list of time stamps
# into a (binned) time series of activity
def bin_spike_times_unitless (spike_times, bin_size):
    last_spike = spike_times [-1]
    num_bins = int (np. ceil (last_spike / bin_size))
    res = np. zeros (num_bins)
    for spike_time in spike_times:
        target_bin = int (np. floor (spike_time / bin_size))
        res [target_bin] = res [target_bin] + 1
    return res

# load the spiketimes
res = np. loadtxt ('./crcns/hc2/ec013.527/ec013.527.res.1')
```

```
# the .res.x files contain the time-stamps of spikes
detected

# by electrode x sampled at 20 kHz, i.e. 0.05 ms per time
steps.

# we want 'spiking activity': spikes added up during a given
# time. usually, ~4ms time bins (windows) is a good first
guess

act = bin_spike_times_unitless (res, bin_size = 80)

# to get error estimates, we create 25 artificial trials by
# splitting the data. not recommended for non-stationary
data

triallen = int (np.floor (len (act)/25))
trials = np.zeros (shape = (25, triallen))

for i in range (0, 25):

    trials [i] = act [i * triallen: (i + 1) * triallen]

# now we could run the analysis and will get error estimates
# out = mre.full_analysis (trials, dt = 4, dtunit = 'ms',
kmax = 800,

# method = 'trialeparated')

# however, in this dataset we will find theta oscillations.
# let's try the other fit functions, too.

out = mre.full_analysis (trials, dt = 4, dtunit = 'ms',
kmax = 800, method = 'trialeparated', fitfuncs = ['exponen-
tial', 'exponential_offset', 'complex'], targetdir = './',
saveoverview = True)

# by assigning the result of mre.full_analysis (...) to a
# variable, we can use fit results for further processing:
# the oscillation frequency nu is fitted by the complex fit
# function as the 7th parameter (see online documentation).
# it is in units of 1/ dtunit and we used 'ms'.

print (f "theta frequency: {out.fits [2]. popt [6] * 1000}
[Hz]")
```

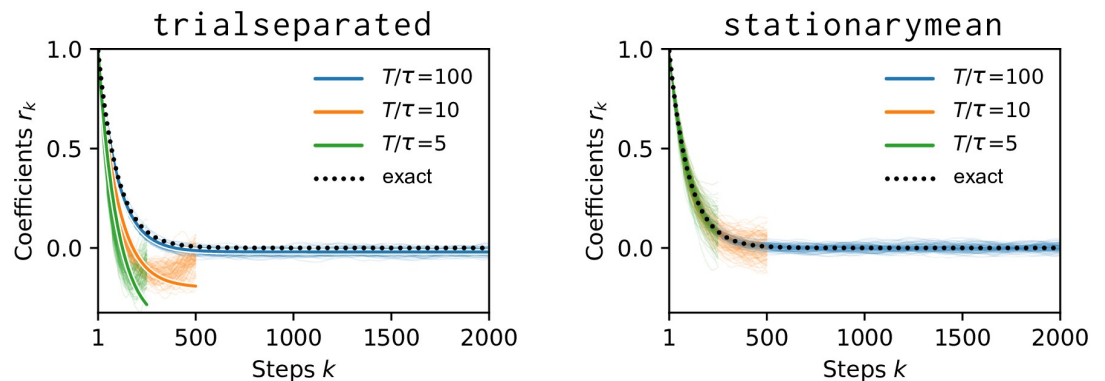


Fig 6. Correlation coefficients r_k for $\tau = 10^2$ (orange in Fig 5). Individual background lines stem from the 100 independent repetitions. **Left:** Coefficients are shifted and skewed for short trial length T/τ when using the `trialsseparated` method. The solid foreground lines are obtained from Eq. 4.07 of [23]. **Right:** With 50 trials and the `stationarymean` method, even very short (green) time series yield unbiased coefficients and, ultimately, precise estimates of the intrinsic timescale.

<https://doi.org/10.1371/journal.pone.0249447.g006>

The spiking data from rats were recorded by Mizuseki et al. [30] with experimental protocols approved by the Institutional Animal Care and Use Committee of Rutgers University. The data were obtained from the NSF-funded CRCNS data sharing website [64].

6.2 B short trials cause bias

The data shown in Fig 5 was created with the `simulation_branching()` function included in the toolbox. Every measurement was repeated 100 times, featured 50 trials, target activity 1000 and no subsampling (the bias investigated here is independent from subsampling). The colored lines correspond to the median across 100 independent simulations. Error estimates were calculated but not plotted for clarity—in the red shaded area of Fig 5, the very short trials lead to low statistics (and large error bars). Error bars represent the standard deviation across the 100 simulations. The included steps k covered $[1 : 20\tau]$, if available, which corresponds to the fit range of the exponential with offset.

To further illustrate the bias we observed in Fig 5, we plot the correlation coefficients r_k that were found by the toolbox with the two different methods in Fig 6. When trials are short, the coefficients found by the `trialsseparated` method are offset and skewed. The `stationarymean` method finds the correct coefficients because the estimation could profit from the trial structure. Since neither the true timescale nor the stationarity assumption are known in experiments, we suggest to compare results from both methods: if they agree, this is a good indication that the trials are long enough.

The black dashed line in Fig 5 is derived from the analytic solution Eq. 4.07 in Ref. [23] that gives the expectation value of the biased correlation coefficient in dependence of the trial length T . For simplicity, we focus on the leading-order estimated branching parameter \hat{m} via the one-step autocorrelation function. Starting from Eq. 4.07 in Ref. [23],

$$\hat{m} \approx C(A_{t+1}, A_t) = r_1 \approx m^1 - \frac{1}{T}[(1 + m)(1) + 2m^1] + O\left(\frac{1}{T^2}\right) \tag{18}$$

$$\approx m \left(1 - \frac{1}{T} \left[3 + \frac{1}{m} \right] \right) \tag{19}$$

cf. Eqs (4) and (11). Inserted into Eq (13) $\hat{\tau} = -\Delta t / \ln(\hat{m})$ and with $m = \exp(-\Delta t/\tau)$, we find

$$\hat{\tau} \approx \frac{-\Delta t}{\ln(m) + \ln\left(1 - \frac{1}{T} \left[3 + \frac{1}{m}\right]\right)} \quad (20)$$

$$\approx \frac{-\Delta t}{\ln(m) - \frac{1}{T} \left[3 + \frac{1}{m}\right]} \quad (21)$$

$$= \frac{-\Delta t}{\frac{-\Delta t}{\tau} - \frac{1}{T} \left[3 + e^{\Delta t/\tau}\right]} \quad (22)$$

$$= \frac{\tau}{1 + \frac{\tau}{T\Delta t} \left[3 + e^{\Delta t/\tau}\right]}. \quad (23)$$

For sufficiently large $\tau > \Delta t$, we obtain to leading order

$$\frac{\hat{\tau}}{\tau} \approx \frac{1}{1 + \frac{\tau}{T} \frac{4}{\Delta t}}. \quad (24)$$

For Fig 5—where $\Delta t = 1$, $x = T/\tau$ and $y = \frac{\hat{\tau}}{\tau}$ —this means that

$$y = 1/(1 + 4/x). \quad (25)$$

Acknowledgments

We thank Leandro Fosque, Gerardo Ortiz and John Beggs as well as Danylo Ulianych and Michael Denker for constructive discussion and helpful comments. We are grateful for careful proofreading and input from Jorge de Heuvel and Christina Stier.

Author Contributions

Conceptualization: F. P. Spitzner, J. Dehning, J. Wilting, J. Zierenberg, V. Priesemann.

Data curation: F. P. Spitzner, J. Dehning.

Formal analysis: F. P. Spitzner, J. Dehning.

Investigation: F. P. Spitzner.

Methodology: F. P. Spitzner, J. Wilting, J. Zierenberg, V. Priesemann.

Project administration: V. Priesemann.

Software: F. P. Spitzner, J. Dehning.

Supervision: V. Priesemann.

Validation: F. P. Spitzner, J. Dehning.

Visualization: F. P. Spitzner.

Writing – original draft: F. P. Spitzner, J. Dehning, J. Zierenberg.

Writing – review & editing: F. P. Spitzner, J. Dehning, J. Wilting, A. Hagemann, J. P. Neto, J. Zierenberg, V. Priesemann.

References

1. Murray JD, Bernacchia A, Freedman DJ, Romo R, Wallis JD, Cai X, et al. A Hierarchy of Intrinsic Timescales across Primate Cortex. *Nat Neurosci*. 2014; 17:1661–1663. <https://doi.org/10.1038/nn.3862> PMID: 25383900
2. Chaudhuri R, Knoblauch K, Gariel MA, Kennedy H, Wang XJ. A Large-Scale Circuit Mechanism for Hierarchical Dynamical Processing in the Primate Cortex. *Neuron*. 2015; 88:419–431. <https://doi.org/10.1016/j.neuron.2015.09.008>
3. Cavanagh SE, Towers JP, Wallis JD, Hunt LT, Kennerley SW. Reconciling Persistent and Dynamic Hypotheses of Working Memory Coding in Prefrontal Cortex. *Nat Commun*. 2018; 9:3498. <https://doi.org/10.1038/s41467-018-05873-3>
4. Wasmuht DF, Spaak E, Buschman TJ, Miller EK, Stokes MG. Intrinsic Neuronal Dynamics Predict Distinct Functional Roles during Working Memory. *Nat Commun*. 2018; 9:3499. <https://doi.org/10.1038/s41467-018-05961-4>
5. Wilting J, Priesemann V. Inferring Collective Dynamical States from Widely Unobserved Systems. *Nat Commun*. 2018; 9:2325. <https://doi.org/10.1038/s41467-018-04725-4>
6. Watanabe T, Rees G, Masuda N. Atypical Intrinsic Neural Timescale in Autism. *eLife*. 2019; 8:e42256. <https://doi.org/10.7554/eLife.42256>
7. Hagemann A, Wilting J, Samimzad B, Mormann F, Priesemann V. No Evidence That Epilepsy Impacts Criticality in Pre-Seizure Single-Neuron Activity of Human Cortex. *ArXiv200410642 Phys Q-Bio*. 2020;.
8. Dehning J, Dotson NM, Hoffman SJ, Gray CM, Priesemann V. Hierarchy and task-dependence of intrinsic timescales across primate cortex. in prep;.
9. Schuecker J, Goedeke S, Helias M. Optimal Sequence Memory in Driven Random Networks. *Phys Rev X*. 2018; 8:041029.
10. Boedecker J, Obst O, Lizier JT, Mayer NM, Asada M. Information Processing in Echo State Networks at the Edge of Chaos. *Theory Biosci*. 2012; 131:205–213. <https://doi.org/10.1007/s12064-011-0146-8>
11. Wibrall M, Lizier JT, Priesemann V. Bits from Brains for Biologically Inspired Computing. *Front Robot AI*. 2015; 2.
12. Cramer B, Stöckel D, Kreft M, Wibrall M, Schemmel J, Meier K, et al. Control of Criticality and Computation in Spiking Neuromorphic Networks with Plasticity. *Nat Commun*. 2020; 11:2853. <https://doi.org/10.1038/s41467-020-16548-3> PMID: 32503982
13. Beggs JM, Plenz D. Neuronal Avalanches in Neocortical Circuits. *J Neurosci*. 2003; 23:11167–11177. <https://doi.org/10.1523/JNEUROSCI.23-35-11167.2003>
14. Zierenberg J, Wilting J, Priesemann V, Levina A. Description of Spreading Dynamics by Microscopic Network Models and Macroscopic Branching Processes Can Differ Due to Coalescence. *Phys Rev E*. 2020; 101:022301. <https://doi.org/10.1103/PhysRevE.101.022301>
15. Wilting J, Priesemann V. 25 Years of Criticality in Neuroscience—Established Results, Open Controversies, Novel Concepts. *Current Opinion in Neurobiology*. 2019; 58:105–111. <https://doi.org/10.1016/j.conb.2019.08.002>
16. Jun JJ, Steinmetz NA, Siegle JH, Denman DJ, Bauza M, Barbarits B, et al. Fully Integrated Silicon Probes for High-Density Recording of Neural Activity. *Nature*. 2017; 551:232–236. <https://doi.org/10.1038/nature24636> PMID: 29120427
17. Stringer C, Pachitariu M, Steinmetz N, Reddy CB, Carandini M, Harris KD. Spontaneous Behaviors Drive Multidimensional, Brainwide Activity. *Science*. 2019; 364:eaav7893. <https://doi.org/10.1126/science.aav7893>
18. Pastor-Satorras R, Castellano C, Van Mieghem P, Vespignani A. Epidemic Processes in Complex Networks. *Rev Mod Phys*. 2015; 87:925–979. <https://doi.org/10.1103/RevModPhys.87.925>
19. Referenced scripts are available at <https://github.com/Priesemann-Group/mrestimator/blob/v0.1.7/examples/paper>.
20. Oliphant TE. *NumPy: A Guide to NumPy*. USA: Trelgol Publishing; 2006. Available from: <http://www.numpy.org/>.
21. van der Walt S, Colbert SC, Varoquaux G. The NumPy Array: A Structure for Efficient Numerical Computation. *Comput Sci Eng*. 2011; 13:22–30. <https://doi.org/10.1109/MCSE.2011.37>
22. Harris CR, Millman KJ, van der Walt SJ, Gommers R, Virtanen P, Cournapeau D, et al. Array Programming with NumPy. *Nature*. 2020; 585:357–362. <https://doi.org/10.1038/s41586-020-2649-2> PMID: 32939066
23. Marriott FHC, Pope JA. Bias in the Estimation of Autocorrelations. *Biometrika*. 1954; 41:390–402. <https://doi.org/10.1093/biomet/41.3-4.390>

24. Grigera TS. Everything You Wish to Know about Correlations but Are Afraid to Ask. ArXiv200201750 Cond-Mat. 2020;.
25. Bernacchia A, Seo H, Lee D, Wang XJ. A Reservoir of Time Constants for Memory Traces in Cortical Neurons. *Nat Neurosci*. 2011; 14:366–372. <https://doi.org/10.1038/nn.2752>
26. Hasson U, Yang E, Vallines I, Heeger DJ, Rubin N. A Hierarchy of Temporal Receptive Windows in Human Cortex. *J Neurosci*. 2008; 28:2539–2550. <https://doi.org/10.1523/JNEUROSCI.5487-07.2008>
27. Chaudhuri R, Bernacchia A, Wang XJ. A Diversity of Localized Timescales in Network Activity. *eLife*. 2014; 3:e01239. <https://doi.org/10.7554/eLife.01239>
28. Helias M, Tetzlaff T, Diesmann M. The Correlation Structure of Local Neuronal Networks Intrinsically Results from Recurrent Dynamics. *PLOS Computational Biology*. 2014; 10:e1003428. <https://doi.org/10.1371/journal.pcbi.1003428>
29. König P. A Method for the Quantification of Synchrony and Oscillatory Properties of Neuronal Activity. *Journal of Neuroscience Methods*. 1994; 54:31–37. [https://doi.org/10.1016/0165-0270\(94\)90157-0](https://doi.org/10.1016/0165-0270(94)90157-0)
30. Mizuseki K, Sirota A, Pastalkova E, Buzsáki G. Theta Oscillations Provide Temporal Windows for Local Circuit Computation in the Entorhinal-Hippocampal Loop. *Neuron*. 2009; 64:267–280. <https://doi.org/10.1016/j.neuron.2009.08.037>
31. Meisel C, Klaus A, Vyazovskiy VV, Pleniz D. The Interplay between Long- and Short-Range Temporal Correlations Shapes Cortex Dynamics across Vigilance States. *J Neurosci*. 2017; 37:10114–10124. <https://doi.org/10.1523/JNEUROSCI.0448-17.2017>
32. Muñoz MA. Colloquium: Criticality and Dynamical Scaling in Living Systems. *Rev Mod Phys*. 2018; 90:031001. <https://doi.org/10.1103/RevModPhys.90.031001>
33. Harris TE. *The Theory of Branching Processes*. Grundlehren Der Mathematischen Wissenschaften. Berlin Heidelberg: Springer-Verlag; 1963. Available from: <https://www.springer.com/gp/book/9783642518683>.
34. Heathcote CR. Random Walks and a Price Support Scheme. *Aust J Stat*. 1965; 7:7–14. <https://doi.org/10.1111/j.1467-842X.1965.tb00256.x>
35. Pakes AG. The Serial Correlation Coefficients of Waiting Times in the Stationary GI/M/1 Queue. *Ann Math Stat*. 1971; 42:1727–1734. <https://doi.org/10.1214/aoms/1177693171>
36. de Heuvel J, Wilting J, Becker M, Priesemann V, Zierenberg J. Characterizing Spreading Dynamics of Subsampled Systems with Non-Stationary External Input. ArXiv200500608 Q-Bio. 2020;.
37. Wei CZ, Winnicki J. Estimation of the Means in the Branching Process with Immigration. *Ann Stat*. 1990; 18:1757–1773.
38. Beggs JM. Neuronal avalanche. *Scholarpedia*. 2007; 2(1):1344. <https://doi.org/10.4249/scholarpedia.1344>
39. Priesemann V, Munk MH, Wibral M. Subsampling Effects in Neuronal Avalanche Distributions Recorded in Vivo. *BMC Neuroscience*. 2009; 10:40. <https://doi.org/10.1186/1471-2202-10-40>
40. Levina A, Priesemann V. Subsampling Scaling. *Nat Commun*. 2017; 8:15140. <https://doi.org/10.1038/ncomms15140>
41. Efron B. *The Jackknife, the Bootstrap, and Other Resampling Plans*. SIAM; 1982.
42. The toolbox is available via pip and on GitHub <https://github.com/Priesemann-Group/mrestimator>.
43. Full online documentation is available at <https://mrestimator.readthedocs.io>.
44. Huang C, Doiron B. Once upon a (Slow) Time in the Land of Recurrent Neuronal Networks. . . . *Current Opinion in Neurobiology*. 2017; 46:31–38. <https://doi.org/10.1016/j.conb.2017.07.003>
45. London M, Roth A, Beeren L, Häusser M, Latham PE. Sensitivity to Perturbations *in Vivo* Implies High Noise and Suggests Rate Coding in Cortex. *Nature*. 2010; 466:123–127. <https://doi.org/10.1038/nature09086>
46. Wilting J, Dehning J, Pinheiro Neto J, Rudelt L, Wibral M, Zierenberg J, et al. Operating in a Reverberating Regime Enables Rapid Tuning of Network States to Task Requirements. *Front Syst Neurosci*. 2018; 12. <https://doi.org/10.3389/fnsys.2018.00055> PMID: 30459567
47. Zierenberg J, Wilting J, Priesemann V, Levina A. Tailored Ensembles of Neural Networks Optimize Sensitivity to Stimulus Statistics. *Phys Rev Research*. 2020; 2:013115. <https://doi.org/10.1103/PhysRevResearch.2.013115>
48. Wilting J, Priesemann V. Between Perfectly Critical and Fully Irregular: A Reverberating Model Captures and Predicts Cortical Spike Propagation. *Cereb Cortex*. 2019; 29:2759–2770. <https://doi.org/10.1093/cercor/bhz049>

49. Demirtaş M, Burt JB, Helmer M, Ji JL, Adkinson BD, Glasser MF, et al. Hierarchical Heterogeneity across Human Cortex Shapes Large-Scale Neural Dynamics. *Neuron*. 2019; 101:1181–1194. e13. <https://doi.org/10.1016/j.neuron.2019.01.017> PMID: 30744986
50. Loidolt M, Rudelt L, Priesemann V. Sequence Memory in Recurrent Neuronal Network Can Develop without Structured Input. *bioRxiv*. 2020; p. 2020.09.15.297580.
51. Chaudhuri R, He BJ, Wang XJ. Random Recurrent Networks Near Criticality Capture the Broadband Power Distribution of Human ECoG Dynamics. *Cereb Cortex*. 2018; 28:3610–3622. <https://doi.org/10.1093/cercor/bhx233>
52. Okun M, Steinmetz NA, Lak A, Dervinis M, Harris KD. Distinct Structure of Cortical Population Activity on Fast and Infralow Timescales. *Cereb Cortex*. 2019; 29:2196–2210. <https://doi.org/10.1093/cercor/bhz023>
53. Zeraati R, Engel TA, Levina A. Estimation of Autocorrelation Timescales with Approximate Bayesian Computations. *Neuroscience*; 2020. Available from: <http://biorxiv.org/lookup/doi/10.1101/2020.08.11.245944>.
54. Shrager RI, W Hendl R. Some Pitfalls in Curve-Fitting and How to Avoid Them: A Case in Point. *J Biochem Biophys Methods*. 1998; 36:157–173. [https://doi.org/10.1016/S0165-022X\(98\)00007-4](https://doi.org/10.1016/S0165-022X(98)00007-4)
55. Beggs JM. The Criticality Hypothesis: How Local Cortical Networks Might Optimize Information Processing. *Philosophical Transactions of the Royal Society A: Mathematical, Physical and Engineering Sciences*. 2008; 366:329–343. <https://doi.org/10.1098/rsta.2007.2092>
56. Fontenele AJ, de Vasconcelos NAP, Feliciano T, Aguiar LAA, Soares-Cunha C, Coimbra B, et al. Criticality between Cortical States. *Phys Rev Lett*. 2019; 122:208101. <https://doi.org/10.1103/PhysRevLett.122.208101> PMID: 31172737
57. Bertschinger N, Natschläger T. Real-Time Computation at the Edge of Chaos in Recurrent Neural Networks. *Neural Comput*. 2004; 16:1413–1436. <https://doi.org/10.1162/089976604323057443>
58. Levina A, Herrmann JM, Geisel T. Dynamical Synapses Causing Self-Organized Criticality in Neural Networks. *Nature Phys*. 2007; 3:857–860. <https://doi.org/10.1038/nphys758>
59. Hellyer PJ, Jachs B, Clopath C, Leech R. Local Inhibitory Plasticity Tunes Macroscopic Brain Dynamics and Allows the Emergence of Functional Brain Networks. *NeuroImage*. 2016; 124:85–95. <https://doi.org/10.1016/j.neuroimage.2015.08.069>
60. Zierenberg J, Wiltling J, Priesemann V. Homeostatic Plasticity and External Input Shape Neural Network Dynamics. *Phys Rev X*. 2018; 8:031018.
61. Ma Z, Turrigiano GG, Wessel R, Hengen KB. Cortical Circuit Dynamics Are Homeostatically Tuned to Criticality In Vivo. *Neuron*. 2019; 104:655–664. e4. <https://doi.org/10.1016/j.neuron.2019.08.031>
62. Beggs JM. The Critically Tuned Cortex. *Neuron*. 2019; 104:623–624. <https://doi.org/10.1016/j.neuron.2019.10.039>
63. Skilling QM, Ognjanovski N, Aton SJ, Zochowski M. Critical Dynamics Mediate Learning of New Distributed Memory Representations in Neuronal Networks. *Entropy*. 2019; 21:1043. <https://doi.org/10.3390/e21111043>
64. The data by Mizuseki et al. is available on [cercns.org](http://dx.doi.org/10.6080/K0Z60KZ9): <http://dx.doi.org/10.6080/K0Z60KZ9>.

3

Sampling effects and measurement overlap can bias the inference of neuronal avalanches


Published in PLoS Computational Biology (2022)

DOI [10.1371/journal.pcbi.1010678](https://doi.org/10.1371/journal.pcbi.1010678)

Preprint [arXiv:1910.09984](https://arxiv.org/abs/1910.09984)

Supplementary material [Appendix A](#)

Source code github.com/Priesemann-Group/criticalavalanches

License 

Own contributions

- ✓ Conceptualization
- ✓ Methodology
- ✓ Software
- ✓ Validation
- ✓ Formal Analysis
- ✓ Investigation

Resources

- ✓ Data Curation
- ✓ Writing — Original Draft
- ✓ Writing — Review & Editing
- ✓ Visualization

Supervision

Project Administration

Funding Acquisition

This work also constitutes a chapter of JPN's PhD thesis, who conducted initial research and implemented a first version of the model. I implemented an independent version of the model, which was later used for the publication. I created figures with contributions from JPN. All authors wrote the manuscript.

RESEARCH ARTICLE

Sampling effects and measurement overlap can bias the inference of neuronal avalanches

Joao Pinheiro Neto¹, F. Paul Spitzner¹, Viola Priesemann^{1,2,3*}

1 Max Planck Institute for Dynamics and Self-Organization, Göttingen, Germany, **2** Bernstein Center for Computational Neuroscience, Göttingen, Germany, **3** Georg-August University Göttingen, Göttingen, Germany

☞ These authors contributed equally to this work.

* viola.priesemann@ds.mpg.de



Abstract

To date, it is still impossible to sample the entire mammalian brain with single-neuron precision. This forces one to either use spikes (focusing on few neurons) or to use coarse-sampled activity (averaging over many neurons, e.g. LFP). Naturally, the sampling technique impacts inference about collective properties. Here, we emulate both sampling techniques on a simple spiking model to quantify how they alter observed correlations and signatures of criticality. We describe a general effect: when the inter-electrode distance is small, electrodes sample overlapping regions in space, which increases the correlation between the signals. For coarse-sampled activity, this can produce power-law distributions even for non-critical systems. In contrast, spike recordings do not suffer this particular bias and underlying dynamics can be identified. This may resolve why coarse measures and spikes have produced contradicting results in the past.

OPEN ACCESS

Citation: Neto JP, Spitzner FP, Priesemann V (2022) Sampling effects and measurement overlap can bias the inference of neuronal avalanches. *PLoS Comput Biol* 18(11): e1010678. <https://doi.org/10.1371/journal.pcbi.1010678>

Editor: Stefan Rotter, University of Freiburg, GERMANY

Received: April 22, 2020

Accepted: October 24, 2022

Published: November 29, 2022

Copyright: © 2022 Pinheiro Neto et al. This is an open access article distributed under the terms of the [Creative Commons Attribution License](https://creativecommons.org/licenses/by/4.0/), which permits unrestricted use, distribution, and reproduction in any medium, provided the original author and source are credited.

Data Availability Statement: All code used to generate the data is available at <https://github.com/Priesemann-Group/criticalavalanches>.

Funding: JPN, FPS and VP received financial support from the Max Planck Society. JPN received financial support from the Brazilian National Council for Scientific and Technological Development (CNPq) under Grant No. 206891/2014-8. VP was supported by the Deutsche Forschungsgemeinschaft (DFG, German Research Foundation) under Germany's Excellence Strategy - EXC 2067/1 - 390729940. The funders had no role

Author summary

The criticality hypothesis associates functional benefits with neuronal systems that operate in a dynamic state at a critical point. A common way to probe the dynamic state of a neuronal systems is measuring characteristics of so-called avalanches—distinct cascades of neuronal activity that are separated in time. For example, the probability distribution of the avalanche size will resemble a power-law if a neuronal system is critical. Thus, power-law distributions have become a common indicator for critical dynamics.

Here, we use simple models and numeric simulations to show that not only the dynamic state of a system has an impact on avalanche distributions. Also aspects that are only related to the sampling of the system (such as inter-electrode distance) or the way avalanches are calculated (such as thresholding and time binning) can shape avalanche distributions. On a mechanistic level we find that, if electrodes record spatially overlapping regions, the signals of electrodes may be *spuriously* correlated; multiple electrodes might pick up activity from the same neuron. Subsequently, when avalanches are inferred, such a measurement overlap can produce power-law distributions even if the underlying system is not critical.

in study design, data collection and analysis, decision to publish, or preparation of the manuscript.

Competing interests: The authors have declared that no competing interests exist.

1 Introduction

For more than two decades, it has been argued that the cortex might operate at a critical point [1–7]. The criticality hypothesis states that by operating at a critical point, neuronal networks could benefit from optimal information-processing properties. Properties maximized at criticality include the correlation length [8], the autocorrelation time [6], the dynamic range [9, 10] and the richness of spatio-temporal patterns [11, 12].

Evidence for criticality in the brain often derives from measurements of *neuronal avalanches*. Neuronal avalanches are cascades of neuronal activity that spread in space and time. If a system is critical, the probability distribution of avalanche size $p(S)$ follows a power law $p(S) \sim S^{-\alpha}$ [8, 13]. Such power-law distributions have been observed repeatedly in experiments since they were first reported by Beggs & Plenz in 2003 [1].

However, not all experiments have produced power laws and the criticality hypothesis remains controversial. It turns out that results for cortical recordings *in vivo* differ systematically:

Studies that use what we here call *coarse-sampled* activity typically produce power-law distributions [1, 14–23]. In contrast, studies that use *sub-sampled* activity typically do not [16, 24–28]. Coarse-sampled activity include LFP, M/EEG, fMRI and potentially calcium imaging, while sub-sampled activity is front-most spike recordings. We hypothesize that the apparent contradiction between coarse-sampled (LFP-like) data and sub-sampled (spike) data can be explained by the differences in the recording and analysis procedures.

In general, the analysis of neuronal avalanches is not straightforward. In order to obtain avalanches, one needs to define discrete events. While spikes are discrete events by nature, a coarse-sampled signal has to be converted into a binary form. This conversion hinges on thresholding the signal, which can be problematic [29–32]. Furthermore, events have to be grouped into avalanches, and this grouping is typically not unique [24]. As a result, avalanche-size distributions depend on the choice of the threshold and temporal binning [1, 33].

In this work, we show how thresholding and temporal binning interact with a commonly ignored effect [16, 34]. Under coarse-sampling, neighboring electrodes may share the same field-of-view. This creates a distance-dependent *measurement overlap* so that the activity that is recorded at different electrodes may show *spurious correlations*, even if the underlying spiking activity is fully uncorrelated. We show that the inter-electrode distance may therefore impact avalanche-size distributions more severely than the underlying neuronal activity.

In this numeric study, we explore the role of the recording and analysis procedures on a locally-connected network of simple binary neurons. Focusing on avalanche distributions, we compare apparent signs of criticality under sub-sampling versus coarse-sampling. To that end, we vary the distance to criticality of the underlying system over a wide range, from uncorrelated (Poisson) to highly-correlated (critical) dynamics. We then employ a typical analysis pipeline to derive signatures of criticality and study how results depend on electrode distance and temporal binning.

2 Results

The aim of this study is to understand *how the sampling of neural activity* affects the inference of the underlying collective dynamics. This requires us to be able to precisely set the underlying dynamics. Therefore, we use the established branching model [35], which neglects many biophysical details, but it allows us to precisely tune the dynamics and to set the distance to criticality.

To study sampling effects, we use a two-level setup inspired by [34]: an underlying network model, on which activity is then *sampled* with a grid of 8×8 virtual electrodes. Where possible,

parameters of the model, the sampling and the analysis are motivated by values from experiments (see [Methods](#)).

In order to evaluate sampling effects, we want to *precisely* set the underlying dynamics. The branching model meets this requirement and is well understood analytically [11, 27, 34–36]. Inspired by biological neuronal networks, we simulate the branching dynamics on a 2D topology with $N_N = 160\,000$ neurons where each neuron is connected to $K \approx 1000$ local neighbors. To emphasize the locality, the synaptic strength of connections decays with the distance d_N between neurons. For a detailed comparison with different topologies, see the Supplemental Information (Fig A in [S1 Text](#)).

2.1 Avalanches are extracted differently under coarse-sampling and sub-sampling

At each electrode, we sample both the spiking activity of the closest neuron (sub-sampling) and a spatially averaged signal that emulates LFP-like coarse-sampling.

Both *coarse-sampling* and *sub-sampling* are sketched in [Fig 1A](#): For coarse-sampling (left), the signal from each electrode channel is composed of varying contributions (orange circles) of all surrounding neurons. The contribution of a particular spike from neuron i to electrode k decays as $1/d_{ik}^\gamma$ with the neuron-to-electrode distance d_{ik} and electrode contribution $\gamma = 1$. In contrast, if spike detection is applied ([Fig 1A](#), right), each electrode signal captures the spiking activity of few individual neurons (highlighted circles).

In order to focus on the key mechanistic differences between the two sampling approaches, we keep the two models as simple as possible. (This also matches the simple underlying dynamics, for which we can precisely set the distance to criticality). However, especially for coarse-sampling, this yields a rather crude approximation: More realistic, biophysically detailed LFP models would yield much more complex distance dependencies, which are an open field of research [37–40]. Our chosen electrode-contribution of $\gamma = 1$ assumes a large field of view, which implies the strongest possible measurement overlap to showcase the coarse-sampling effect. As this is an important assumption, we consider electrodes with a smaller field of view in [Sec. 2.5](#) and provide an extended discussion in the Supplemental Information ([Fig B](#) in [S1 Text](#)).

To test both recording types for criticality, we apply the standard analysis that provides a probability distribution $p(S)$ of the *avalanche size* S : In theory, an avalanche describes a cascade of activity where individual units—here neurons—are consecutively and causally activated. Each activation is called an event. The avalanche size is then the total number of events in the time between the first and the last activation. A power law in the size distribution of these avalanches is a hallmark of criticality [6]. In practice, the actual size of an avalanche is hard to determine because individual avalanches are not clearly separated in time; the coarse-sampled signal is continuous-valued and describes the local population. In order to extract binary events for the avalanche analysis ([Fig 2](#)), the signal has to be thresholded—which is not necessary for spike recordings, where binary events are inherently present as timestamps.

2.2 The branching parameter m sets the distance to criticality

In order to compare apparent signatures of criticality with the true, underlying dynamics, we first give some intuition about the branching model. The *branching parameter* m quantifies the probability of *postsynaptic activations*, or in other words, how many subsequent spikes are caused (on average) by a single spike. With increasing $m \rightarrow 1$, a single spike triggers increasingly long cascades of activity. These cascades determine the timescale over which fluctuations

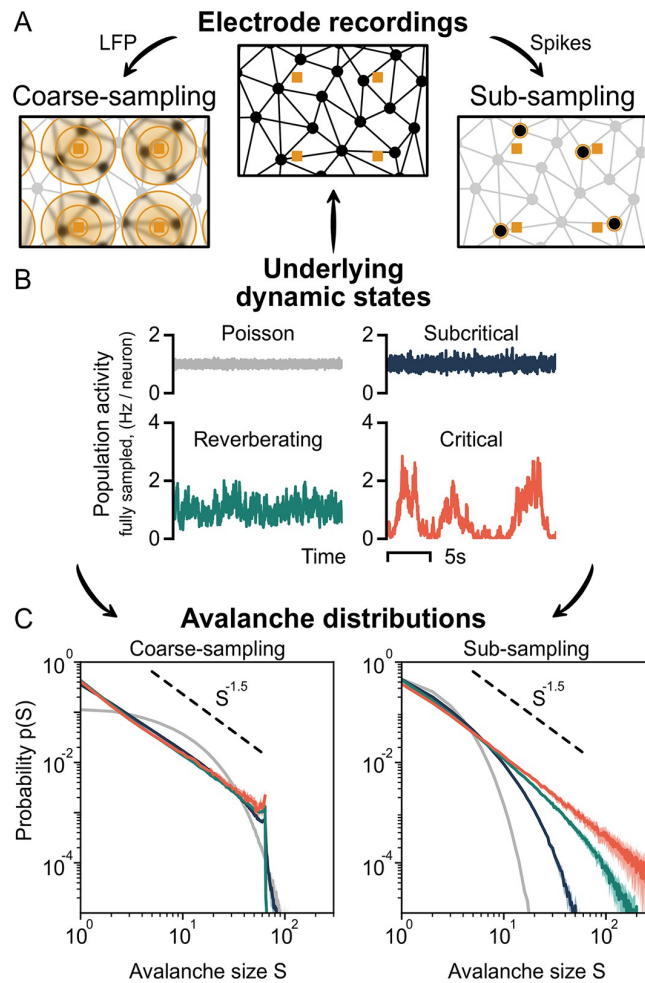


Fig 1. Sampling affects the assessment of dynamic states from neuronal avalanches. **A:** Representation of the sampling process of neurons (black circles) using electrodes (orange squares). Under coarse-sampling (e.g. LFP), activity is measured as a weighted average in the electrode’s vicinity. Under sub-sampling (spikes), activity is measured from few individual neurons. **B:** Fully sampled population activity of the neuronal network, for states with varying intrinsic timescales τ : Poisson ($\hat{\tau}_{psn} \approx 0$ ms), subcritical ($\hat{\tau}_{sub} \approx 19$ ms), reverberating ($\hat{\tau}_{rev} \approx 98$ ms) and critical ($\hat{\tau}_{crit} \approx 1.6$ s). **C:** Avalanche-size distribution $p(S)$ for coarse-sampled (left) and sub-sampled (right) activity. Sub-sampling allows for separating the different states, whereas coarse-sampling leads to $p(S) \sim S^{-\alpha}$ for all states except Poisson. **Parameters:** Electrode contribution $\gamma = 1$, inter-electrode distance $d_E = 400 \mu\text{m}$ and time-bin size $\Delta t = 8$ ms.

<https://doi.org/10.1371/journal.pcbi.1010678.g001>

occur in the population activity—this *intrinsic timescale* τ describes the dynamic state of the system and its distance to criticality.

The intrinsic timescale can be analytically related to the branching parameter by $\tau \sim -1/\ln(m)$. As $m \rightarrow 1$, $\tau \rightarrow \infty$ and the population activity becomes “bursty”. We illustrate this in Fig 1B and Table 1: For Poisson dynamics ($m \approx 0$), the intrinsic timescale is zero ($\hat{\tau}_{psn} \approx 0$ ms) and the activity between neurons is uncorrelated. As the distance to criticality becomes smaller ($m \rightarrow 1$), the intrinsic timescale becomes larger ($\hat{\tau}_{sub} \approx 19$ ms, $\hat{\tau}_{rev} \approx 98$ ms, $\hat{\tau}_{crit} \approx 1.6$ s), fluctuations become stronger, and the spiking activity becomes more and more correlated in space and time. Apart from critical dynamics, of particular interest in the above list is the “reverberating regime”: For practical reasons, we assign a specific value of m

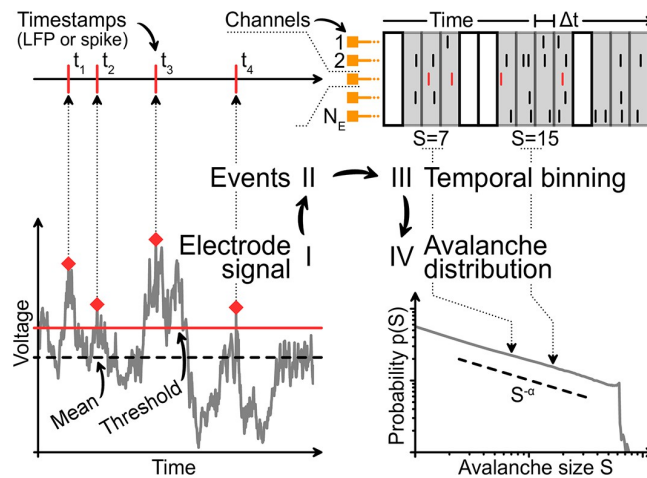


Fig 2. Analysis pipeline for avalanches from sampled data. I: Under coarse-sampling (LFP-like), the recording is demeaned and thresholded. II: The timestamps of events are extracted. Under sub-sampling (spikes), timestamps are obtained directly. III: Events from all channels are binned with time-bin size Δt and summed. The size S of each neuronal avalanche is calculated. IV: The probability of an avalanche size is given by the (normalized) count of its occurrences throughout the recording.

<https://doi.org/10.1371/journal.pcbi.1010678.g002>

(Table 1), which represents typical values observed *in vivo* [41, 42]. However, this choice is meant as a representation for a regime that is close-to-critical, but not directly at the critical point. In this regime, many of the benefits of criticality emerge, while the system can maintain a safety-margin from instability [41].

2.3 Coarse-sampling can cloud differences between dynamic states

Irrespective of the applied sampling, the inferred avalanche distribution *should* represent the true dynamic state of the system.

However, under coarse-sampling (Fig 1C, left), the avalanche-size distributions of the subcritical, reverberating and critical state are virtually indistinguishable. Intriguingly, all three show a power law. The observed exponent $\alpha = 1.5$ is associated with a critical branching process. Only the uncorrelated (Poisson-like) dynamics produce a non-power-law decay of the avalanche-size distribution.

Under sub-sampling (Fig 1C, right), each dynamic state produces a unique avalanche-size distribution. Only the critical state, with the longest intrinsic timescale, produces the characteristic power law. Even the close-to-critical, reverberating regime is clearly distinguishable and features a “subcritical decay” of $p(S)$.

Table 1. Parameters and intrinsic timescales of dynamic states. All combinations of branching parameter m and per-neuron drive h result in a stationary activity of 1 Hz per neuron. Due to the recurrent topology, it is more appropriate to consider the measured autocorrelation time $\hat{\tau}$ rather than the analytic timescale τ .

State name	m	$\hat{\tau}$ (measured)	$\tau = \frac{-2 \text{ ms}}{\ln m}$	h
Poisson	0.0	0.1 ± 0.1 ms	0.0 ms	2×10^{-3}
Subcritical	0.9	18.96 ± 0.09 ms	18.9 ms	2×10^{-4}
Reverberating	0.98	98.3 ± 1.0 ms	98.9 ms	4×10^{-5}
Critical	0.999	1.58 ± 0.12 s	1.99 s	2×10^{-6}

<https://doi.org/10.1371/journal.pcbi.1010678.t001>

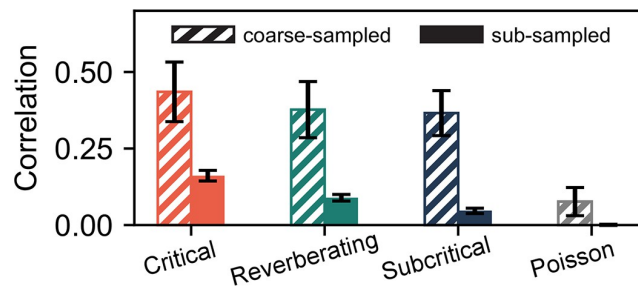


Fig 3. Coarse-sampling leads to greater correlations than sub-sampling. Pearson correlation coefficient between the signals of two adjacent electrodes for the different dynamic states. Even for independent (uncorrelated) Poisson activity, measured correlations under coarse-sampling are non-zero. **Parameters:** Electrode contribution $\gamma = 1$, inter-electrode distance $d_E = 400 \mu\text{m}$ and time-bin size $\Delta t = 8 \text{ms}$.

<https://doi.org/10.1371/journal.pcbi.1010678.g003>

2.4 Measurement overlap causes spurious correlations

Why are the avalanche-size distributions of different dynamic states hard to distinguish under coarse-sampling? The answer is hidden within the cascade of steps involved in the recording and analysis procedure. Here, we separate the impact of the involved processing steps. Most importantly, we discuss the consequences of *measurement overlap*—which we identify as a key explanation for the ambiguity of the distributions under coarse-sampling.

In order to obtain discrete events from the continuous time series for the avalanche analysis, each electrode signal is filtered and thresholded, binned with a chosen time-bin size Δt and, subsequently, the events from all channels are stacked. This procedure is problematic because (i) electrode proximity adds spatial correlations, (ii) temporal binning adds temporal correlations, and (iii) thresholding adds various types of bias [29–31].

As a result of the involved analysis of coarse-sampled data, spurious correlations are introduced that are not present in sub-sampled data. We showcase this effect in Fig 3, where the Pearson correlation coefficient between two virtual electrodes is compared for both the (thresholded and binned) coarse-sampled and sub-sampled activity. For the same parameters and dynamic state, coarse-sampling leads to larger correlations than sub-sampling.

Depending on the sensitivity and distance between electrodes, multiple electrodes might record activity from the same neuron. This **measurement overlap** (or volume conduction effect) increases the spatial correlations between electrodes—and because the signals from multiple electrode channels are combined in the analysis, correlations can originate from measurement overlap alone.

2.5 Measurement overlap depends on electrodes' field of view

The amount of measurement overlap between electrodes is determined effectively by the electrodes' field of view, thus the distance dependence with which a neuron's activity s_i contributes to the electrode signal V_k (Fig 4). We consider electrode signals $V_k(t) = \sum_i^{N_N} s_i(t)/d_{ik}^\gamma$, where the exponent γ indicates how narrow ($\gamma = 2$) or wide ($\gamma = 1$) the field of view is. Note that realistic distance dependencies are more complex and depend on many factors, such as neuron morphology and tissue filtering [37–40].

We find that the collapse of avalanche-size distributions from different dynamic states is strongest when the field of view is wide—i.e. if there is stronger measurement overlap. In that case, coarse-sampled distributions are hardly distinguishable (Fig 4C and 4D). For a narrow field of view, distributions are still hard to distinguish but do not fully collapse (Fig 4E and 4F).

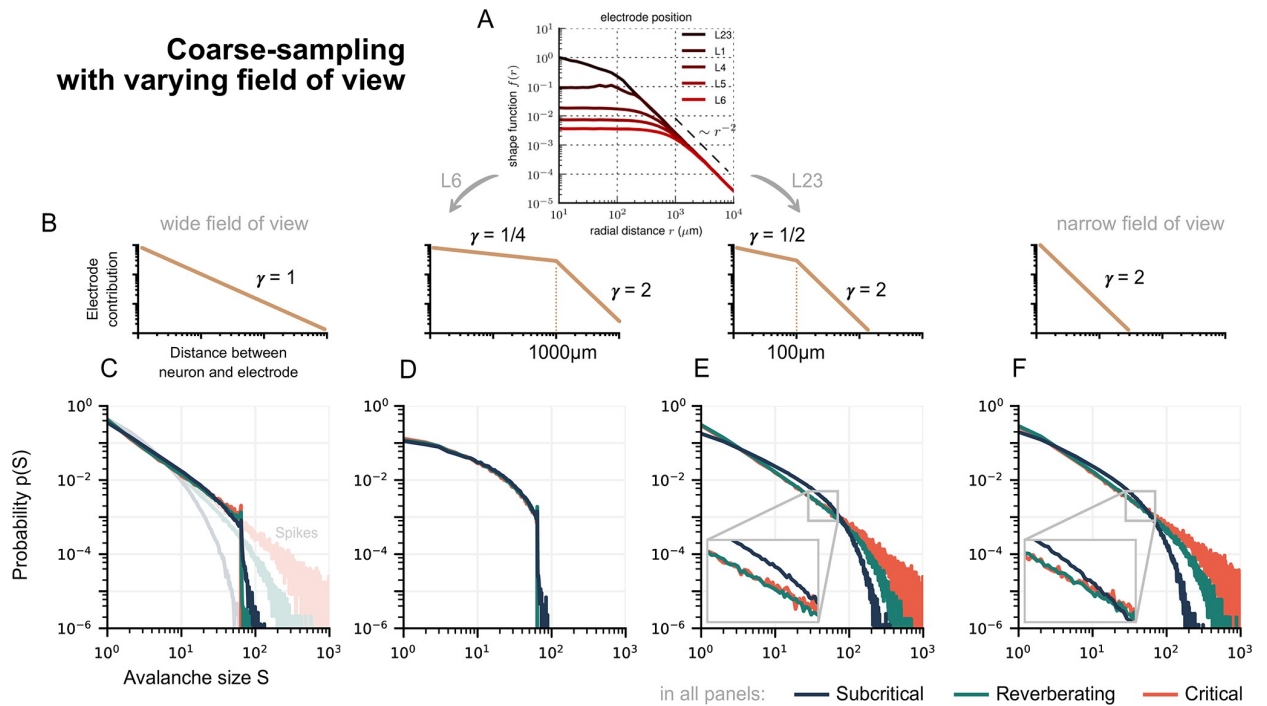


Fig 4. The signal of an extracellular neuronal recording depends on neuronal morphologies, tissue filtering, and other factors, which all impact the coarse-sampling effect. In effect, an important factor is the distance of the neuron to the electrode. Here, we show how the distance-dependence, with which a neuron’s activity contributes to an electrode, determines the collapse of avalanche distributions. **A:** Biophysically plausible distance dependence of LFP, reproduced from [38]. **B:** Sketch of a neuron’s contribution to an electrode at distance d_{ik} , as motivated by (A). The decay exponent γ characterizes the field of view. **C–F:** Avalanche-size distribution $p(S)$ for coarse-sampling with the sketched electrode contributions. **C, D:** With a wide-field of view, distributions are hardly distinguishable between dynamic states. In contrast, for spiking activity the differences are clear (light shades in C). **E, F:** With a narrower field of view, distributions do not fully collapse on top of each other, but differences between reverberating and critical dynamics remain hard to identify. **Parameters:** Inter-electrode distance $d_E = 400 \mu\text{m}$ and time-bin size $\Delta t = 8 \text{ ms}$. Other parameter combinations in Fig B in S1 Text.

<https://doi.org/10.1371/journal.pcbi.1010678.g004>

In order to study the impact of inter-electrode distance and temporal binning, in the following we focus on the wide field of view ($\gamma = 1$) where the avalanche collapse is most pronounced.

2.6 The effect of inter-electrode distance

Similar to the field of view of electrodes, avalanche-size distributions under coarse-sampling depend on the inter-electrode distance d_E (Fig 5A). For small inter-electrode distances, the overlap is strong. Thus, the spatial correlations are strong. Strong correlations manifest themselves in larger avalanches. However, under coarse-sampling the maximal observed size S of an avalanche is in general limited by the number of electrodes N_E [34] (cf. Fig B in S1 Text). This limit due to N_E manifests as a sharp cut-off and—in combination with spurious measurement correlations due to d_E —can shape the probability distribution. In the following, we show that these factors can be more dominant than the actual underlying dynamics.

In theory, supercritical dynamics are characterized by a sharp peak in the avalanche distribution at $S = N_E$. Independent of the underlying dynamics, such a peak can originate from small electrode distances (Fig 5A, $d_E = 100 \mu\text{m}$): Avalanches are likely to span the small area covered by the electrode array. Furthermore, due to strong measurement overlap, individual events of the avalanche may contribute strongly to multiple electrodes.

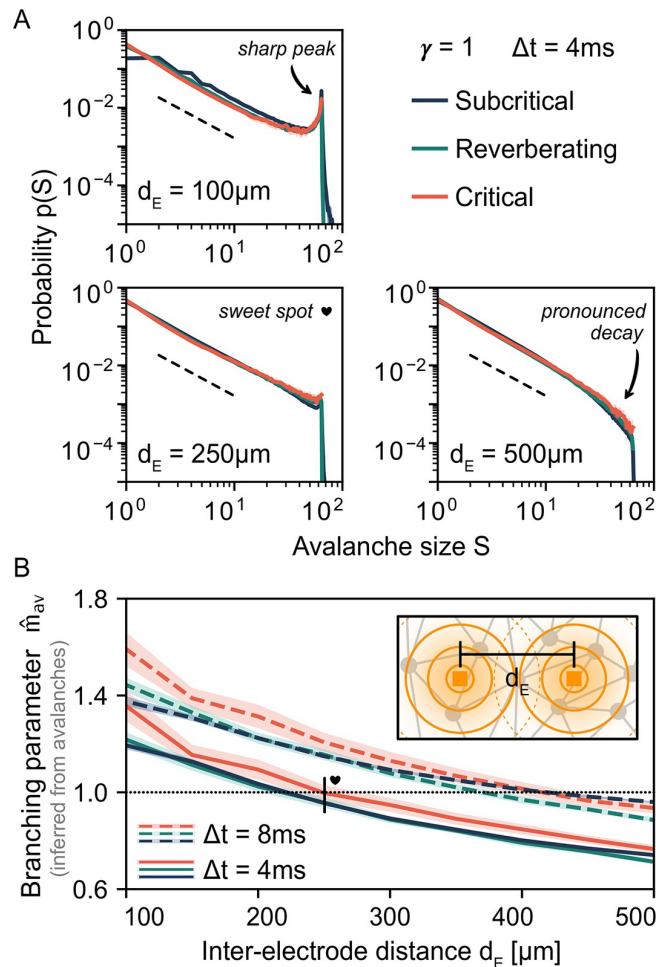


Fig 5. Under coarse-sampling, apparent dynamics depend on the inter-electrode distance d_E . A: For small distances ($d_E = 100 \mu\text{m}$), the avalanche-size distribution $p(S)$ indicates (apparent) supercritical dynamics: $p(S) \sim S^{-\alpha}$ with a *sharp peak* near the electrode number $N_E = 64$. For large distances ($d_E = 500 \mu\text{m}$), $p(S)$ indicates subcritical dynamics: $p(S) \sim S^{-\alpha}$ with a *pronounced decay* already for $S < N_E$. There exists a *sweet-spot* value ($d_E = 250 \mu\text{m}$) for which $p(S)$ indicates critical dynamics: $p(S) \sim S^{-\alpha}$ until the the cut-off is reached at $S = N_E$. The particular sweet-spot value of d_E depends on time-bin size (here, $\Delta t = 4 \text{ ms}$). As a guide to the eye, dashed lines indicate $S^{-1.5}$. B: The inferred branching parameter \hat{m}_{av} is also biased by d_E when estimated from neuronal avalanches. Apparent criticality ($\hat{m}_{av} \approx 1$, dotted line) is obtained with $d_E = 250 \mu\text{m}$ and $\Delta t = 4 \text{ ms}$ but also with $d_E = 400 \mu\text{m}$ and $\Delta t = 8 \text{ ms}$. B, Inset: representation of the measurement overlap between neighboring electrodes; when electrodes are placed close to each other, spurious correlations are introduced.

<https://doi.org/10.1371/journal.pcbi.1010678.g005>

Subcritical dynamics are characterized by a *pronounced decay* already for $S < N_E$. Independent of the underlying dynamics, such a decay can originate from large electrode distances (Fig 5A, $d_E = 500 \mu\text{m}$): Locally propagating avalanches are unlikely to span the large area covered by the electrode array. Furthermore, due to the weaker measurement overlap, individual events of the avalanche may contribute strongly to one electrode (or to multiple electrodes but only weakly).

Consequently, there exists a *sweet-spot* value of the inter-electrode distance d_E for which $p(S)$ appears convincingly critical (Fig 5A, $d_E = 250 \mu\text{m}$): a power law $p(S) \sim S^{-\alpha}$ spans all sizes up to the cut-off at $S = N_E$. However, the dependence on the underlying dynamic state is minimal.

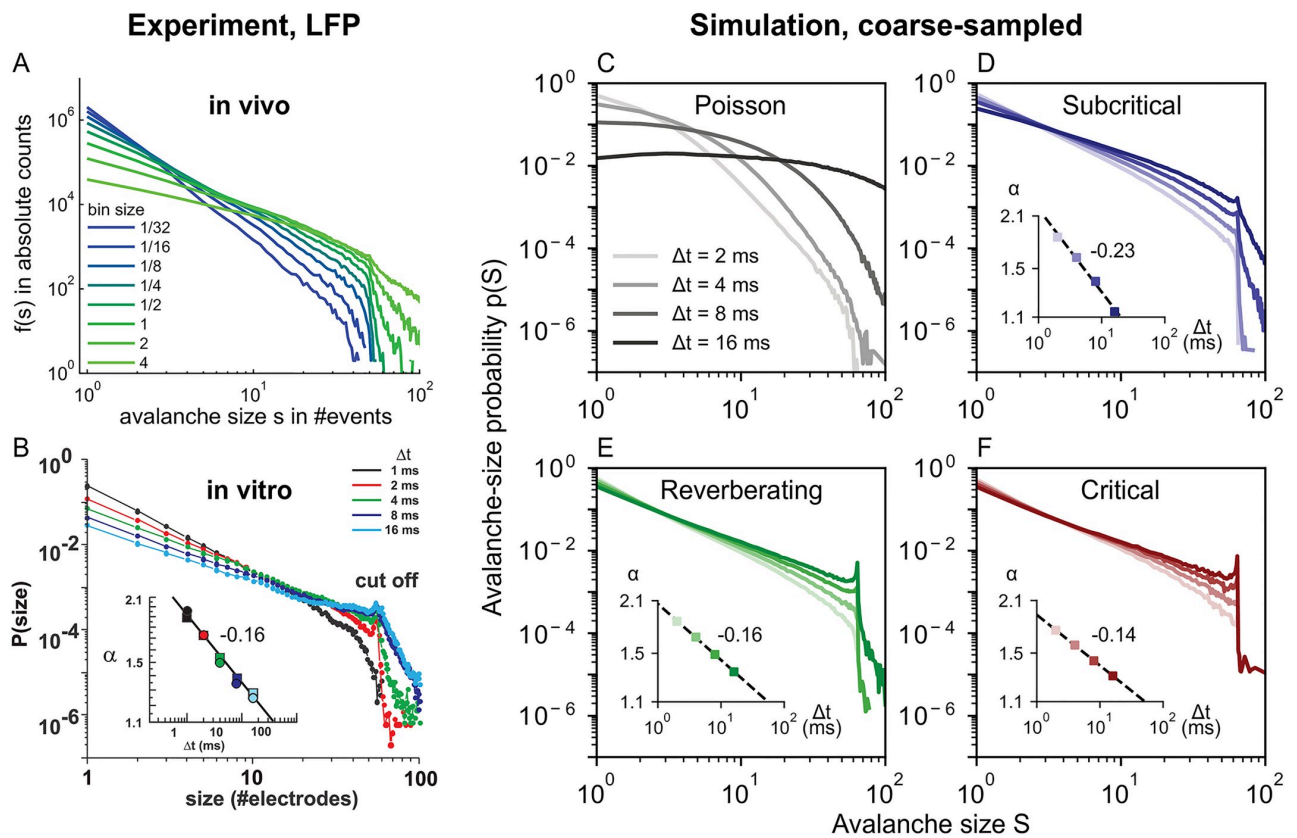


Fig 6. In vivo and in vitro avalanche-size distributions $p(S)$ from LFP depend on time-bin size Δt . Experimental LFP results are reproduced by many dynamics states of coarse-sampled simulations. **A:** Experimental *in vivo* results (LFP, human) from an array of 60 electrodes, adapted from [43]. **B:** Experimental *in vitro* results (LFP, culture) from an array with 60 electrodes, adapted from [1]. **C–F:** Simulation results from an array of 64 virtual electrodes and varying dynamic states, with time-bin sizes between $2 \text{ ms} \leq \Delta t \leq 16 \text{ ms}$, $\gamma = 1$ and $d_E = 400 \mu\text{m}$. Subcritical, reverberating and critical dynamics produce approximate power-law distributions with bin-size-dependent exponents α . **Insets:** Log-Log plot, distributions are fitted to $p(S) \sim S^{-\alpha}$, fit range $S \leq 50$. The magnitude of α decreases as $\Delta t^{-\beta}$ with $-\beta$ indicated next to the insets, cf. Table 2.

<https://doi.org/10.1371/journal.pcbi.1010678.g006>

Independently of the apparent dynamics, we observe the discussed cut-off at $S = N_E$, which is also often seen in experiments (Fig 6). Note, however, that this cut-off only occurs under coarse-sampling (see again Fig 1C). When spikes are used instead (Fig 7), the same avalanche can reach an electrode repeatedly in quick succession—whereas such double-events are circumvented when thresholding at the population level. For more details see Fig B in S1 Text.

A further signature of criticality is obtained by inferring the branching parameter. If the inference is unbiased, the inferred \hat{m} matches the underlying branching parameter m . We have developed a sub-sampling invariant estimator (based on the population activity inferred from spikes [27]), but \hat{m} is traditionally inferred from avalanches. Then, \hat{m}_{av} is defined as the average ratio of events between subsequent time bins in an avalanche, i.e. during non-zero activity [1, 33].

Obtaining \hat{m}_{av} for different electrode distances results in a picture consistent with the one from avalanche-size distributions (Fig 5B). In general, the dependence on the electrode distance is stronger than the dependence on the underlying state. At the particular value of the inter-electrode distance where $\hat{m}_{av} = 1$, the distributions appear critical. If $\hat{m}_{av} < 1$ ($\hat{m}_{av} > 1$),

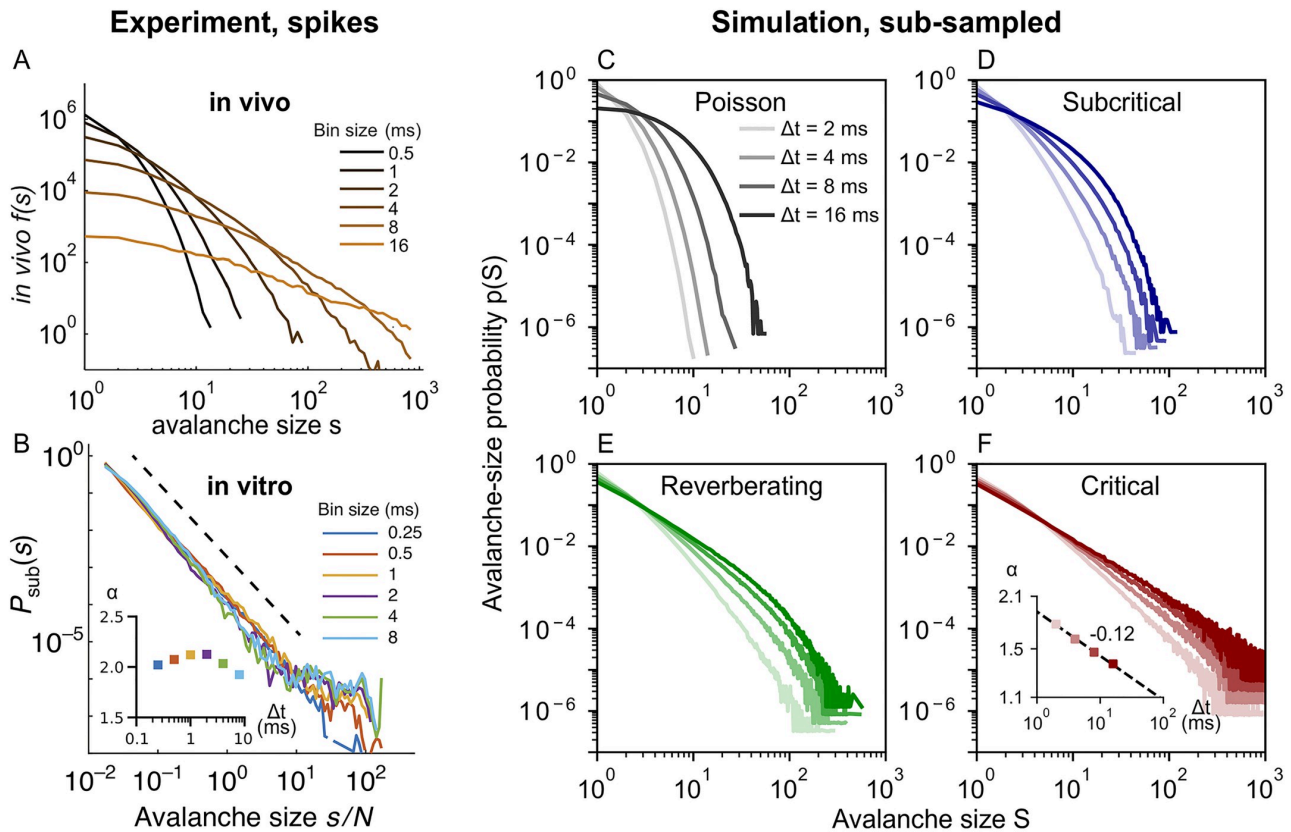


Fig 7. *In vivo* avalanche-size distributions $p(S)$ from spikes depend on time-bin size Δt . *In vivo* results from spikes are reproduced by sub-sampled simulations of subcritical to reverberating dynamics. Neither spike experiments nor sub-sampled simulations show the cut-off that is characteristic under coarse-sampling. **A:** Experimental *in vivo* results (spikes, awake monkey) from an array of 16 electrodes, adapted from [24]. The pronounced decay and the dependence on bin size indicate subcritical dynamics. **B:** Experimental *in vitro* results (spikes, culture DIV 34) from an array with 59 electrodes, adapted from [44]. Avalanche-size distributions are largely independent of time-bin size and resemble a power law over four orders of magnitude. In combination, this indicates a separation of timescales and critical dynamics (or even super critical dynamics [45]). **B, Inset:** Log-Lin plot of fitted α , fit range $s/N \leq 5$. **C–F:** Simulation for sub-sampling, analogous to Fig 6. Subcritical dynamics do not produce power-law distributions and are clearly distinguishable from critical dynamics. **F:** Only the (close-to) critical simulation produces power-law distributions. **F, Inset:** Log-Log plot of fitted α , fit range $S \leq 50$. In contrast to the *in vitro* culture (in B), the simulation does not feature a separation of time scales (due to external drive and stationary activity), and therefore the slope shows a systematic bin-size dependence here.

<https://doi.org/10.1371/journal.pcbi.1010678.g007>

the distributions appear subcritical (supercritical). Notably, the supercritical $m > 1$ corresponds to dynamics where activity increases indefinitely, which is not possible for systems of finite size and exposes $\hat{m}_{av} > 1$ as an inference effect. More precisely, in case of our simulations, \hat{m}_{av} suffers two sources of bias: firstly, the coarse-sampling bias that is rooted in the preceding avalanche analysis, and secondly the estimator assumes a pure branching process without specific topology or coalescence effects [36].

Concluding, because the probability distributions and the inferred branching parameter share the dependence on electrode distance, a wide range of dynamic states would be consistently misclassified—solely as a function of the inter-electrode distance.

2.7 Temporal binning determines scaling exponents

Apart from the inter-electrode distance, the choice of temporal discretization that underlies the analysis may alter avalanche-size distributions. This *time-bin size* Δt varies from study to

Table 2. Fitted exponents of $\alpha \sim \Delta t^{-\beta}$.

Dynamic state	β	
	$d_E = 200 \mu\text{m}$	$d_E = 400 \mu\text{m}$
in vitro (LFP) [1]	0.16 ± 0.01	
Critical (coarse)	0.113 ± 0.001	0.141 ± 0.001
Reverberating (coarse)	0.127 ± 0.003	0.156 ± 0.002
Subcritical (coarse)	0.159 ± 0.004	0.231 ± 0.016
Critical (spikes)	0.143 ± 0.010	0.123 ± 0.005

<https://doi.org/10.1371/journal.pcbi.1010678.t002>

study and it can severely impact the observed distributions [1, 24, 43, 44]. With smaller bin sizes, avalanches tend to be separated into small clusters, whereas larger bin sizes tend to “glue” subsequent avalanches together [24]. Interestingly, this not only leads to larger avalanches, but specifically to $p(S) \sim S^{-\alpha}$, where the exponent α increases systematically with bin size [1, 43]. Such a changing exponent is not expected for conventional systems that self-organize to criticality: Avalanches would be *separated in time*, and α should be fairly bin-size invariant for a large range of Δt [24, 44, 46].

Our coarse-sampled model reproduces these characteristic experimental results (Fig 6). It also reproduces the previously reported scaling [1] of the exponent with bin size $\alpha \sim \Delta t^{-\beta}$ (cf. Fig 6 insets and Table 2). Except for the Poisson dynamics, all the model distributions show power laws. Moreover the distributions are strikingly similar, not just to the experimental results, but also to each other. This emphasizes how sensitive signs of criticality are to analysis parameters: All the shown dynamic states are consistent with the ubiquitous avalanche-size distributions that are observed in coarse-sampled experiments [45] (cf. Table A in S1 Text).

When spikes are used instead, power-law distributions only arise from critical dynamics. For comparison with the coarse-sampled results in Fig 6, we show avalanche-size distributions from experimental spike recordings and sub-sampled simulations in Fig 7.

In vivo spike recordings of awake animals produce distributions that feature a pronounced decay instead of power laws (Fig 7A). Interestingly, spike recordings of in vitro cultures often show power-laws and, here, even little-to-no bin-size dependence, which indicates a fairly good separation of timescales (Fig 7B). In this example, the power-law extends over several orders of magnitude, and the slope does not decrease systematically with the bin size. This indicates close-to-critical dynamics; the slight bump that represents an excess of very large avalanche, however, might also point to slight super-criticality [44, 45].

Considering our simulations of sub-sampling (Fig 7C–7F), we only observe approximate power laws if the model is (close-to) critical (Fig 7F). Note that in critical systems, the avalanche distribution should not change with bin size, and that here the bin-size dependence of the slope is caused by the finite system size and by the non-zero spike rate, which impede a proper separation of timescales. Nonetheless, in contrast to coarse-sampling, the avalanche distributions that stem from sub-sampled measures (spikes) allow us to clearly tell apart the underlying dynamic states from one another.

Overall, as our results on coarse-sampling have shown, different sources of bias—here the measurement overlap and the bin size—can perfectly outweigh each other. For instance, smaller electrode distances (that increase correlations) can be compensated by making the time-bin size smaller (which again decreases correlations). This was particularly evident in Fig 5B, where increasing d_E could be outweighed by increasing Δt in order to obtain a particular value for the branching parameter m_{av} . The same relationship was again visible in Fig 6C–6F:

For the shown $d_E = 400 \mu\text{m}$ (see also [S1 Text](#) for $d_E = 200 \mu\text{m}$), only $\Delta t = 8 \text{ ms}$ results in $\alpha = 1.5$ —the correct exponent for the underlying dynamics. Since the electrode distance cannot be varied in most experiments, selecting anything but the one “lucky” Δt will cause a bias.

3 Discussion

When inferring collective network dynamics from partially sampled systems, it is crucial to understand how the sampling biases the measured observables. Without this understanding, an elaborate analysis procedure—such as the one needed to study neuronal avalanches from coarse-sampled data—can result in a misclassification of the underlying dynamics.

We have shown that the analysis of neuronal avalanches based on (LFP-like) coarse-sampled data can cloud differences of avalanche distributions from systems with different spatio-temporal signatures. These signatures derive from underlying dynamic states that, in this work, range from subcritical to critical—a range over which the intrinsic timescale undergoes a hundred-fold increase. And yet, the resulting avalanche-size distributions can be ambiguous ([Fig 1](#)).

The ambiguity of neuronal avalanches partially originates from spurious correlations. We have demonstrated the generation of spurious correlations from two sampling- and processing mechanisms: measurement overlap (due to volume conduction) and temporal binning. Other studies found further mechanisms that can generate apparent power-law distributions by (purposely or accidentally) introducing correlations into the *observed* system. For instance, correlated input introduces temporal correlations already into the *underlying* system [[47](#), [48](#)]. Along with thresholding and low-pass frequency filtering—which add temporal correlations to the *observed* system [[25](#), [49](#)—this creates a large space of variables that either depend on the system, sampling and processing, or a combination of both.

As our results focus on sampling and processing, we believe that the observed impact on avalanche-size distributions is general and model independent. We deliberately used simple models and confirmed that our results are robust to parameter and model changes: First, our model for coarse-sampling prioritizes simplicity over biophysical details—in order to be consistent with our simplified but well-controlled neuronal dynamics—but we checked that our results are consistent with different distance-dependencies or adding a cut-off (Figs B and C in [S1 Text](#)). Second, employing a more realistic topology causes no qualitative difference (Fig A in [S1 Text](#)). Third, as a proof of concept, we investigated the impact of measurement overlap in the 2D Ising model (Fig G in [S1 Text](#)). Even in such a fundamental model a measurement overlap can bias the assessment of criticality. Lastly, we investigated scaling relations (of avalanche size- and duration distributions) and found that under coarse-sampling, the inference is severely hindered (Fig F in [S1 Text](#)). Under sub-sampling, scaling relations hold but with a different collapse exponent than expected for our model. This is consistent with other recent work showing that sampling can affect the collapse exponent [[50](#)].

Despite these efforts, our work remains a mechanistic modeling study and we want to stress its limitations: Our virtual sampling did not account for neuron morphology nor the individual neuron’s connectivity profiles. As spikes are non-local events, both these aspects impact the sampling range of an electrode and the decay of e.g. an LFP signal [[38](#), [40](#)]. Sampling also depends on effects that occur prior to recording, such as possible filtering due to extracellular tissue [[25](#), [51](#)] or filtering due to neuron morphology [[40](#), [52](#)]. In particular, low-pass filtering can arise from synaptic dynamics or the propagation within dendrites [[53](#)]. Clearly, as high frequencies get stripped from the signal, this could attenuate deflections of the recorded time series. Because these deflections are central to the avalanche detection, low-pass filtering could, in principle, affect avalanche statistics. However, preliminary tests showed that our main result

of overlapping distributions for different dynamics states remains intact when the raw time series are low-pass filtered (Fig E in [S1 Text](#)).

Our results seemingly contradict experimental studies that demonstrate that the avalanche analysis is sensitive to pharmacological manipulations such as anesthesia [18, 54–57]. Following a sufficient manipulation, a system's dynamic state will change—which should be reflected by a visible difference of avalanche distributions. We showed that under coarse-sampling, the precise dynamic state could be misclassified. Whereas *subtle* differences between the avalanche distributions from different dynamic states are indeed visible (Fig 5), in general, they are clouded under coarse-sampling due to the measurement overlap. However, the smaller the measurement overlap becomes (e.g. through increasing the electrode-distance), the clearer the differences between dynamic states become (Fig B in [S1 Text](#)). In experiments the measurement overlap is unknown; it is also a priori unknown how strong a pharmacological perturbation is (relative to the equally unknown initial dynamic state) and how much coarse-sampling affects its inference. In modeling studies such as ours, these circumstances are well controlled—providing an explanation on a mechanistic level that can now be taken into consideration (and accounted for) when analyzing experimental data.

With our results on sampling effects, we can revisit the previous literature on neuronal avalanches. In Ref. [26] Ribeiro and colleagues show that “undersampling” biases avalanche distributions near criticality. In this case, undersampling was modeled by electrodes picking up a variable number of closest neurons. Here, we separated the effect of sub-sampling (electrodes cannot record all neurons) from coarse-sampling (electrodes record multiple neurons with distance-dependent contributions) and can add to previous results: In our model, we found that coarse-sampling clouds the differences between subcritical, reverberating, and critical dynamics; for $\gamma = 1$, the avalanche distributions always resemble power laws (Fig 4). Because of this ambiguity, the power-law distributions obtained ubiquitously from LFP, EEG, MEG and BOLD activity should be taken as evidence of neuronal activity with spatio-temporal correlations—but not necessarily of criticality proper; the coarse-sampling might hinder such a precise classification. In this regard, the interpretation of results from calcium imaging (which has a lower temporal resolution than electrode recordings) remains open (cf. Table A in [S1 Text](#) for an overview).

In contrast, a more precise classification seems possible when using spikes. If power-law distributions are observed from (sub-sampled) spiking activity, they do point to critical dynamics. For spiking activity, we even have mathematical tools to infer the precise underlying state in a sub-sampling-invariant manner that does not rely on avalanche distributions [27, 58]. However, not all spike recordings point to critical dynamics: Whereas in vitro recordings typically do produce power-law distributions [44, 59–61], extracellular spike recordings from awake animals typically do not [16, 18, 24, 62].

Lastly, our results might offer a solution to resolve an inconsistency between avalanche distributions that derive from spikes vs. LFP-like sampling: For experiments on awake animals, spike-based studies typically indicate subcritical dynamics. Although coarse measures typically produce power laws that indicate criticality, in this work we showed that they might cloud the difference between critical and subcritical dynamics. Consistent with both, a brain that operates in a *near*-critical regime—as opposed to a fixed dynamic state—could harness benefits associated with criticality while flexibly tuning its response properties [43, 63–69].

4 Methods

4.1 Model details

Our model is comprised of a two-level configuration, where a 2D network of $N_N = 160000$ spiking neurons is sampled by a square array of $N_E = 8 \times 8$ virtual electrodes. Neurons are

Table 3. Values and descriptions of the model parameters.

Symbol	Value	Description
Δt	2 – 16 ms	Time-bin size (duration) for temporal binning
Θ_k	3	Activity threshold, in units of standard deviations of the time series of electrode k
δt	2 ms	Simulation time step
r	1 Hz	Average spike rate
N_N	1.6×10^5	Number of neurons
d_N	50 μm	Inter-neuron distance (measured between nearest neighbors)
L	4 cm	Linear system size
ρ	100/ mm^2	Neuronal density
K	1000	Average network degree (outgoing connections per neuron)
d_{max}	1.78 mm	Connection length; all neurons within d_{max} are connected
σ	300 μm	Effective length of synaptic connections, sets the distance-dependence of the probabilities of recurrent activations
N_E	8×8	Number of electrodes
d_E	50 – 500 μm	Inter-electrode distance
d_E^*	10 μm	Dead-zone around each electrode (no neurons present)
γ	1	Decay exponent. Contributions of each spike to the coarse electrode signal scale as $V(d) \sim 1/d^\gamma$. See SI for results and discussion of different electrode contributions.

<https://doi.org/10.1371/journal.pcbi.1010678.t003>

distributed randomly in space (with periodic boundary conditions) and, on average, nearest neighbors are $d_N = 50 \mu\text{m}$ apart. While the model is inherently unit-less, it is more intuitive to assign some length scale—in our case the inter-neuron distance d_N —to set that scale: all other size-dependent quantities can then be expressed in terms of the chosen d_N . For instance, the linear system size L can be derived by realizing that the random placement of neurons corresponds to an ideal gas. It follows that $L = 2\sqrt{N_N} d_N = 4\text{cm}$ for uniformly distributed neurons. (For comparison, on a square lattice, the packing ratio would be higher and it is easy to see that the system size would be $\sqrt{N_N} d_N$.) Given the system size and neuron number, the overall neuronal density is $\rho = 100/\text{mm}^2$. With our choice of parameters, the model matches typical experimental conditions in terms of inter-neuron distance and system size (see Table 3 for details). Whereas the apparent neuron density of $\rho = 100/\text{mm}^2$ is on the lower end of literature values [70, 71], this parameter choice avoids boundary effects that can be particularly dominant near criticality due to the long spatial correlation. The implementation of the model in C++, and the python code used to analyze the data and generate the figures, are available online at <https://github.com/Priesemann-Group/criticalavalanches>.

4.2 Topology

We consider a topology that enforces *local* spreading dynamics. Every neuron is connected to all of its neighbors within a threshold distance d_{max} . The threshold is chosen so that on average $K = 10^3$ outgoing connections are established per neuron. We thus seek the radius d_{max} of a disk whose area contains K neurons. Using the already known neuron density, we find $d_{\text{max}} = \sqrt{K/\pi\rho} \approx 1.78 \text{ mm}$. For every established connection, the probability of a recurrent activation decreases with increasing neuron distance. Depending on the particular distance d_{ij} between the two neurons i and j , the connection has a normalized weight $w_{ij} = e^{-d_{ij}^2/2\sigma^2} / \Omega_i$ (with normalization constant $\Omega_i = \sum_j e^{-d_{ij}^2/2\sigma^2}$). Our weight definition approximates the distance dependence of average synaptic strength. The parameter σ sets the *effective* distance over which connections can form (d_{max} is an upper limit for σ and mainly speeds up computation.)

In the limit $\sigma \rightarrow \infty$, the network is all-to-all connected. In the limit $\sigma \rightarrow 0$, the network is completely disconnected. Therefore, the effective connection length σ enables us to fine tune *how local* the dynamic spreading of activity is. In our simulations, we choose $\sigma = 6d_N = 300 \mu\text{m}$. Thus, the overall reach is much shorter than d_{max} ($\sigma \approx 0.16 d_{\text{max}}$).

4.3 Dynamics

To model the dynamic spreading of activity, time is discretized to a chosen simulation time step, here $\delta t = 2 \text{ ms}$, which is comparable to experimental evidence on synaptic transmission [72]. Our simulations run for 10^6 time steps on an ensemble of 50 networks for each configuration (combination of parameters and dynamic state). This corresponds to ~ 277 hours of recordings for each dynamic state.

The activity spreading is modeled using the dynamics of a branching process with external drive [27, 35]. At every time step t , each neuron i has a state $s_i(t) = 1$ (spiking) or 0 (quiescent). If a neuron is spiking, it tries to activate its connected neighbors—so that they will spike in the next time step. All of these recurrent activations depend on the *branching parameter* m : Every attempted activation has a probability $p_{ij} = m w_{ij}$ to succeed. (Note that the distance-dependent weights are normalized to 1 but the activation probabilities are normalized to m .) In addition to the possibility of being activated by its neighbors, each neuron has a probability h to spike spontaneously in the next time step. After spiking, a neuron is reset to quiescence in the next time step if it is not activated again.

Our model gives us full control over the dynamic state of the system—and its distance to criticality. The dynamic state is described by the *intrinsic timescale* τ . We can analytically calculate the intrinsic timescale $\tau = -\delta t / \ln(m)$, where δt is the duration of each simulated time step. Note that m —the control parameter that *tunes the system*—is set on the neuron level while τ is a (collective) network property (that in turn allows us to deduce an *effective* m). As the system is pushed more towards criticality (by setting $m \rightarrow 1$), the intrinsic timescale diverges $\tau \rightarrow \infty$.

For consistency, we measure the intrinsic timescale during simulations. To that end, the (fully sampled) population activity at each time step is given by the number of active neurons $A(t) = \sum_i s_i(t)$. A linear least-squares fit of the autoregressive relation $A(t+1) = e^{-\delta t/\tau} A(t) + N_N h$ over the full simulated time series yields an estimate $\hat{\tau}$ that describes each particular realization.

By adjusting the branching parameter m (setting the dynamic state) *and* the probability for spontaneous activations h (setting the drive), we control the distance to criticality *and* the average stationary activity. The activity is given by the *average spike rate* $r = h/(\delta t(1-m))$ of the network. For all simulations, we fix the rate to $r = 1 \text{ Hz}$ in order to avoid rate effects when comparing different states (see Table 1 for the list of parameter combinations). Note that, due to the non-zero drive h and the desired stationary activity, the model cannot be perfectly critical ($\hat{\tau} \rightarrow \infty$, see Table 1).

4.4 Coalescence compensation

With our probability-based update rules, it may happen that target neurons are simultaneously activated by multiple sources. This results in so-called *coalescence effects* that are particularly strong in our model due to the local activity spreading [36]. For instance, naively setting $m = 1$ (with $\sigma = 300 \mu\text{m}$) would result in an effective (measured) $\hat{m} \approx 0.98$, which has considerably different properties. Compared to e.g. $m = 0.999$ this would result in a 20-fold decrease in τ .

In order to compensate these coalescence effects, we apply a simple but effective fix: If an activation attempt is successful but the target neuron is already marked to spike in the next

time step, another (quiescent) target is chosen. Because our implementation stores all the connected target neurons as a list sorted by their distance to the source, it is easy to activate the next neuron in that list. Thereby, the equivalent probability of the performed activation is as close to the originally attempted one as possible.

4.5 Virtual electrode recordings

Our simulations are designed to mimic sampling effects of electrodes in experimental approaches. To simulate sampling, we use the readout of $N_E = 64$ virtual electrodes that are placed in an 8×8 grid. Electrodes are separated by an inter-electrode distance that we specify in multiples of inter-neuron distance d_N . It is kept constant for each simulation and we study the impact of the inter-electrode distance by repeated simulations spanning electrode distances between $1d_N = 50 \mu\text{m}$ and $10d_N = 500 \mu\text{m}$. The electrodes are modeled to be point-like objects in space that have a small dead-zone of $d_E^* = d_N/5 = 10 \mu\text{m}$ around their origin. Within the dead-zone, no signal can be recorded (in fact, we implement this by placing the electrodes first and the neurons second—and forbid neuron placements too close to electrodes).

Using this setup, we can apply sampling that emulates either the detection of spike times or LFP-like recordings. To model the detection of spike times, each electrode only observes the single neuron that is closest to it. Whenever this particular neurons spikes, the timestamp of the spike is recorded. All other neurons are neglected—and the dominant sampling effect is *sub-sampling*. On the other hand, to model LFP-like recordings, each electrode integrates the spiking of all neurons in the system. Contributions are strictly positive, matching the underlying branching dynamics (for more biophysically detailed LFP models, contributions would depend on neuron types and other factors). The contribution of a single spike, e.g. from neuron i to electrode k , decays as $1/d_{ik}$ with the neuron-to-electrode distance. (See Fig B in [S1 Text](#) for a detailed discussion of the qualitative impact of changing the distance dependence, e.g. to $1/d_{ik}^2$.) The total signal of the electrode at time t is then $V_k(t) = \sum_i^{N_N} s_i(t)/d_{ik}$. Diverging electrode signals are prevented by the forbidden zone around the electrodes. For such coarse-sampled activity, all neurons contribute to the signal and the contribution is weighted by their distance.

4.6 Avalanches

Taking into account all 64 electrodes, a new avalanche starts (by definition [1]) when there is at least one event (spike) in a time bin—given there was no event in the previous time bin (see [Fig 2](#)). An avalanche ends whenever an empty bin is observed (no event over the duration of the time bin). Hence, an avalanche persists for as long as every consecutive time bin contains at least one event—which is called the *avalanche duration* D . From here, it is easy to count the total number of events that were recorded across all electrodes and included time bins—which is called the *avalanche size* S . The number of occurrences of each avalanche size (or duration) are sorted into a histogram that describes the avalanche distribution.

4.7 Analysis of avalanches under coarse and sub-sampling

We analyze avalanche size distributions in a way that is as close to experimental practice as possible (see [Fig 2](#)). From the simulations described above, we obtain two outputs from each electrode: a) a list containing spike times of the single closest neuron and b) a time series of the integrated signal to which all neurons contributed.

In case of the (sub-sampled) spike times a), the spiking events are already present in binary form. Thus, to define a neural avalanche, the only required parameter is the size of the time bin Δt (for instance, we may choose $\Delta t = 4$ ms).

In case of the (coarse-sampled) time series b), binary events need to be extracted from the continuous electrode signal. The extraction of spike times from the continuous signal relies on a criterion to differentiate if the set of observed neurons is spiking or not—which is commonly realized by applying a threshold. (Note that now thresholding takes place on the electrode level, whereas previously, an event belonged to a single neuron.) Here, we obtain avalanches by thresholding as follows: First, all time series are frequency filtered to $0.1 \text{ Hz} < f < 200 \text{ Hz}$. This demeans and smoothes the signal (and reflects common hardware-implemented filters of LFP recordings). Second, the mean and standard deviation of the full time series are computed for each electrode. The mean is virtually zero due to cutting low frequencies when band-pass filtering. Each electrode's threshold is set to three standard deviations above the mean. Third, for every positive excursion of the time series (i.e. $V_k(t) > 0$), we recorded the timestamp $t = t_{\max}$ of the maximum value of the excursion. An event was defined when $V_k(t_{\max})$ was larger than the threshold Θ_k of three standard deviations of the (electrode-specific) time series. (Whenever the signal *passes the threshold*, the timestamps of all local maxima become candidates for the event; however, only the one largest maximum between two *crossings of the mean* assigns the final event-time.) Once the continuous signal of each electrode has been mapped to binary events with timestamps, the remaining analysis steps were the same for coarse-sampled and sub-sampled data. Last, avalanche size and duration distributions are fitted to power-laws using the powerlaw package [73].

Supporting information

S1 Text. Supplementary text, figures and extended modeling. We provide additional computations, numerical simulations, and an extended discussion of the model and its parametrizations. (PDF)

Acknowledgments

We thank Jordi Soriano, Johannes Zierenberg and all members of our group, for valuable input. We thank Johannes Zierenberg and Bettina Royen for careful proofreading of the manuscript.

Author Contributions

Conceptualization: Joao Pinheiro Neto, F. Paul Spitzner, Viola Priesemann.

Data curation: Joao Pinheiro Neto, F. Paul Spitzner.

Formal analysis: Joao Pinheiro Neto, F. Paul Spitzner, Viola Priesemann.

Investigation: Joao Pinheiro Neto, F. Paul Spitzner, Viola Priesemann.

Methodology: Joao Pinheiro Neto, F. Paul Spitzner, Viola Priesemann.

Project administration: Viola Priesemann.

Software: Joao Pinheiro Neto, F. Paul Spitzner.

Supervision: Viola Priesemann.

Validation: Joao Pinheiro Neto, F. Paul Spitzner.

Visualization: Joao Pinheiro Neto, F. Paul Spitzner.

Writing – original draft: Joao Pinheiro Neto, F. Paul Spitzner, Viola Priesemann.

Writing – review & editing: Joao Pinheiro Neto, F. Paul Spitzner, Viola Priesemann.

References

1. Beggs JM, Plenz D. Neuronal Avalanches in Neocortical Circuits. *Journal of Neuroscience*. 2003; 23(35):11167–11177. <https://doi.org/10.1523/JNEUROSCI.23-35-11167.2003> PMID: 14657176
2. Dunkelmann S, Radons G. Neural Network and Abelian Sandpile Models of Self-Organized Criticality. In: Marinaro M, Morasso PG, editors. *Proceedings of International Conference Artificial Neural Networks*. Springer-Verlag; 1994. p. 867–870.
3. Beggs JM. The criticality hypothesis: how local cortical networks might optimize information processing. *Philosophical Transactions of the Royal Society A: Mathematical, Physical and Engineering Sciences*. 2008; 366(1864):329–343. <https://doi.org/10.1098/rsta.2007.2092> PMID: 17673410
4. Muñoz MA. Colloquium: Criticality and dynamical scaling in living systems. *Reviews of Modern Physics*. 2018; 90(3):031001. <https://doi.org/10.1103/RevModPhys.90.031001>
5. Cocchi L, Gollo LL, Zalesky A, Breakspear M. Criticality in the brain: A synthesis of neurobiology, models and cognition. *Progress in Neurobiology*. 2017; 158:132–152. <https://doi.org/10.1016/j.pneurobio.2017.07.002> PMID: 28734836
6. Plenz D, Niebur E, editors. *Criticality in Neural Systems*. vol. 9783527411. Weinheim, Germany: Wiley-VCH Verlag GmbH & Co. KGaA; 2014. Available from: <http://doi.wiley.com/10.1002/9783527651009>.
7. Zeraati R, Priesemann V, Levina A. Self-Organization Toward Criticality by Synaptic Plasticity. *Front Phys*. 2021; 9. <https://doi.org/10.3389/fphys.2021.619661>
8. Sethna JP. *Statistical Mechanics: Entropy, Order Parameters, and Complexity*. 1st ed. New York: Oxford University Press; 2006.
9. Kinouchi O, Copelli M. Optimal dynamical range of excitable networks at criticality. *Nature Physics*. 2006; 2(5):348–351. <https://doi.org/10.1038/nphys289>
10. Zierenberg J, Wiltling J, Priesemann V, Levina A. Tailored ensembles of neural networks optimize sensitivity to stimulus statistics. *Physical Review Research*. 2020; 2(1):013115. <https://doi.org/10.1103/PhysRevResearch.2.013115>
11. Haldeman C, Beggs JM. Critical Branching Captures Activity in Living Neural Networks and Maximizes the Number of Metastable States. *Physical Review Letters*. 2005; 94(5):058101. <https://doi.org/10.1103/PhysRevLett.94.058101> PMID: 15783702
12. Tkačik G, Mora T, Marre O, Amodei D, Palmer SE, Berry MJ, et al. Thermodynamics and signatures of criticality in a network of neurons. *Proceedings of the National Academy of Sciences*. 2015; 112(37):11508–11513. <https://doi.org/10.1073/pnas.1514188112>
13. Sethna JP, Dahmen KA, Myers CR. Crackling noise. *Nature*. 2001; 410(6825):242–250. <https://doi.org/10.1038/35065675> PMID: 11258379
14. Gireesh ED, Plenz D. Neuronal avalanches organize as nested theta- and beta/gamma-oscillations during development of cortical layer 2/3. *Proceedings of the National Academy of Sciences*. 2008; 105(21):7576–7581. <https://doi.org/10.1073/pnas.0800537105> PMID: 18499802
15. Petermann T, Thiagarajan TC, Lebedev MA, Nicolelis MAL, Chialvo DR, Plenz D. Spontaneous cortical activity in awake monkeys composed of neuronal avalanches. *Proceedings of the National Academy of Sciences*. 2009; 106(37):15921–15926. <https://doi.org/10.1073/pnas.0904089106> PMID: 19717463
16. Dehghani N, Hatsopoulos NG, Haga ZD, Parker RA, Greger B, Halgren E, et al. Avalanche Analysis from Multielectrode Ensemble Recordings in Cat, Monkey, and Human Cerebral Cortex during Wakefulness and Sleep. *Frontiers in Physiology*. 2012; 3(August):1–18. <https://doi.org/10.3389/fphys.2012.00302> PMID: 22934053
17. Clawson WP, Wright NC, Wessel R, Shew WL. Adaptation towards scale-free dynamics improves cortical stimulus discrimination at the cost of reduced detection. *PLOS Computational Biology*. 2017; 13(5): e1005574. <https://doi.org/10.1371/journal.pcbi.1005574> PMID: 28557985
18. Ribeiro TL, Copelli M, Caixeta F, Belchior H, Chialvo DR, Nicolelis MAL, et al. Spike Avalanches Exhibit Universal Dynamics across the Sleep-Wake Cycle. *PLoS ONE*. 2010; 5(11):e14129. <https://doi.org/10.1371/journal.pone.0014129> PMID: 21152422

19. Shriki O, Alstott J, Carver F, Holroyd T, Henson RNA, Smith ML, et al. Neuronal Avalanches in the Resting MEG of the Human Brain. *Journal of Neuroscience*. 2013; 33(16):7079–7090. <https://doi.org/10.1523/JNEUROSCI.4286-12.2013> PMID: 23595765
20. Arviv O, Goldstein A, Shriki O. Near-Critical Dynamics in Stimulus-Evoked Activity of the Human Brain and Its Relation to Spontaneous Resting-State Activity. *Journal of Neuroscience*. 2015; 35(41):13927–13942. <https://doi.org/10.1523/JNEUROSCI.0477-15.2015> PMID: 26468194
21. Palva JM, Zhigalov A, Hirvonen J, Korhonen O, Linkenkaer-Hansen K, Palva S. Neuronal long-range temporal correlations and avalanche dynamics are correlated with behavioral scaling laws. *Proceedings of the National Academy of Sciences*. 2013; 110(9):3585–3590. <https://doi.org/10.1073/pnas.1216855110> PMID: 23401536
22. Tagliacucchi E, Balenzuela P, Fraiman D, Chialvo DR. Criticality in Large-Scale Brain fMRI Dynamics Unveiled by a Novel Point Process Analysis. *Frontiers in Physiology*. 2012; 3(February):1–12. <https://doi.org/10.3389/fphys.2012.00015> PMID: 22347863
23. Ponce-Alvarez A, Jouary A, Privat M, Deco G, Sumbre G. Whole-Brain Neuronal Activity Displays Crackling Noise Dynamics. *Neuron*. 2018; 100(6):1446–1459. <https://doi.org/10.1016/j.neuron.2018.10.045> PMID: 30449656
24. Priesemann V, Wibral M, Valderrama M, Pröpper R, Le Van Quyen M, Geisel T, et al. Spike avalanches in vivo suggest a driven, slightly subcritical brain state. *Frontiers in Systems Neuroscience*. 2014; 8 (June):108. <https://doi.org/10.3389/fnsys.2014.00108> PMID: 25009473
25. Bédard C, Kröger H, Destexhe A. Does the $1/f$ Frequency Scaling of Brain Signals Reflect Self-Organized Critical States? *Physical Review Letters*. 2006; 97(11):118102. PMID: 17025932
26. Ribeiro TL, Ribeiro S, Belchior H, Caixeta F, Copelli M. Undersampled critical branching processes on small-world and random networks fail to reproduce the statistics of spike avalanches. *PLoS ONE*. 2014; 9(4). <https://doi.org/10.1371/journal.pone.0094992> PMID: 24751599
27. Wiltling J, Priesemann V. Inferring collective dynamical states from widely unobserved systems. *Nature Communications*. 2018; 9(1):2325. <https://doi.org/10.1038/s41467-018-04725-4> PMID: 29899335
28. Wiltling J, Dehning J, Pinheiro Neto J, Rudelt L, Wibral M, Zierenberg J, et al. Operating in a Reverberating Regime Enables Rapid Tuning of Network States to Task Requirements. *Frontiers in Systems Neuroscience*. 2018; 12(November). <https://doi.org/10.3389/fnsys.2018.00055> PMID: 30459567
29. Font-Clos F, Pruessner G, Moloney NR, Deluca A. The perils of thresholding. *New Journal of Physics*. 2015; 17(4):043066. <https://doi.org/10.1088/1367-2630/17/4/043066>
30. Laurson L, Illa X, Alava MJ. The effect of thresholding on temporal avalanche statistics. *Journal of Statistical Mechanics: Theory and Experiment*. 2009; 2009(01):P01019. <https://doi.org/10.1088/1742-5468/2009/01/P01019>
31. Villegas P, di Santo S, Burioni R, Muñoz MA. Time-series thresholding and the definition of avalanche size. *Physical Review E*. 2019; 100(1):012133. <https://doi.org/10.1103/PhysRevE.100.012133> PMID: 31499802
32. Dalla Porta L, Copelli M. Modeling neuronal avalanches and long-range temporal correlations at the emergence of collective oscillations: Continuously varying exponents mimic M/EEG results. *PLOS Computational Biology*. 2019; 15(4):e1006924. <https://doi.org/10.1371/journal.pcbi.1006924> PMID: 30951525
33. Klaus A, Yu S, Plenz D. Statistical analyses support power law distributions found in neuronal avalanches. *PLoS ONE*. 2011; 6(5). <https://doi.org/10.1371/journal.pone.0019779> PMID: 21720544
34. Yu S, Klaus A, Yang H, Plenz D. Scale-Invariant Neuronal Avalanche Dynamics and the Cut-Off in Size Distributions. *PLoS ONE*. 2014; 9(6):e99761. <https://doi.org/10.1371/journal.pone.0099761> PMID: 24927158
35. Harris TE. *The Theory of Branching Processes*. Berlin: Springer-Verlag; 1963.
36. Zierenberg J, Wiltling J, Priesemann V, Levina A. Description of spreading dynamics by microscopic network models and macroscopic branching processes can differ due to coalescence. *Physical Review E*. 2020; 101(2):022301. <https://doi.org/10.1103/PhysRevE.101.022301> PMID: 32168601
37. Pettersen KH, Einevoll GT. Amplitude Variability and Extracellular Low-Pass Filtering of Neuronal Spikes. *Biophysical Journal*. 2008; 94(3):784–802. <https://doi.org/10.1529/biophysj.107.111179> PMID: 17921225
38. Linden H, Tetzlaff T, Potjans TC, Pettersen KH, Grün S, Diesmann M, et al. Modeling the spatial reach of the LFP. *Neuron*. 2011; 72(5):859–872. <https://doi.org/10.1016/j.neuron.2011.11.006> PMID: 22153380
39. Riera JJ, Ogawa T, Goto T, Sumiyoshi A, Nonaka H, Evans A, et al. Pitfalls in the Dipolar Model for the Neocortical EEG Sources. *J Neurophysiol*. 2012; 108:956–975. <https://doi.org/10.1152/jn.00098.2011> PMID: 22539822

40. Einevoll GT, Kayser C, Logothetis NK, Panzeri S. Modelling and analysis of local field potentials for studying the function of cortical circuits. *Nature Reviews Neuroscience*. 2013; 14(11):770–785. <https://doi.org/10.1038/nrn3599> PMID: 24135696
41. Wilting J, Priesemann V. 25 Years of Criticality in Neuroscience—Established Results, Open Controversies, Novel Concepts. 2019;.
42. Ma Z, Turrigiano GG, Wessel R, Hengen KB. Cortical Circuit Dynamics Are Homeostatically Tuned to Criticality In Vivo. *Neuron*. 2019; 104:655–664.e4. <https://doi.org/10.1016/j.neuron.2019.08.031> PMID: 31601510
43. Priesemann V, Valderrama M, Wibral M, Le Van Quyen M. Neuronal Avalanches Differ from Wakefulness to Deep Sleep—Evidence from Intracranial Depth Recordings in Humans. *PLoS Computational Biology*. 2013; 9(3):e1002985. <https://doi.org/10.1371/journal.pcbi.1002985> PMID: 23555220
44. Levina A, Priesemann V. Subsampling scaling. *Nature Communications*. 2017; 8(1):15140. <https://doi.org/10.1038/ncomms15140> PMID: 28469176
45. Plenz D, Ribeiro TL, Miller SR, Kells PA, Vakili A, Capek EL. Self-Organized Criticality in the Brain. *Front Phys*. 2021; 9. <https://doi.org/10.3389/fphy.2021.639389>
46. Bak P, Tang C, Wiesenfeld K. Self-organized criticality: An explanation of the 1/f noise. *Physical Review Letters*. 1987; 59(4):381–384. <https://doi.org/10.1103/PhysRevLett.59.381> PMID: 10035754
47. Priesemann V, Shriki O. Can a time varying external drive give rise to apparent criticality in neural systems? *PLOS Computational Biology*. 2018; 14(5):e1006081. <https://doi.org/10.1371/journal.pcbi.1006081> PMID: 29813052
48. Touboul J, Destexhe A. Power-law statistics and universal scaling in the absence of criticality. *Physical Review E*. 2015; 95(1):2–6.
49. Touboul J, Destexhe A. Can Power-Law Scaling and Neuronal Avalanches Arise from Stochastic Dynamics? *PLoS ONE*. 2010; 5(2):e8982. <https://doi.org/10.1371/journal.pone.0008982> PMID: 20161798
50. Carvalho TTA, Fontenele AJ, Girardi-Schappo M, Feliciano T, Aguiar LAA, Silva TPL, et al. Subsampled Directed-Percolation Models Explain Scaling Relations Experimentally Observed in the Brain. *Front Neural Circuits*. 2021; 14:576727. <https://doi.org/10.3389/fncir.2020.576727> PMID: 33519388
51. Gabriel S, Lau RW, Gabriel C. The dielectric properties of biological tissues: \uppercase{I}l. Measurements in the frequency range 10\uppercase{H}z to 20\uppercase{GH}z. *Physics in Medicine and Biology*. 1996; 41(11):2251–2269. <https://doi.org/10.1088/0031-9155/41/11/002> PMID: 8938025
52. Buzsáki G, Anastassiou Ca, Koch C. The origin of extracellular fields and currents—EEG, ECoG, LFP and spikes. *Nature Reviews Neuroscience*. 2012; 13(6):407–420. <https://doi.org/10.1038/nrn3241> PMID: 22595786
53. Lindén H, Pettersen KH, Einevoll GT. Intrinsic Dendritic Filtering Gives Low-Pass Power Spectra of Local Field Potentials. *J Comput Neurosci*. 2010; 29:423–444. <https://doi.org/10.1007/s10827-010-0245-4> PMID: 20502952
54. Scott G, Fagerholm ED, Mutoh H, Leech R, Sharp DJ, Shew WL, et al. Voltage Imaging of Waking Mouse Cortex Reveals Emergence of Critical Neuronal Dynamics. *Journal of Neuroscience*. 2014; 34(50):16611–16620. <https://doi.org/10.1523/JNEUROSCI.3474-14.2014> PMID: 25505314
55. Bellay T, Klaus A, Seshadri S, Plenz D. Irregular spiking of pyramidal neurons organizes as scale-invariant neuronal avalanches in the awake state. *eLife*. 2015; 4(JULY 2015):1–25. <https://doi.org/10.7554/eLife.07224> PMID: 26151674
56. Fagerholm ED, Scott G, Shew WL, Song C, Leech R, Knöpfel T, et al. Cortical Entropy, Mutual Information and Scale-Free Dynamics in Waking Mice. *Cerebral Cortex*. 2016; 26(10):3945–3952. <https://doi.org/10.1093/cercor/bhw200> PMID: 27384059
57. Fekete T, Omer DB, O'Hashi K, Grinvald A, van Leeuwen C, Shriki O. Critical Dynamics, Anesthesia and Information Integration: Lessons from Multi-Scale Criticality Analysis of Voltage Imaging Data. *NeuroImage*. 2018; 183:919–933. <https://doi.org/10.1016/j.neuroimage.2018.08.026> PMID: 30120988
58. Wilting J, Priesemann V. Between Perfectly Critical and Fully Irregular: A Reverberating Model Captures and Predicts Cortical Spike Propagation. *Cerebral Cortex*. 2019; 29(6):2759–2770. <https://doi.org/10.1093/cercor/bhz049> PMID: 31008508
59. Tetzlaff C, Okujeni S, Egert U, Wörgötter F, Butz M. Self-Organized Criticality in Developing Neuronal Networks. *PLoS Computational Biology*. 2010; 6(12):e1001013. <https://doi.org/10.1371/journal.pcbi.1001013> PMID: 21152008
60. Friedman N, Ito S, Brinkman BAW, Shimono M, Deville REL, Dahmen KA, et al. Universal critical dynamics in high resolution neuronal avalanche data. *Physical Review Letters*. 2012; 108(20):1–5. <https://doi.org/10.1103/PhysRevLett.108.208102> PMID: 23003192

61. Pasquale V, Massobrio P, Bologna LL, Chiappalone M, Martinoia S. Self-organization and neuronal avalanches in networks of dissociated cortical neurons. *Neuroscience*. 2008; 153(4):1354–1369. <https://doi.org/10.1016/j.neuroscience.2008.03.050> PMID: 18448256
62. Hahn G, Petermann T, Havenith MN, Yu S, Singer W, Plenz D, et al. Neuronal avalanches in spontaneous activity in vivo. *Journal of neurophysiology*. 2010; 104(6):3312–3322. <https://doi.org/10.1152/jn.00953.2009> PMID: 20631221
63. Fox MD, Snyder AZ, Vincent JL, Corbetta M, Van Essen DC, Raichle ME. The human brain is intrinsically organized into dynamic, anticorrelated functional networks. *Proceedings of the National Academy of Sciences*. 2005; 102(27):9673–9678. <https://doi.org/10.1073/pnas.0504136102> PMID: 15976020
64. Hellyer PJ, Jachs B, Clopath C, Leech R. Local inhibitory plasticity tunes macroscopic brain dynamics and allows the emergence of functional brain networks. *NeuroImage*. 2016; 124:85–95. <https://doi.org/10.1016/j.neuroimage.2015.08.069> PMID: 26348562
65. Shew WL, Clawson WP, Pobst J, Karimipناه Y, Wright NC, Wessel R. Adaptation to sensory input tunes visual cortex to criticality. *Nature Physics*. 2015; 11(8):659–663. <https://doi.org/10.1038/nphys3370>
66. Simola J, Zhigalov A, Morales-Muñoz I, Palva JM, Palva S. Critical dynamics of endogenous fluctuations predict cognitive flexibility in the Go/NoGo task. *Scientific Reports*. 2017; 7(1):2909. <https://doi.org/10.1038/s41598-017-02750-9> PMID: 28588303
67. Deco G, Jirsa VK, McIntosh AR. Emerging concepts for the dynamical organization of resting-state activity in the brain. *Nature Reviews Neuroscience*. 2011; 12(1):43–56. <https://doi.org/10.1038/nrn2961> PMID: 21170073
68. Hahn G, Ponce-Alvarez A, Monier C, Benvenuti G, Kumar A, Chavane F, et al. Spontaneous cortical activity is transiently poised close to criticality. *PLOS Computational Biology*. 2017; 13(5):e1005543. <https://doi.org/10.1371/journal.pcbi.1005543> PMID: 28542191
69. Tomen N, Rotermund D, Ernst U. Marginally subcritical dynamics explain enhanced stimulus discriminability under attention. *Frontiers in Systems Neuroscience*. 2014; 8(August):1–15. <https://doi.org/10.3389/fnsys.2014.00151> PMID: 25202240
70. Wagenaar DA, Pine J, Potter SM. An Extremely Rich Repertoire of Bursting Patterns during the Development of Cortical Cultures. *BMC Neurosci*. 2006; p. 18. <https://doi.org/10.1186/1471-2202-7-11> PMID: 16464257
71. Ivshitz M, Segal M. Neuronal Density Determines Network Connectivity and Spontaneous Activity in Cultured Hippocampus. *Journal of Neurophysiology*. 2010; 104(2):1052–1060. <https://doi.org/10.1152/jn.00914.2009> PMID: 20554850
72. Sabatini BL, Regehr WG. Timing of Synaptic Transmission. *Annual Review of Physiology*. 2002; 64(1):521–542. <https://doi.org/10.1146/annurev.physiol.64.1.521>
73. Alstott J, Bullmore E, Plenz D. powerlaw: A Python Package for Analysis of Heavy-Tailed Distributions. *PLoS ONE*. 2014; 9(1):e85777. <https://doi.org/10.1371/journal.pone.0085777> PMID: 24489671

4 Modular architecture facilitates noise-driven control of synchrony in neuronal networks

Published in Science Advances

DOI [10.1126/sciadv.ade1755](https://doi.org/10.1126/sciadv.ade1755)

Preprint [arXiv:2205.10563](https://arxiv.org/abs/2205.10563)

Supplementary material [Appendix B](#)

Data gin.g-node.org/pspitzner/stimulating_modular_cultures

Source code github.com/Priesemann-Group/stimulating_modular_cultures

License 

Own contributions

- ✓ Conceptualization
- Methodology
- ✓ Software
- ✓ Validation
- ✓ Formal Analysis
- ✓ Investigation
- Resources
- ✓ Data Curation
- ✓ Writing — Original Draft
- Writing — Review & Editing
- ✓ Visualization
- Supervision
- Project Administration
- Funding Acquisition

I conceptualized the study together with HY, VP, JZ and JS. HY and his lab performed the experiments and acquired data. I analyzed the data. I implemented the models with contributions from JZ and VB. I created all figures. All authors wrote the manuscript.

NEUROSCIENCE

Modular architecture facilitates noise-driven control of synchrony in neuronal networks

Hideaki Yamamoto^{1,2,*†}, F. Paul Spitzner^{3†}, Taiki Takemuro^{1,4}, Victor Buendía^{5,6,7}, Hakuba Murota^{1,2}, Carla Morante^{8,9}, Tomohiro Konno¹⁰, Shigeo Sato^{1,2}, Ayumi Hirano-Iwata^{1,2,4,11}, Anna Levina^{5,6}, Viola Priesemann^{3,12‡}, Miguel A. Muñoz^{7,13‡}, Johannes Zierenberg^{3‡}, Jordi Soriano^{8,9‡*}

High-level information processing in the mammalian cortex requires both segregated processing in specialized circuits and integration across multiple circuits. One possible way to implement these seemingly opposing demands is by flexibly switching between states with different levels of synchrony. However, the mechanisms behind the control of complex synchronization patterns in neuronal networks remain elusive. Here, we use precision neuroengineering to manipulate and stimulate networks of cortical neurons *in vitro*, in combination with an *in silico* model of spiking neurons and a mesoscopic model of stochastically coupled modules to show that (i) a modular architecture enhances the sensitivity of the network to noise delivered as external asynchronous stimulation and that (ii) the persistent depletion of synaptic resources in stimulated neurons is the underlying mechanism for this effect. Together, our results demonstrate that the inherent dynamical state in structured networks of excitable units is determined by both its modular architecture and the properties of the external inputs.

INTRODUCTION

The mammalian brain is in a state of perpetual ongoing activity characterized by high levels of irregularity in single-neuron response (1, 2) and correlated fluctuations across brain regions (3–7). Understanding the origin and functional significance of such neuronal activity has been challenging for both physics and neuroscience, and diverse competing hypotheses have been proposed to rationalize its nature. A compelling concept in statistical physics is that cortical networks operate nearby a critical point, *i.e.*, at the edge of a nonequilibrium phase transition (8–15). One possibility is that such a transition separates synchronous and asynchronous phases (16, 17). Synchrony in this context refers to the collective activation of neurons in a fast-cascading event, a phenomenon also referred to as neuronal avalanches (8, 18). Such synchronous states can be argued to enable coherent or robust information transfer integrated across distance and time (19), while asynchronous states have been argued to enable segregated processing in local circuits with reduced redundancy (17). Flexible switching between states with different levels of synchrony would enable networks to transiently

exploit diverse functional advantages, all the most in modular networks where the phase transition can be very broad, with a rich hierarchy of intermediate states of partial synchronization (20).

Transitions between synchronized and desynchronized states are well-known to occur in the mammalian brain and have mostly been described in the context of dynamical properties of individual neurons (21) and the dynamical consequences of the network architectures they form (20–27). Recent findings, however, suggest that such transitions can also be induced depending on the nature of external inputs (28, 29). For instance, the thalamus projects asynchronous background inputs to the cortex (30–32), which decreases the level of synchrony. Consistent with this, anesthesia, which reduces the thalamocortical input (33), enhances neuronal synchrony in the rat somatosensory cortex (34). The deprivation of such inputs by anatomical lesions has also been shown to increase cortical synchrony and generate epileptic seizure-like activity in slice preparations (35). Meanwhile, theoretical studies reveal that the response of a generic network to external perturbations strongly depends on network architecture and on the strength of synaptic interactions (36). Therefore, given that cortical networks are nonrandom (37) and exhibit strong modularity (5, 38–43), it is reasonable to hypothesize that cortical dynamics rely on the underlying network architecture in conjunction with the asynchronous input they constantly receive from subcortical areas, such as the thalamus. However, despite the accumulated evidence, the actual mechanisms that allow cortical networks to transiently regulate their level of synchronization remains elusive, both experimentally and theoretically.

To fill this gap, here, we use *in vitro* cortical networks grown on engineered substrates (44). Three different types of modular networks with diverse degrees of modularity were grown, and their responses to asynchronous stimulation delivered via optogenetics were assessed using fluorescence calcium imaging. The results show that modularity, together with asynchronous external input, enhances the dynamical repertoire by fostering desynchronization. This effect weakens when inhibitory synapses are pharmacologically

¹Research Institute of Electrical Communication (RIEC), Tohoku University, Sendai, Japan. ²Graduate School of Engineering, Tohoku University, Sendai, Japan. ³Max Planck Institute for Dynamics and Self-Organization, Göttingen, Germany. ⁴Graduate School of Biomedical Engineering, Tohoku University, Sendai, Japan. ⁵Max Planck Institute for Biological Cybernetics, Tübingen, Germany. ⁶Department of Computer Science, University of Tübingen, Tübingen, Germany. ⁷Departamento de Electromagnetismo y Física de la Materia, Universidad de Granada, Granada, Spain. ⁸Departament de Física de la Matèria Condensada, Universitat de Barcelona, Barcelona, Spain. ⁹Universitat de Barcelona Institute of Complex Systems (UBICS), Barcelona, Spain. ¹⁰Graduate School of Pharmaceutical Sciences, Tohoku University, Sendai, Japan. ¹¹Advanced Institute for Materials Research (WPI-AIMR), Tohoku University, Sendai, Japan. ¹²Institute for the Dynamics of Complex Systems, University of Göttingen, Göttingen, Germany. ¹³Instituto Carlos I de Física Teórica y Computacional, Universidad de Granada, Granada, Spain.

*Corresponding author. Email: hideaki.yamamoto.e3@tohoku.ac.jp (H.Y.); jordi.soriano@ub.edu (J.S.)

†These authors contributed equally to this work.

‡These authors contributed equally to this work.

blocked, i.e., when the network is purely excitatory driven. The results are then compared with *in silico* analyses of a spiking neural network model to show that a combination of sparser (stochastic) intermodular interactions and decreased level of available synaptic resources is the underlying mechanism behind the experimentally observed desynchronization. Last, we derive a mesoscopic model incorporating a state-dependent gating of intermodular interactions that allows us to rationalize the previous results in a parsimonious way. Together, our findings demonstrate a potential network mechanism by which asynchronous input can serve as a control parameter for tuning the dynamical state of structured neuronal networks.

RESULTS

Disruption of synchrony by optogenetic stimulation

We first assessed how external perturbations influence synchronized neuronal activity in networks of primary cortical neurons, containing both excitatory and inhibitory neurons, grown *in vitro*. We designed ring-modular micropatterns consisting of four small squares (200 μm by 200 μm each) with connection lines that allowed a fraction of the neurites to interconnect the squares (Fig. 1A). The neuronal activity of the micropatterned networks was recorded by fluorescence calcium imaging using the calcium probe GCaMP6s (Fig. 1B and movies S1 and S2), which was virally expressed under the Synapsin promoter that transduces both excitatory and inhibitory neuronal populations in the cortex (45). Neurons were perturbed either by irradiating patterned light to individual neurons transfected with the photoactivatable cation channel ChrimsonR (optogenetic stimulation; Fig. 1C) expressed in both excitatory and inhibitory populations or by increasing the extracellular potassium concentration $[\text{K}^+]_o$ (chemical stimulation). The former induces spiking activity in targeted neurons (46), whereas the latter increases the frequency of collective activity of neurons in the entire culture, effectively raising the overall neuronal excitability (47).

In the nonstimulated state (Fig. 1D), the activity of the cultures was characterized by quasi-periodic episodes of network-wide bursting activity with some variability in population rate amplitude due to the modular architecture (44). External perturbation via optogenetic stimulation induced a qualitative change in network dynamics. This stimulation was delivered as alternating patterns of red light illuminating the soma of up to 10 neurons selected from the lower two of the four modules (Fig. 1A). Only the neurons expressing ChrimsonR were selected as potential targets, with no imposed bias in excitatory/inhibitory cell types. The illumination pattern was switched every 400 ms, and in each time window, each neuron was targeted with a probability of 40%. During stimulation, the frequency of collective events as well as the variety of activity patterns increased (Fig. 1, E and G). These enriched network dynamics were observed during ongoing stimulation and diminished when it was switched off (Fig. 1F). Representative snapshots of network behavior before, during, and after stimulation are provided in Fig. 1G, illustrating the shift in collective activity from a synchronized to a desynchronized state upon optogenetic (asynchronous) stimulation. Such a transient shift in the network state was also observed when the asynchronous stimulation was delivered to all four modules and when a uniform stimulation was delivered locally to one of the modules (see section S1B and fig. S1 for details). In

contrast, chemical stimulation imposed a qualitatively different change in network dynamics (Fig. 1, H and I, and movies S3 and S4). Contrary to optogenetic stimulation, network-wide collective activity remained dominant, even in the perturbed state. These results indicate that a mere increase in excitability was insufficient and that an asynchronous stimulation was necessary to break synchrony and increase the dynamical repertoire of the cortical cultures.

Changes in collective activity during stimulation were quantified by measuring the distribution of event sizes, i.e., the fraction of neurons entrained in each collective activity episode (Fig. 1J, left). Optogenetic stimulation led to a significant decrease in event size indicating a loss of synchrony. This change was accompanied by a decreased median and a broadened distribution of pairwise correlation coefficients (Fig. 1J, middle), the latter of which manifested in an increased functional complexity (Fig. 1J, right), a signature of enhanced integration-segregation balance (48). Chemical stimulation, however, preserved synchrony in network dynamics and showed the opposite trend in both the event size and functional complexity.

The overall effect induced by optogenetic stimulation was abolished in the presence of bicuculline (20 μM), a γ -aminobutyric acid type A receptor antagonist that blocks inhibitory synapses, and the effect was thus γ -aminobutyric acid (GABA) dependent (fig. S2 and movies S5 and S6). This indicates that GABAergic balancing of excitation and inhibition (49, 50) is required for external input to alter the network dynamics. This observation suggests that when a network is in an exceedingly excited state, neurons become mostly depleted of neurotransmitters between collective activity events (51, 52), leading to a state that is insensitive to perturbations.

Impact of modular architecture

Next, we assessed how the effect of asynchronous stimulation depends on the network topology, specifically its modular architecture. Hence, we prepared three types of networks with a constant number of neurons and different degrees of modularity (Fig. 2, top drawings, and fig. S3). The modular micropattern used in the aforementioned experiments is hereafter referred to as the "single-bond" (1-b) micropattern. Similarly, a "triple-bond" (3-b) micropattern was designed by increasing the number of connection lines to three. Last, the "merged" micropattern was a single square of 400 μm by 400 μm . The modularity of the network, defined as the fraction of intermodular connections within a network greater than the expected fraction in a random network, decreased in the order of 1-b, 3-b, and merged (44, 53).

A comparison of the distribution of event sizes and correlation coefficients between these three cases revealed that noise perturbations have stronger effects when modularity is higher. As shown in Fig. 2A, the decrease in median event size via optogenetic stimulation was 54% for the 1-b network, whereas the values were 21 and 25% for the 3-b and merged networks, respectively. A similar trend in structure dependence was also observed for the correlation coefficients (Fig. 2B), which decreased by 49, 13, and 19% for the 1-b, 3-b, and merged networks, respectively. To understand the mechanism of this structure dependence, we analyzed the shift in the correlation coefficient between two generic neurons i - j , r_{ij} , during perturbation (Fig. 2C). For the 1-b network, the decrease in correlation largely stemmed from the neuron pairs that included at least one stimulated neuron, in which case r_{ij} broadly scattered below the

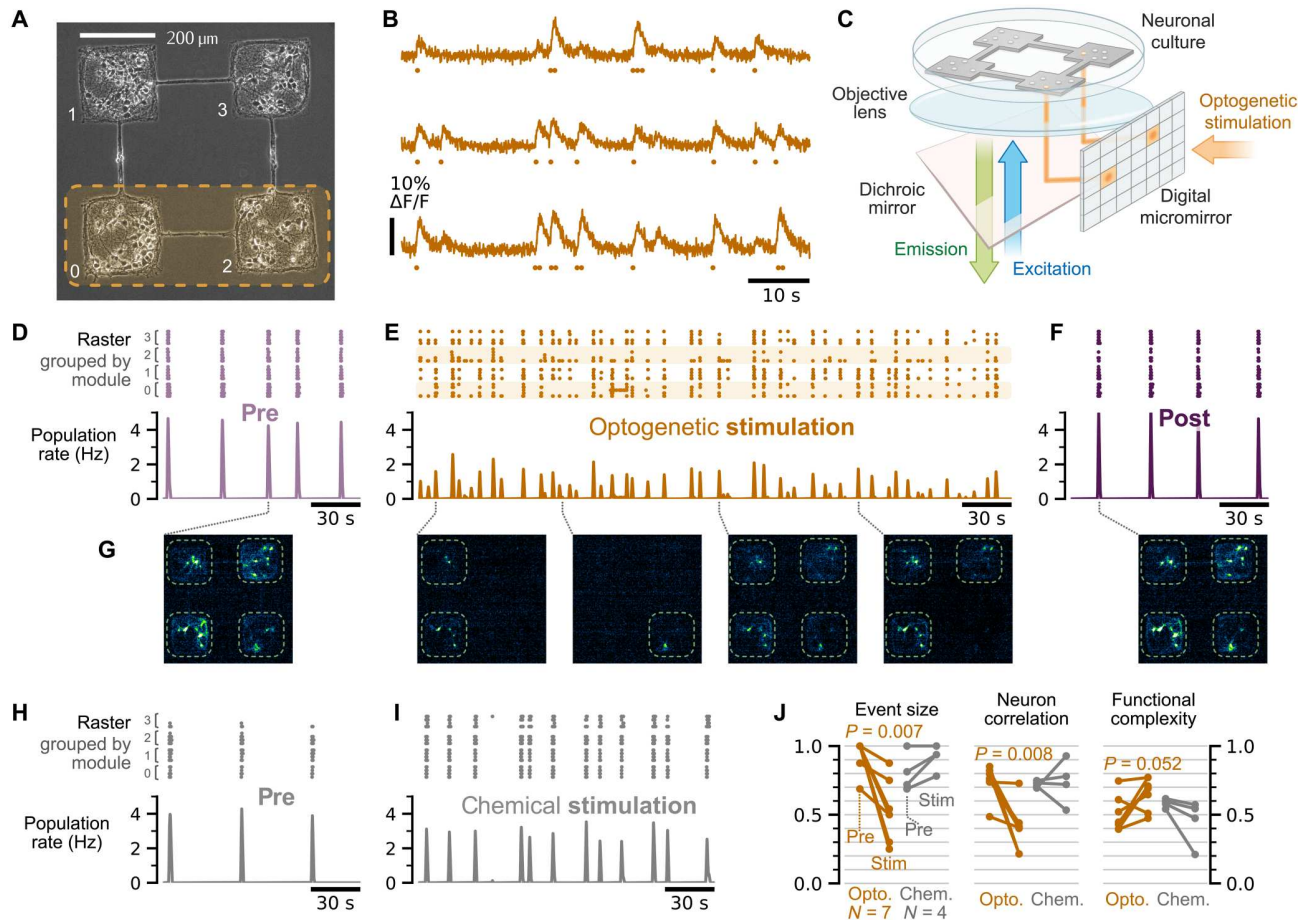


Fig. 1. Optogenetic stimulation on modular neuronal cultures increases the variability in collective network dynamics. (A) Phase-contrast image of a representative single-bond modular network. Neurons appear as dark round objects with a white contour. Ten neurons were selected from the bottom module pair (orange box) and optogenetically targeted in a random manner. (B) Representative fluorescence traces and inferred spike events (dots) of three neurons along 1 min. (C) Sketch of the experimental setup. Neuronal cultures were transfected with ChrimsonR for optogenetic stimulation (orange arrow) and GCaMP6s for simultaneous activity monitoring (blue and green arrows). (D) Pre-stimulation raster plot (top panel) of network spontaneous activity, with neurons grouped according to their module, and the corresponding population activity (bottom). (E) Corresponding data upon optogenetic stimulation, wherein population activity markedly increases in variability. Targeted modules are marked as orange bands. (F) Spontaneous activity post-stimulation, with a return to strong network-wide bursting. (G) Representative snapshots of calcium imaging recordings for the above data. All modules activate synchronously without stimulation. Upon stimulation, activity events extend over individual neurons, multiple modules, or all modules. (H and I) Raster plot and population activity before and during chemical stimulation. Chemical stimulation increases the frequency of events but maintains the network-wide activity. (J) Effect of optogenetic and chemical stimulation on bursting median event sizes, median correlation coefficients, and functional complexity (paired-sample t test, two-sided). For chemical stimulation with $N = 4$, no test was performed.

unit line in the pre-stim plane. The median r_{ij} strongly decreased when either one or both neurons in a pair were located within the stimulated modules, a feature that was not observed for neuron pairs in unstimulated modules (Fig. 2D). The spatial dependence was less pronounced when modularity was low (3-b) or absent (merged).

The tendency for strongly modular networks (1-b pattern) to be more sensitive to the optogenetic perturbation was also evident in the realization-level estimates (Fig. 2, E to H). These changes were independent of firing rate (Fig. 2E). In addition, the broadened distribution of correlation coefficients during stimulation increased the value of functional complexity (Fig. 2H), which was largest in the 1-b network under stimulation. Summarizing, modularity fostered local and transient decorrelation from asynchronous

stimulation to dampen the collective activity events that propagate globally throughout the entire network.

Microscopic spiking neural network model

To rationalize the underlying mechanisms behind the enhanced sensitivity to external perturbations in modular networks, we next constructed a spiking neural network (SNN) model based on leaky integrate-and-fire (LIF) neurons (see Materials and Methods, section S2, and movies S7 and S8 for details). The networks were generated on the basis of the metric construction approach described previously (18), and modularity was tuned by specifying the number of axons k that crossed from one module to another (Fig. 3, A and B). To control the modularity while retaining the overall connectivity, the mean in-degree of neurons was fixed to

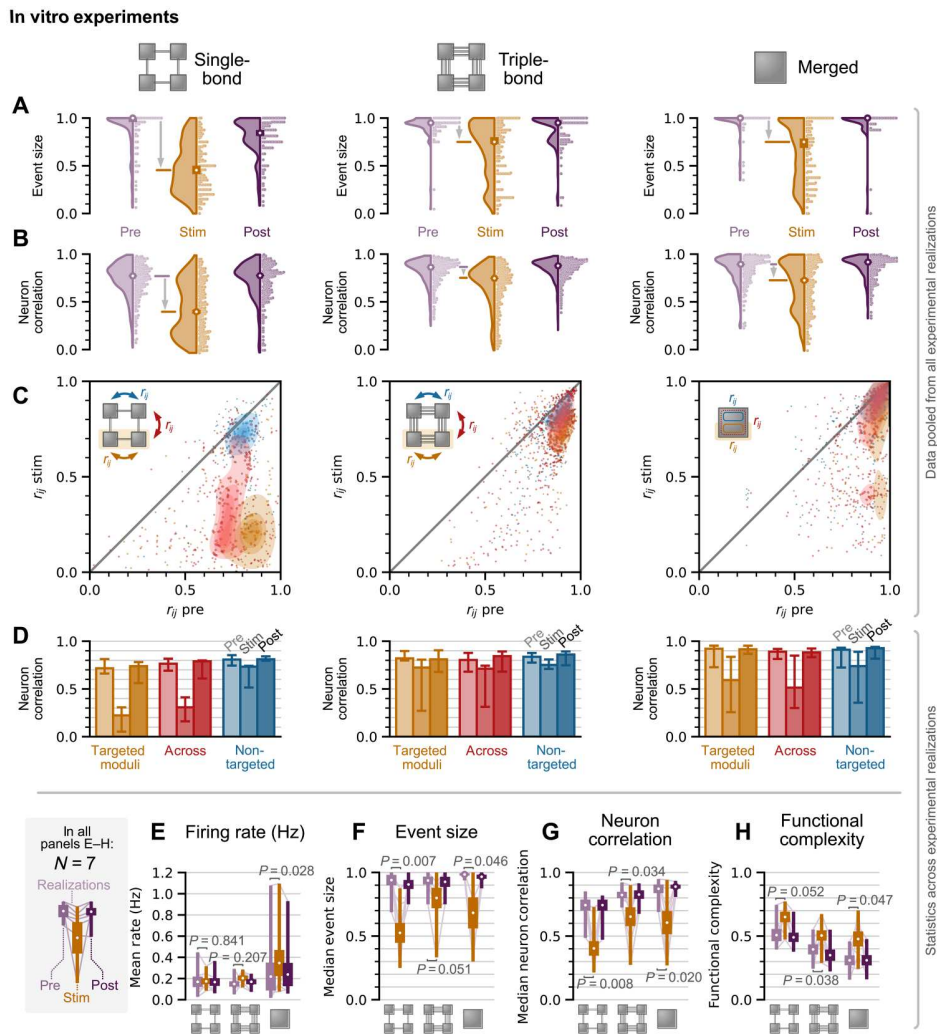


Fig. 2. Disruption of network-wide collective activity upon optogenetic stimulation is facilitated by modular architecture. (A) From left to right, event size distribution before, during, and after optogenetic stimulation for the 1-b, 3-b, and merged networks. Violin plots (left side of distribution) represent smooth kernel estimates of the events observed across all networks, while individual observations are shown in swarms (right side). Error bars (middle) are obtained via bootstrapping. White dots indicate the median of the 500 bootstrap estimates, and bars represent the 95 percentiles. (B) Corresponding distribution of pairwise Pearson correlation coefficients between neurons calculated from binned spike counts. A substantial drop is only observed for 1-b. Data are presented as in (A). (C) Change of correlation coefficients r_{ij} between the pre-stimulated and stimulated conditions, grouped according to the regions in which neurons are located. Both neurons may either reside in regions that are targeted by stimulation (yellow), both reside in nontargeted regions (blue), or the pair spans across a targeted and nontargeted regions (red). For modular networks, the regions correspond directly to modules. Decorrelation is more pronounced when one or both neurons are in regions that are targeted. Colored areas are fitted probability density estimates for each data group. (D) Same as (C) but showing realization-level statistics. Bar heights represent the medians of independent estimates in each realization, and error bars represent 95 percentiles. cf. table S7. (E to H) Estimates for each realization: mean firing rates (E), median event sizes (F), median correlation coefficients (G), and functional complexity (H) for the three topologies. Thin lines, individual realizations (networks); white dots, means of 500 bootstrap samples; thick bars, SEM; thin bars, extrema. P values are from paired-sample t test (two-sided), cf. tables S1 and S7.

be the same in all topologies (fig. S4). Spontaneous activity was driven by Poisson noise, representing the spontaneous release of neurotransmitters in biological presynaptic terminals (18, 51). Note that we focus on the optogenetic stimulation, as the change in the extracellular potassium concentration induced in the chemical stimulation does not simply translate to a single parameter in the LIF model. With $k = 3$, we obtained dynamic behaviors comparable to experiments in 1-b networks (Fig. 3, C and D). The model accurately recapitulated the experimental observations made in the

optogenetic stimulation paradigm. In the pre-stimulated state (Fig. 3C), activity patterns composed of sporadic activity with reoccurring network-wide events. Stimulation, introduced in the two lower modules as an additional noise input (mimicking inward current pulses from optogenetic inputs), led to a breakdown of synchrony among modules and an increase of events localized to a fraction of modules (Fig. 3D). As shown in the panels of Fig. 3E, the median event size decreased from 0.81 to 0.27, and the median correlation among neuron pairs decreased from 0.84 to 0.58 (cf. table

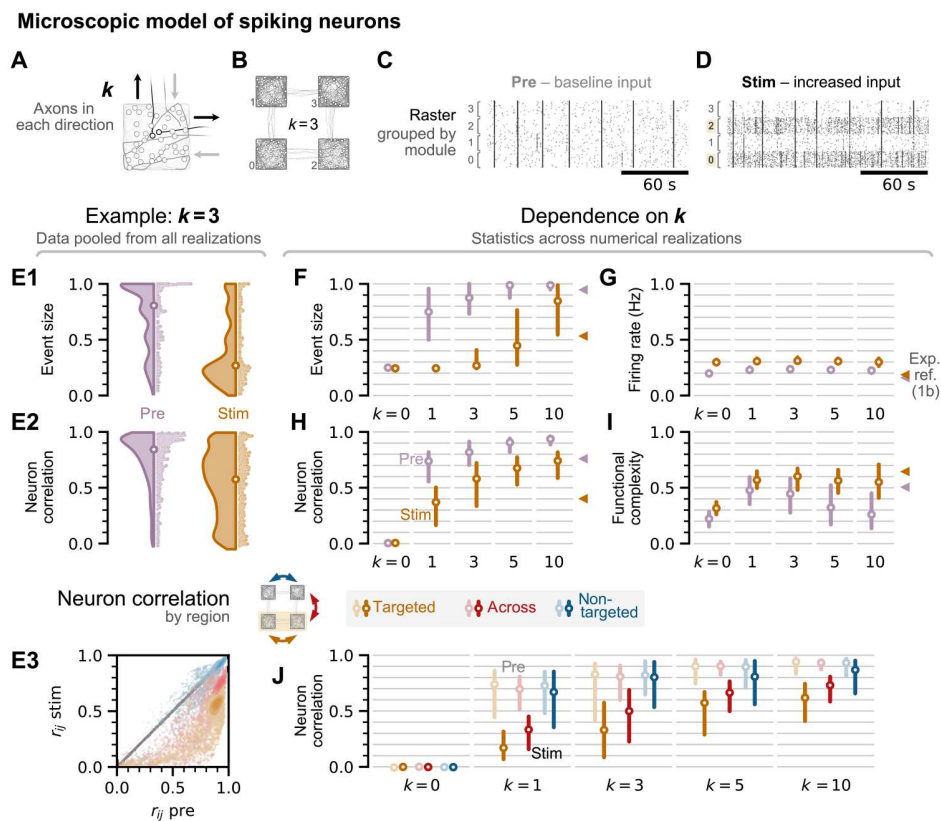


Fig. 3. Microscopic-level simulations of modular networks using LIF neuron models. (A) Sketch of a single module, where k axons connect to each adjacent neighbor (shown for $k = 1$). (B) Sketch of a simulated modular network with $k = 3$. (C and D) Representative raster plots in the pre-stimulated (C) and stimulated (D) regimes. Modules targeted with an increased noise are #0 and #2. (E1 and E2) Joint distributions of event size and pairwise correlation coefficients from data pooled from 50 independent numerical realizations, comparing pre and stim conditions. Both distributions exhibit a substantial drop towards smaller values upon stimulation. White dots are the median of 500 bootstrap estimates, and error bars representing the 95 percentiles are smaller than the symbol size. (E3) Change of correlation coefficients r_{ij} between the pre-stimulated and stimulated conditions (yellow: neuronal pairs reside in target modules; blue: reside in nontargeted; red: span across a target and a nontargeted module). The diagonal black line is the no-change reference condition. As in the experiments, decorrelation is more pronounced when one or both neurons are in modules with increased noise. (F to I) Dependence of four descriptors (event size, firing rate, neuron correlation, and functional complexity) on k . The higher k , the lower the modularity of the networks. Statistics are obtained across realizations where each realization yields a single scalar. White dots are the median of single-realization estimates. Rounded bars are 68 percentiles, indicating the variability between realizations. Triangles on the right of each panel indicate the values from single-bond experiments. (J) Correlation of neuron pairs grouped by the neurons' respective modules (yellow, red, and blue). For each k , the pre- and post-conditions are compared (faint versus dark colors). The strongest decorrelation is observed when both neurons are in noise-targeted modules (yellow) or modularity is high ($k = 1$ and 3).

S6). Corroborating the experiments, a greater decrease in the correlation coefficient was observed for cell pairs wherein one of the cells belonged to the targeted modules (Fig. 3, E and J), whereas the change was less pronounced for cell pairs in nontargeted modules.

For a systematic investigation of the effect of network modularity, we explored topologies with different numbers of axons crossing the modules: $k = 1, 3, 5,$ and 10 , corresponding to modularity $Q = 0.71, 0.62, 0.53,$ and 0.32 , respectively (cf. section S2B for analytical details). The simulations showed that desynchronization caused by stimulation strongly depends on the underlying network topology (Fig. 3, F to I). As a general trend, the event sizes and pairwise correlations increased with k due to increased coupling between modules (44). In the absence of any intermodule connection ($k = 0$) event sizes and correlation coefficients correspond to activity that is confined to individual modules (synchronized only at chance level) and, as expected, stimulation had little effect.

For $k > 0$, the presence of additional noise input (stim) decreased the median event size (Fig. 3F), and at low coupling ($k = 1$ and 3), event sizes consistently reached the single-module level. For higher coupling ($k = 5$ and 10) and in the absence of stimulation, the system was synchronous (with event sizes ~ 1), and stimulation caused a decrease to intermediate values. Note that the percentile bars (Fig. 3, F to J) represent the variability between realizations, which stems from the randomness in the amount of actual connections that are formed by bridging axons. This stresses that the response to noise stimulation, and thus the sensitivity of the network, is strongly constrained by its topology.

Pairwise correlations (Fig. 3H) showed a similar trend, where networks with low k were already quite desynchronized even without stimulation. Networks with larger k also desynchronized upon stimulation, but median values did not go as low as those for low k . Since the functional complexity (Fig. 3I) is maximal for

a flat distribution of correlation coefficients (48), large values coincide with a median correlation near 0.5. Consistently, the functional complexity is maximal for $k = 1$ and 3. Correlation distributions at those k are already broad without stimulation (Fig. 3E2), and therefore, the effect of stimulation on functional complexity is stronger at higher k . We note that, for all k , these observations were independent of the changes in firing rates, which were consistent across networks (Fig. 3G, see also fig. S7).

Overall, simulations confirmed that the coupling between modules shapes the impact of the noise input, with the effect most prominently visible in the regions that directly received stimulation (Fig. 3J). The coupling between modules—which, besides from k , depends on the particular network realization—forms the substrate for dynamics that are then mediated by the noise level. For instance, highly modular networks ($k = 1$ and 3) feature rich dynamics already at baseline (pre, Fig. 3, F and I), but less modular networks ($k = 5$) may still be enriched through noisy input (stim, Fig. 3, F and I). However, strong coupling between modules ($k = 10$) may lock the system in an integrated state where the additional noise only mildly decreases the median event size and neuron correlations. This can be explained by the heterogeneous degree distributions (cf. fig. S5): The connectivity between modules scales with k and affects the probability of activity spreading between modules (fig. S6), while the connectivity within modules is always high, so that modules are effectively synchronized units.

Network mechanisms: The importance of synaptic resources

To understand the network mechanisms that enable the increased sensitivity to external noise input in modular networks, we analyzed the dynamics of synaptic resources in each simulated neuron. For this purpose, we plotted the evolution of the mean synaptic resources in each module as a function of the module-averaged firing rate of the neurons. The characteristic behaviors of the mean synaptic resources $R \in [0, 1]$ are depicted in Fig. 4 (A to C). Abrupt discharges during bursting events are followed by gradual recharges between the events. In the baseline condition (pre), R had a maximal value of ~ 0.8 when charged but dropped to ~ 0.3 after network-wide bursting events. When neurons were subjected to additional noise input (stim), R of the targeted modules (Fig. 4B, orange trajectories) only recovered to ~ 0.5 , effectively reducing the synaptic efficacy. While, in general, R of the nontargeted modules (blue trajectories) was only indirectly affected by the stimulation, the precise cycles depended on the individual realizations (cf. dark blue versus light blue, Fig. 4, B and C). Independent of the network architecture, increased noise decreased the overall size of the cycles in targeted modules, but modularity still affected cycles of nontargeted modules (fig. S4). This stresses that the combination of network topology and asynchronous stimulation determines the charge-discharge dynamics on the module level.

To complete these results, we investigated how the degree of synchrony between modules changed with the strength of external input, as parameterized here by its frequency (Fig. 4D). In general, we observed that the correlation between module-level firing rates of targeted modules (Fig. 4D, top) decreased with stimulation but that stronger noise was required for larger k . For example, in $k = 1$ networks, an increase of 10 Hz in external input reduced correlation from 0.4 to 0.25, but to cause the same drop in correlation for $k = 10$, an increase of about 25 Hz was

required. To further illustrate the effect of noise on modular networks, we revisited $k = 3$ and computed the fraction of events that spanned a given number of modules, from 1 to 4 (Fig. 4D, bottom; cf. zoom-ins in Fig. 4C). Without stimulation, about 50% of the events encompassed the four modules, i.e., network-wide bursting. The addition of noise of just 10 Hz provided a more balanced dynamics in which the occurrence of 1-module and 4-module activations was both about 35%.

Mesoscopic description

As illustrated in the raster plots for both the pre and stim cases (Fig. 4C, insets), in which neurons activate in a quasi-synchronous manner within each module, much of the noise-induced changes in network dynamics occurred between modules. This implies that, to study global effects, some microscopic details can be neglected and that modules can be reduced to an effective dynamical unit. Thus, to extrapolate the microscopic behavior of individual neurons to the macroscopic dynamics, we built a mesoscopic module-level model that captures the key empirical results. Here, the dynamics of each module were described by a rate model with resource depletion (12), where two coupled differential equations represent the evolution of firing rate ρ and synaptic resources R , respectively (see Materials and Methods and section S3A for details).

As a first exploration of the model, we considered the case in which each module received input through a nonlinear activation function that depended on the rate and resources of the connected modules and an external input that captured the main (average) effect of stimulation. In such a case, increasing the amplitude of external input (which reflects enhanced stimulation frequency in both the experiments and the microscopic model) decreased the size of the resource-rate cycles of each module but did not affect synchronization (fig. S10). Thus, we introduced nondeterministic intermodular interactions as “gates” that stochastically disconnect when synaptic resources are depleted and reconnect after a characteristic time (Fig. 4E and section S3C). The stochastic gating reflects the following neuron-level dynamics which we embedded into the underlying module-level equations (figs. S11 and S12): When a module starts bursting, resources of all involved neurons are rapidly consumed, so that also those connecting to other modules will not transmit activity. Accordingly, outgoing gates will deactivate with a short time constant and remain disconnected for a relatively long time while neuron resources recharge. In this period, should the module burst again, the propagation of activity to other modules hinges on the few intermodular connections and is less probable to spread. This probability is reflected by the gate being already reconnected or not. If still disconnected, activity cannot spread to the neighboring modules. Hence, if modules tend to burst with a time scale faster than the gate recovery, the mutual entrainment of activity between modules is hindered, because the crucial initiating inputs cannot pass through the disconnected gates, and, therefore, the system cannot synchronize. Thus, these gates capture the essence of the microscopic dynamics—wherein intermodular coupling only operates when the synapses projecting from one module to another are not fully depleted—on the mesoscopic level.

Numerical simulations revealed that the addition of the gating mechanism was indeed sufficient to recapitulate the noise-dependent breakdown of synchrony observed in the experiments and SNN model (Fig. 4, B and C versus Fig. 4, F and G). Network-

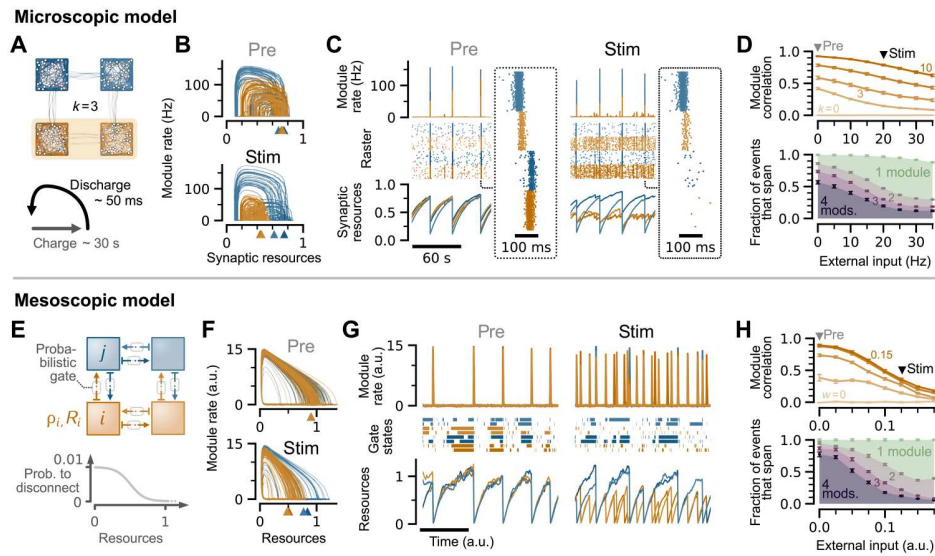


Fig. 4. Desynchronization can be understood through charge-discharge cycles in the resource-rate plane, which is captured by a minimal mesoscopic model. (Top row) Microscopic model using LIF neurons. (Bottom row) Mesoscopic model, where modules are the smallest functional unit. (A) Top: Sketch of the microscopic model, in which orange modules are those targeted by an increased noise. Bottom: Conceptual representation of the resource-rate cycles and the contrasting timescales involved. (B) Resource-rate cycles in a representative simulation with $k = 3$. Orange trajectories correspond to targeted modules, and blue trajectories correspond to nontargeted ones. Under stimulation, resources are more depleted on average (smaller excursions), and discharge events start at lower resources (colored triangles). (C) Module-level firing rates, raster plot, and average module-level resources under pre and stim conditions. Insets show a detail of neuronal activity during a network-wide activity event. (D) Top: Correlation between module-level firing rates of targeted modules as a function of the external input (added noise). Curves from bottom to top correspond to gradually higher k values. Triangles indicate the values of external input for the pre and stim conditions, from which the cycles and raster plots of (B) and (C) are built. Bottom: Average fraction of modules that participate in an event for $k = 3$ as a function of external input. (E) Top: Sketch of the mesoscopic model with probabilistic gates between modules. Bottom: Gates have a high probability to disconnect when resources of the source module are low. (F) Resource-rate cycles and the effect of stimulation for the mesoscopic model. (G) Module rate, gate state (solid when connected), and module resources as a function of time. Note the disconnection of gates after high-rate discharge events. (H) Top: Correlation of the firing rates of targeted modules as a function of the external input. Bottom: Average fraction of modules involved in events ($w = 0.1$). a.u., arbitrary units.

wide events were decreased under stimulation (Fig. 4, G and H), despite stimulated modules remaining in a more oscillatory regime than in the SNN (stim condition in Fig. 4G). Yet, the mesoscopic model successfully captured the noise-dependent reduction of intermodular correlation with external input and its dependence on the coupling strength (here denoted by w ; Fig. 4H, top). Weakly coupled networks (low w) exhibited a systematic lower correlation than strongly coupled ones (high w). Similarly to the SNN model, the fraction of events that spanned a given number of modules for medium $w = 0.1$ quickly changed from a 4-module dominated regime in the absence of stimulation to a richer repertoire of activation patterns for increased external input (Fig. 4H, bottom).

Furthermore, the simplicity of the mesoscopic model allows for an analytic understanding of the input-dependent change in the size of resource-rate cycles (fig. S10). In the resource-rate plane, the fixed point corresponding to a charging, nonfiring module i that receives no input is at $(\rho_i, R_i) = (0, 1)$. Spontaneous fluctuations (depending on external input and noise) may push the module out of its (slow, $\rho = 0$) path toward the fixed point and ignite a burst along the flow field in the resource-rate plane (fig. S10). As the external input to a module effectively reduces the activation threshold, it determines how easily a burst can be ignited. During a burst, the trajectory moves fast at high rates in the negative R direction, due to the small-time constants of the rate equation (τ_ρ) and of the discharge term (τ_d). However, the trajectory is slow in the positive R direction

due to the large time constant in the resource charge term (τ_c). Thus, at large external inputs (low threshold), a module may start a burst before completing its slow return to the fixed point, which explains the reduced cycle size. Further details and the mechanisms linking resource cycles to the synchronization between modules are provided in section S3B. In summary, the simple mesoscopic approach elucidates the critical role of stochastic intermodular interaction in determining the network dynamics of modular networks and provides an intuitive understanding of the noise-induced breakdown of synchrony in modular neuronal networks.

DISCUSSION

Taking advantage of in vitro experiments using cultured neuronal networks as a model biological system, we showed that modular architecture enhances the sensitivity of the network to external asynchronous perturbation. In particular, network-wide collective bursts are much reduced in the presence of modular structures driven by noise. This occurs only when noise is asynchronous (optogenetic stimulation of targeted neurons) and not homogeneous across the network (chemical stimulation) and happens only in balanced networks, while when inhibition is blocked, bursty events persist even in the presence of noise. Furthermore, computational in silico modeling enabled us to identify the mechanisms behind the noise-driven decrease of synchrony reported in experiments.

Focusing on the modular architecture that entrains burst-like activity within modules and stochastically propagated activity across modules (44, 54, 55), we showed that asynchronous input reduces the average level of synaptic resources, which only weakly affects activity propagation within modules but decreases the probability to propagate activity across modules. This can be understood at the neuron level, where the probability of a neuron to spike depends on the strength and number of incoming synaptic connections. Whereas the reduction of average synaptic resources affects the synaptic strengths in all neurons, the modular architecture only reduces the expected number of connections between neurons of different modules, which together results in the reduction of activity propagation across modules (fig. S6). Hence, our results extend previous theoretical studies that identified the strength of external noise as control parameter to interpolate between bursting and reverberating dynamics in neural networks (29).

To demonstrate the robustness of our results, we coarse-grained our microscopic simulations of spiking neurons into a mesoscopic model (12), where the depletion of resources is expressed in a minimalistic way. In both micro and meso approaches, stochastic intermodular connections were essential and were grounded on the heterogeneous degree distribution in the spiking neuron model and the gating mechanism in the mesoscopic one.

Our mesoscopic description opens an intriguing perspective: As we have shown, a coarse description of neuron populations through scalar variables can suffice to capture those dynamics that are most relevant on large scales, which was also explored recently in hippocampal networks (56). This is implicitly often assumed, for instance, whenever measures such as local-field potentials are used. In such cases, single-neuron dynamics cannot be inferred, raising valid criticism about the gained understanding of population dynamics (57). Our comparison between microscopic and mesoscopic dynamics supports that—if the applied coarse scale is correct—such population-level measures are indeed sufficient to study the large-scale dynamics. As a related remark, we note that an ensemble of quadratic LIF neurons, such as those used in here as the spiking neuron model, could, in principle, be represented in the mean field (58–60), even with limited stochastic noise (61). While not applicable for our small and noise-driven modules, the mean-field approach can provide a complementary theoretical description in cases where the assumption of near infinite size and low noise are justified.

In a more general scope, noise is a ubiquitous property of brain networks. For example, while the fundamental role of the thalamus is to relay peripheral sensory information to the cortex (62), thalamic neurons are also known to deliver asynchronous, weakly correlated inputs to the cortex in the spontaneous state (30). Intracellular recordings in the barrel cortex also show that the temporal correlation of membrane potential fluctuations is close to zero when the cortex is driven solely by the thalamus (31). Such input from subcortical areas could act merely as a source of noise, but it could also change the dynamical state of the targeted cortical region to modulate its stimulus sensitivity, dynamical repertoires, and computational capabilities (9, 13, 14, 63). By adapting a ubiquitous property of brain networks (in vivo) to well-controlled cultures of cortical neurons (in vitro), our work provides an understanding of how asynchronous inputs modulate the ongoing activity of cortical networks.

In previous studies, electrical stimulation with multielectrode arrays (64–66) and more recently optogenetic stimulation (67) have been used to show that multisite stimulation effectively reduces the occurrence of collective activity events in cortical cultures on uniform substrates. These experimental investigations correspond to the merged topology of our study, wherein a similar suppression of collective events has been confirmed, even if at a smaller degree than in highly modular preparations. A number of works (64, 66, 67) also suggested a plastic change induced in network dynamics, an effect that was not observed in the present study. The difference could originate not only from the culture age or the duration of stimulation but also from extracellular calcium condition (68), opening future applications of in vitro cortical networks to the understanding of the cellular mechanisms underlying learning and memory. Besides the precision micropatterning approach used in the present work, the overall extent of network modularity can also be controlled through the modulation of cell affinity of the scaffold (54, 55) or through pharmacological manipulation of neurite outgrowth (69, 70), which could be beneficial in tuning network structures at a larger scale.

We note that twenty percent of neurons in the mammalian cortex are inhibitory, with some variation across species and areas (71, 72), and this presence of inhibition is believed to be crucial for computational purposes (17). Our experiments revealed that GABAergic inhibition is necessary for the neuronal network to modulate its level of synchrony, because when inhibition was blocked, synchronous epileptic-like activity prevailed (fig. S2). The same trend was also observed in the computational model of spiking neurons (fig. S8). The fundamental role of inhibition in shaping asynchronous states has been explored both experimentally and theoretically, revealing that networks of purely excitatory neurons are not able to generate stable asynchronous states (17). The critical role of inhibition in stabilizing system dynamics (50) and in increasing input-dependent flexibility (figs. S2 and S8) highlights the evolutionary significance of preserving the balance of electrical-chemical signal transduction in the nervous system.

It has been conjectured that the function of neural networks requires the segregated processing of diverse inputs in specialized circuits as well as the integration of all of them to generate high-level information processing and response (73). This demands a flexible balance of segregation and integration, the loss of which may induce dysfunction (74). In dynamical terms, such an optimal balance is necessarily associated with high diversity and variability of underlying synchronization patterns of neuronal activity to be sustained (75). Therefore, understanding how network structural features and dynamical aspects collectively shape complex synchronization patterns is crucial for advances in the field. Our findings might also be relevant to understand other networked systems that have modular architectures and are subjected to noise, such as gene, epidemic, and social networks.

MATERIALS AND METHODS

Micropatterned substrate

Microcontact printing was used to pattern protein ink onto glass coverslips. First, glass coverslips (C018001, Matsunami Glass Ind.) were cleaned by sonication in 100% ethanol, rinsed in Milli-Q water, and treated with air plasma for 60 s (PM-100, Yamato). The cleaned coverslips were then treated with a 0.2% solution of poly(2-

methacryloyloxyethyl phosphorylcholine-co-3-methacryloyloxypropyl triethoxysilane) (76) in ethanol for 10 s, dried in an ethanol environment for 20 min, baked in an oven at 70°C for 4 hours, and dried under vacuum overnight. The coverslips were then sterilized by immersion in ethanol, rinsed in Milli-Q water, and dried. Protein ink [extracellular matrix gel (E1270, Sigma-Aldrich; 1:100 dilution) + poly-D-lysine (50 $\mu\text{g ml}^{-1}$; P0899, Sigma-Aldrich)] was patterned using a polydimethylsiloxane (PDMS) stamp. The fabrication of the PDMS stamp has been detailed previously (44). Four pieces of thin PDMS films (approximately 2 mm by 2 mm and 0.5-mm thickness) were then attached to the periphery of the coverslip, which served as spacers. Last, the coverslips were dried overnight in a fume hood and immersed in neuronal plating medium [minimum essential medium (MEM; 11095-080, Gibco) + 5% fetal bovine serum +0.6% D-glucose].

Cell culture

The culture protocol of primary rat cortical neurons has been described previously (44, 77). Briefly, primary neurons were obtained from the cortices of embryonic day 18 pups, plated on a microfabricated coverslip at a density of 360 to 480 cells mm^{-2} , and cocultured with astrocyte feeder cells in N2 medium containing MEM + N2 supplement + ovalbumin (0.5 mg ml^{-1}) + 10 mM HEPES. Half of the medium was changed at day in vitro (DIV) 4 and DIV 8 with a conditioned neurobasal medium containing neurobasal (21103-049, Gibco) + 2% B-27 supplement (17504-044, Gibco) + 1% GlutaMAX-I (35050-061, Gibco). In some experiments, neurons were cultured in the neuron culture medium (FujiFilm Wako Pure Chemical Corp. 148-09671), a glia-conditioned medium. The astrocyte feeder layer was not used when culturing the neurons in the latter medium.

During cultivation, neurons were transfected with adeno-associated virus (AAV) vectors encoding the fluorescent calcium probe GCaMP6s (Addgene viral prep #100843-AAV9) and a red-shifted channelrhodopsin ChrimsonR (Addgene viral prep #59171-AAV9) under the Synapsin promoter. The as-received viral preparations were aliquoted and added at concentrations of 1 $\mu\text{l ml}^{-1}$ (GCaMP6s) and 0.7 $\mu\text{l ml}^{-1}$ (ChrimsonR) at DIV 4. The AAVs were diluted during medium exchange but remained in the growth medium until the end of the culture. All procedures were approved by the Tohoku University Center for Laboratory Animal Research, Tohoku University (approval number: 2020AmA-001) and Tohoku University Center for Gene Research (2019AmLMO-001).

Calcium imaging

At DIV 10 to 11, the coverslips with micropatterned neurons were rinsed in HEPES-buffered saline (HBS) containing 128 mM NaCl, 4 mM KCl, 1 mM CaCl_2 , 1 mM MgCl_2 , 10 mM D-glucose, 10 mM HEPES, and 45 mM sucrose and transferred to a glass-bottom dish (3960-035, Iwaki) filled with HBS (44, 77). GCaMP6s fluorescence was imaged using an inverted microscope (Olympus IX83) equipped with a 20 \times objective lens (numerical aperture, 0.75), a white-light light-emitting diode (LED) (Sutter Lambda HPX), a scientific complementary metal-oxide-semiconductor camera (Andor Zyla 4.2P), and a stage-top incubator (Tokai Hit). All recordings were performed at 37°C, inside the stage-top incubator that kept the temperature constant and humidified the sample. All recordings were performed approximately 10 min after transferring the sample

from the cell culture incubator to the stage-top incubator, to eliminate the potential effect of environmental temperature on neuronal activity (78). Two networks were selected from a coverslip for the recording. A recording session of a network consisted of three phases: Phase 1 was a spontaneous activity recording, phase 2 a recording with optogenetic stimulation (see below), and phase 3 a spontaneous activity recording. Each phase lasted for 10 min, and time-lapse images were taken at 20 frames s^{-1} using Solis software (Andor).

Stimulation

For the optogenetic stimulation, patterned light illumination for activating ChrimsonR was delivered using a digital micromirror device (DMD) (Mightex Polygon400G) coupled to a high-power LED (Thorlabs Solis 623C; nominal wavelength, 623 nm) via a liquid light guide. The DMD was mounted on the inverted microscope, and patterned light was reflected onto the sample stage using a short-pass dichroic mirror with an edge frequency of 556 nm (Semrock FF556-SDi01). The spatiotemporal pattern of light illumination was designed in custom MATLAB script and programmed to the DMD using PolyScan2 software (Mightex). In the MATLAB script, somas of 10 neurons expressing ChrimsonR were randomly selected from the lower half of the cultured neuronal network. Subsequently, a circular illumination area centered around the soma (diameter, 25 μm) was generated randomly with a probability of 40% for each position. Last, 750 black-and-white bitmap files with the illumination pattern were generated and imported into PolyScan2. The duration of each frame was set to 400 ms, which was sufficiently long to initiate one or more spiking activities in the illuminated neuron. Identical spatiotemporal patterns were repeated in the first and second halves of the 10-min session. Chemical stimulation was realized by increasing the extracellular potassium concentration from 4 to 6 mM.

Spike detection

To extract the neuronal activity, regions of interest (ROIs) were manually set around the neuronal somas using the CellMagicWand plugin in ImageJ2, and the mean intensity within the ROIs was extracted for each time step. ROIs with no activity were not used, and an equal number of neurons were selected from each of the four modules. Spikes were detected from calcium fluorescence traces using the MLSpike algorithm (79). The first 1 min of each 10-min recording was removed to eliminate artifacts originating from the session onset. The algorithm occasionally detected pulse signals originating in the residual stimulation light as spikes, which were manually inspected and removed based on their shape and duration.

SNN model

The neurons were modeled using as LIF neurons, as described previously (18, 80). In short, the single-neuron dynamics are described by the coupled differential equations

$$\begin{aligned}\tau_v \dot{v} &= a(v - v_{\text{ref}})(v - v_{\text{thr}}) - u + I_{\text{AMPA}} - I_{\text{GABA}} \\ \tau_u \dot{u} &= b(v - v_{\text{ref}}) - u\end{aligned}$$

where v and u are variables representing the membrane potential and membrane recovery, respectively (with time constants τ_x). Neurons interact through excitatory and inhibitory currents

(I_{AMPA} and I_{GABA}), which are described by a relaxation $\tau_x \dot{I}_x = -I_x$ and are increased instantaneously at the postsynaptic neuron upon presynaptic firing by $I_{x,\text{post}} \rightarrow I_{x,\text{post}} + j_{x,\text{pre}} R_{\text{pre}}$, where $j_{x,\text{pre}}$ is a constant to describe the current strength, and R is the presynaptic resource variable that decreases upon firing by $R \rightarrow \beta R$ and recovers as $\tau_R \dot{R} = 1 - R$. In addition, all neurons are spontaneously driven by a Poisson shot noise added to I_{AMPA} , which accounts for spontaneous synaptic release and, depending on the noise rate, the optogenetic stimulation.

A modular network was constructed by considering four squares (200 μm by 200 μm) separated by 200 μm , locating 40 neurons randomly within each square, and simulating axon growth. Of these, 80% were excitatory neurons and 20% were inhibitory neurons, resembling the ratio reported for both in vivo and in vitro networks of the mammalian cortex (49, 81, 82). To create a model with k inter-modular connections, the corresponding number of axons was forced to grow between each pair of modules. Binary adjacency matrices were then generated by forming synaptic connections when the axon of a presynaptic neuron intersected a circular region around a postsynaptic neuron within a radius of $150 \pm 20 \mu\text{m}$ (mean \pm SD). The corresponding connection probability was adjusted for each topology, so that the average in-degree per neuron was fixed to $k_{\text{in}} \sim 30$. Full details of the model are provided in section S2 (figs. S4 to S9).

Mesoscopic model

Each node i in the mesoscopic model corresponds to a module, and its dynamics were modeled using a coupled rate model with resource depletion (12)

$$\begin{aligned} \dot{\rho}_i(t) &= -\frac{1}{\tau_\rho} \rho_i(t) + F[I_i(t)] + \sigma \xi_i(t) \\ \dot{R}_i(t) &= -\frac{1}{\tau_d} \rho_i(t) R_i(t) + \frac{1}{\tau_c} [R_0 - R_i(t)] \end{aligned}$$

where ρ and R are firing rate and synaptic resource variables, respectively, R_0 is the baseline resource level, and τ_x are time constants. $F(I_i)$ is a nonlinear function mapping the total input to module i , I_i , to a rate change (section S3A). Modules were spontaneously driven by Gaussian noise ξ with an amplitude σ , which was associated with internal biological variability.

Network models were constructed by coupling four modules together in a grid-like pattern (as in the 1-b and 3-b topologies), encoded by the adjacency matrix $A = [A_{ij}]$. Then, I_i was the sum of external input h , activity propagation within the module, and activity propagation from connected neighbors

$$I_i(t) = h + \rho_i(t) R_i(t) + w \sum_{j \neq i} A_{ij} g_{ij}(t) \rho_j(t) R_j(t)$$

where w is the coupling strength, and g_{ij} is the gating variable that describes whether modules i - j are connected or disconnected. h was varied to simulate perturbed conditions. The merged topology in the experiments corresponded to the behavior of a single module unit. Further details of the model are provided in section S3 (figs. S10 to S12).

Data analysis

For the analysis of collective activity events in the experimental data, the spike trains were first summed across all neurons and convolved

with a normalized Gaussian kernel (SD = 200 ms), yielding a continuous time series that resembles a network-wide firing rate (averaged either per module or the whole population). The start and end times of the events were then obtained by thresholding the population rate at 10% of the maximum observed for any recording. An event thus begins whenever the population rate exceeds the threshold and ends when the rate drops below the threshold. To account for fluctuations during an event, we also merged consecutive events if a start time was separated by less than 100 ms from a previous end time. Event size was then defined as the number of unique neurons that contributed to the event normalized by the total number of neurons in the network. Events in SNN models were defined analogously to experiments with the following parameters: SD of the Gaussian kernel = 20 ms and threshold = 2.5%. The adjustments were motivated by designing a kernel that scaled with the shortest observed interspike interval and were necessary to account for the different sampling rates in simulations (5 ms) and experiments (50 ms).

To measure neuron correlation, Pearson correlation coefficients r_{ij} were calculated to quantify the synchronicity between a given pair of neurons i - j . For this analysis, the spike train was binned at 500 ms, and the number of spikes in each time bin was counted for each neuron. From here, r_{ij} was calculated by

$$r_{ij} = \frac{\sum_t [x_i(t) - \bar{x}_i][x_j(t) - \bar{x}_j]}{\sqrt{\sum_t [x_i(t) - \bar{x}_i]^2} \sqrt{\sum_t [x_j(t) - \bar{x}_j]^2}}$$

where $x_i(t)$ is the time-binned spike train of neuron i , and \bar{x}_i is the time average of $x_i(t)$. When comparing to the mesoscopic model, we further calculated the module correlation as the Pearson correlation coefficient between the time series of module-averaged firing rates (calculated as described above).

The functional complexity χ (48) was evaluated as

$$\chi = 1 - \frac{m}{2(m-1)} \sum_{\mu=1}^m \left| p_\mu(r_{ij}) - \frac{1}{m} \right|$$

where $p_\mu(r_{ij})$ is the probability distribution of r_{ij} in bin μ , $m = 20$ is the number of bins for r_{ij} used to estimate the distribution, and $|\cdot|$ denotes the absolute value. The definition of the error bars is described in the captions of the corresponding figures. Note that the choice of bin size (500 ms) affects the absolute value of correlation coefficients and functional complexity, and we confirmed that the reported results remain consistent with bin sizes of 250, 500, and 1000 ms.

Supplementary Materials

This PDF file includes:

Supplementary Text
Figs. S1 to S12
Tables S1 to S7
Legends for movies S1 to S8
References

Other Supplementary Material for this manuscript includes the following:

Movies S1 to S8

REFERENCES AND NOTES

- W. R. Softky, C. Koch, The highly irregular firing of cortical cells is inconsistent with temporal integration of random EPSPs. *J. Neurosci.* **13**, 334–350 (1993).
- A. Arieli, A. Sterkin, A. Grinvald, A. D. Aertsen, Dynamics of ongoing activity: Explanation of the large variability in evoked cortical responses. *Science* **273**, 1868–1871 (1996).
- M. E. Raichle, The restless brain. *Brain Connect.* **1**, 3–12 (2011).
- J. Aru, J. Aru, V. Priesemann, M. Wibral, L. Lana, G. Pipa, W. Singer, R. Vicente, Untangling cross-frequency coupling in neuroscience. *Curr. Opin. Neurobiol.* **31**, 51–61 (2015).
- A. Fornito, A. Zalesky, E. Bullmore, in *Fundamentals of brain network analysis*. (Academic Press, 2016).
- R. M. Hutchison, T. Womelsdorf, E. A. Allen, P. A. Bandettini, V. D. Calhoun, M. Corbetta, S. Penna, J. H. Duyn, G. H. Glover, J. Gonzalez-Castillo, D. A. Handwerker, S. Keilholz, V. Kiviniemi, D. A. Leopold, F. Pasquale, O. Sporns, M. Walter, C. Chang, Dynamic functional connectivity: Promise, issues, and interpretations. *Neuroimage* **80**, 360–378 (2013).
- T. Matsui, T. Q. Pham, K. Jimura, J. Chikazoe, On co-activation pattern analysis and non-stationarity of resting brain activity. *Neuroimage* **249**, 118904 (2022).
- J. M. Beggs, D. Plenz, Neuronal avalanches in neocortical circuits. *J. Neurosci.* **23**, 11167–11177 (2003).
- R. Legenstein, W. Maass, Edge of chaos and prediction of computational performance for neural circuit models. *Neural Netw.* **20**, 323–334 (2007).
- D. R. Chialvo, Emergent complex neural dynamics. *Nat. Phys.* **6**, 744–750 (2010).
- L. Cocchi, L. L. Gollo, A. Zalesky, M. Breakspear, Criticality in the brain: A synthesis of neurobiology, models and cognition. *Prog. Neurobiol.* **158**, 132–152 (2017).
- S. di Santo, P. Villegas, R. Burioni, M. A. Muñoz, Landau-Ginzburg theory of cortex dynamics: Scale-free avalanches emerge at the edge of synchronization. *Proc. Natl. Acad. Sci. U.S.A.* **115**, E1356 (2018).
- M. A. Muñoz, *Colloquium: Criticality and dynamical scaling in living systems*. *Rev. Mod. Phys.* **90**, 031001 (2018).
- B. Cramer, D. Stöckel, M. Kreft, M. Wibral, J. Schemmel, K. Meier, V. Priesemann, Control of criticality and computation in spiking neuromorphic networks with plasticity. *Nat. Commun.* **11**, 2853 (2020).
- D. Plenz, T. L. Ribeiro, S. R. Miller, P. A. Kells, A. Vakili, Self-organized criticality in the brain. *Front. Phys.* **9**, 639389 (2021).
- N. Brunel, Dynamics of sparsely connected networks of excitatory and inhibitory spiking neurons. *J. Comput. Neurosci.* **8**, 183–208 (2000).
- A. Renart, J. de la Rocha, P. Bartho, L. Hollender, N. Parga, A. Reyes, K. D. Harris, The asynchronous state in cortical circuits. *Science* **327**, 587–590 (2010).
- J. G. Orlandi, J. Soriano, E. Alvarez-Lacalle, S. Teller, J. Casademunt, Noise focusing and the emergence of coherent activity in neuronal cultures. *Nat. Phys.* **9**, 582–590 (2013).
- P. Fries, Rhythms for cognition: Communication through coherence. *Neuron* **88**, 220–235 (2015).
- P. Villegas, P. Moretti, M. A. Muñoz, Frustrated hierarchical synchronization and emergent complexity in the human connectome network. *Sci. Rep.* **4**, 5990 (2014).
- M. I. Rabinovich, P. Varona, A. Selverston, H. D. I. Abarbanel, Dynamical principles in neuroscience. *Rev. Mod. Phys.* **78**, 1213–1265 (2006).
- E. Tognoli, J. A. S. Kelso, The metastable brain. *Neuron* **81**, 35–48 (2014).
- O. Weinberger, P. Ashwin, From coupled networks of systems to networks of states in phase space. *Discrete Continuous Dyn. Syst. Ser. B* **23**, 2043–2063 (2018).
- L. Donetti, P. I. Hurtado, M. A. Muñoz, Entangled networks, synchronization, and optimal network topology. *Phys. Rev. Lett.* **95**, 188701 (2005).
- A. Arenas, A. Diaz-Guilera, J. Kurths, Y. Moreno, C. Zhou, Synchronization in complex networks. *Phys. Rep.* **469**, 93–153 (2008).
- Y. M. Lai, M. A. Porter, Noise-induced synchronization, desynchronization, and clustering in globally coupled nonidentical oscillators. *Phys. Rev. E* **88**, 012905 (2013).
- M. Dazza, S. Méten, P. Monceau, S. Bottani, A novel methodology to describe neuronal networks activity reveals spatiotemporal recruitment dynamics of synchronous bursting states. *J. Comput. Neurosci.* **49**, 375–394 (2021).
- A. Y. Y. Tan, Y. Chen, B. Scholl, E. Seidemann, N. J. Priebe, Sensory stimulation shifts visual cortex from synchronous to asynchronous states. *Nature* **509**, 226–229 (2014).
- J. Zierenberg, J. Wiltng, V. Priesemann, Homeostatic plasticity and external input shape neural network dynamics. *Phys. Rev. X* **8**, 031018 (2018).
- R. M. Bruno, B. Sakmann, Cortex is driven by weak but synchronously active thalamo-cortical synapses. *Science* **312**, 1622–1627 (2006).
- K. C.-K. Malina, B. Mohar, A. N. Rappaport, I. Lampl, Local and thalamic origins of correlated ongoing and sensory-evoked cortical activities. *Nat. Commun.* **7**, 12740 (2016).
- H. Mizuno, K. Ikezoe, S. Nakazawa, T. Sato, K. Kitamura, T. Iwasato, Patchwork-type spontaneous activity in neonatal barrel cortex layer 4 transmitted via thalamocortical projections. *Cell Rep.* **22**, 123–135 (2018).
- M. H. Friedberg, S. M. Lee, F. F. Ebner, Modulation of receptive field properties of thalamic somatosensory neurons by the depth of anesthesia. *J. Neurophysiol.* **81**, 2243–2252 (1999).
- D. S. Greenberg, A. R. Houweling, J. D. Kerr, Population imaging of ongoing neuronal activity in the visual cortex of awake rats. *Nat. Neurosci.* **11**, 749–751 (2008).
- W.-P. Chang, J.-S. Wu, C.-M. Lee, B. A. Vogt, B.-C. Shyu, Spatiotemporal organization and thalamic modulation of seizures in the mouse medial thalamic-anterior cingulate slice. *Epilepsia* **52**, 2344–2355 (2011).
- Ł. Kuśmierz, S. Ogawa, T. Toyozumi, Edge of chaos and avalanches in neural networks with heavy-tailed synaptic weight distribution. *Phys. Rev. Lett.* **125**, 028101 (2020).
- C. W. Lynn, D. S. Bassett, The physics of brain network structure, function and control. *Nat. Rev. Phys.* **1**, 318–332 (2019).
- J. W. Scannell, M. P. Young, The connective organization of neural systems in the cat cerebral cortex. *Curr. Biol.* **3**, 191–200 (1993).
- J. W. Scannell, G. A. P. C. Burns, C. C. Hilgetag, M. A. O’Neil, M. P. Young, The connective organization of the cortico-thalamic system of the cat. *Cereb. Cortex* **9**, 277–299 (1999).
- C.-C. Hilgetag, G. A. P. C. Burns, M. A. O’Neill, J. W. Scannell, M. P. Young, Anatomical connectivity defines the organization of clusters of cortical areas in the macaque monkey and the cat. *Phil. Trans. R. Soc. Lond. B* **355**, 91–110 (2000).
- D. Meunier, R. Lambiotte, E. T. Bullmore, Modular and hierarchically modular organization of brain networks. *Front. Neurosci.* **4**, 200 (2010).
- M. P. van den Heuvel, E. T. Bullmore, O. Sporns, Comparative connectomics. *Trends Cogn. Sci.* **20**, 345–361 (2016).
- W.-C. A. Lee, V. Bonin, M. Reed, B. J. Graham, G. Hood, K. Glatfelter, R. C. Reid, Anatomy and function of an excitatory network in the visual cortex. *Nature* **532**, 370–374 (2016).
- H. Yamamoto, S. Moriya, K. Ide, T. Hayakawa, H. Akima, S. Sato, S. Kubota, T. Tanii, M. Niwano, S. Teller, J. Soriano, A. Hirano-Iwata, Impact of modular organization on dynamical richness in cortical networks. *Sci. Adv.* **4**, eaau4914 (2018).
- J. L. Nathanson, Y. Yanagawa, K. Obata, E. M. Callaway, Preferential labeling of inhibitory and excitatory cortical neurons by endogenous tropism of adeno-associated virus and lentivirus vectors. *Neuroscience* **161**, 441–450 (2009).
- N. C. Klapoetke, Y. Murata, S. S. Kim, S. R. Pulver, A. Birdsey-Benson, Y. K. Cho, T. K. Morimoto, A. S. Chuong, E. J. Carpenter, Z. J. Tian, J. Wang, Y. L. Xie, Z. X. Yan, Y. Zhang, B. Y. Chow, B. Surek, M. Melkonian, V. Jayaraman, M. Constantine-Paton, G. K. S. Wong, E. S. Boyden, Independent optical excitation of distinct neural populations. *Nat. Methods* **11**, 338–346 (2014).
- Y. Penn, M. Segal, E. Moses, Network synchronization in hippocampal neurons. *Proc. Natl. Acad. Sci. U.S.A.* **113**, 3341–3346 (2016).
- G. Zamora-López, Y. Chen, G. Deco, M. L. Kringelbach, C. Zhou, Functional complexity emerging from anatomical constraints in the brain: The significance of network modularity and rich-clubs. *Sci. Rep.* **6**, 38424 (2016).
- N. Sukenik, O. Vinogradov, E. Weinreb, M. Segal, A. Levina, E. Moses, Neuronal circuits overcome imbalance in excitation and inhibition by adjusting connection numbers. *Proc. Natl. Acad. Sci. U.S.A.* **118**, e2018459118 (2021).
- S. Sadeh, C. Clopath, Inhibitory stabilization and cortical computation. *Nat. Rev. Neurosci.* **22**, 21–37 (2021).
- D. Cohen, M. Segal, Network bursts in hippocampal microcultures are terminated by exhaustion of vesicle pools. *J. Neurophysiol.* **106**, 2314–2321 (2011).
- E. Tibau, M. Valencia, J. Soriano, Identification of neuronal network properties from the spectral analysis of calcium imaging signals in neuronal cultures. *Front. Neural Circuits* **7**, 199 (2013).
- E. A. Leicht, M. E. J. Newman, Community structure in directed networks. *Phys. Rev. Lett.* **100**, 118703 (2008).
- S. Teller, C. Granell, M. De Domenico, J. Soriano, S. Gómez, A. Arenas, Emergence of assortative mixing between clusters of cultured neurons. *PLoS Comput. Biol.* **10**, e1003796 (2014).
- M. A. Rabadan, E. D. De La Cruz, S. B. Rao, Y. Chen, C. Gong, G. Crabtree, B. Zu, S. Markx, J. A. Gogos, R. Yuste, R. Tomer, An in vitro model of neuronal ensembles. *Nat. Commun.* **13**, 3340 (2022).
- B. Pietras, V. Schmutz, T. Schwalger, Mesoscopic description of hippocampal replay and metastability in spiking neural networks with short-term plasticity. *PLoS Comput. Biol.* **18**, e1010809 (2022).
- J. P. Neto, F. P. Spitzner, V. Priesemann, Sampling effects and measurement overlap can bias the inference of neuronal avalanches. *PLoS Comput. Biol.* **18**, e1010678 (2022).
- E. Montbrío, D. Pазó, A. Roxin, Macroscopic description for networks of spiking neurons. *Phys. Rev. X* **5**, 021028 (2015).
- Á. Byrne, R. D. O’Dea, M. Forrester, J. Ross, S. Coombes, Next-generation neural mass and field modeling. *J. Neurophysiol.* **123**, 726–742 (2020).

60. C. Bick, M. Goodfellow, C. R. Laing, E. A. Martens, Understanding the dynamics of biological and neural oscillator networks through exact mean-field reductions: A review. *J. Math. Neurosci.* **10**, 9 (2020).
61. I. V. Tyulkina, D. S. Goldobin, L. S. Klimenko, A. Pikovsky, Dynamics of noisy oscillator populations beyond the Ott-Antonsen ansatz. *Phys. Rev. Lett.* **120**, 264101 (2018).
62. S. M. Sherman, R. W. Guillery, The role of the thalamus in the flow of information to the cortex. *Phil. Trans. R. Soc. Lond. B* **357**, 1695–1708 (2002).
63. M. D. McDonnell, L. M. Ward, The benefits of noise in neural systems: Bridging theory and experiment. *Nat. Rev. Neurosci.* **12**, 415–425 (2011).
64. G. Shahaf, S. Marom, Learning in networks of cortical neurons. *J. Neurosci.* **21**, 8782–8788 (2001).
65. D. A. Wagenaar, R. Madhavan, J. Pine, S. M. Potter, Controlling bursting in cortical cultures with closed-loop multi-electrode stimulation. *J. Neurosci.* **25**, 680–688 (2005).
66. M. Chiappalone, P. Massobrio, S. Martinoia, Network plasticity in cortical assemblies. *Eur. J. Neurosci.* **28**, 221–237 (2008).
67. X. Zhang, F.-C. Yeh, H. Ju, Y. Jiang, G. F. W. Quan, A. M. J. VanDongen, Familiarity detection and memory consolidation in cortical assemblies. *eNeuro* **7**, ENEURO.0006–19.2020 (2020).
68. Y. Inglebert, J. Aljadeff, N. Brunel, D. Debanne, Synaptic plasticity rules with physiological calcium levels. *Proc. Natl. Acad. Sci. U.S.A.* **117**, 33639–33648 (2020).
69. S. Okujeni, U. Egert, Self-organization of modular network architecture by activity-dependent neuronal migration and outgrowth. *eLife* **8**, e47996 (2019).
70. S. Okujeni, U. Egert, Structural modularity tunes mesoscale criticality in biological neuronal networks. *J. Neurosci.* **43**, 2515–2526 (2023).
71. F. M. Krienen, M. Goldman, Q. Zhang, R. C. H. del Rosario, M. Florio, R. Machold, A. Saunders, K. Levandowski, H. Zaniewski, B. Schuman, C. Wu, A. Lutservitz, C. D. Mullally, N. Reed, E. Bien, L. Bortolin, M. Fernandez-Otero, J. D. Lin, A. Wysoker, J. Nemes, D. Kulp, M. Burns, V. Tkachev, R. Smith, C. A. Walsh, J. Dimidschstein, B. Rudy, L. S. Kean, S. Berretta, G. Fishell, G. Feng, S. A. McCarroll, Innovations present in the primate interneuron repertoire. *Nature* **586**, 262–269 (2020).
72. S. Loomba, J. Straehle, V. Gangadharan, N. Heike, A. Khalifa, A. Motta, N. Ju, M. Sievers, J. Gempt, H. S. Meyer, M. Helmstaedter, Connectomic comparison of mouse and human cortex. *Science* **377**, ea0924 (2022).
73. G. Tononi, O. Sporns, G. M. Edelman, A measure for brain complexity: Relating functional segregation and integration in the nervous system. *Proc. Natl. Acad. Sci. U.S.A.* **91**, 5033–5037 (1994).
74. L.-D. Lord, A. B. Stevner, G. Deco, M. L. Kringelbach, Understanding principles of integration and segregation using whole-brain computational connectomics: Implications for neuropsychiatric disorders. *Philos. Trans. A Math. Phys. Eng. Sci.* **375**, 20160283 (2017).
75. G. Deco, V. K. Jirsa, P. A. Robinson, M. Breakspear, K. Friston, The dynamic brain: From spiking neurons to neural masses and cortical fields. *PLOS Comput. Biol.* **4**, e1000092 (2008).
76. Y. Xu, M. Takai, T. Konno, K. Ishihara, Microfluidic flow control on charged phospholipid-polymer interface. *Lab Chip* **7**, 199–206 (2007).
77. H. Yamamoto, S. Kubota, Y. Chida, M. Morita, S. Moriya, H. Akima, S. Sato, A. Hirano-Iwata, T. Tanii, M. Niwano, Size-dependent regulation of synchronized activity in living neuronal networks. *Phys. Rev. E* **94**, 012407 (2016).
78. C. M. Hales, J. D. Rolston, S. M. Potter, How to culture, record and stimulate neuronal networks on micro-electrode arrays (MEAs). *J. Vis. Exp.* **39**, 2056 (2010).
79. T. Deneux, A. Kaszas, G. Szalay, G. Katona, T. Lakner, A. Grinvald, B. Rózsa, I. Vanzetta, Accurate spike estimation from noisy calcium signals for ultrafast three-dimensional imaging of large neuronal populations in vivo. *Nat. Commun.* **7**, 12190 (2016).
80. E. M. Izhikevich, Simple model of spiking neurons. *IEEE Trans. Neural Netw.* **14**, 1569–1572 (2003).
81. S. Sahara, Y. Yanagawa, D. D. M. O'Leary, C. F. Stevens, The fraction of cortical GABAergic neurons is constant from near the start of cortical neurogenesis to adulthood. *J. Neurosci.* **32**, 4755–4761 (2012).
82. J. Soriano, M. R. Martínez, T. Tlustý, E. Moses, Development of input connections in neural cultures. *Proc. Natl. Acad. Sci. U.S.A.* **105**, 13758–13763 (2008).
83. T. Takemuro, H. Yamamoto, S. Sato, A. Hirano-Iwata, Polydimethylsiloxane microfluidic films for in vitro engineering of small-scale neuronal networks. *Jpn. J. Appl. Phys.* **59**, 117001 (2020).
84. M. Newman, in *Networks* (Oxford University Press, ed. 2, 2018).
85. R. Guimerà, M. Sales-Pardo, L. A. Nunes Amaral, Modularity from fluctuations in random graphs and complex networks. *Phys. Rev. E* **70**, 025101(R) (2004).
86. E. Alvarez-Lacalle, E. Moses, Slow and fast pulses in 1-D cultures of excitatory neurons. *J. Comput. Neurosci.* **26**, 475–493 (2009).
87. J. S. Isaacson, M. Scanziani, How inhibition shapes cortical activity. *Neuron* **72**, 231–243 (2011).
88. K. A. Ferguson, F. Njap, W. Nicola, F. K. Skinner, S. A. Campbell, Examining the limits of cellular adaptation bursting mechanisms in biologically-based excitatory networks of the hippocampus. *J. Comput. Neurosci.* **39**, 289–309 (2015).
89. M. Stimberg, R. Brette, D. F. Goodman, Brian 2, an intuitive and efficient neural simulator. *eLife* **8**, e47314 (2019).
90. L. Huang, P. Ledochowitsch, U. Knoblich, J. Lecoq, G. J. Murphy, R. C. Reid, S. E. J. de Vries, C. Koch, H. Zeng, M. A. Buice, J. Waters, L. Li, Relationship between simultaneously recorded spiking activity and fluorescence signal in GCaMP6 transgenic mice. *eLife* **10**, e51675 (2021).
91. H. R. Wilson, J. D. Cowan, Excitatory and inhibitory interactions in localized populations of model neurons. *Biophys. J.* **12**, 1–24 (1972).
92. M. Jedynak, Collective excitability in a mesoscopic neuronal model of epileptic activity. *Phys. Rev. E* **97**, 012204 (2018).
93. W. Gerstner, W. M. Kistler, R. Naud, L. Paninski, in *Neuronal dynamics: From single neurons to networks and models of cognition* (Cambridge Univ. Press, 2014).
94. M. V. Tsodyks, H. Markram, The neural code between neocortical pyramidal neurons depends on neurotransmitter release probability. *Proc. Natl. Acad. Sci. U.S.A.* **94**, 719–723 (1997).
95. D. Holcman, M. Tsodyks, The emergence of Up and Down states in cortical networks. *PLOS Comput. Biol.* **2**, e23 (2006).
96. V. Buendía, P. Villegas, R. Burioni, M. A. Muñoz, Hybrid-type synchronization transitions: Where incipient oscillations, scale-free avalanches, and bistability live together. *Phys. Rev. Research* **3**, 023224 (2021).
97. P. C. Bressloff, J. N. Maclaurin, Stochastic hybrid systems in cellular neuroscience. *J. Math. Neurosci.* **8**, 12 (2018).

Acknowledgments

Funding: H.Y., A.H.-I., and S.S. acknowledge MEXT Grant-in-Aid for Transformative Research Areas (B) "Multicellular Neurobiocomputing" (21H05164), JSPS KAKENHI (18H03325, 19H00846, 20H02194, 20K20550, 22H03657, 22K19821, 22KK0177, and 23H03489), JST-PRESTO (JMPJPR18MB), JST-CREST (JPMJCR19K3), and Tohoku University RIEC Cooperative Research Project Program for financial support. F.P.S., V.P., and J.Z. received support from the Max-Planck-Society. F.P.S. acknowledges funding by SMARTSTART, the joint training program in computational neuroscience by the VolkswagenStiftung and the Bernstein Network. F.P.S. and V.P. were funded by the German Research Foundation (Deutsche Forschungsgemeinschaft, DFG), SFB-1528–Cognition of Interaction. V.P. was supported by the DFG under Germany's Excellence Strategy EXC 2067/1- 390729940. V.B. and A.L. were supported by a Sofja Kovalevskaja Award from the Alexander von Humboldt Foundation, endowed by the Federal Ministry of Education and Research. A.L. is a member of the Machine Learning Cluster of Excellence EXC 2064/1- 39072764. M.A.M. acknowledges the Spanish Ministry and Agencia Estatal de Investigación (AEI) through Project of I + D + i (PID2020-113681GB-I00), financed by MICIN/AEI/10.13039/501100011033 and FEDER "A way to make Europe", and the Consejería de Conocimiento, Investigación Universidad, Junta de Andalucía and European Regional Development Fund (P20-00173) for financial support. J.Z. received financial support from the Joachim Herz Stiftung. J.S. acknowledges Horizon 2020 Future and Emerging Technologies (grant agreement 964877-NEUChIP), Ministerio de Ciencia, Innovación y Universidades (PID2019-108842GB-C21), and Departament de Recerca i Universitats, Generalitat de Catalunya (2017-SGR-1061 and 2021-SGR-00450) for financial support. **Author contributions:** Conceptualization: H.Y., F.P.S., V.P., J.Z., and J.S. Methodology: H.Y., T.K., S.S., A.H.-I., A.L., V.P., M.A.M., and J.S. Investigation (experiments): H.Y., T.T., and H.M. Investigation (SNN simulation): F.P.S. and J.Z. Investigation (mesoscopic simulation): F.P.S., V.B., and M.A.M. Analysis: H.Y., F.P.S., T.T., V.B., C.M., and J.S. Visualization: F.P.S. Supervision: S.S., A.H.-I., A.L., V.P., M.A.M., J.Z., and J.S. Writing—original draft: H.Y., F.P.S., V.B., V.P., M.A.M., J.Z., and J.S. Writing—review and editing: T.T., H.M., C.M., T.K., S.S., A.H.-I., and A.L. **Competing interests:** The authors declare that they have no competing interests. **Data and materials availability:** The data and processed analysis results for this study have been deposited in G-Node GIN <https://doi.org/10.12751/g-node.t77b3p>. The source code for analysis and simulation have been deposited in Zenodo <https://doi.org/10.5281/zenodo.7962283> and in GitHub https://github.com/Priesemann-Group/stimulating_modular_cultures. All data needed to evaluate the conclusions in the paper are present in the paper and/or the Supplementary Materials.

Submitted 29 July 2022
 Accepted 21 July 2023
 Published 25 August 2023
 10.1126/sciadv.ade1755

5

How contact patterns destabilize and modulate epidemic outbreaks


Published in New Journal of Physics (2023)

DOI [10.1088/1367-2630/acd1a7](https://doi.org/10.1088/1367-2630/acd1a7)

Preprint [arXiv:2109.12180](https://arxiv.org/abs/2109.12180)

Supplementary material [Appendix C](#)

Source code github.com/Priesemann-Group/contact_pattern_outbreak

License 

Own contributions

- ✓ Conceptualization
- ✓ Methodology
- ✓ Software
- ✓ Validation
- ✓ Formal Analysis
- ✓ Investigation

Resources

- ✓ Data Curation
- ✓ Writing — Original Draft
- ✓ Writing — Review & Editing
- ✓ Visualization

Supervision

Project Administration

Funding Acquisition

JZ and I jointly developed the models and implemented the code.
I created all figures. All authors wrote the manuscript.



PAPER







How contact patterns destabilize and modulate epidemic outbreaks

OPEN ACCESS

RECEIVED
17 February 2023REVISED
20 April 2023ACCEPTED FOR PUBLICATION
2 May 2023PUBLISHED
30 May 2023

Original Content from
this work may be used
under the terms of the
[Creative Commons
Attribution 4.0 licence](#).

Any further distribution
of this work must
maintain attribution to
the author(s) and the title
of the work, journal
citation and DOI.

**Johannes Zierenberg^{1,5,*}** , **F Paul Spitzner^{1,5}** , **Jonas Dehning¹** , **Viola Priesemann^{1,2}** ,
Martin Weigel³  and **Michael Wilczek^{1,4}** ¹ Max Planck Institute for Dynamics and Self-Organization, 37077 Göttingen, Germany² Institute for the Dynamics of Complex Systems, University of Göttingen, 37077 Göttingen, Germany³ Institut für Physik, Technische Universität Chemnitz, 09107 Chemnitz, Germany⁴ Theoretical Physics I, University of Bayreuth, 95440 Bayreuth, Germany⁵ J Z and F P S contributed equally.

* Author to whom any correspondence should be addressed.

E-mail: johannes.zierenberg@ds.mpg.de**Keywords:** human contact patterns, non-Markovian dynamics, epidemic outbreak, latent periodSupplementary material for this article is available [online](#)

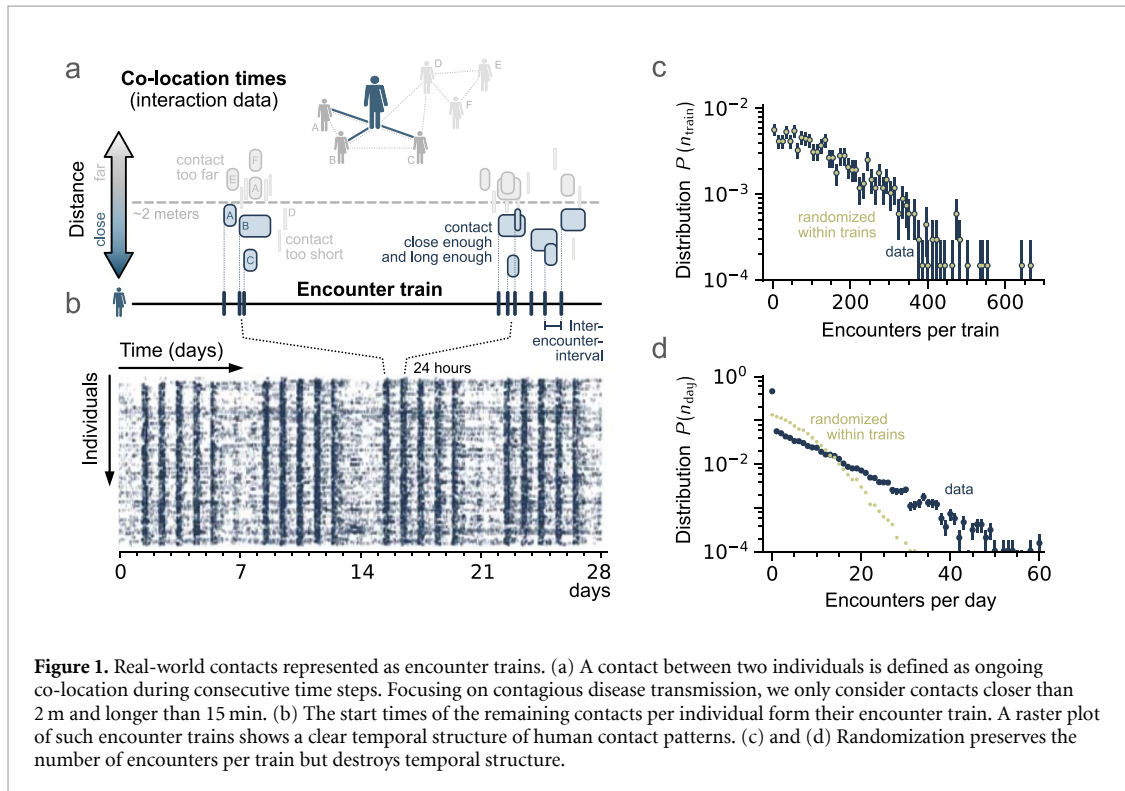
Abstract

The spread of a contagious disease clearly depends on when infected individuals come into contact with susceptible ones. Such effects, however, have remained largely unexplored in the study of epidemic outbreaks. In particular, it remains unclear how the timing of contacts interacts with the latent and infectious stages of the disease. Here, we use real-world physical proximity data to study this interaction and find that the temporal statistics of actual human contact patterns (i) destabilize epidemic outbreaks and (ii) modulate the basic reproduction number R_0 . We explain both observations by distinct aspects of the observed contact patterns. On the one hand, we find the destabilization of outbreaks to be caused by the temporal clustering of contacts leading to over-dispersed offspring distributions and increased probabilities of otherwise rare events (zero- and super-spreading). Notably, our analysis enables us to disentangle previously elusive sources of over-dispersion in empirical offspring distributions. On the other hand, we find the modulation of R_0 to be caused by a periodically varying contact rate. Both mechanisms are a direct consequence of the memory in contact behavior, and we showcase a generative process that reproduces these non-Markovian statistics. Our results point to the importance of including non-Markovian contact timings into studies of epidemic outbreaks.

1. Introduction

As contagious diseases are passed on through contacts, the number of secondary infections depends crucially on the contact patterns of infectious individuals. These contact patterns encode relevant information such as the number of interaction partners and contact timing. However, the majority of prevailing models for disease spread prioritize simpler descriptions that neglect these aspects—despite evidence from studies that show the effects of contact patterns to be crucial for disease spread: structurally, when interaction partners are modeled by a static complex network [1], the network structure affects disease spread through the occurrence of hubs [2, 3], multiscale link communities [4] and influential spreaders [5]. Dynamically, real-world interaction times generally follow a non-Markovian process (in contrast to commonly assumed memoryless processes), which influences epidemics through the occurrence of bursts [6, 7] and daily and weekly variations in human interaction [8, 9].

Thus, for a better understanding of disease spread through human contacts, a complete description of time-varying interactions in the form of so-called temporal networks [10, 11] seems necessary. However, constructing detailed temporal networks from real-world contacts requires extensive amounts of recorded data, which in principle can be collected in field studies [12–14] but such data are notoriously limited in



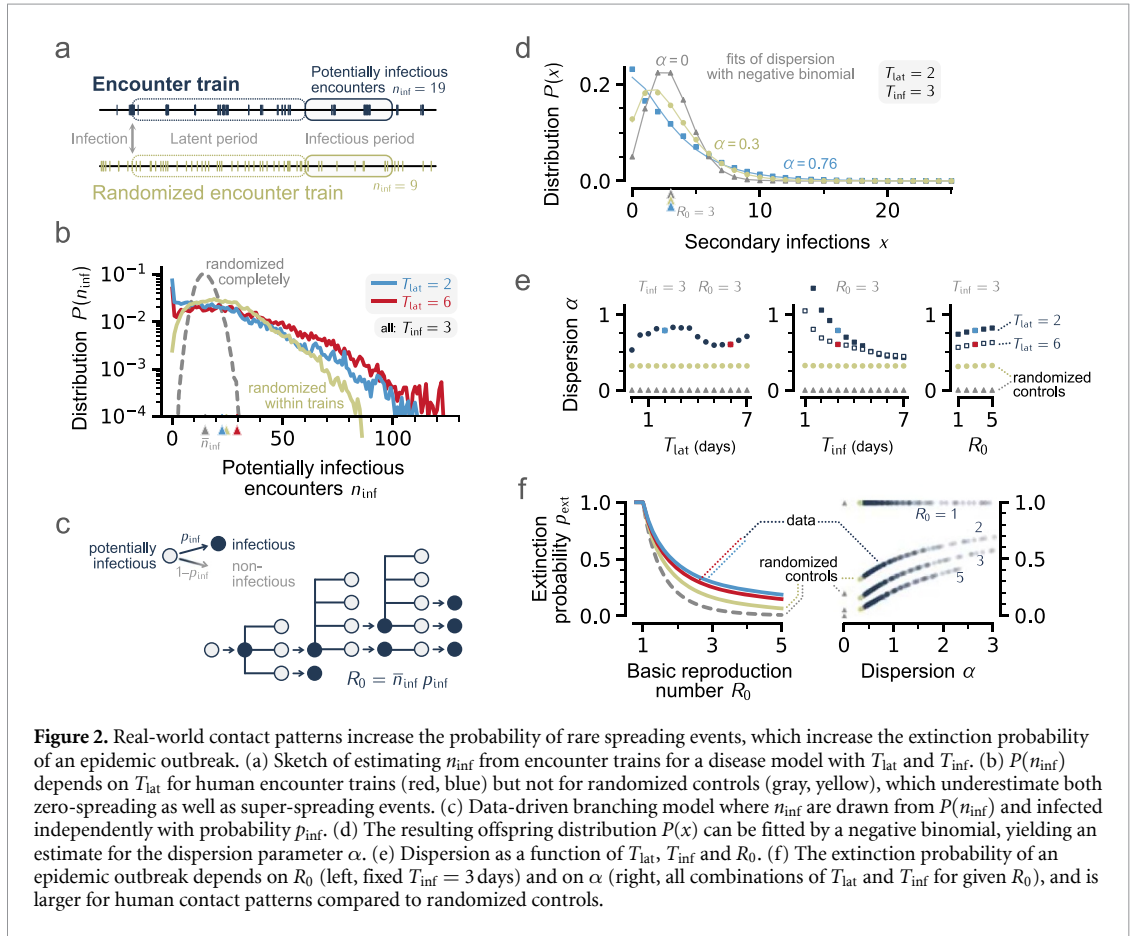
duration and system size. Although such limitations of real-world data can be partly remedied by generating surrogate data [15, 16], it is often unclear to which extent they represent the real system. An unsolved task is thus to generate surrogate data that mimics temporal statistics and individual variations of actual human contact data.

Here, we address this gap by identifying and isolating features of contact behavior that affect epidemic outbreaks using a novel analysis of real-world contact data. Instead of characterizing full epidemic outbreaks on a large (likely under-determined) temporal network, we develop an effective description through *potentially infectious encounters* that propagates statistics of contacts to statistics of disease spread. This approach avoids treating microscopic (non-linear) network effects [17–19] and allows us to focus on how contact patterns statistically affect epidemic outbreaks. Our analysis reveals two main mechanisms: (i) contact clustering destabilizes outbreaks by increasing the dispersion of offspring distributions and the probability of zero-spreading events, and (ii) temporal variation of the contact rate modulates the mean basic reproduction number, R_0 , due to an interference between contact patterns and disease progression. Finally, we showcase a non-Markovian process that faithfully reproduces the temporal statistics and their effect on disease spread as a proof of principle for a new class of generative models for surrogate data that mimic human contact patterns.

2. Results

To shed light on the interplay of contact patterns and epidemic outbreaks, we analyse proximity data from the Copenhagen Networks Study [20] and, in the supplementary material, from SocioPatterns [13, 21]. We filter each individual's contacts by distance and duration, and define encounters as their starting times (see methods). The resulting *encounter trains* are a point-process-like representation that captures the non-Markovian statistics of the underlying contact patterns (figure 1). The importance of these non-Markovian statistics can be seen when comparing to randomized encounter trains. In these surrogate data, encounter times are uniformly reassigned within the duration of the experiment—which preserves the number of encounters per train, i.e. the inter-individual variability (figure 1(c)), but destroys any temporal structure (figure 1(d)).

In order to quantify the effect of contact patterns on epidemic outbreaks, we focus on potential secondary infections and assume a contagious disease that can be transmitted only during infectious encounters. Further, if τ is the time elapsed since infection, infected individuals undergo a (non-infectious) latent period $\tau \in [0, T_{\text{lat}})$ and an infectious period $\tau \in [T_{\text{lat}}, T_{\text{lat}} + T_{\text{inf}})$ during which all n_{inf} encounters are



potentially infectious. We estimate n_{inf} by considering every encounter in the data set as a potential start for an infection (figure 2(a), see methods). As we show in figure 2(b), empirical contact patterns increase both the probability of very few n_{inf} (related to zero-spreading events) as well as very many n_{inf} (related to super-spreading events) when compared to randomized controls. This increase in variability influences whether a single infection results in an epidemic outbreak or not.

2.1. Human contact patterns destabilize epidemic outbreaks

To demonstrate the effect of empirical contact patterns on epidemic outbreaks, we map the probability distribution of n_{inf} to an offspring distribution using a two-step, data-driven branching process (figure 2(c)): Each infected individual first generates encounters according to the empirical distribution $P(n_{\text{inf}})$, and then infects each of them independently with probability p_{inf} resulting in binomial-distributed secondary infections. Taking the expectation value yields the offspring distribution

$$P(x) = \sum_{n_{\text{inf}}=x}^{\infty} P(n_{\text{inf}}) \binom{n_{\text{inf}}}{x} p_{\text{inf}}^x (1-p_{\text{inf}})^{n_{\text{inf}}-x}. \quad (1)$$

Similar to empirical distributions from contact tracing [22], $P(x)$ can be well described by a negative binomial distribution (figure 2(d)) with mean $\bar{x} = R_0 = p_{\text{inf}} \bar{n}_{\text{inf}}$ and variance $\overline{(x - R_0)^2} = R_0 + \alpha R_0^2$, where α is the dispersion parameter that characterizes the increase in variance relative to a Poisson distribution.

Our data analysis provides a systematic approach to identifying sources of the dispersion observed in empirical offspring distributions [23–25]. We analyze step by step the dispersion occurring because of human contact patterns, and how it depends on T_{lat} , T_{inf} and R_0 (figure 2(e), left to right). For a completely randomized control, where encounters are uniformly distributed across trains and time, we consistently find Poissonian offspring distributions (figure 2(d), gray) with vanishing dispersion ($\alpha = 0$), independent of the three disease parameters (figure 2(e), gray triangles). When including variability of contact rates into the control, while still randomizing within trains, the dispersion of the offspring distribution increases ($\alpha \approx 0.3$) but remains mostly independent of disease parameters (yellow circles). Lastly, when also including the precise timing of human contact patterns, offspring distributions show a large dispersion that depends on

T_{lat} and T_{inf} (blue symbols). In particular, dispersion is strongest for short T_{inf} but decays as T_{inf} increases. Hence, part of the empirical dispersion can be attributed to variability of contact rates between individuals, but the non-Markovian timing of human contact patterns causes a further increase—for realistic parameters roughly by a factor of two.

From $P(x)$ we derive the extinction probability p_{ext} , defined as the fraction of outbreaks that asymptotically end up in the absorbing state of zero infections (figure 2(f)). It can be calculated using the probability generating function, $\pi(\theta) = \sum_{x=0}^{\infty} P(x)\theta^x$, as the smallest θ^* that solves $\theta^* = \pi(\theta^*)$ [26]. In addition to the anticipated monotonic decrease of $p_{\text{ext}} = \theta^*$ with increasing R_0 , we find that extinction is more likely for actual human contact patterns (red, blue) than for randomized controls (gray, yellow). Moreover, for fixed R_0 , we find that an increased dispersion α due to human contact patterns non-linearly increases p_{ext} (figure 2(f), right).

Summarizing, we find that the non-Markovian timing of human contact patterns can be a strong source of variability, relevant to explaining the over-dispersion of empirical offspring distributions. In particular, increasing the dispersion for a fixed R_0 increases the probability of zero-spreading events (figure 2(d), blue vs gray), and results in a higher extinction probability (figure 2(f)) — in other words, the non-Markovian temporal structure of human contact patterns destabilizes epidemic outbreaks.

2.2. Interplay between contact pattern and disease progression modulates basic reproduction number

As highlighted in figure 2(b), \bar{n}_{inf} depends on T_{lat} for human encounter trains. This might be at first glance surprising, because for memory-less processes, \bar{n}_{inf} is proportional to T_{inf} but independent of T_{lat} . Hence, in the following, we systematically vary T_{lat} and T_{inf} to study how the interplay between human contact patterns and disease progression affects \bar{n}_{inf} (figure 3).

Considering a fixed $T_{\text{inf}} = 3$ days (figure 3(a)) and scanning T_{lat} leads to a periodic modulation of \bar{n}_{inf} from human encounter trains (black, dashed) around the constant estimate from randomized trains (yellow). Thus, we consider \bar{n}_{inf} relative to randomized (figure 3(b)), which accounts for the trivial increase of \bar{n}_{inf} with increasing T_{inf} . For small $T_{\text{inf}} < 1$ day, we find daily modulations as a function of T_{lat} , with regions below-randomized (blue) and above-randomized (red). This effect diminishes for larger T_{inf} , where we find extended, triangular regions with interfaces located at $T_{\text{lat}} + T_{\text{inf}} = 7$ days and $T_{\text{lat}} = 7$ days. We thus find periodic modulations of \bar{n}_{inf} on the scale of days (small T_{lat}) and weeks (large T_{lat}).

In the following, we uncover the origin of these periodic modulations using what we call *conditional encounter rate* $\Psi(\tau)$, see methods. In short, $\Psi(\tau)$ describes the average rate of encounters conditioned on an initial encounter (figure 3(c)). Considering the initial encounter as an infection, $\Psi(\tau)$ measures the rate of potentially infectious encounters but neglects variability and dispersion. We find that $\Psi(\tau)$ features a peak at 0 (which implies strong clustering [6]) and the anticipated periodic modulations between high and low encounter rates (which cause a time-dependent secondary attack rate). Both, the initial peak and modulations are again lost for randomized controls (yellow line).

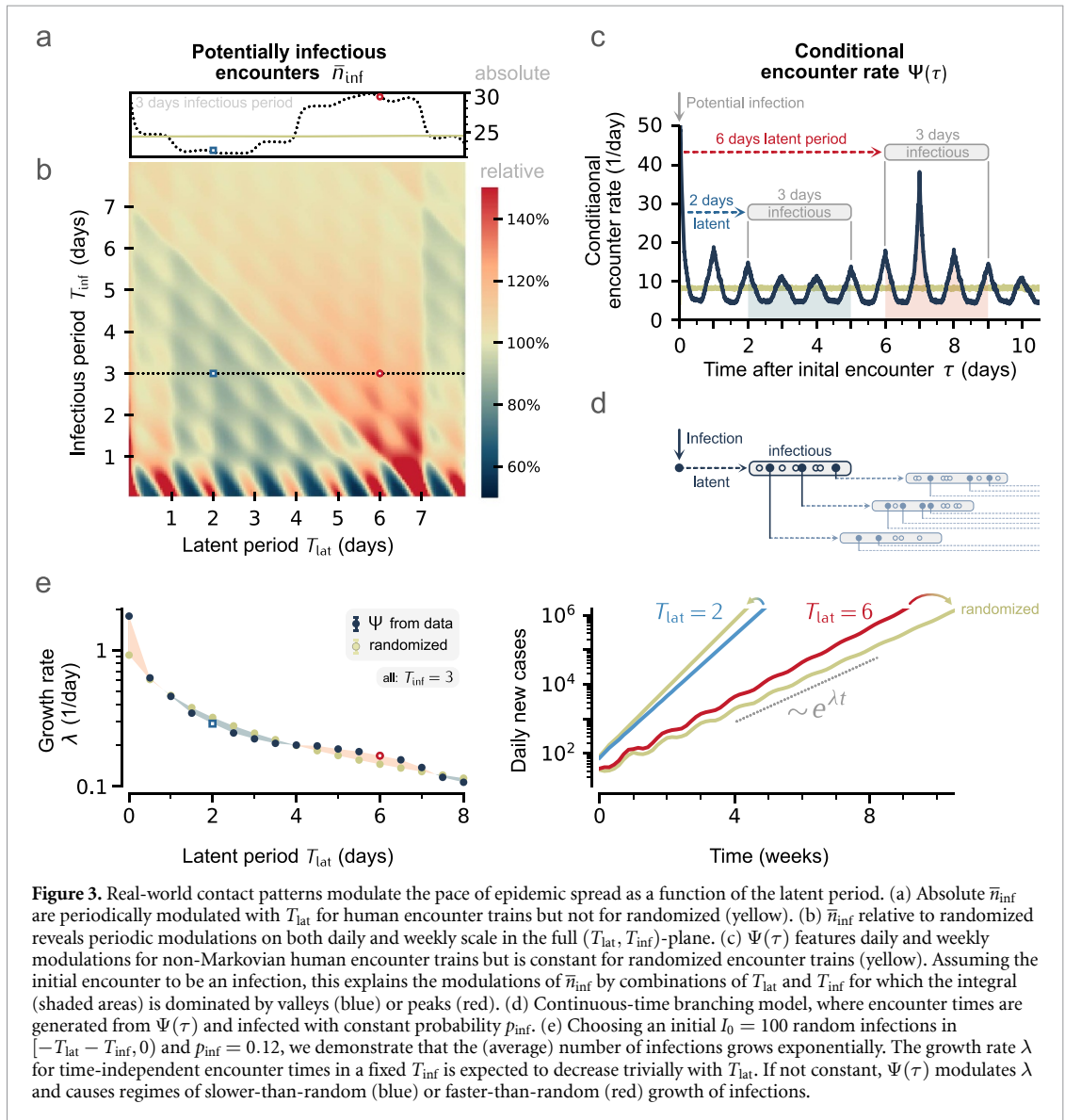
Note that we can directly obtain an estimate of \bar{n}_{inf} for a particular disease progression ($T_{\text{lat}}, T_{\text{inf}}$) by integrating $\Psi(\tau)$ over the infectious period (figure 3(c), shaded areas). Reconsidering the previous examples, this explains the lower \bar{n}_{inf} for $T_{\text{lat}} = 2$ days (blue area covering the valley) and the larger \bar{n}_{inf} for $T_{\text{lat}} = 6$ days (red area covering the 7 day peak). The examples showcase that \bar{n}_{inf} is determined by the alignment of the infectious period with regions of low or high $\Psi(\tau)$.

Consequently, since \bar{n}_{inf} is related to R_0 , the interplay between contact patterns and disease progression modulates the pace of epidemic spread. To illustrate this, we construct a continuous-time branching process, where each exposed individual generates encounters according to $\Psi(\tau)$. During the infectious period, encounters again have a probability p_{inf} to become infected (figure 3(d)). Assuming an outbreak that survived the initial generations, we prepare the system with 100 random initial infections in the interval $[-T_{\text{lat}} - T_{\text{inf}}, 0)$. The resulting time evolution of daily new cases shows clear exponential growth, where the growth rate λ trivially decreases with the generation time and, thus, T_{lat} (figure 3(e)). However, this expected decrease of λ for memoryless encounter timings (yellow) is modulated in the model due to variations in $\Psi(\tau)$, which results in slower-than-random (blue) or faster-than-random (red) growth.

Summarizing, human contact patterns cause a dependence of \bar{n}_{inf} on T_{lat} that modulates R_0 and thereby the growth rate of an epidemic outbreak.

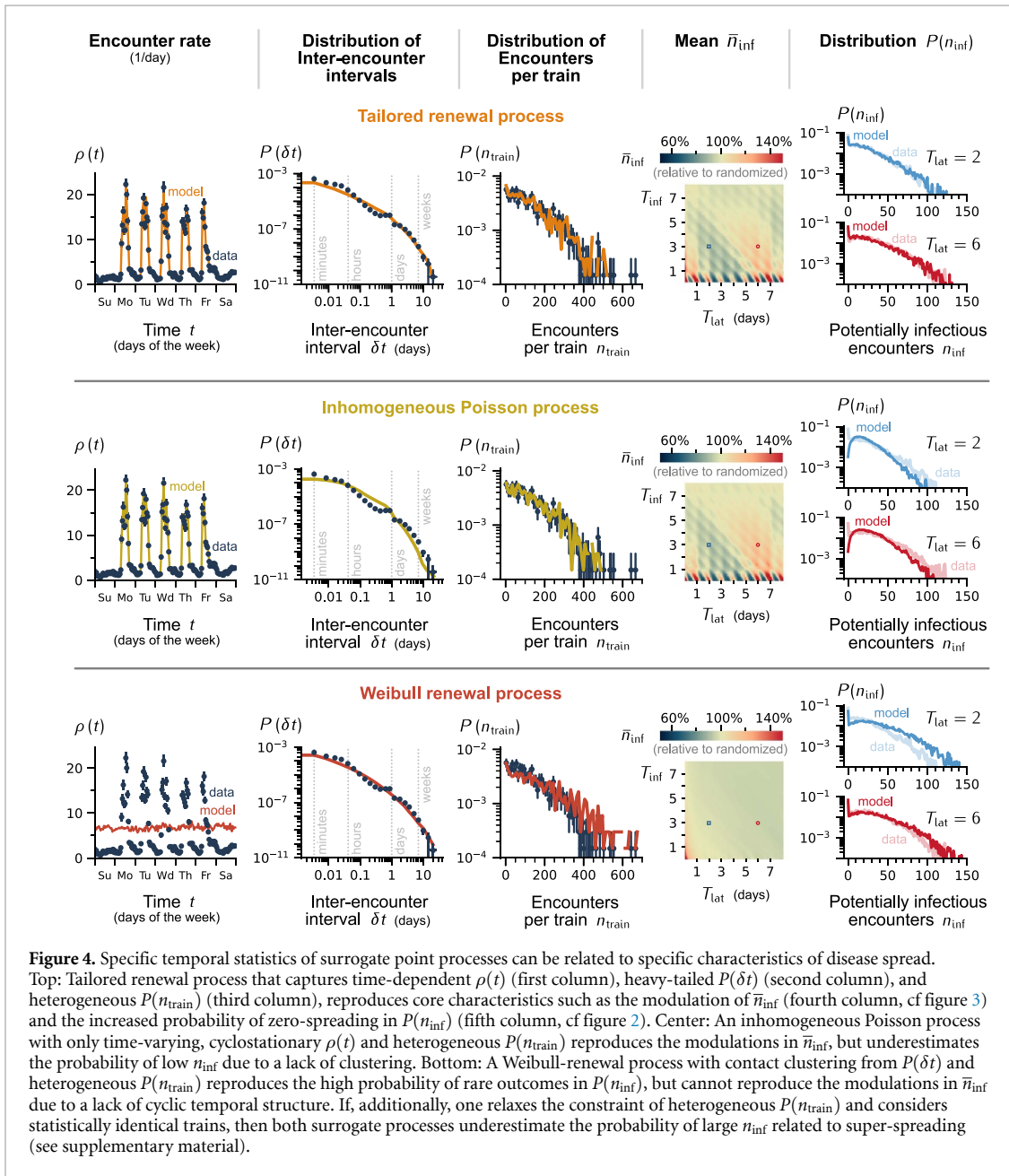
2.3. Destabilization and modulation of epidemic spread can be attributed to specific temporal statistics of contact patterns

After illustrating that non-Markovian statistics can destabilize and modulate epidemic outbreaks, it seems natural to ask how they can be included in models of disease spread. In such models it is common to approximate encounter times between individuals as memoryless (Poisson) processes [1]. Assuming independence, these processes can be merged to result in encounter trains with Poisson statistics—the same



statistics as our randomized encounter trains. In the following, we construct encounter trains with non-Markovian statistics and identify three specific features of contact patterns that are necessary to reproduce the relevant statistics of encounters. As a proof of principle, we showcase a novel *tailored renewal process* that is constrained by data and reproduces all salient features (figure 4, top row):

- i) Focusing on temporal statistics, the encounter rate $\rho(t)$ averaged across individuals and weeks is time-dependent but cyclostationary; $\rho(t)$ repeats in a weekly cycle with differences between day and night, and between weekdays and weekends (figure 4, first column). This can be captured by an inhomogeneous Poisson process (figure 4, middle row), which reproduces the periodic modulation of \bar{n}_{inf} (fourth column) and $\Psi(\tau)$ (see supplemental figure S3).
- ii) The distribution of inter-encounter intervals $P(\delta t)$ has high probability for small δt and a heavy tail of non-vanishing probability for large δt (second column). Because this tail corresponds to long periods without any encounter, it causes the high probability of $n_{\text{inf}} \approx 0$ (last column) that strongly contributes to the destabilization of epidemic outbreaks. $P(\delta t)$ is dominantly shaped by the clustering of human contacts and can be well approximated by a Weibull distribution [7, 27]. Accordingly, a Weibull-renewal processes (last row) reproduces $P(\delta t)$ and $P(n_{\text{inf}})$ well, but it does not have a time-varying $\rho(t)$ and cannot reproduce the period modulations of $\Psi(\tau)$ and \bar{n}_{inf} .
- iii) Encounter rates vary between individuals (third column). This variability can be attributed to intrinsic differences in contact behavior (cf figure 2, gray vs yellow) and is partly captured by the degree distribution of the contact network [28]. Recall that such across-individual variability is crucial to



reproduce the heavy tails of $P(n_{inf})$ and offspring distributions (see also supplemental figure S3 for generative processes where individuals share a common rate).

Clearly, models of disease spread can benefit from a generative process that reproduces those relevant features of human contact patterns, such as the tailored Weibull-renewal process showcased here. However, although our process reproduces all discussed features, it is built heuristically, and future work is needed to construct microscopic models that give rise to cyclostationary rates with clustering in a principled way, while remaining mathematically tractable.

3. Discussion

We analyzed real-world human contact patterns and found that their non-Markovian timings shape epidemic spread in two important ways. Firstly, they increase the over-dispersion of offspring distributions, compared to random (Poisson) contact patterns, which (a) leads to more zero- and super-spreading events, and (b) decreases the probability of an epidemic outbreak from an initial infection. While clustering is typically associated with super-spreading events, it inevitably causes periods of low contact rate that increase the probability of zero-spreading events. The resulting increase in extinction probability (despite

super-spreading) is consistent with previous results, where individual variation of R_0 captured the over-dispersion of empirical offspring distributions [23]. Still, the sources of this variation remained poorly understood, with candidates ranging from environmental factors (behavior, seasonality) to intrinsic ones (viral load, susceptibility) [29]. Here, we disentangled two sources based on contact patterns and identified heterogeneous contact rates and the non-Markovian timing of contacts as relevant factors for over-dispersion in disease transmissibility.

Secondly, human contact patterns non-trivially modulate the pace of epidemic spread depending on the latent period, which we attribute to time-dependent but cyclostationary encounter rates. A cyclostationary rate leads to periods of statistically high and low encounter rates conditioned on a potential infection. How these periods typically align with the infectious period is affected by the latent period and determines whether the number of potential secondary infections, and in turn R_0 , increases or decreases. This modulation of R_0 can thus be understood as a resonance following either a constructive or destructive interference between a periodically changing contact rate and the disease progression. This resonance is a new mechanism to explain the previously observed slow-down or speed-up of diffusion processes on temporal networks due to non-Markovian characteristics [30].

In the main manuscript we focus on deterministic disease progression with fixed periods (T_{lat} , T_{inf}), but we also considered non-deterministic disease progression with gamma-distributed periods [31–33]; the results are summarized in the supplementary material (figure S1). We find our main conclusion verified for non-deterministic disease progression: the probability of zero-spreading events is reliably higher for human contact patterns compared to randomized; however, the modulation of \bar{n}_{inf} with T_{lat} is smeared out with increasing variability in the period durations. Thus, in the unrealistic (but commonly adopted) limit of exponentially distributed periods, human contact patterns still reduce the robustness of outbreaks but no longer modulate the pace of epidemic spread.

To reproduce the relevant temporal features of human contact patterns, we introduced non-Markovian contact dynamics in the form of Weibull-distributed inter-encounter intervals (clustering) or inhomogeneous encounter rates (cyclostationarity). Previous studies of non-Markovian disease spread [7] found that clustering drastically affects the epidemic threshold for $T_{\text{lat}} = 0$, which is caused by the high frequency of small inter-encounter intervals [34] that, in our context, manifests as a near-zero peak in the conditional encounter rate (figure 3). Although it was shown that some non-Markovian models can be mapped onto effective Markov models [35, 36], our results suggest that the non-Markovian and cyclostationary features of human contact patterns make a similar general mapping elusive. This highlights the necessity for generative models that are non-Markovian, yet well understood and simple enough to find broad use in epidemic modeling and beyond.

Our work is a first step towards providing such models. We identified temporal statistics of real-world contact data that affect disease spread, and faithfully reproduced them with our tailored Weibull-renewal process. Thereby, our work provides an accessible pathway towards including non-Markovian statistics into spreading processes, in general, and paves the way to systematically study their non-equilibrium physics.

4. Methods

Extracting contacts from real-world physical proximity data: Consider data composed of a list of co-locations (physical proximity) described by the tuple (timestamp, user id A, user id B). We first sort the co-location times into unique lists for all id pairs (A, B) and (B, A). For each valid A, we then iterate over its list of (A, B) and merge co-location times that span consecutive time steps to construct pairwise contacts with starting time s and duration D . Combining these contacts yields a list of contacts $\{(s_i, D_i)\}_A$ for each participant A.

From the lists of contacts, we construct a point-process-like representation for each participant that we call encounter train (see figure 1). Throughout the manuscript, an encounter refers to the starting time of a contact. The encounter train of participant A is the time-sorted list of all contact starting times s_i and can formally be written as

$$T(t) = \sum_i \delta(t - s_i). \quad (2)$$

The main data set from the Copenhagen Networks Study [12, 20] is based on Bluetooth signals between phones of individuals that participated in the study. The published data is a list of interactions described by the tuple (timestamp, A, B, RSSI), where user id B can be negative if the interaction is with a device outside of the study or an empty scan, and RSSI is the received (Bluetooth) signal strength indicator. The RSSI can be considered as a proxy for interaction distance, especially since all participants used the same device [37], with an RSSI ≈ -80 dBm corresponding to a distance of about $2\text{ m} \pm 0.5\text{ m}$. Since the data provides a maximal

RSSI per time window, we consider $\text{RSSI} < -80$ dBm to indicate interactions to be further apart than 2 m throughout the full time window [37], and exclude them. Consequently, we filter the raw data to only include those interactions that are within the study (user id $B \geq 0$) and have $\text{RSSI} \geq -80$ dBm. See supplementary material for various controls. The data set covers a duration of $t_{\max} = 28$ days, with a time step of 5 min, for 675 encounter trains.

Average time-dependent encounter rate $\rho(t)$: Because encounter trains are a point-process-like representation, we can define an encounter rate as the number of encounters in a window of size Δt . Assuming statistical independence between weeks and between participants, we determine the average time-dependent encounter rate $\rho(t)$ by averaging the number of encounters in a time windows of size $\Delta t = 1$ h throughout the week (i.e. first hour of a Sunday until last hour of a Saturday) across weeks of the experiment and across participants. Statistical errors are calculated on the level of participants using delete- m jackknife error analysis.

Inter-encounter interval δt : To study temporal clustering and contact bursts, we measure the interval δt between consecutive encounter times. Since we are interested in the encounter statistics, each encounter has the same statistical weight independent of its encounter train origin. Consequently, the distribution $P(\delta t)$ is simply the distribution over all observed intervals. To estimate statistical errors, we take into account that the number of encounters n_j differs between individual trains (hence also the number of inter-encounter intervals $n_j - 1$), and evaluate statistical errors on the level of observed intervals using delete- m_j jackknife error analysis with $m_j = n_j - 1$.

Conditional encounter rate $\Psi(\tau)$: To investigate how contact patterns interact with disease spread, we measure the encounter rate $\Psi(\tau)$ upon a hypothetical infection from an encounter at $\tau = 0$. To construct $\Psi(\tau)$, we iterate over all encounters to measure the time-dependent encounter rate with temporal resolution of the experiment, starting from the encounter time, i.e. $\tau = t - s_i = 0$, until $\tau = \tau_{\max}$ (we typically chose $\tau_{\max} = 10$ days) or, if $t_{\max} - s_i < \tau_{\max}$, until $\tau = t_{\max} - s_i$. We then average over all these time-dependent encounter rates taking into account their different lengths. To estimate statistical errors, we take into account that the number of encounters n_j differs between individual trains by using delete- m_j jackknife error analysis with $m_j = n_j$.

Disease model: We consider a disease that progresses in three discrete states upon infection: exposed-infectious-recovered. The duration T_{lat} within the exposed state is called latent period and the duration T_{inf} within the infectious state is called infectious period. For our main results, we consider the simple and intuitive case of a deterministic disease progression, where these periods are always the same. This corresponds to drawing the periods from delta distributions, which is quite different to commonly employed approximations that draw periods from exponential distributions (as expected for Poisson processes that describe many state transitions, from radioactive decay to chemical reactions). To confirm that our results also apply to non-deterministic disease progression, we repeated our analysis for the more realistic case of gamma-distributed periods [31–33] and obtained consistent results (supplemental material).

Potentially infectious encounters n_{inf} : To avoid assumptions on the probability of infection upon encounter, we introduce potentially infectious encounters as the number of encounters that occur during the infectious period of a hypothetical disease. For the deterministic disease progression, we can enumerate the statistics by iterating over all encounters of the data set. For each encounter s_i , we check whether the disease progression still fits into the experimental duration ($s_i + T_{\text{lat}} + T_{\text{inf}} \leq t_{\max}$), and if true, estimate n_{inf} as the number of subsequent encounter s_j for which $T_{\text{lat}} < s_j - s_i < T_{\text{lat}} + T_{\text{inf}}$. For the non-deterministic disease progression, we need to sample disease realizations (see supplemental material). Statistical errors are calculated again on the level of encounters using the delete- m_j jackknife analysis with $m_j = n_j$.

Branching process with empirical distribution: To estimate the survival probability from the empirical distribution of potentially infectious encounters, $P(n_{\text{inf}})$, we construct a discrete-time data-driven branching process (figure 2(c)). In a first step, each infection causes $X \sim P(n_{\text{inf}})$ potentially infectious encounters. In a second step, each of these encounters can cause a secondary infection with probability p_{inf} , such that the number of secondary infections is binomial, $Y \sim \mathcal{B}(X, p_{\text{inf}})$. From Z_t infections in generation t , we thus obtain $Z_{t+1} = \sum_{i=1}^{Z_t} Y_i$ infections in the next generation.

Continuous-time branching process with inhomogeneous contacts: To study the pace of epidemic spread, we construct a continuous-time branching process that captures the conditional encounter rates but neglects interactions between infected individuals. Here, each infected individual generates an independent encounter train starting from their initial infection time as an inhomogeneous Poisson process with a time-dependent rate given by $\Psi(\tau)$ (figure 3(d)). Only those encounters that occur during the infectious period cause secondary infections with a chosen probability p_{inf} . Every secondary infection then generates a new encounter train and so on. For simplicity, we restrict our example to deterministic diseases with fixed latent and infectious periods.

Point process models to approximate human contact patterns: To disentangle the effect of distinct features of human contact patterns on the statistics of encounters, we constructed point-process models that captured (i) the distribution of rates across individuals, (ii), a time-dependent average encounter rate, and (iii), the distribution of inter-encounter intervals, or a combination thereof (see supplementary material for comparison of combinations).

To reproduce the inter-individual variability, we consider the same number of encounter trains as present in the data and weight each train i with their relative rates, i.e. $w_i = n_{\text{train},i}/\langle n_{\text{train}} \rangle$, where $\langle \cdot \rangle$ is the average across trains.

To reproduce a time-dependent encounter rate $\rho(t)$, we employ thinning [38]: From a hidden process with rate $\max_t[\rho(t)]$ we accept events at time t with probability $p(t) = \rho(t)/\max_t[\rho(t)]$. This procedure can formally only be applied for memory-less hidden processes, i.e. Poisson processes, in which case it results in an inhomogeneous Poisson process. To further reproduce heterogeneous rates in the inhomogeneous Poisson process, we rescale the rates of the hidden processes, $\rho_i(t) = w_i \rho(t)$, which keeps $p(t)$ fixed.

To reproduce the empirical distribution of inter-encounter intervals, we construct a Weibull-renewal process: inter-encounter intervals are drawn from a Weibull distribution with scale parameter λ and shape parameter k . The Weibull distribution was parameterized by a fit to the data yielding $(k, \lambda) = (0.3690, 3030)$. To further reproduce heterogeneous rates in the Weibull-renewal process, we notice that the mean rate of a Weibull-renewal process is given by $\rho_i = [\lambda_i \Gamma(1 + 1/k_i)]^{-1}$, such that we can simply choose $k_i = k$ and $\lambda_i = \lambda/w_i$.

To combine all features in a single model, we construct a tailored renewal process: A Weibull-renewal process with heterogeneous rates and additional (heuristic) thinning. We start with a set of hidden Weibull-renewal processes with $k_i = k$, $\lambda_i = \lambda/w_i$, and time-dependent acceptance probability $p(t)$ with time-average $\overline{p(t)}$. The mean rate of each process is $\rho_i = \overline{p(t)} w_i / \lambda \Gamma(1 + 1/k)$. Since we cannot fit (k, λ) of the hidden process, we further constrain the parameters with the mean rate from data, i.e. $\overline{\rho(t)} = \langle \rho_i \rangle = \overline{p(t)} / \lambda \Gamma(1 + 1/k)$, with $\langle w_i \rangle = 1$ by construction. Since $\overline{\rho(t)} / \overline{p(t)} = \max_t[\rho(t)]$, we thus find $\lambda = [\max_t[\rho(t)] \Gamma(1 + 1/k)]^{-1}$, such that k remains the only free parameter. We obtained our best estimate of k by minimizing the Kullback–Leibler divergence [39] between the distribution tails ($\delta t \gtrsim 0.5$ days) of model and empirical $P(\delta t)$, finding $k \approx 0.24$.

Jackknife error estimation: To estimate statistical errors of our results, we use jackknife error estimation while carefully taking into account the size of the left-out data set. The basic idea of the jackknife method is to estimate from some data $X = \{x_1, \dots, x_g\}$ the variance of an observable $\hat{O} = f(X)$ using a resampling approach [40]. Jackknife samples O_j are generated by systematically leaving out data, e.g. $\hat{O}_j = f(X_{\bar{j}})$ with $X_{\bar{j}} = \{x_1, \dots, x_{j-1}, x_{j+1}, \dots, x_g\}$. Importantly, here each x_j can be a block of (differently many) data points. While typically these blocks have the same size m (delete- m jackknife), they could have different sizes m_j (delete- m_j jackknife), which is relevant for some of our cases. From the jackknife samples, one can show that bias-reduced estimators of the mean and variance are given by [41]

$$\begin{aligned} \hat{O}_J &= \sum_{j=1}^g \frac{1}{h_j} \left(h_j \hat{O} - (h_j - 1) \hat{O}_j \right), \\ \hat{\sigma}_J^2 &= \frac{1}{g} \sum_{j=1}^g \frac{1}{h_j - 1} \left(h_j \hat{O} - (h_j - 1) \hat{O}_j - \hat{O}_J \right)^2, \end{aligned} \quad (3)$$

where $h_j = (\sum_{i=1}^g m_i) / m_j$, and $\hat{O} = f(X)$ is the naive estimate. For blocks of equal size, $m_j = m$, we have $h_j = g$ and this simplifies to

$$\begin{aligned} \hat{O}_J &= g \hat{O} - \frac{g-1}{g} \sum_{j=1}^g \hat{O}_j, \\ \hat{\sigma}_J^2 &= \frac{g-1}{g} \sum_{j=1}^g \left(\hat{O}_j - \frac{1}{g} \sum_{j=1}^g \hat{O}_j \right)^2. \end{aligned} \quad (4)$$

In our case, the data X is the set of all encounter trains and in the resampling step we leave out individual encounter trains. Since trains include differently many encounters, this can result in removing blocks of different sizes. In particular, all observables that derive from the number of encounters, e.g. \bar{n}_{inf} or $P(n_{\text{inf}})$, require the delete- m_j analysis, equation (3), to estimate the statistical error. On the other hand, for observables that depend on time-binned data, e.g. the time-dependent rate, each encounter train has the

same size given by the number of time bins during the recording such that the delete- m analysis, equation (4), is sufficient to estimate the statistical error.

Data availability statements

The data that support the findings of this study are openly available [13, 20] and our code is available at the following URL: https://github.com/Priesemann-Group/contact_pattern_outbreak [42].

Acknowledgments

We would like to thank Peter Sollich and Sune Lehmann for helpful discussions. J Z received financial support from the Joachim Herz Stiftung. F P S and V P acknowledge funding from the SFB 1528 *Cognition of Interaction*. V P received support from the Federal Ministry of Education and Research (BMBF) via the RESPINOW (031L0298) and infoXpand (031L0300A) projects. J Z, F P S, J D, V P, and M Wi acknowledge funding by the Max Planck Society.

ORCID iDs

Johannes Zierenberg  <https://orcid.org/0000-0001-5840-3791>

F Paul Spitzner  <https://orcid.org/0000-0001-9774-4572>

Jonas Dehning  <https://orcid.org/0000-0002-1728-2505>

Viola Priesemann  <https://orcid.org/0000-0001-8905-5873>

Martin Weigel  <https://orcid.org/0000-0002-0914-1147>

Michael Wilczek  <https://orcid.org/0000-0002-1423-8285>

References

- [1] Pastor-Satorras R, Castellano C, Van Mieghem P and Vespignani A 2015 Epidemic processes in complex networks *Rev. Mod. Phys.* **87** 925–79
- [2] Newman M E J and Park J 2003 Why social networks are different from other types of networks *Phys. Rev. E* **68** 036122
- [3] Goltsev A V, Dorogovtsev S N, Oliveira J G and Mendes J F F 2012 Localization and spreading of diseases in complex networks *Phys. Rev. Lett.* **109** 128702
- [4] Ahn Y-Y, Bagrow J P and Lehmann S 2010 Link communities reveal multiscale complexity in networks *Nature* **466** 761–4
- [5] Kitsak M, Gallos L K, Havlin S, Liljeros F, Muchnik L, Stanley H E and Makse H A 2010 Identification of influential spreaders in complex networks *Nat. Phys.* **6** 888–93
- [6] Barabási A-L 2005 The origin of bursts and heavy tails in human dynamics *Nature* **435** 207–11
- [7] Van Mieghem P and van de Bovenkamp R 2013 Non-Markovian infection spread dramatically alters the susceptible-infected-susceptible epidemic threshold in networks *Phys. Rev. Lett.* **110** 108701
- [8] Du Z, Fox S J, Holme P, Liu J, Galvani A P and Ancel Meyers L 2018 Periodicity in movement patterns shapes epidemic risk in urban environments (arXiv:1809.05203)
- [9] Towers S and Chowell G 2012 Impact of weekday social contact patterns on the modeling of influenza transmission and determination of the influenza latent period *J. Theor. Biol.* **312** 87–95
- [10] Masuda N and Holme P 2013 Predicting and controlling infectious disease epidemics using temporal networks *F1000Prime Rep* **5** 6
- [11] Holme P 2015 Modern temporal network theory: a colloquium *Eur. Phys. J. B* **88** 234
- [12] Sekara V, Stopczynski A and Lehmann S 2016 Fundamental structures of dynamic social networks *Proc. Natl. Acad. Sci.* **113** 9977–82
- [13] Génois M and Barrat A 2018 Can co-location be used as a proxy for face-to-face contacts? *EPJ Data Sci.* **7** 1–18
- [14] Schlosser F, Maier B F, Jack O, Hinrichs D, Zachariae A and Brockmann D 2020 COVID-19 lockdown induces disease-mitigating structural changes in mobility networks *Proc. Natl. Acad. Sci.* **117** 32883–90
- [15] Leitch J, Alexander K A and Sengupta S 2019 Toward epidemic thresholds on temporal networks: a review and open questions *Appl. Netw. Sci.* **4** 105
- [16] Presigny C, Holme P and Barrat A 2021 Building surrogate temporal network data from observed backbones *Phys. Rev. E* **103** 052304
- [17] Kiss Ian Z, Miller J C and Simon Peter L 2017 *Mathematics of Epidemics on Networks: From Exact to Approximate Models (Interdisciplinary Applied Mathematics)* vol 46 (Cham: Springer)
- [18] Zierenberg J, Wilting J, Priesemann V and Levina A 2020 Description of spreading dynamics by microscopic network models and macroscopic branching processes can differ due to coalescence *Phys. Rev. E* **101** 022301
- [19] Nie Y, Zhong X, Tao W, Liu Y, Lin T and Wang W 2022 Effects of network temporality on coevolution spread epidemics in higher-order network *J. King Saud Univ. - Comput. Inf. Sci.* **34** 2871–82
- [20] Sapijzynski P, Stopczynski A, Dreyer Lassen D and Lehmann S 2019 Interaction data from the Copenhagen networks study *Sci. Data* **6** 1–10
- [21] SocioPatterns (available at: <http://www.sociopatterns.org>)
- [22] Lloyd-Smith J O and Rees M 2007 Maximum likelihood estimation of the negative binomial dispersion parameter for highly overdispersed data, with applications to infectious diseases *PLoS One* **2** e180
- [23] Lloyd-Smith J O, Schreiber S J, Kopp P E and Getz W M 2005 Superspreading and the effect of individual variation on disease emergence *Nature* **438** 355–9
- [24] Peak C M, Childs L M, Grad Y H and Buckee C O 2017 Comparing nonpharmaceutical interventions for containing emerging epidemics *Proc. Natl. Acad. Sci.* **114** 4023–8

- [25] Hellewell J et al 2020 Feasibility of controlling COVID-19 outbreaks by isolation of cases and contacts *Lancet Glob. Health* **8** e488–96
- [26] Harris T E 1963 *The Theory of Branching Processes* (Berlin: Springer)
- [27] Jiang Z-Q, Xie W-J, Li M-X, Podobnik B, Zhou W-X and Eugene Stanley H 2013 Calling patterns in human communication dynamics *Proc. Natl Acad. Sci.* **110** 1600–5
- [28] Newman M E J 2010 *Networks: An Introduction* (Oxford: Oxford University Press)
- [29] Chen P Z, Koopmans M, Fisman D N and Gu F X 2021 Understanding why superspreading drives the COVID-19 pandemic but not the H1N1 pandemic *Lancet Infect. Dis.* **21** 1203–4
- [30] Scholtes I, Wider N, Pfitzner Re, Garas A, Tessone C J and Schweitzer F 2014 Causality-driven slow-down and speed-up of diffusion in non-Markovian temporal networks *Nat. Commun.* **5** 5024
- [31] Bailey N T J 1964 Some stochastic models for small epidemics in large populations *Appl. Stat.* **13** 9
- [32] Anderson D and Watson R 1980 On the spread of a disease with gamma distributed latent and infectious periods *Biometrika* **67** 191–8
- [33] Lloyd A L 2001 Destabilization of epidemic models with the inclusion of realistic distributions of infectious periods *Proc. R. Soc. B* **268** 985–93
- [34] Masuda N and Holme P 2020 Small inter-event times govern epidemic spreading on networks *Phys. Rev. Res.* **2** 023163
- [35] Starnini M, Gleeson J P and Boguñá Man 2017 Equivalence between Non-Markovian and Markovian dynamics in epidemic spreading processes *Phys. Rev. Lett.* **118** 128301
- [36] Feng Mi, Cai S-M, Tang M and Lai Y-C 2019 Equivalence and its invalidation between non-Markovian and Markovian spreading dynamics on complex networks *Nat. Commun.* **10** 3748
- [37] Sekara V and Lehmann S 2014 The strength of friendship ties in proximity sensor data *PLoS One* **9** e100915
- [38] Lewis P A W and Shedler G S 1979 Simulation of nonhomogeneous Poisson processes by thinning *Nav. Res. Logist. Q.* **26** 403–13
- [39] Kullback S and Leibler R A 1951 On information and sufficiency *Ann. Math. Stat.* **22** 79–86
- [40] Efron B 1982 *The Jackknife, the Bootstrap and Other Resampling Plans* (Philadelphia: Society of Industrial and Applied Mathematics)
- [41] Busing F M T A, Meijer E and Van Der Leeden R 1999 Delete-m jackknife for unequal m *Stat. Comput.* **9** 3–8
- [42] Analysis code (available at: https://github.com/Prieseemann-Group/contact_pattern_outbreak)

Comparison with real-world dispersion

In the published manuscript, our focus was to gain a mechanistic understanding of contact patterns, and how they give rise to dispersed offspring distributions. Because of this focus, we did not compare the amount of dispersion that can be attributed to contact patterns with dispersion values observed from real-world measurements.

This is of course a question of general interest, but to answer it, one faces several challenges. For example, one challenge is that up-to-date real-world data for the basic reproduction number R_0 — and more so, its dispersion — are hard to come by: Because R_0 does not just depend on the transmission properties of the pathogen, but also on the large-scale behavior of the susceptible population, literature values become outdated as societal habits change over time [138]. Further, real-world estimates of k are likely biased because they are often based on single outbreaks with fewer than 100 individuals [139, 140]. To our knowledge, since the seminal work by Lloyd-smith *et al.* in 2005 [139], no comprehensive overview of dispersion values has been published. We leave the cultivation of such an updated overview for future work, but, as a preliminary result, compare in the figure below our model to the existing literature values. Our estimates of dispersion are on the lower end of the references (in terms of $1/k$), likely because our model does not yet account for variable transmission probabilities between individuals, as could arise from differing viral loads. However, because our estimates are already on the right order of magnitude, this supports the hypothesis that contact patterns constitute a baseline of dispersion, and properties specific to the pathogen modulate from this baseline. This idea is explored in more detail in the discussion (Section 6.2).

5 How contact patterns destabilize and modulate epidemic outbreaks

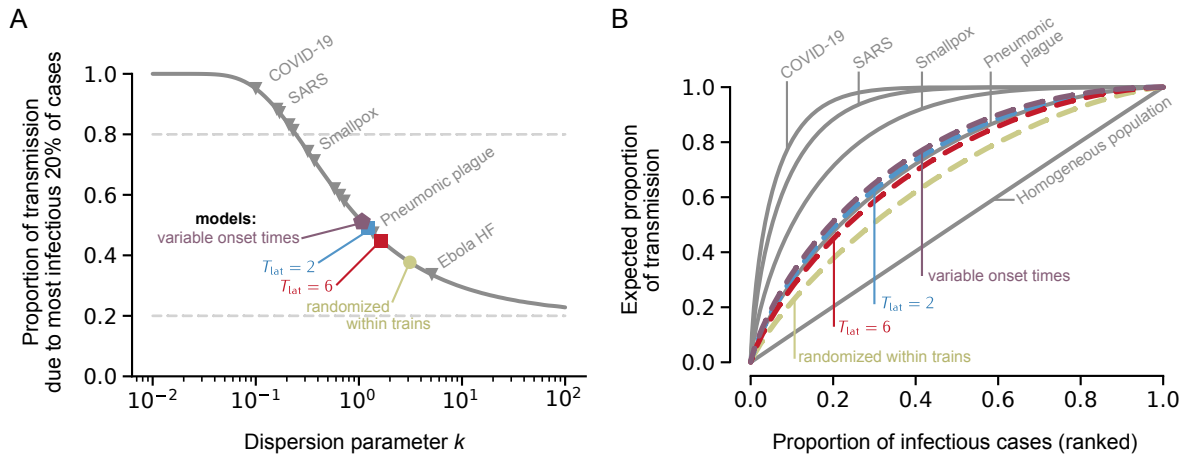


Figure 5.1: **How does dispersion caused by contact patterns compare to measurements of real-world disease outbreaks?** We follow the approach by Lloyd-smith *et al.* [139] to calculate all shown quantities as a function of the dispersion parameter ($k = 1/\alpha$ in the notation of our manuscript). **A:** Transmissions caused by the most infectious 20% of cases (i.e. have the highest individual reproduction number). For a homogeneous population, all infection chains have the same R_0 and $k \rightarrow \infty$ (lower right, consistent with completely randomized encounter trains, not shown). **B:** In this case, the proportion of transmissions due to a given proportion of cases is the same for all cases (straight line). For highly dispersed diseases, a small proportion of cases causes a large fraction of the total transmissions (left part of the graph). **Models** correspond to our reference examples of the two-step branching process with $T_{inf} = 3$ days. When the model has variable onset times, dispersion is further increased (cf. supplementary material in appendix C for details on the non-deterministic disease progression). **Data sources:** supplementary material of [139], and [141, 142]. Values should be interpreted with caution, see notes within respective references. Visualization inspired by figures 1b and 1c in [139].

6 Discussion

In this thesis, we investigated spreading processes on a structural backbone, and how distinct structural features interplay with the emergent dynamics.

We first developed inference tools that allow an unbiased treatment, taking into account that each analysis has to be tailored to the question: In Chapter 2, we developed a software package to infer the distance to criticality in a sub-sampling invariant manner, which is of particular interest to the neuroscience community: Ever-more-powerful techniques enable recording thousands of neurons in parallel, but full spatial sampling *in vivo* is still limited to few exemplary organisms with comparably small brains. In Chapter 3, we demonstrated an application and compared the MR-estimator to the conventional method of probing criticality through power-law distributions. We showed that power-law distributions are no robust indicator of criticality, and that avalanche-analysis based on spiking data are less susceptible to sampling bias than from coarse measures, such as the Local Field Potential. Revisiting the literature, these two results can resolve a long-standing controversy.

In Chapter 4, we employed a combination of precision-engineered *in vitro* cultures and phenomenological *in silico* models at different scales to elucidate how modularity and background input determine the collective dynamics of a neuron population. This combined approach strikes the balance between biologically plausible single-unit neural dynamics, near-perfect spatial sampling, control over the network topology, and, crucially, mechanistic tractability. Our work confirmed that i) a heterogeneous topological backbone is a key ingredient for cultures of dissociated neurons to desynchronize, and ii) it showed that noisy background input can act as a control parameter of synchrony.

Switching context, in Chapter 5, we considered a real-life human contact network, and developed a statistical description that enabled us to study the interactions between this temporal network and disease spread. Notably, we drew heavy inspiration from the previous chapters — e.g. in the form of spike-trains as a minimal, point-like representation that propagates the relevant, non-Markovian statistics of contact patterns into the statistics of disease spread. This enabled us to identify how the memory in contact behavior destabilizes epidemic outbreaks, modulates the basic reproduction number, and causes over-dispersed distributions of secondary infections. Our results stress the relevance of

contact patterns for disease modeling, and the need for empirical studies that measure contact data (across social contexts and geographic regions) and make them openly available.

Throughout all chapters, we employed causal models constrained by data, where we profited from the universal yet flexible nature of this approach. Both topics, the collective activity of neuronal systems and disease spread on contact networks, evolve around a spreading process interacting with a structural backbone. This naturally leads to similarities, which we could exploit during the investigation, but also to subtle-yet-key differences that we needed to take into account when developing our analysis. Some examples of these similarities, differences and, sometimes, curious consequences are discussed in the following.

6.1 A question of perspective

Despite its complexity, human behavior is surprisingly predictable [120, 125, 126]: For example, every night at 19:30 you will find me feeding my dog. Yet, predicting collective behavior such as the effectiveness of non-pharmaceutical interventions or election results from conventional polling is becoming increasingly difficult [143].

6.1.1 *The micro-macro problem*

Part of this seeming contradiction is due to perspective: The microscopic behavior of individual people can in principle be well inferred (using social surveys and behavioral experiments), but the relation to macroscopic phenomena on the population level generally remains non-trivial [144]. Similarly, the dynamics and responses of a cultured neuron can be well determined (e.g. through patch-clamping), but the formation of bursts is an emergent phenomenon involving more than a superposition of individual neurons [83]. One reason for this *micro-macro problem* [144] is that the microscopic properties can be widely distributed — in stark contrast to many classical examples from statistical physics, such as condensation in a homogeneous particle system [Ps12]. The variability of microscopic constituents makes it hard to derive a macroscopic description for the ensemble, which has motivated approaches where it can be directly implemented (like agent-based modeling [145] or *in silico* simulations of networks of spiking neurons [146]). These approaches are not as rigorous as traditional analytic formalisms, but when taking a statistical perspective — considering an ensemble of trajectories, initial conditions, and realizations — they still allow us to gain a principled insight into the underlying mechanisms. In certain cases, as we demonstrated in chapters 4 and 5, distinct aspects of

the microscopic dynamics can thereby be linked to features of the emergent, meso- and macroscopic dynamics.

6.1.2 Inference and causal modeling

When case numbers of the COVID-19 pandemic in Germany were on the rise in early 2020, we published a study on the effectiveness of political interventions that linked a series of assumed change-points of a simple model to the (macroscopic) changes of daily new cases [Ps8]. Touching on a sensitive political topic, the work subsequently caused a bit of controversy, which highlighted how important it is to communicate model assumptions and limitations clearly [Ps11, 147].

For example, a key variable that often appeared in public media was the reproduction number R to describe how many further infections are caused by an infected individual (think “cases per case” [138]). What usually did not make an appearance is that R represents the control parameter of a reproductive process and that its meaning depends on this assumed process. This issue is often hidden because the focus lies on *inferring* R , rather than finding out its role as a model parameter. After all, that role seems *a priori* clear: Irrespective of the details, large R should imply an increase in case numbers, and small R should imply a decrease. When inferring the parameters of a causal model, we thus control some other aspect of the system, such as the average number of contacts, and then quantify the change we caused by measuring R . In other words, the model encodes our understanding of the mapping of a potentially unknown system onto a well-known process, and we seek the parameters that best describe the data: *If this unknown system was a branching process, then its branching parameter would be 0.98*. However, we need to keep in mind that the system might *not be* a branching process, with a simple control parameter R .

To illustrate this, it helps to differentiate the various meanings of the reproduction number: For example, the *basic* reproduction number R_0 is the epidemiologic metric to describe the number of secondary cases due to a single infected individual in a *completely susceptible* population — e.g. the first case at the start of an outbreak. It is an indicator for transmissibility, influenced by many factors like viral contagiousness or regional differences in contact behavior, but, because the susceptible fraction of the population changes during an outbreak, and because R_0 lacks a time-unit, it is not a direct indicator for the pace of epidemic spread or for the effect of vaccination campaigns [138]. This role is better filled by the effective reproduction number R^{eff} , which depends on R_0 but also takes into account immunity and that the behavior of the population might change during an outbreak [138]. It is often expressed with an explicit time-dependence R_t^{eff} , to describe the current stability of the system as outlined above. Because R_t^{eff} is a heuristic description, it

reflects hidden factors, but it can only be interpreted in the context of the chosen model and its assumptions (such as e.g. the generation time [Ps11]). Therefore, R_t^{eff} generally remains hidden, and it cannot be trivially inferred from the daily new cases. This becomes clear when considering that cases are detected and reported only with a certain probability so that the *observed* reproduction number R_t^{obs} cannot simply be the control parameter of a branching process of observed cases; in order to faithfully account for effects like undetected infection chains, more involved models are required [Ps6, Ps7]. Together, although these seem like mere word-level differences, they offer great potential for misinterpretation [138] and reiterate that all models have limits.

6.2 Dispersion, an example for the role of non-Markovian dynamics

The simple branching process is a classic example of a model with the Markov property, where possible future states only depend on the current state, but not on past ones. However, the history of their past states is relevant for many processes in nature, which motivates the question of how Markovian models compare to non-Markovian ones, and under which conditions they might become inadequate. Examples where this has been investigated range from gene-regulatory networks [129] to quantum systems [130], polymer reaction-kinetics [131], particulate flow [132], diffusion on networks [133], credit rating [134], decision making [135] and epidemic spreading [136], and they cover a broad range of fields from biology to physics, chemistry, finance, neuroscience, and epidemiology. With Chapter 5, we add to this list the interplay of contact patterns with disease spread. As we showed, one aspect of disease spread that cannot be explained by a memoryless process is the over-dispersion of offspring distributions¹.

6.2.1 Contact patterns cause dispersion

It has been long known that empiric distributions of secondary infections are wider than expected from a Poisson distribution, but, so far, the sources of this over-dispersion remain largely elusive [139]. One likely cause is the variable probability of disease transmission as viral shedding varies from one person to the next. This viral heterogeneity has been put forward as the main cause for dispersion and super-spreading in the context of the COVID-19 pandemic [141, 149]. However, because transmissions of infectious diseases occur through physical proximity, contact patterns necessarily must play a central role, too.

¹ Note that we considered contact data from an uninformed and fully susceptible population. Accordingly, we report dispersion for R_0 , as common [139, 148].

Our approach in Chapter 5 builds on this intuition and isolates those contributions to the dispersion that derive from contact patterns while remaining agnostic about the probabilistic uncertainties that stem from the transmission. We find that the over-dispersion deriving from contact patterns can be attributed to i) the heterogeneity across individuals, that is, the personal differences in each participant’s contact behavior, and ii) the non-Markovian timing of contacts, e.g. regularly reoccurring events such as a Monday-afternoon seminar.

A natural question is how our estimates for the dispersion parameter k compare to typical empirical values². Depending on the disease, k inferred from data of traced cases ranges from $k \approx 0.16$ (SARS) to $k \approx 1.37$ (Pneumonic plague) [139], with estimates for COVID-19 around $k \approx 0.1$ [141, 148]. Our results for a generic disease (with latent and infectious periods $T_{\text{lat}} = 2$ and $T_{\text{inf}} = 3$ days) are well within that region, yielding $k \approx 1.3$ when all considered sources were included. For a control that neglected contact timing but considered that individuals have differently many contacts, we found $k \approx 3.3$, very much in line with a comparable case in [141]. Our estimates of k are likely on the upper end of literature values because of finite-size effects: For our dataset [13], a hypothetical super-spreading event could not extend beyond the recorded 675 individuals, but real-life super-spreading events have been found to cause more than a thousand secondary infections after mass-gatherings, with even more participants [150]. Also considering that estimates of k tend to be biased upward [140], this highlights the severity of the effect of contact patterns. Together, our results indicate that viral heterogeneity of infectious diseases is not the sole cause of dispersed offspring distributions, and that non-Markovian contact patterns contribute considerably.

6.2.2 Encounter-trains: a powerful representation of contact networks

Our results on dispersion were enabled by a data-efficient description of the contact network that was inspired by the spike-trains common in neuroscience. Our *encounter-trains* reduce physical contacts (extended periods of time-varying proximity between pairs of individuals) to a series of time points for each individual — maintaining important statistics of the underlying contact network.

At first glance, encounter-trains might seem like a too strong simplification, whereas spike-trains are the canonical way for describing outgoing neuronal signals. For example, because we binarize via thresholds, contacts with long durations contribute as much as short ones, or

² In Chapter 5, we expressed the dispersion of the negative binomial distribution via α , the increase in variance relative to a Poisson distribution. This facilitates fitting, but in the literature, dispersion is more commonly reported via $k = 1/\alpha$, where $k \rightarrow 0$ indicates strong dispersion, $k = 1$ recovers a geometric distribution, and $k \rightarrow \infty$ approaches the Poisson distribution [140].

close ones as much as far ones (within the respective thresholds). However, note that spike-trains are a simplification, too. Although (most) neurons do spike, from the spike-times alone it remains unclear what effect the spike has on the postsynaptic neuron. For instance, whether a spike will increment or decrement the postsynaptic membrane potential depends on the type of the presynaptic neuron. Also, the strength of postsynaptic currents is not represented by spike-trains, although it is relevant for neural activity propagation, similar to the duration of contacts for disease spread.

Despite these simplifications, both spike-trains and encounter-trains faithfully capture many relevant statistics and effects, including non-Markovian ones: Refractory periods, history dependence, inter-event-intervals, synchronization, reoccurring patterns, and other spatio-temporal structures. As an example to illustrate how underlying phenomena manifest in encounter-trains, consider a gathering, where an individual meets a larger group. It might appear that people meeting in a close space, at the same time, and over an extended period, could not be faithfully represented. However, our thresholding filters for encounters that are relevant (close enough and long enough), and because gatherings are coordinated events, the time between encounters will be short, as all participants arrive roughly at a designated starting time. When looking at the ensemble of encounter-trains, the number of encounters (due to pairs of individuals coming together in the gathering) scales with group size, $\sim N^2$, clearly marking such synchronized “*contact bursts*” [123] in the overall encounter rate. The close resemblance between such contact bursts and the neuronal bursts of *in vitro* cultures highlights how similar the two representations are: Both prioritize the timing of events, while spatial aspects and the identity of interaction partners are not expressed explicitly. As such, inferring the connectivity of a neuron population from recorded spike-trains is a topic of ongoing research [151]. For the encounter-trains, we consciously prioritized the onset times over identity because this i) allows aggregating statistics over individuals and ii) treating repeated contacts the same as unique ones is a decent approximation for low transmission probabilities.

As a final consideration, note that a point-like representation opens the door to constructing surrogate contact data via generative processes. We demonstrated such a generative process that features non-Markovian encounter times, which produces encounter-trains that closely resemble real-life data, and reproduces key statistics relevant to disease spread. Our tailored renewal process is derived heuristically but provides a basis for deriving such processes from first principles [152], which will enable a new class of epidemic models to close the gap between macroscopic compartmental models (which mostly ignore contact patterns) and microscopic agent-based models (which have to explicitly implement them).

6.2.3 Next steps

We introduced a minimal representation of contact data that enabled us to treat disease spread from a novel perspective, in which contact patterns are first described independently from the disease spread, and required details (both, of contact patterns and disease spread) can be added in a second stage. We found that, independent of many details of the assumed disease, the non-Markovian timing of encounters causes over-dispersion with a subsequently high probability of “rare events” (super-spreading, but also zero-spreading). As a control, we investigated non-deterministic disease progression (where latent and infectious periods are random variables), which decreased the modulation of R_0 (supplementary material in [Ps2]), but, on the other hand, preliminary analysis suggested that the dispersion of offspring distributions was further increased. Notably, all our identified sources of dispersion appear complementary to viral heterogeneity [141].

This motivates an intriguing hypothesis, when considering together viral heterogeneity and sources of dispersion due to contact patterns: Because contact patterns form the backbone of disease spread, they alone should explain dispersion values that fall within the range of empirically observed values — as we found in Chapter 5. Then, relative to the baseline set by contact patterns, the variability that depends on a particular disease (viral load, infectiousness, transmission probability, latent and infectious periods) would further fine-tune the dispersion. This calls for a straight-forward next step. A plausible approach to include viral heterogeneity would be to model transmission probabilities dependent on contact duration, which could be easily added as a “weight” to each encounter. Because we already identified complementary sources of heterogeneity that cause dispersion (the variability between individuals, non-Markovian timing, and variable disease stages), this might yield a complete picture: Adding durations as a proxy for heterogeneous transmission probabilities into our framework could enable us to *fully disentangle* the origin of the wide range of empirically observed dispersion.

6.3 Sampling bias

In this thesis, we encountered and treated various forms of sampling biases. Sampling biases generally arise when the measurement or recording technique leads to a non-representative view of the data. For instance, in Chapter 3 we coined the term coarse-sampling to describe an overlapping field of view (e.g. of the recording electrodes) which can bias the measured avalanche distributions of neuronal activity. However, we do not see this as a flaw of the recording technique, but argue for embracing that sampling bias is a natural consequence of the data-acquisition. In many cases, a full observation of all involved actors in a system

is unlikely, leading to sub-sampling (Chapter 2), or more commonly, limited resources and general constraints lead to scarce data. In Chapter 5 we dealt with scarce data through a statistical description that aggregates data across those details that are not most relevant for the question. In this case, we tailored the analysis (of existing data), model and method to the question. However, it may also be productive to re-evaluate existing methods, as we did in Chapter 3.

6.4 Revisiting the working point of neuronal systems

The debate about the dynamic working point of the brain has endured for over two decades [29]. In particular, the controversy around the critical brain hypothesis is not just caused by experimental results, but conceptual questions remain, too. How are diverging correlations near a second-order phase transition compatible with the computational requirement for reliable responses? What is the type of this transition [153, 154]? And is this even a useful question to ask, given that neural dynamics could be seen as a mere “*footprint of information processing*” [155] that allows us only indirectly to probe how brain functions arise?

6.4.1 A unified picture of neuronal avalanches

In light of the persistent controversy, the results in this thesis, and Chapter 3 in particular, add to a growing list of efforts to consolidate the differing perspectives and conflicting evidence (see e.g. [37] for a recent example). An emerging theme is that the brain’s “*working point*” is not a point. More likely, neuronal systems operate in an extended region in the (high-dimensional) vicinity of, rather than at, a critical point. Such an extended region could be created by a heterogeneous (modular-hierarchic) structure [154, 156] that is shaped through activity-dependent adaptation [98] and external input [157, 158]. Notably, this interpretation is consistent with established concepts like the neural Griffiths phase [59], dynamic adaptive computation [40], integration-segregation balance [159], or a hierarchy of timescales [160, 161] — and it is supported also by our results.

Considering the type of criticality associated to neuronal avalanches [23, 154], one controversy was stirred by contradicting experimental evidence. Because critical systems are scale-free, the size- and duration-distributions of avalanches in a critical system are expected to follow a power-law. However, although power-law distributions have become a hallmark of brain dynamics, appearing both *in vitro* and *in vivo*, exceptions have been found consistently — in particular, from spiking-data of awake cortex *in vivo* [44, 162, 163]. Due to the coarse-sampling effect (Chapter 3), this can now be unified into a consistent

picture of neuronal avalanches: On the one hand, awake cortex is likely poised in a slightly subcritical regime, flexibly tuning to task-demands while maintaining a safety-distance from instability [40]. This regime can be perturbed by neuro-modulators [164, 165], or under anesthesia—blocking relevant asynchronous thalamic input, leading to more synchronous activity [166, 167] and scale-free avalanches. On the other hand, mature *in vitro* cultures show scale-free distributions consistently, which can be explained by their lack of background input [32]. Notably, many studies reported power-law avalanches for awake animals *in vivo*, incompatible with this picture (see Table A in Appendix A for an overview). However, because many of these results derive from measures like local field potentials, they are now compatible with a subcritical cortex due to the coarse-sampling bias.

According to this perspective, when (super-) critical systems such as developing cultures are exposed to the right input, they should deviate from their characteristic bursting behavior. The idea to stimulate cultured neurons to control their emergent dynamics is not new [168–171]. However, in Chapter 4 we provided the input through precise optogenetic stimulation, which enabled us to asynchronously target individual neurons with relative ease compared to electrical methods [172]. Further, our approach mimics noisy background activity, as opposed to aiming for a stimulus-evoked response [169, 173], which further differentiates it from previous studies that used electrical stimulation and often required a closed-loop setup [170, 174].

As the core mechanism to explain the input-dependence, we proposed short-term depression [175, 176], and that the depletion of synaptic resources affects the (heterogeneously connected) neuron population unevenly. Although the short timescales of this mechanism and our experiments limit our scope to transient changes, our results still highlight the role of heterogeneous structures into which cultures grow. Here we created the heterogeneity by forcibly growing the cultures into a modular topology, which enabled noisy input to effectively act as a control parameter of synchrony.

6.4.2 Next steps

From our results, two complementary next steps arise naturally. First, given the dynamical benefits attributed to hierarchical organization [88, 177, 178], a next step will be to adapt our setup to larger networks consisting of 4×4 modules arranged into nested 2×2 rings. Our proposed mechanism should extend to those systems, and because of the hierarchical-modular structure, this setup will allow us to probe how far synchronization extends across the hierarchical levels, as a function of the asynchronous input. Embedding synchronization in the context of integration-segregation balance [159], even minute-long

stimulation should shift the cultures from an integrated state (corresponding to system-wide synchronization across the hierarchy) towards more segregated states (where the levels of modules that synchronize should depend on the input strength).

Second, the durations of our recordings were limited to several minutes. However, activity-dependent structural changes and self-organization of topology take place on longer timescales [98]. Therefore, we here constrained our scope to short-term changes of dynamics, and a predetermined topology. In a next step, optogenetic stimulation should be applied over the whole course of development. This is already being investigated in collaboration with Neef *et al.*³, and it has also been studied in the past using electrical methods e.g. to investigate learning in cultures [169, 173]. Long-term stimulation is particularly interesting because it has been suggested that the underlying structure should reflect the emergent dynamics, and, driven by long-term adaptation mechanisms, *vice versa* [32, 159, 179]. In particular, near-critical dynamics would go hand-in-hand with an underlying network structure that is also poised in-between lattice-like order and randomness. This idea invites careful speculation about tentative long-term stimulation patterns: For example, when assuming a Hebbian learning rule, an asynchronous pattern would foster long-range projections, whereas a stimulation with a wave-like pattern (mimicking network bursts or retinal waves) would foster local connections. Clearly, the required experimental setup needs to permit long-term (optogenetic) stimulation with simultaneous activity recordings, which poses tremendous engineering challenges [171]. However, these challenges are likely only addressable with *in vitro* approaches, again stressing their potential as an exciting and promising research avenue.

6.5 Conclusion and outlook

In this thesis, we investigated examples of spreading processes interacting with an underlying complex network. For a modular network of dissociated neurons *in vitro*, we showed that noisy background input can act as a *control parameter of synchrony*. As a tentative next step, future work should focus on longer timescale, tracking such a system over days and weeks to further elucidate how modular and hierarchical structures form in response to a given activity pattern (Section 6.4.2). For a temporal contact network of university students, we showed how the temporal stages of disease progression can interact with human contact patterns in a principled way. We found that real-life contact patterns can *modulate the reproduction number* (by roughly up to 30%) and pose a source of

³ Neef and colleagues have independently developed a refined *in vitro* setup and analysis pipeline, which enable long-term optical stimulation with various patterns, as well as simultaneous recordings. We are currently working together to analyze preliminary data.

over-dispersed offspring distributions that has so far received little attention in the literature. With our novel framework of encounter-trains, it will be straight-forward in future work to model contact patterns and viral heterogeneity simultaneously (Section 6.2.3). This should allow us to fully disentangle the sources that cause over-dispersion in the spread of infectious diseases, with possible implications for the design of future non-pharmaceutical interventions.

For both these phenomena, non-Markovian dynamics played a crucial role. Although we listed a few specific examples where models that take non-Markovian dynamics into account have been compared to memoryless formulations, this is still a largely unexplored field (Section 6.2). We are convinced that it will receive more attention in the future, which will lead to novel, data- and simulation-driven approaches like we demonstrated here.

Bibliography

1. S. Herculano-Houzel. “*The Human Brain in Numbers: A Linearly Scaled-up Primate Brain*”. *Frontiers in Human Neuroscience* 3 (2009): 31.
DOI: [10.3389/neuro.09.031.2009](https://doi.org/10.3389/neuro.09.031.2009)
2. A. Barrat, M. Barthélemy, and A. Vespignani. *Dynamical Processes on Complex Networks*. Cambridge University Press, Cambridge, 2008.
DOI: [10.1017/CB09780511791383](https://doi.org/10.1017/CB09780511791383)
3. M. Newman. *Networks*. Oxford University Press, Oxford, 2018.
DOI: [10.1093/oso/9780198805090.001.0001](https://doi.org/10.1093/oso/9780198805090.001.0001)
4. M. P. van den Heuvel and O. Sporns. “*Network Hubs in the Human Brain*”. *Trends in Cognitive Sciences* 17 (2013): 683–696. DOI: [10.1016/j.tics.2013.09.012](https://doi.org/10.1016/j.tics.2013.09.012)
5. D. J. Watts and S. H. Strogatz. “*Collective Dynamics of ‘Small-World’ Networks*”. *Nature* 393 (1998): 440–442. DOI: [10.1038/30918](https://doi.org/10.1038/30918)
6. S. Wasserman and K. Faust. *Social Network Analysis: Methods and Applications*. Cambridge University Press, Cambridge, 1994.
DOI: [10.1017/CB09780511815478](https://doi.org/10.1017/CB09780511815478)
7. M. E. J. Newman. “*Clustering and Preferential Attachment in Growing Networks*”. *Physical Review E* 64 (2001): 025102. DOI: [10.1103/PhysRevE.64.025102](https://doi.org/10.1103/PhysRevE.64.025102)
8. M. E. J. Newman. “*Modularity and Community Structure in Networks*”. *Proceedings of the National Academy of Sciences* 103 (2006): 8577–8582.
DOI: [10.1073/pnas.0601602103](https://doi.org/10.1073/pnas.0601602103)
9. A.-L. Barabási. *Network Science*. URL: <http://networksciencebook.com>
10. R. Pastor-Satorras, C. Castellano, P. Van Mieghem, and A. Vespignani. “*Epidemic Processes in Complex Networks*”. *Reviews of Modern Physics* 87 (2015): 925–979.
DOI: [10.1103/RevModPhys.87.925](https://doi.org/10.1103/RevModPhys.87.925)
11. H. Yamamoto *et al.* “*Impact of Modular Organization on Dynamical Richness in Cortical Networks*”. *Science Advances* 4 (2018): eaau4914.
DOI: [10.1126/sciadv.aau4914](https://doi.org/10.1126/sciadv.aau4914)

Bibliography

12. Y. Humeau and D. Choquet. “The next Generation of Approaches to Investigate the Link between Synaptic Plasticity and Learning”. *Nature Neuroscience* 22 (2019): 1536–1543. DOI: [10.1038/s41593-019-0480-6](https://doi.org/10.1038/s41593-019-0480-6)
13. A. Stopczynski, V. Sekara, P. Sapiezynski, A. Cuttone, M. M. Madsen, J. E. Larsen, and S. Lehmann. “Measuring Large-Scale Social Networks with High Resolution”. *PLoS ONE* 9 (2014): e95978. DOI: [10.1371/journal.pone.0095978](https://doi.org/10.1371/journal.pone.0095978)
14. Suryadi, R.-K. Cheng, E. Birkett, S. Jesuthasan, and L. Y. Chew. “Dynamics and Potential Significance of Spontaneous Activity in the Habenula”. *eNeuro* 9 (2022). DOI: [10.1523/ENEURO.0287-21.2022](https://doi.org/10.1523/ENEURO.0287-21.2022)
15. L. J. Fosque, A. Alipour, M. Zare, R. V. Williams-García, J. M. Beggs, and G. Ortiz. “Quasicriticality Explains Variability of Human Neural Dynamics across Life Span”. *Frontiers in Computational Neuroscience* 16 (2022): 1037550. DOI: [10.3389/fncom.2022.1037550](https://doi.org/10.3389/fncom.2022.1037550)
16. D. R. W. Burrows, G. Diana, B. Pimpel, F. Moeller, M. P. Richardson, D. S. Bassett, M. P. Meyer, and R. E. Rosch. “Microscale Neuronal Activity Collectively Drives Chaotic and Inflexible Dynamics at the Macroscale in Seizures”. *Journal of Neuroscience* 43 (2023): 3259–3283. DOI: [10.1523/JNEUROSCI.0171-22.2023](https://doi.org/10.1523/JNEUROSCI.0171-22.2023)
17. Y. Xu, A. Schneider, R. Wessel, and K. B. Hengen. “Sleep Restores an Optimal Computational Regime in Cortical Networks”. *bioRxiv*. 2023. DOI: [10.1101/2022.12.07.519478](https://doi.org/10.1101/2022.12.07.519478)
18. H. Hinrichsen. “Non-Equilibrium Critical Phenomena and Phase Transitions into Absorbing States”. *Advances in Physics* 49 (2000): 815–958. DOI: [10.1080/00018730050198152](https://doi.org/10.1080/00018730050198152)
19. M. Henkel, H. Hinrichsen, and S. Lübeck. *Non-Equilibrium Phase Transitions*. Vol. 1. Springer, Dordrecht, 2008. DOI: [10.1007/978-1-4020-8765-3](https://doi.org/10.1007/978-1-4020-8765-3)
20. M. A. Muñoz. “Colloquium: Criticality and Dynamical Scaling in Living Systems”. *Reviews of Modern Physics* 90 (2018): 031001. DOI: [10.1103/RevModPhys.90.031001](https://doi.org/10.1103/RevModPhys.90.031001)
21. J. Zierenberg, J. Wiltig, V. Priesemann, and A. Levina. “Description of Spreading Dynamics by Microscopic Network Models and Macroscopic Branching Processes Can Differ Due to Coalescence”. *Physical Review E* 101 (2020): 022301. DOI: [10.1103/PhysRevE.101.022301](https://doi.org/10.1103/PhysRevE.101.022301)
22. T. E. Harris. *The Theory of Branching Processes*. Springer, Berlin, 1963. URL: <https://www.springer.com/gp/book/9783642518683>

23. J. M. Beggs and D. Plenz. “Neuronal Avalanches in Neocortical Circuits”. *Journal of Neuroscience* 23 (2003): 11167–11177.
DOI: [10.1523/JNEUROSCI.23-35-11167.2003](https://doi.org/10.1523/JNEUROSCI.23-35-11167.2003)
24. S. E. Cavanagh, J. P. Towers, J. D. Wallis, L. T. Hunt, and S. W. Kennerley. “Reconciling Persistent and Dynamic Hypotheses of Working Memory Coding in Prefrontal Cortex”. *Nature Communications* 9 (2018): 3498.
DOI: [10.1038/s41467-018-05873-3](https://doi.org/10.1038/s41467-018-05873-3)
25. D. F. Wasmuht, E. Spaak, T. J. Buschman, E. K. Miller, and M. G. Stokes. “Intrinsic Neuronal Dynamics Predict Distinct Functional Roles during Working Memory”. *Nature Communications* 9 (2018): 3499. DOI: [10.1038/s41467-018-05961-4](https://doi.org/10.1038/s41467-018-05961-4)
26. C. G. Langton. “Computation at the Edge of Chaos: Phase Transitions and Emergent Computation”. *Physica D: Nonlinear Phenomena* 42 (1990): 12–37.
DOI: [10.1016/0167-2789\(90\)90064-V](https://doi.org/10.1016/0167-2789(90)90064-V)
27. C. Meisel, A. Klaus, V. V. Vyazovskiy, and D. Plenz. “The Interplay between Long- and Short-Range Temporal Correlations Shapes Cortex Dynamics across Vigilance States”. *The Journal of Neuroscience* 37 (2017): 10114–10124.
DOI: [10.1523/JNEUROSCI.0448-17.2017](https://doi.org/10.1523/JNEUROSCI.0448-17.2017)
28. K. Linkenkaer-Hansen, V. V. Nikouline, J. M. Palva, and R. J. Ilmoniemi. “Long-Range Temporal Correlations and Scaling Behavior in Human Brain Oscillations”. *Journal of Neuroscience* 21 (2001): 1370–1377.
DOI: [10.1523/JNEUROSCI.21-04-01370.2001](https://doi.org/10.1523/JNEUROSCI.21-04-01370.2001)
29. J. Wilting and V. Priesemann. “25 Years of Criticality in Neuroscience — Established Results, Open Controversies, Novel Concepts”. *Current Opinion in Neurobiology* 58 (2019): 105–111. DOI: [10.1016/j.conb.2019.08.002](https://doi.org/10.1016/j.conb.2019.08.002)
30. B. Cramer, D. Stöckel, M. Kreft, M. Wibral, J. Schemmel, K. Meier, and V. Priesemann. “Control of Criticality and Computation in Spiking Neuromorphic Networks with Plasticity”. *Nature Communications* 11 (2020): 2853.
DOI: [10.1038/s41467-020-16548-3](https://doi.org/10.1038/s41467-020-16548-3)
31. D. R. Chialvo. “Emergent Complex Neural Dynamics”. *Nature Physics* 6 (2010): 744–750. DOI: [10.1038/nphys1803](https://doi.org/10.1038/nphys1803)
32. J. Hesse and T. Gross. “Self-Organized Criticality as a Fundamental Property of Neural Systems”. *Frontiers in Systems Neuroscience* 8 (2014): 166.
DOI: [10.3389/fnsys.2014.00166](https://doi.org/10.3389/fnsys.2014.00166)

Bibliography

33. L. Cocchi, L. L. Gollo, A. Zalesky, and M. Breakspear. “Criticality in the Brain: A Synthesis of Neurobiology, Models and Cognition”. *Progress in Neurobiology* 158 (2017): 132–152. DOI: [10.1016/j.pneurobio.2017.07.002](https://doi.org/10.1016/j.pneurobio.2017.07.002)
34. J. M. Beggs. “The Critically Tuned Cortex”. *Neuron* 104 (2019): 623–624. DOI: [10.1016/j.neuron.2019.10.039](https://doi.org/10.1016/j.neuron.2019.10.039)
35. N. Tomen, J. M. Herrmann, and U. Ernst, eds. *The Functional Role of Critical Dynamics in Neural Systems*. Springer, Cham, 2019. DOI: [10.1007/978-3-030-20965-0](https://doi.org/10.1007/978-3-030-20965-0)
36. V. Zimmern. “Why Brain Criticality Is Clinically Relevant: A Scoping Review”. *Frontiers in Neural Circuits* 14 (2020): 54. DOI: [10.3389/fncir.2020.00054](https://doi.org/10.3389/fncir.2020.00054)
37. S. A. Jones, J. H. Barfield, V. K. Norman, and W. L. Shew. “Scale-Free Behavioral Dynamics Directly Linked with Scale-Free Cortical Dynamics”. *eLife* 12 (2023): e79950. DOI: [10.7554/eLife.79950](https://doi.org/10.7554/eLife.79950)
38. C. Haldeman and J. M. Beggs. “Critical Branching Captures Activity in Living Neural Networks and Maximizes the Number of Metastable States”. *Physical Review Letters* 94 (2005): 058101. DOI: [10.1103/PhysRevLett.94.058101](https://doi.org/10.1103/PhysRevLett.94.058101)
39. L. L. Gollo. “Coexistence of Critical Sensitivity and Subcritical Specificity Can Yield Optimal Population Coding”. *Journal of The Royal Society Interface* 14 (2017): 20170207. DOI: [10.1098/rsif.2017.0207](https://doi.org/10.1098/rsif.2017.0207)
40. J. Wilting, J. Dehning, J. Pinheiro Neto, L. Rudelt, M. Wibral, J. Zierenberg, and V. Priesemann. “Operating in a Reverberating Regime Enables Rapid Tuning of Network States to Task Requirements”. *Frontiers in Systems Neuroscience* 12 (2018): 55. DOI: [10.3389/fnsys.2018.00055](https://doi.org/10.3389/fnsys.2018.00055)
41. S. Azizpour, V. Priesemann, J. Zierenberg, and A. Levina. “Available Observation Time Regulates Optimal Balance between Sensitivity and Confidence”. arXiv. 2023. DOI: [10.48550/arXiv.2307.07794](https://doi.org/10.48550/arXiv.2307.07794)
42. M. Scheffer *et al.* “Anticipating Critical Transitions”. *Science* 338 (2012): 344–348. DOI: [10.1126/science.1225244](https://doi.org/10.1126/science.1225244)
43. J. Wilting and V. Priesemann. “Between Perfectly Critical and Fully Irregular: A Reverberating Model Captures and Predicts Cortical Spike Propagation”. *Cerebral Cortex* 29 (2019): 2759–2770. DOI: [10.1093/cercor/bhz049](https://doi.org/10.1093/cercor/bhz049)

44. V. Priesemann, M. Wibral, M. Valderrama, R. Pröpper, M. Le Van Quyen, T. Geisel, J. Triesch, D. Nikolić, and M. H. J. Munk. “Spike Avalanches in Vivo Suggest a Driven, Slightly Subcritical Brain State”. *Frontiers in Systems Neuroscience* 8 (2014): 108. DOI: [10.3389/fnsys.2014.00108](https://doi.org/10.3389/fnsys.2014.00108)
45. D. Braess. “Über ein Paradoxon aus der Verkehrsplanung”. *Unternehmensforschung* 12 (1968): 258–268. DOI: [10.1007/BF01918335](https://doi.org/10.1007/BF01918335)
46. B. Schäfer, T. Pesch, D. Manik, J. Gollenstede, G. Lin, H.-P. Beck, D. Witthaut, and M. Timme. “Understanding Braess’ Paradox in Power Grids”. *Nature Communications* 13 (2022): 5396. DOI: [10.1038/s41467-022-32917-6](https://doi.org/10.1038/s41467-022-32917-6)
47. K. Zilles and K. Amunts. “Anatomical Basis for Functional Specialization”. In: *fMRI: From Nuclear Spins to Brain Functions*. Springer, Boston, 2015: 27–66. DOI: [10.1007/978-1-4899-7591-1_4](https://doi.org/10.1007/978-1-4899-7591-1_4)
48. K. Amunts and K. Zilles. “Architectonic Mapping of the Human Brain beyond Brodmann”. *Neuron* 88 (2015): 1086–1107. DOI: [10.1016/j.neuron.2015.12.001](https://doi.org/10.1016/j.neuron.2015.12.001)
49. K. Brodman. *Vergleichende Lokalisationslehre der Grosshirnrinde*. Barth, Leipzig, 1909.
50. B. G. Rash and E. A. Grove. “Area and Layer Patterning in the Developing Cerebral Cortex”. *Current Opinion in Neurobiology* 16 (2006): 25–34. DOI: [10.1016/j.conb.2006.01.004](https://doi.org/10.1016/j.conb.2006.01.004)
51. M. E. Larkum, L. S. Petro, R. N. S. Sachdev, and L. Muckli. “A Perspective on Cortical Layering and Layer-Spanning Neuronal Elements”. *Frontiers in Neuroanatomy* 12 (2018): 56. DOI: [10.3389/fnana.2018.00056](https://doi.org/10.3389/fnana.2018.00056)
52. V. B. Mountcastle. “The Columnar Organization of the Neocortex.” *Brain* 120 (1997): 701–722. DOI: [10.1093/brain/120.4.701](https://doi.org/10.1093/brain/120.4.701)
53. B. J. Molyneaux, P. Arlotta, J. R. L. Menezes, and J. D. Macklis. “Neuronal Subtype Specification in the Cerebral Cortex”. *Nature Reviews Neuroscience* 8 (2007): 427–437. DOI: [10.1038/nrn2151](https://doi.org/10.1038/nrn2151)
54. S. Lodato and P. Arlotta. “Generating Neuronal Diversity in the Mammalian Cerebral Cortex”. *Annual review of cell and developmental biology* 31 (2015): 699–720. DOI: [10.1146/annurev-cellbio-100814-125353](https://doi.org/10.1146/annurev-cellbio-100814-125353)
55. S. Genon, S. B. Eickhoff, and S. Kharabian. “Linking Interindividual Variability in Brain Structure to Behaviour”. *Nature Reviews Neuroscience* 23 (2022): 307–318. DOI: [10.1038/s41583-022-00584-7](https://doi.org/10.1038/s41583-022-00584-7)

Bibliography

56. T. A. Machado, I. V. Kauvar, and K. Deisseroth. “Multiregion Neuronal Activity: The Forest and the Trees”. *Nature Reviews Neuroscience* 23 (2022): 683–704.
DOI: [10.1038/s41583-022-00634-0](https://doi.org/10.1038/s41583-022-00634-0)
57. R. Chaudhuri, K. Knoblauch, M.-A. Gariel, H. Kennedy, and X.-J. Wang. “A Large-Scale Circuit Mechanism for Hierarchical Dynamical Processing in the Primate Cortex”. *Neuron* 88 (2015): 419–431. DOI: [10.1016/j.neuron.2015.09.008](https://doi.org/10.1016/j.neuron.2015.09.008)
58. M. Rubinov, O. Sporns, J.-P. Thivierge, and M. Breakspear. “Neurobiologically Realistic Determinants of Self-Organized Criticality in Networks of Spiking Neurons”. *PLoS Computational Biology* 7 (2011): e1002038.
DOI: [10.1371/journal.pcbi.1002038](https://doi.org/10.1371/journal.pcbi.1002038)
59. P. Moretti and M. A. Muñoz. “Griffiths Phases and the Stretching of Criticality in Brain Networks”. *Nature Communications* 4 (2013): 2521.
DOI: [10.1038/ncomms3521](https://doi.org/10.1038/ncomms3521)
60. S. Valverde, S. Ohse, M. Turalska, B. J. West, and J. Garcia-Ojalvo. “Structural Determinants of Criticality in Biological Networks”. *Frontiers in Physiology* 6 (2015): 127. DOI: [10.3389/fphys.2015.00127](https://doi.org/10.3389/fphys.2015.00127)
61. T. Vojta. “Rare Region Effects at Classical, Quantum and Nonequilibrium Phase Transitions”. *Journal of Physics A: Mathematical and General* 39 (2006): R143.
DOI: [10.1088/0305-4470/39/22/R01](https://doi.org/10.1088/0305-4470/39/22/R01)
62. R. B. Griffiths. “Nonanalytic Behavior Above the Critical Point in a Random Ising Ferromagnet”. *Physical Review Letters* 23 (1969): 17–19.
DOI: [10.1103/PhysRevLett.23.17](https://doi.org/10.1103/PhysRevLett.23.17)
63. M. A. Muñoz, R. Juhász, C. Castellano, and G. Ódor. “Griffiths Phases on Complex Networks”. *Physical Review Letters* 105 (2010): 128701.
DOI: [10.1103/PhysRevLett.105.128701](https://doi.org/10.1103/PhysRevLett.105.128701)
64. P. G. Nelson. “Nerve and Muscle Cells in Culture”. *Physiological Reviews* 55 (1975): 1–61. DOI: [10.1152/physrev.1975.55.1.1](https://doi.org/10.1152/physrev.1975.55.1.1)
65. M. Chiappalone, V. Pasquale, and M. Frega. *In Vitro Neuronal Networks: From Culturing Methods to Neuro-Technological Applications*. Springer, Cham, 2019.
DOI: [10.1007/978-3-030-11135-9](https://doi.org/10.1007/978-3-030-11135-9)
66. O. P. Hamill, A. Marty, E. Neher, B. Sakmann, and F. J. Sigworth. “Improved Patch-Clamp Techniques for High-Resolution Current Recording from Cells and Cell-Free Membrane Patches”. *Pflügers Archiv* 391 (1981): 85–100.
DOI: [10.1007/BF00656997](https://doi.org/10.1007/BF00656997)

67. B. Sakmann and E. Neher. "Patch Clamp Techniques for Studying Ionic Channels in Excitable Membranes". *Annual Review of Physiology* 46 (1984): 455–472.
DOI: [10.1146/annurev.ph.46.030184.002323](https://doi.org/10.1146/annurev.ph.46.030184.002323)
68. J. Pine. "A History of MEA Development". In: *Advances in Network Electrophysiology: Using Multi-Electrode Arrays*. Springer, Boston, 2006: 3–23.
DOI: [10.1007/0-387-25858-2_1](https://doi.org/10.1007/0-387-25858-2_1)
69. C. Grienberger, A. Giovannucci, W. Zeiger, and C. Portera-Cailliau. "Two-Photon Calcium Imaging of Neuronal Activity". *Nature Reviews Methods Primers* 2 (2022): 1–23. DOI: [10.1038/s43586-022-00147-1](https://doi.org/10.1038/s43586-022-00147-1)
70. N. Sukenik, O. Vinogradov, E. Weinreb, M. Segal, A. Levina, and E. Moses. "Neuronal Circuits Overcome Imbalance in Excitation and Inhibition by Adjusting Connection Numbers". *Proceedings of the National Academy of Sciences* 118 (2021): e2018459118. DOI: [10.1073/pnas.2018459118](https://doi.org/10.1073/pnas.2018459118)
71. D. A. Wagenaar, J. Pine, and S. M. Potter. "An Extremely Rich Repertoire of Bursting Patterns during the Development of Cortical Cultures". *BMC Neuroscience* 7 (2006): 11. DOI: [10.1186/1471-2202-7-11](https://doi.org/10.1186/1471-2202-7-11)
72. J. van Pelt, I. Vajda, P. S. Wolters, M. A. Corner, and G. J. A. Ramakers. "Dynamics and Plasticity in Developing Neuronal Networks in Vitro". In: *Progress in Brain Research*. Vol. 147. Elsevier, 2005: 171–188.
DOI: [10.1016/S0079-6123\(04\)47013-7](https://doi.org/10.1016/S0079-6123(04)47013-7)
73. M. Chiappalone, M. Bove, A. Vato, M. Tedesco, and S. Martinoia. "Dissociated Cortical Networks Show Spontaneously Correlated Activity Patterns during in Vitro Development". *Brain Research* 1093 (2006): 41–53.
DOI: [10.1016/j.brainres.2006.03.049](https://doi.org/10.1016/j.brainres.2006.03.049)
74. C. Tetzlaff, S. Okujeni, U. Egert, F. Wörgötter, and M. Butz. "Self-Organized Criticality in Developing Neuronal Networks". *PLoS Computational Biology* 6 (2010): e1001013. DOI: [10.1371/journal.pcbi.1001013](https://doi.org/10.1371/journal.pcbi.1001013)
75. J. Pu, H. Gong, X. Li, and Q. Luo. "Developing Neuronal Networks: Self-organized Criticality Predicts the Future". *Scientific Reports* 3 (2013): 1081.
DOI: [10.1038/srep01081](https://doi.org/10.1038/srep01081)
76. E. Tibau, M. Valencia, and J. Soriano. "Identification of Neuronal Network Properties from the Spectral Analysis of Calcium Imaging Signals in Neuronal Cultures". *Frontiers in Neural Circuits* 7 (2013): 199.
DOI: [10.3389/fncir.2013.00199](https://doi.org/10.3389/fncir.2013.00199)

Bibliography

77. S. Teller, C. Granell, M. De Domenico, J. Soriano, S. Gómez, and A. Arenas. “Emergence of Assortative Mixing between Clusters of Cultured Neurons”. *PLoS Computational Biology* 10 (2014): e1003796.
DOI: [10.1371/journal.pcbi.1003796](https://doi.org/10.1371/journal.pcbi.1003796)
78. S. Okujeni, S. Kandler, and U. Egert. “Mesoscale Architecture Shapes Initiation and Richness of Spontaneous Network Activity”. *Journal of Neuroscience* 37 (2017): 3972–3987. DOI: [10.1523/JNEUROSCI.2552-16.2017](https://doi.org/10.1523/JNEUROSCI.2552-16.2017)
79. E. Tibau, A.-A. Ludl, S. Rüdiger, J. G. Orlandi, and J. Soriano. “Neuronal Spatial Arrangement Shapes Effective Connectivity Traits of in Vitro Cortical Networks”. *IEEE Transactions on Network Science and Engineering* 7 (2020): 435–448.
DOI: [10.1109/TNSE.2018.2862919](https://doi.org/10.1109/TNSE.2018.2862919)
80. I. Breskin, J. Soriano, E. Moses, and T. Tlusty. “Percolation in Living Neural Networks”. *Physical Review Letters* 97 (2006): 188102.
DOI: [10.1103/PhysRevLett.97.188102](https://doi.org/10.1103/PhysRevLett.97.188102)
81. J. Eckmann, O. Feinerman, L. Gruendlinger, E. Moses, J. Soriano, and T. Tlusty. “The Physics of Living Neural Networks”. *Physics Reports* 449 (2007): 54–76.
DOI: [10.1016/j.physrep.2007.02.014](https://doi.org/10.1016/j.physrep.2007.02.014)
82. J. Soriano, M. R. Martínez, T. Tlusty, and E. Moses. “Development of Input Connections in Neural Cultures”. *Proceedings of the National Academy of Sciences* 105 (2008): 13758–13763. DOI: [10.1073/pnas.0707492105](https://doi.org/10.1073/pnas.0707492105)
83. J. G. Orlandi, J. Soriano, E. Alvarez-Lacalle, S. Teller, and J. Casademunt. “Noise Focusing and the Emergence of Coherent Activity in Neuronal Cultures”. *Nature Physics* 9 (2013): 582–590. DOI: [10.1038/nphys2686](https://doi.org/10.1038/nphys2686)
84. D. Lonardoni, H. Amin, S. D. Marco, A. Maccione, L. Berdondini, and T. Nieuw. “Recurrently Connected and Localized Neuronal Communities Initiate Coordinated Spontaneous Activity in Neuronal Networks”. *PLoS Computational Biology* 13 (2017): e1005672. DOI: [10.1371/journal.pcbi.1005672](https://doi.org/10.1371/journal.pcbi.1005672)
85. O. Feinerman and E. Moses. “Transport of Information along Unidimensional Layered Networks of Dissociated Hippocampal Neurons and Implications for Rate Coding”. *Journal of Neuroscience* 26 (2006): 4526–4534.
DOI: [10.1523/JNEUROSCI.4692-05.2006](https://doi.org/10.1523/JNEUROSCI.4692-05.2006)
86. O. Feinerman, A. Rotem, and E. Moses. “Reliable Neuronal Logic Devices from Patterned Hippocampal Cultures”. *Nature Physics* 4 (2008): 967–973.
DOI: [10.1038/nphys1099](https://doi.org/10.1038/nphys1099)

87. I. Baruchi, V. Volman, N. Raichman, M. Shein, and E. Ben-Jacob. “The Emergence and Properties of Mutual Synchronization in *in Vitro* Coupled Cortical Networks”. *European Journal of Neuroscience* 28 (2008): 1825–1835.
DOI: [10.1111/j.1460-9568.2008.06487.x](https://doi.org/10.1111/j.1460-9568.2008.06487.x)
88. M. A. Rabadan *et al.* “An *in Vitro* Model of Neuronal Ensembles”. *Nature Communications* 13 (2022): 3340. DOI: [10.1038/s41467-022-31073-1](https://doi.org/10.1038/s41467-022-31073-1)
89. J. Barral, X.-J. Wang, and A. D. Reyes. “Propagation of Temporal and Rate Signals in Cultured Multilayer Networks”. *Nature Communications* 10 (2019): 3969.
DOI: [10.1038/s41467-019-11851-0](https://doi.org/10.1038/s41467-019-11851-0)
90. V. Pasquale, P. Massobrio, L. L. Bologna, M. Chiappalone, and S. Martinoia. “Self-Organization and Neuronal Avalanches in Networks of Dissociated Cortical Neurons”. *Neuroscience* 153 (2008): 1354–1369.
DOI: [10.1016/j.neuroscience.2008.03.050](https://doi.org/10.1016/j.neuroscience.2008.03.050)
91. A. Levina and V. Priesemann. “Subsampling Scaling”. *Nature Communications* 8 (2017): 15140. DOI: [10.1038/ncomms15140](https://doi.org/10.1038/ncomms15140)
92. S. Okujeni and U. Egert. “Structural Modularity Tunes Mesoscale Criticality in Biological Neuronal Networks”. *Journal of Neuroscience* 43 (2023): 2515–2526.
DOI: [10.1523/JNEUROSCI.1420-22.2023](https://doi.org/10.1523/JNEUROSCI.1420-22.2023)
93. J. H. Downes, M. W. Hammond, D. Xydas, M. C. Spencer, V. M. Becerra, K. Warwick, B. J. Whalley, and S. J. Nasuto. “Emergence of a Small-World Functional Network in Cultured Neurons”. *PLoS Computational Biology* 8 (2012): e1002522. DOI: [10.1371/journal.pcbi.1002522](https://doi.org/10.1371/journal.pcbi.1002522)
94. M. Ichikawa, K. Muramoto, K. Kobayashi, M. Kawahara, and Y. Kuroda. “Formation and Maturation of Synapses in Primary Cultures of Rat Cerebral Cortical Cells: An Electron Microscopic Study”. *Neuroscience Research* 16 (1993): 95–103. DOI: [10.1016/0168-0102\(93\)90076-3](https://doi.org/10.1016/0168-0102(93)90076-3)
95. K. Muramoto, M. Ichikawa, M. Kawahara, K. Kobayashi, and Y. Kuroda. “Frequency of Synchronous Oscillations of Neuronal Activity Increases during Development and Is Correlated to the Number of Synapses in Cultured Cortical Neuron Networks”. *Neuroscience Letters* 163 (1993): 163–165.
DOI: [10.1016/0304-3940\(93\)90372-R](https://doi.org/10.1016/0304-3940(93)90372-R)
96. Y. Penn, M. Segal, and E. Moses. “Network Synchronization in Hippocampal Neurons”. *Proceedings of the National Academy of Sciences* 113 (2016): 3341–3346.
DOI: [10.1073/pnas.1515105113](https://doi.org/10.1073/pnas.1515105113)

Bibliography

97. P. C. Antonello, T. F. Varley, J. Beggs, M. Porcionatto, O. Sporns, and J. Faber. “Self-Organization of *in Vitro* Neuronal Assemblies Drives to Complex Network Topology”. *eLife* 11 (2022): e74921. DOI: [10.7554/eLife.74921](https://doi.org/10.7554/eLife.74921)
98. S. Okujeni and U. Egert. “Self-Organization of Modular Network Architecture by Activity-Dependent Neuronal Migration and Outgrowth”. *eLife* 8 (2019): e47996. DOI: [10.7554/eLife.47996](https://doi.org/10.7554/eLife.47996)
99. P. Dayan and L. F. Abbott. *Theoretical Neuroscience: Computational and Mathematical Modeling of Neural Systems*. MIT press, Cambridge, 2001.
100. A. R. McFarlan, C. Y. C. Chou, A. Watanabe, N. Cherepacha, M. Haddad, H. Owens, and P. J. Sjöström. “The Plasticitome of Cortical Interneurons”. *Nature Reviews Neuroscience* 24 (2023): 80–97. DOI: [10.1038/s41583-022-00663-9](https://doi.org/10.1038/s41583-022-00663-9)
101. D. O. Hebb. *The Organization of Behavior: A Neuropsychological Theory*. Wiley, New York, 1949.
102. C. J. Shatz. “The Developing Brain”. *Scientific American* 267 (1992): 60–67. URL: <https://www.jstor.org/stable/24939213>
103. H. Markram, W. Gerstner, and P. J. Sjöström. “A History of Spike-Timing-Dependent Plasticity”. *Frontiers in Synaptic Neuroscience* 3 (2011): 4. DOI: [10.3389/fnsyn.2011.00004](https://doi.org/10.3389/fnsyn.2011.00004)
104. D. A. Arroyo and M. B. Feller. “Spatiotemporal Features of Retinal Waves Instruct the Wiring of the Visual Circuitry”. *Frontiers in Neural Circuits* 10 (2016): 54. DOI: [10.3389/fncir.2016.00054](https://doi.org/10.3389/fncir.2016.00054)
105. J. B. Ackman, T. J. Burbridge, and M. C. Crair. “Retinal Waves Coordinate Patterned Activity throughout the Developing Visual System”. *Nature* 490 (2012): 219–225. DOI: [10.1038/nature11529](https://doi.org/10.1038/nature11529)
106. D. Stellwagen and C. J. Shatz. “An Instructive Role for Retinal Waves in the Development of Retinogeniculate Connectivity”. *Neuron* 33 (2002): 357–367. DOI: [10.1016/S0896-6273\(02\)00577-9](https://doi.org/10.1016/S0896-6273(02)00577-9)
107. M. Loidolt, L. Rudelt, and V. Priesemann. “Sequence Memory in Recurrent Neuronal Network Can Develop without Structured Input”. *bioRxiv*. 2020. DOI: [10.1101/2020.09.15.297580](https://doi.org/10.1101/2020.09.15.297580)
108. R. M. Bruno and B. Sakmann. “Cortex Is Driven by Weak but Synchronously Active Thalamocortical Synapses”. *Science* 312 (2006): 1622–1627. DOI: [10.1126/science.1124593](https://doi.org/10.1126/science.1124593)

109. K. Cohen-Kashi Malina, B. Mohar, A. N. Rappaport, and I. Lampl. “Local and Thalamic Origins of Correlated Ongoing and Sensory-Evoked Cortical Activities”. *Nature Communications* 7 (2016): 12740. DOI: [10.1038/ncomms12740](https://doi.org/10.1038/ncomms12740)
110. H. Mizuno, K. Ikezoe, S. Nakazawa, T. Sato, K. Kitamura, and T. Iwasato. “Patchwork-Type Spontaneous Activity in Neonatal Barrel Cortex Layer 4 Transmitted via Thalamocortical Projections”. *Cell Reports* 22 (2018): 123–135. DOI: [10.1016/j.celrep.2017.12.012](https://doi.org/10.1016/j.celrep.2017.12.012)
111. D. Easley and J. Kleinberg. *Networks, Crowds, and Markets: Reasoning about a Highly Connected World*. Cambridge University Press, Cambridge, 2010. DOI: [10.1017/CB09780511761942](https://doi.org/10.1017/CB09780511761942)
112. J. Guare. *Six Degrees of Separation: A Play*. Vintage, New York, 1990.
113. S. Milgram. “The Small World Problem”. *Psychology Today* 1 (1967): 60–67.
114. M. Newman, A.-L. Barabási, and D. Watts, eds. *The Structure and Dynamics of Networks*. Princeton University Press, Princeton, 2006. DOI: [10.1515/9781400841356](https://doi.org/10.1515/9781400841356)
115. P. Mac Carron, K. Kaski, and R. Dunbar. “Calling Dunbar’s Numbers”. *Social Networks* 47 (2016): 151–155. DOI: [10.1016/j.socnet.2016.06.003](https://doi.org/10.1016/j.socnet.2016.06.003)
116. A.-L. Barabási and R. Albert. “Emergence of Scaling in Random Networks”. *Science* 286 (1999): 509–512. DOI: [10.1126/science.286.5439.509](https://doi.org/10.1126/science.286.5439.509)
117. A. V. Goltsev, S. N. Dorogovtsev, J. G. Oliveira, and J. F. F. Mendes. “Localization and Spreading of Diseases in Complex Networks”. *Physical Review Letters* 109 (2012): 128702. DOI: [10.1103/PhysRevLett.109.128702](https://doi.org/10.1103/PhysRevLett.109.128702)
118. M. Kitsak, L. K. Gallos, S. Havlin, F. Liljeros, L. Muchnik, H. E. Stanley, and H. A. Makse. “Identification of Influential Spreaders in Complex Networks”. *Nature Physics* 6 (2010): 888–893. DOI: [10.1038/nphys1746](https://doi.org/10.1038/nphys1746)
119. Y. Ge, Z. Song, X. Qiu, H. Song, and Y. Wang. “Modular and Hierarchical Structure of Social Contact Networks”. *Physica A: Statistical Mechanics and its Applications* 392 (2013): 4619–4628. DOI: [10.1016/j.physa.2013.05.051](https://doi.org/10.1016/j.physa.2013.05.051)
120. A. Clauset, C. Moore, and M. E. J. Newman. “Hierarchical Structure and the Prediction of Missing Links in Networks”. *Nature* 453 (2008): 98–101. DOI: [10.1038/nature06830](https://doi.org/10.1038/nature06830)

Bibliography

121. G. Palla, I. Derényi, I. Farkas, and T. Vicsek. “Uncovering the Overlapping Community Structure of Complex Networks in Nature and Society”. *Nature* 435 (2005): 814–818. DOI: [10.1038/nature03607](https://doi.org/10.1038/nature03607)
122. Y.-Y. Ahn, J. P. Bagrow, and S. Lehmann. “Link Communities Reveal Multiscale Complexity in Networks”. *Nature* 466 (2010): 761–764. DOI: [10.1038/nature09182](https://doi.org/10.1038/nature09182)
123. P. Holme. “Modern Temporal Network Theory: A Colloquium”. *The European Physical Journal B* 88 (2015): 234. DOI: [10.1140/epjb/e2015-60657-4](https://doi.org/10.1140/epjb/e2015-60657-4)
124. G. Palla, A.-L. Barabási, and T. Vicsek. “Quantifying Social Group Evolution”. *Nature* 446 (2007): 664–667. DOI: [10.1038/nature05670](https://doi.org/10.1038/nature05670)
125. V. Sekara, A. Stopczynski, and S. Lehmann. “Fundamental Structures of Dynamic Social Networks”. *Proceedings of the National Academy of Sciences* 113 (2016): 9977–9982. DOI: [10.1073/pnas.1602803113](https://doi.org/10.1073/pnas.1602803113)
126. C. Song, Z. Qu, N. Blumm, and A.-L. Barabási. “Limits of Predictability in Human Mobility”. *Science* 327 (2010): 1018–1021. DOI: [10.1126/science.1177170](https://doi.org/10.1126/science.1177170)
127. P. Brémaud. *Markov Chains: Gibbs Fields, Monte Carlo Simulation, and Queues*. Springer, Cham, 2001. DOI: [10.1007/978-3-030-45982-6](https://doi.org/10.1007/978-3-030-45982-6)
128. B. P. Bean. “The Action Potential in Mammalian Central Neurons”. *Nature Reviews Neuroscience* 8 (2007): 451–465. DOI: [10.1038/nrn2148](https://doi.org/10.1038/nrn2148)
129. E. Herrera-Delgado and P. Sollich. “The Nonlinearity of Life”. *Europhysics News* 51 (2020): 35–37. DOI: [10.1051/ePN/2020506](https://doi.org/10.1051/ePN/2020506)
130. H.-P. Breuer, E.-M. Laine, J. Piilo, and B. Vacchini. “Colloquium: Non-Markovian Dynamics in Open Quantum Systems”. *Reviews of Modern Physics* 88 (2016): 021002. DOI: [10.1103/RevModPhys.88.021002](https://doi.org/10.1103/RevModPhys.88.021002)
131. T. Guérin, O. Bénichou, and R. Voituriez. “Non-Markovian Polymer Reaction Kinetics”. *Nature Chemistry* 4 (2012): 568–573. DOI: [10.1038/nchem.1378](https://doi.org/10.1038/nchem.1378)
132. A. Gabrielli, J. Talbot, and P. Viot. “Non-Markovian Models of Blocking in Concurrent and Countercurrent Flows”. *Physical Review Letters* 110 (2013): 170601. DOI: [10.1103/PhysRevLett.110.170601](https://doi.org/10.1103/PhysRevLett.110.170601)
133. I. Scholtes, N. Wider, R. Pfitzner, A. Garas, C. J. Tessone, and F. Schweitzer. “Causality-Driven Slow-down and Speed-up of Diffusion in Non-Markovian Temporal Networks”. *Nature Communications* 5 (2014): 5024. DOI: [10.1038/ncomms6024](https://doi.org/10.1038/ncomms6024)

134. D. Lando and T. M. Skødeberg. “Analyzing Rating Transitions and Rating Drift with Continuous Observations”. *Journal of Banking & Finance* 26 (2002): 423–444.
DOI: [10.1016/S0378-4266\(01\)00228-X](https://doi.org/10.1016/S0378-4266(01)00228-X)
135. A. M. Clarke, J. Friedrich, E. M. Tartaglia, S. Marchesotti, W. Senn, and M. H. Herzog. “Human and Machine Learning in Non-Markovian Decision Making”. *PLoS ONE* 10 (2015): e0123105.
DOI: [10.1371/journal.pone.0123105](https://doi.org/10.1371/journal.pone.0123105)
136. M. Feng, S.-M. Cai, M. Tang, and Y.-C. Lai. “Equivalence and Its Invalidation between Non-Markovian and Markovian Spreading Dynamics on Complex Networks”. *Nature Communications* 10 (2019): 3748.
DOI: [10.1038/s41467-019-11763-z](https://doi.org/10.1038/s41467-019-11763-z)
137. J. Wilting and V. Priesemann. “Inferring Collective Dynamical States from Widely Unobserved Systems”. *Nature Communications* 9 (2018): 2325.
DOI: [10.1038/s41467-018-04725-4](https://doi.org/10.1038/s41467-018-04725-4)
138. P. L. Delamater, E. J. Street, T. F. Leslie, Y. T. Yang, and K. H. Jacobsen. “Complexity of the Basic Reproduction Number (R_0)”. *Emerging infectious diseases* 25 (2019): 1–4. DOI: [10.3201/eid2501.171901](https://doi.org/10.3201/eid2501.171901)
139. J. O. Lloyd-Smith, S. J. Schreiber, P. E. Kopp, and W. M. Getz. “Superspreading and the Effect of Individual Variation on Disease Emergence”. *Nature* 438 (2005): 355–359. DOI: [10.1038/nature04153](https://doi.org/10.1038/nature04153)
140. J. O. Lloyd-Smith. “Maximum Likelihood Estimation of the Negative Binomial Dispersion Parameter for Highly Overdispersed Data, with Applications to Infectious Diseases”. *PLoS ONE* 2 (2007): e180. DOI: [10.1371/journal.pone.0000180](https://doi.org/10.1371/journal.pone.0000180)
141. K. Sneppen, B. F. Nielsen, R. J. Taylor, and L. Simonsen. “Overdispersion in COVID-19 Increases the Effectiveness of Limiting Nonrepetitive Contacts for Transmission Control”. *Proceedings of the National Academy of Sciences* 118 (2021): e2016623118. DOI: [10.1073/pnas.2016623118](https://doi.org/10.1073/pnas.2016623118)
142. Y. Liu, A. A. Gayle, A. Wilder-Smith, and J. Rocklöv. “The Reproductive Number of COVID-19 Is Higher Compared to SARS Coronavirus”. *Journal of Travel Medicine* 27 (2020): taaa021. DOI: [10.1093/jtm/taaa021](https://doi.org/10.1093/jtm/taaa021)
143. Z. Zhou, M. Serafino, L. Cohan, G. Caldarelli, and H. A. Makse. “Why Polls Fail to Predict Elections”. *Journal of Big Data* 8 (2021): 1–28.
DOI: [10.1186/s40537-021-00525-8](https://doi.org/10.1186/s40537-021-00525-8)

Bibliography

144. M. Mäs. “Analytical Sociology and Complexity Research”. In: *Research Handbook on Analytical Sociology*. Edward Elgar Publishing, Northampton, 2021: 100–118. DOI: [10.4337/9781789906851.00011](https://doi.org/10.4337/9781789906851.00011)
145. D. Helbing. “Agent-Based Modeling”. In: *Social Self-Organization: Agent-Based Simulations and Experiments to Study Emergent Social Behavior*. Springer, Berlin, 2012: 25–70. DOI: [10.1007/978-3-642-24004-1_2](https://doi.org/10.1007/978-3-642-24004-1_2)
146. R. Brette *et al.* “Simulation of Networks of Spiking Neurons: A Review of Tools and Strategies”. *Journal of Computational Neuroscience* 23 (2007): 349–398. DOI: [10.1007/s10827-007-0038-6](https://doi.org/10.1007/s10827-007-0038-6)
147. J. K. Kruschke. “Bayesian Analysis Reporting Guidelines”. *Nature Human Behaviour* 5 (2021): 1282–1291. DOI: [10.1038/s41562-021-01177-7](https://doi.org/10.1038/s41562-021-01177-7)
148. A. Endo, S. Abbott, A. J. Kucharski, and S. Funk. “Estimating the Overdispersion in COVID-19 Transmission Using Outbreak Sizes Outside China”. *Wellcome Open Research* 5 (2020): 67. DOI: [10.12688/wellcomeopenres.15842.3](https://doi.org/10.12688/wellcomeopenres.15842.3)
149. P. Z. Chen, M. Koopmans, D. N. Fisman, and F. X. Gu. “Understanding Why Superspreading Drives the COVID-19 Pandemic but Not the H1N1 Pandemic”. *The Lancet Infectious Diseases* 21 (2021): 1203–1204. DOI: [10.1016/S1473-3099\(21\)00406-0](https://doi.org/10.1016/S1473-3099(21)00406-0)
150. N. F. Che Mat, H. A. Edinur, M. K. A. Abdul Razab, and S. Safuan. “A Single Mass Gathering Resulted in Massive Transmission of COVID-19 Infections in Malaysia with Further International Spread”. *Journal of Travel Medicine* 27 (2020): taaa059. DOI: [10.1093/jtm/taaa059](https://doi.org/10.1093/jtm/taaa059)
151. I. Magrans de Abril, J. Yoshimoto, and K. Doya. “Connectivity Inference from Neural Recording Data: Challenges, Mathematical Bases and Research Directions”. *Neural Networks* 102 (2018): 120–137. DOI: [10.1016/j.neunet.2018.02.016](https://doi.org/10.1016/j.neunet.2018.02.016)
152. Personal communication with Dario Barone in the context of his Master’s thesis.
153. A. J. Fontenele *et al.* “Criticality between Cortical States”. *Physical Review Letters* 122 (2019): 208101. DOI: [10.1103/PhysRevLett.122.208101](https://doi.org/10.1103/PhysRevLett.122.208101)
154. D. Dahmen, S. Grün, M. Diesmann, and M. Helias. “Second Type of Criticality in the Brain Uncovers Rich Multiple-Neuron Dynamics”. *Proceedings of the National Academy of Sciences* 116 (2019): 13051–13060. DOI: [10.1073/pnas.1818972116](https://doi.org/10.1073/pnas.1818972116)

155. L. Rudelt, D. G. Marx, M. Wibral, and V. Priesemann. “*Embedding Optimization Reveals Long-Lasting History Dependence in Neural Spiking Activity*”. *PLoS Computational Biology* 17 (2021): e1008927.
DOI: [10.1371/journal.pcbi.1008927](https://doi.org/10.1371/journal.pcbi.1008927)
156. V. Buendía, P. Villegas, R. Burioni, and M. A. Muñoz. “*The Broad Edge of Synchronization: Griffiths Effects and Collective Phenomena in Brain Networks*”. *Philosophical Transactions of the Royal Society A* 380 (2022): 20200424.
DOI: [10.1098/rsta.2020.0424](https://doi.org/10.1098/rsta.2020.0424)
157. J. Zierenberg, J. Wilting, and V. Priesemann. “*Homeostatic Plasticity and External Input Shape Neural Network Dynamics*”. *Physical Review X* 8 (2018): 031018.
DOI: [10.1103/PhysRevX.8.031018](https://doi.org/10.1103/PhysRevX.8.031018)
158. F. Y. K. Kossio, S. Goedeke, B. van den Akker, B. Ibarz, and R.-M. Memmesheimer. “*Growing Critical: Self-Organized Criticality in a Developing Neural System*”. *Physical Review Letters* 121 (2018): 058301.
DOI: [10.1103/PhysRevLett.121.058301](https://doi.org/10.1103/PhysRevLett.121.058301)
159. G. Deco, G. Tononi, M. Boly, and M. L. Kringelbach. “*Rethinking Segregation and Integration: Contributions of Whole-Brain Modelling*”. *Nature Reviews Neuroscience* 16 (2015): 430–439. DOI: [10.1038/nrn3963](https://doi.org/10.1038/nrn3963)
160. J. D. Murray *et al.* “*A Hierarchy of Intrinsic Timescales across Primate Cortex*”. *Nature Neuroscience* 17 (2014): 1661–1663. DOI: [10.1038/nn.3862](https://doi.org/10.1038/nn.3862)
161. U. Hasson, J. Chen, and C. J. Honey. “*Hierarchical Process Memory: Memory as an Integral Component of Information Processing*”. *Trends in Cognitive Sciences* 19 (2015): 304–313. DOI: [10.1016/j.tics.2015.04.006](https://doi.org/10.1016/j.tics.2015.04.006)
162. T. L. Ribeiro, M. Copelli, F. Caixeta, H. Belchior, D. R. Chialvo, M. A. L. Nicolelis, and S. Ribeiro. “*Spike Avalanches Exhibit Universal Dynamics across the Sleep-Wake Cycle*”. *PLoS ONE* 5 (2010): e14129. DOI: [10.1371/journal.pone.0014129](https://doi.org/10.1371/journal.pone.0014129)
163. G. Hahn, T. Petermann, M. N. Havenith, S. Yu, W. Singer, D. Plenz, and D. Nikolić. “*Neuronal Avalanches in Spontaneous Activity In Vivo*”. *Journal of Neurophysiology* 104 (2010): 3312–3322. DOI: [10.1152/jn.00953.2009](https://doi.org/10.1152/jn.00953.2009)
164. E. Marder. “*Neuromodulation of Neuronal Circuits: Back to the Future*”. *Neuron* 76 (2012): 1–11. DOI: [10.1016/j.neuron.2012.09.010](https://doi.org/10.1016/j.neuron.2012.09.010)

Bibliography

165. J. M. Shine, E. J. Müller, B. Munn, J. Cabral, R. J. Moran, and M. Breakspear. “Computational Models Link Cellular Mechanisms of Neuromodulation to Large-Scale Neural Dynamics”. *Nature Neuroscience* 24 (2021): 765–776. DOI: [10.1038/s41593-021-00824-6](https://doi.org/10.1038/s41593-021-00824-6)
166. D. S. Greenberg, A. R. Houweling, and J. N. D. Kerr. “Population Imaging of Ongoing Neuronal Activity in the Visual Cortex of Awake Rats”. *Nature Neuroscience* 11 (2008): 749–751. DOI: [10.1038/nn.2140](https://doi.org/10.1038/nn.2140)
167. W.-P. Chang, J.-S. Wu, C.-M. Lee, B. A. Vogt, and B.-C. Shyu. “Spatiotemporal Organization and Thalamic Modulation of Seizures in the Mouse Medial Thalamic-Anterior Cingulate Slice: Cingulate Cortical Epileptiform Activity”. *Epilepsia* 52 (2011): 2344–2355. DOI: [10.1111/j.1528-1167.2011.03312.x](https://doi.org/10.1111/j.1528-1167.2011.03312.x)
168. D. Heck. “Investigating Dynamic Aspects of Brain Function in Slice Preparations: Spatiotemporal Stimulus Patterns Generated with an Easy-to-Build Multi-Electrode Array”. *Journal of Neuroscience Methods* 58 (1995): 81–87. DOI: [10.1016/0165-0270\(94\)00161-9](https://doi.org/10.1016/0165-0270(94)00161-9)
169. G. Shahaf and S. Marom. “Learning in Networks of Cortical Neurons”. *Journal of Neuroscience* 21 (2001): 8782–8788. DOI: [10.1523/JNEUROSCI.21-22-08782.2001](https://doi.org/10.1523/JNEUROSCI.21-22-08782.2001)
170. D. A. Wagenaar. “Controlling Bursting in Cortical Cultures with Closed-Loop Multi-Electrode Stimulation”. *Journal of Neuroscience* 25 (2005): 680–688. DOI: [10.1523/JNEUROSCI.4209-04.2005](https://doi.org/10.1523/JNEUROSCI.4209-04.2005)
171. M. Schottdorf. “The Reconstitution of Visual Cortical Feature Selectivity in Vitro”. PhD thesis. Universität Göttingen, 2017. DOI: [10.53846/goediss-6721](https://doi.org/10.53846/goediss-6721)
172. S. Ronchi, M. Fiscella, C. Marchetti, V. Viswam, J. Müller, U. Frey, and A. Hierlemann. “Single-Cell Electrical Stimulation Using CMOS-Based High-Density Microelectrode Arrays”. *Frontiers in Neuroscience* 13 (2019): 208. DOI: [10.3389/fnins.2019.00208](https://doi.org/10.3389/fnins.2019.00208)
173. J. le Feber, J. Stegenga, and W. L. C. Rutten. “The Effect of Slow Electrical Stimuli to Achieve Learning in Cultured Networks of Rat Cortical Neurons”. *PLoS ONE* 5 (2010): e8871. DOI: [10.1371/journal.pone.0008871](https://doi.org/10.1371/journal.pone.0008871)
174. M. D’Andola, M. Giulioni, V. Dante, P. Del Giudice, and M. V. Sanchez-Vives. “Control of Cortical Oscillatory Frequency by a Closed-Loop System”. *Journal of NeuroEngineering and Rehabilitation* 16 (2019): 7. DOI: [10.1186/s12984-018-0470-z](https://doi.org/10.1186/s12984-018-0470-z)

175. R. S. Zucker and W. G. Regehr. “Short-Term Synaptic Plasticity”. *Annual Review of Physiology* 64 (2002): 355–405.
DOI: [10.1146/annurev.physiol.64.092501.114547](https://doi.org/10.1146/annurev.physiol.64.092501.114547)
176. E. Alvarez-Lacalle and E. Moses. “Slow and Fast Pulses in 1-D Cultures of Excitatory Neurons”. *Journal of Computational Neuroscience* 26 (2009): 475–493.
DOI: [10.1007/s10827-008-0123-5](https://doi.org/10.1007/s10827-008-0123-5)
177. D. Meunier, R. Lambiotte, and E. Bullmore. “Modular and Hierarchically Modular Organization of Brain Networks”. *Frontiers in Neuroscience* 4 (2010): 200.
DOI: [10.3389/fnins.2010.00200](https://doi.org/10.3389/fnins.2010.00200)
178. F. Pulvermüller, R. Tomasello, M. R. Henningsen-Schomers, and T. Wennekers. “Biological Constraints on Neural Network Models of Cognitive Function”. *Nature Reviews Neuroscience* 22 (2021): 488–502. DOI: [10.1038/s41583-021-00473-5](https://doi.org/10.1038/s41583-021-00473-5)
179. T. Birkoben and H. Kohlstedt. “Matter & Mind Matter”. arXiv. 2022.
DOI: [10.48550/arXiv.2204.12774](https://doi.org/10.48550/arXiv.2204.12774)

A Supplementary material for “*Sampling effects and measurement overlap can bias the inference of neuronal avalanches*”

Supplementary Information

Please note that a double-column version of this SI with working hyperlinks is available on arXiv:1910.09984.

1.1 Sampling bias remains under alternative topologies

The network topology used in the main paper is local: on average, each neuron is connected to its nearest $K = 10^3$ neighbors. It is of interest to check if alternative topologies can impact the distinguishability of the underlying dynamic state under coarse-sampling.

For that, we select two additional topologies. The first ("Orlandi") mimics the growth process of a neuronal culture. In short, axons grow outward on a semiflexible path of limited length and have a given probability to form a synapse when they intersect the (circular) dendritic tree of another neuron. Thereby, this topology is local without requiring distance-dependent synaptic weights (refer to [1] for more details). The second ("Random") implements a purely random connectivity, with each neuron being connected to $K = 10^3$ neurons. Note that this is an unrealistic setup as this topology is completely non-local.

We find that, under coarse-sampling, reverberating and critical dynamics remain indistinguishable with the alternative topologies (Fig A, left). Meanwhile, under sub-sampling, all dynamic states are clearly distinguishable for all topologies (Fig A, right).

1.2 Influence of the electrode field-of-view

In the main paper we considered that the contribution of a spiking neuron to the electrode signal decays with distance d as $\sim 1/d$ (see Ref. [3, 4]). The precise way neuronal activity is recorded by extracellular electrodes depends on many factors such as neuronal morphology and the level of correlation between synapses [2, 4]. Because it is difficult to account for all relevant factors, we instead prioritized a simple, mechanistic approach.

In more detail, we are interested in the impact of a spike as a function of the distance to the electrode. Thus, two main contributions arise: first, the transmembrane currents along the pre-synaptic neuron and the currents at the synapses and post-synaptic neurons (which do not necessarily cause further spikes). This creates a distance-dependence of the LFP contribution that depends on the neuron's morphology and the connectivity profile. Second, the LFP signal has a distance-dependent decay depending on whether the source corresponds to an electric monopole ($1/d$) or dipole ($1/d^2$). The particular decay was found to depend, among other factors, on neuron type and morphology, and it effectively varies from $1/d$ near the soma to $1/d^2$ (and steeper) in the far-field limit [2–4]. Together, a more realistic LFP model would need to incorporate the connectivity profile of the neurons and the signal decay (the final effect of a neuron would be a convolution of both functions).

In our simplified model, we neglect neuron morphology (because our simple binary neurons only feature a

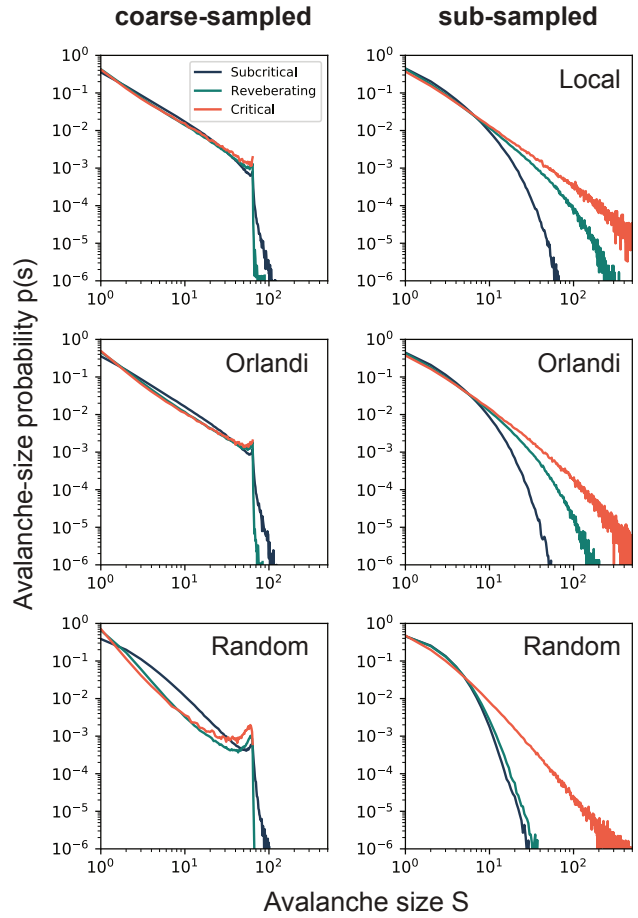


Fig A: Effect of alternative network topologies. Avalanche-size probability $p(S)$ from coarse-sampled activity (left) and sub-sampled activity (right) for subcritical, reverberating and critical dynamics. **Top:** results for the topology used in the main paper ("Local"). **Middle:** results for a topology that mimics culture growth [1] ("Orlandi"). **Bottom:** results for a random topology. Under coarse-sampling, reverberating and critical dynamics are indistinguishable with all topologies. Parameters: $d_E = 400 \mu\text{m}$ and $\Delta t = 8 \text{ms}$.

single compartment) and the connectivity profile (because our topology is homogeneous and local). Thus, our implemented distance-dependence of the electrode signal merely serves an effective description that sensibly depends on the considered population.

As a sensitivity analysis for our effective description, we here study the impact of a varying electrode field of view (Fig B). An important detail that we neglect in the main manuscript is that the $1/d$ contribution does not extend into the far-field limit (beyond 100–1000 μm) [2, 3]. We implemented various different effective distance-dependencies, which are motivated by the work of Einevoll and colleagues, especially Fig 2D of Ref. [2]. Note however, that the reported shape function describes the LFP contribution as a function of a neuron receiving input, whereas, in our case, the potential describes the contribution of a spiking neuron.

In particular, we checked $\gamma = 2$ (Fig B, right column), which represents a very narrow electrodes' field of view. In

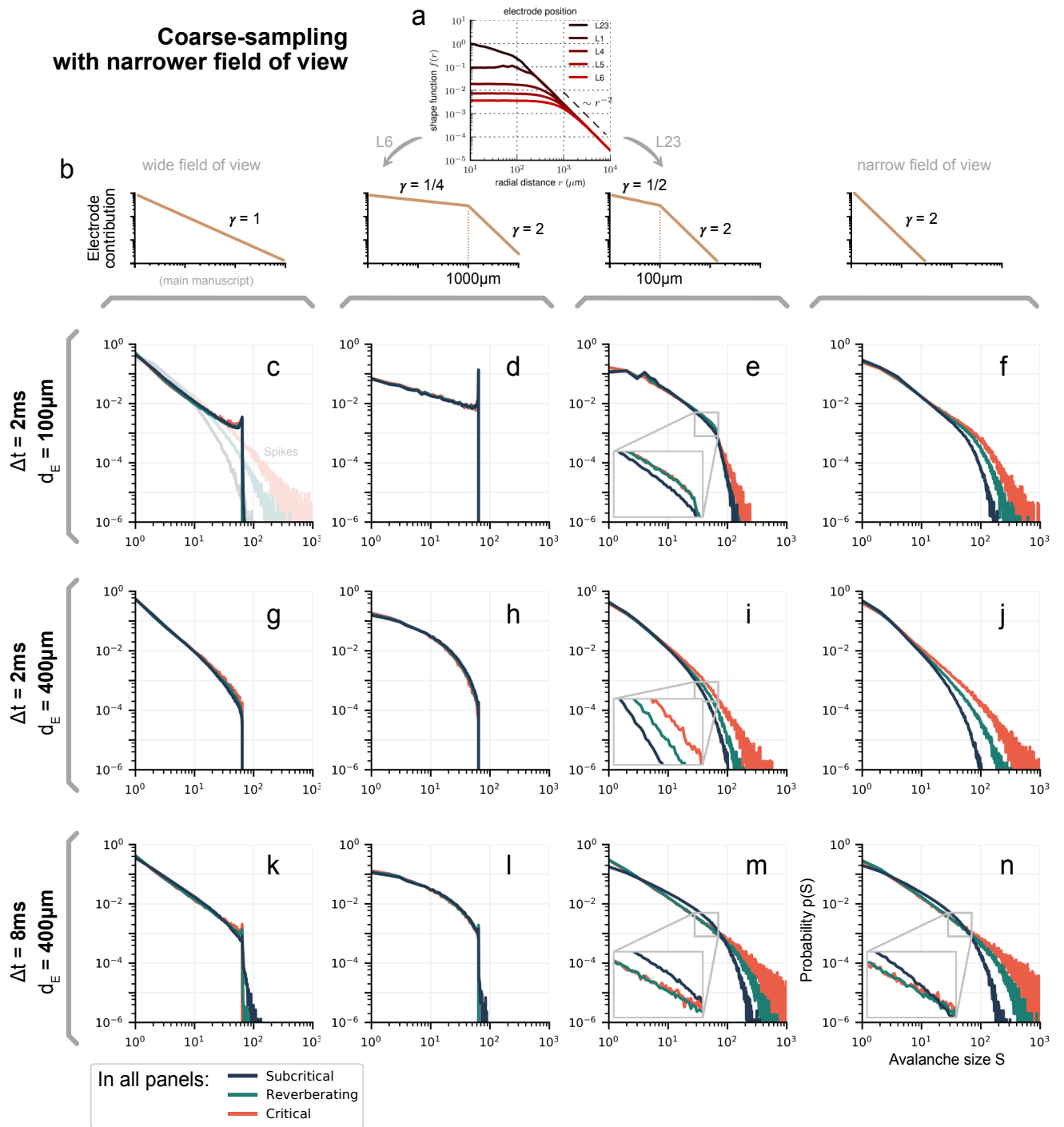


Fig B: Effect of changing the electrode contribution of a spiking neuron at distance d . **a**: Biophysically more plausible distance dependence of LFP, reproduced from [2]. **b**: Sketch of distance dependencies of tested effective electrode contribution that are motivated by (A). See accompanying text. Large decay exponents γ correspond to a narrow field of view of the electrodes (right column). When the transition from shallow to large exponents occurs at smaller d , electrodes can record fewer units and measurement overlap decreases. Eventually, distributions become distinguishable. As a notable side-effect, also the cut-off near $S = 64$ starts to vanish.

this case, avalanche-distributions become distinguishable, but the particular shape, cut-off and the amount of overlap between states again depends on the electrode distance and time-bin size.

We also checked contributions with a shallow exponent

($\gamma \leq 1$) near the electrode, which changes into a steep exponent ($\gamma = 2$) beyond a certain distance. For shallow exponents that reach far (transition at $1000\mu\text{m}$, Fig B d, h, l), the distributions of all considered states overlap, as in the main manuscript. Notably, the change in shape due to

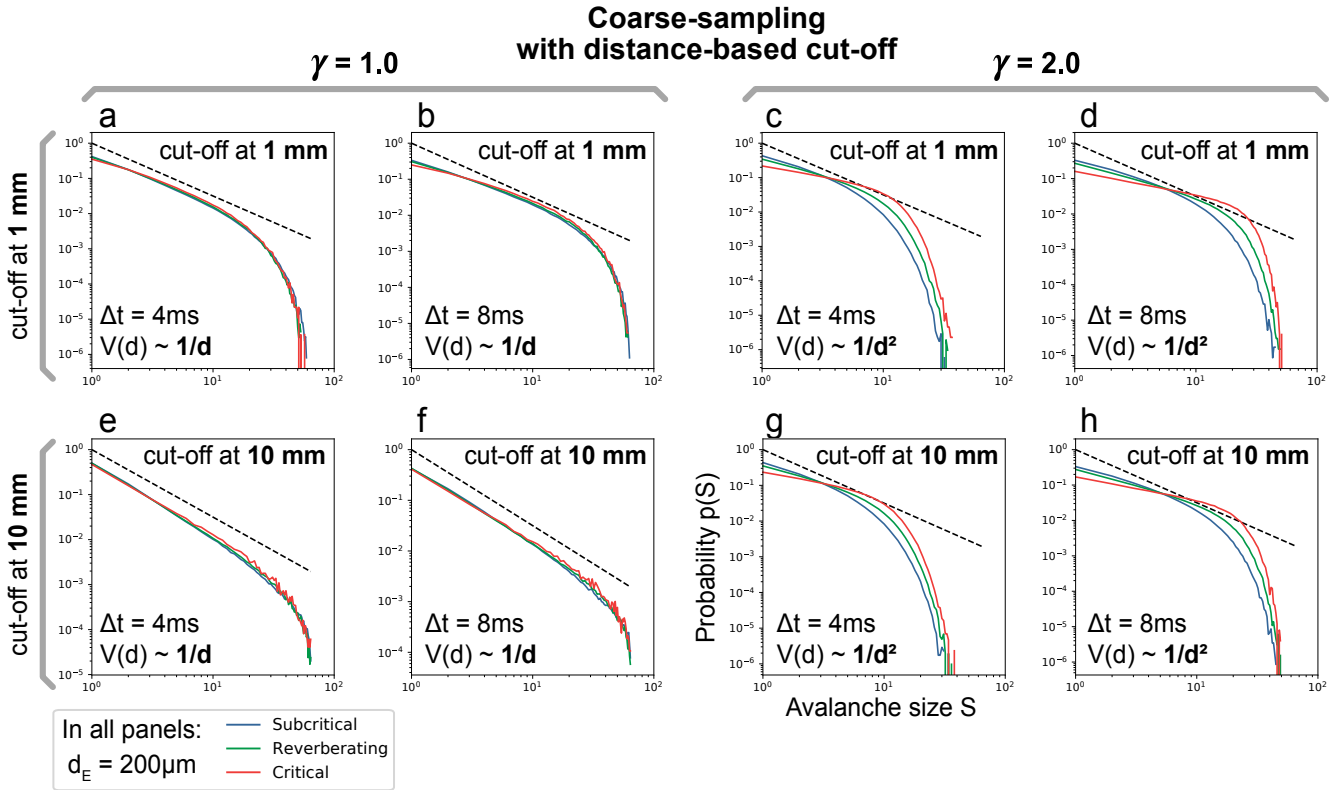


Fig C: Coarse-sampled avalanche-size distributions remain ambiguous under limited spatial reach. Results from the same model of the main paper, but with a hard cut-off at 1mm (top row) and 10mm (bottom row). Neurons farther away than the cut-off do not contribute to an electrode’s signal. The effect of the cut-off stacks with the effect of the electrode decay-exponent γ . When $\gamma = 1$, dynamic states remain indistinguishable, independent from the cut-off. (For larger decay exponent states are distinguishable, cf. Fig B.) Notably, also for $\gamma = 1$, the shape of distributions is altered by the cut-off. As a guide to the eye, dashed lines indicate a power law with exponent -1.5 . **Parameters:** $\gamma = 1$ (left half) and $\gamma = 2$ (right half), $d_E = 200\mu\text{m}$ in all panels.

changing the inter-electrode distance is even more severe than for $\gamma = 1$. For shallow exponents that do not reach far (transition at $100\mu\text{m}$, Fig B e, i, m), distributions start to be distinguishable. However, in the usually considered range of avalanche sizes extending up to the number of electrodes ($S = 64$), reverberating and critical dynamics still tend to overlap (E, M). Only for short time bins ($\Delta t = 2\text{ms}$) along large inter-electrode distances ($d_E = 400\mu\text{m}$) are the two states distinguishable (I).

Summarizing Fig B, we find that a main cause of collapsing avalanche distributions is a large electrodes’ field of view. As the field of view becomes narrower, the relative contribution of the closest neurons to the electrode increases, and coarse-sampling becomes more similar to sub-sampling. The cut-off at $S \sim N_E$ vanishes for steeper decays (large γ), and the different dynamic states become distinguishable.

For completeness, we performed further checks which follow the same reasoning. First, instead of changing exponents, we implemented a hard cut-off, beyond which neurons cannot contribute to an electrodes’ signal (Fig C). We again found that, for cut-off values ($\geq 1\text{mm}$), our main finding that avalanche distributions from different dynamic states are hardly distinguishable is unaltered. For short-range cut-off values that approach the distance between

neurons ($d_N = 50\mu\text{m}$), distributions become distinguishable (not shown). This effect is similar to what we saw for increasing the decay exponent $\gamma \rightarrow 2.0$, where only individual neurons remain in the field of view of the electrode. In both these cases, coarse-sampling starts to observe single-unit properties and becomes similar to the case of applying spike detection (here, sub-sampling).

Second, as our electrode potential is only an effective description and cannot be directly compared to Ref. [2], we additionally considered a hypothetical decay with exponent $\gamma = 1.5$ and repeated the analysis on different topologies (Figs. H and I). In all cases, $\gamma \geq 1.5$ causes the cut-off near $S = N_E$ to vanish, and an increase of γ weakens the coarse-sampling effect. Note, however, that even with relatively narrow field of view, avalanche distribution from coarse-sampling still differ from those of spike analysis.

The above changes of the electrode model indicate that in real electrode recordings both effects are present, sub-sampling *and* coarse-sampling. In particular, the resulting avalanche distributions change on a continuous scale where our descriptions of coarse-sampling and sub-sampling are the extremes. Underlying dynamic states are better distinguishable when the sampling is “closer” to sampling single units instead of weighted averages—and when the measurement overlap that is characteristic to coarse-sampling

goes to zero.

Lastly, we want to caution about a peculiarity of $1/d^1$. From a geometric point of view, one has to consider how the number of neurons per volume element increases with distance from the electrode. In two dimensions, the number of neurons contained in a thin ring around an electrode scales $N \sim 2\pi d$. If $\gamma = 1$, the contributions of far-away neurons could be as strong as the contributions of close-by neurons, especially if activity is correlated.

In more detail, let the ring be of inner radius d and outer radius $d + \epsilon$, then its area is $A = 2\pi(d\epsilon + \epsilon^2)$. At a constant density ρ , the number of neurons in this ring is given by $N = \rho A$, so that, up to a constant, $N \sim 2\pi d\epsilon\rho$. Let $x_i = \{0, 1\}$ denote the state of a single neuron. Here, we assume that all neurons are uncorrelated and independent identically distributed random variables, with expectation value $\langle x \rangle = \mu$ and the same variance $\text{Var}[x]$. Our electrode potential was modeled as

$$V = \sum_{i=1}^N x_i/d_i. \quad (1)$$

For every ring, we assume a constant $d_i = d$ for all neurons in the ring. Then, the expected potential for the ring is

$$\langle V(d) \rangle = \left\langle \sum_{i=1}^N x_i/d \right\rangle = \sum_{i=1}^N \langle x_i/d \rangle = N\mu/d. \quad (2)$$

Thus, when $N \sim 2\pi d\epsilon\rho$, then $\langle V(d) \rangle \sim \mu$. Indeed, this implies that the contributed potential of any of these rings is constant and that many neurons in a far-away ring can “contribute as much” as few local ones.

However, the variance of the potential per ring is not constant. For uncorrelated x , the variance of their sum is equal to the sum of their variances:

$$\text{Var}[V(d)] = \text{Var} \left[\sum_{i=1}^N x_i/d \right] = \sum_{i=1}^N \text{Var}[x_i/d]. \quad (3)$$

With

$$\text{Var}[x_i/d] = \langle (x_i/d)^2 \rangle - \langle x_i/d \rangle^2 \quad (4)$$

$$= \frac{1}{d^2} (\langle x_i^2 \rangle - \langle x_i \rangle^2) \quad (5)$$

$$= \frac{1}{d^2} \text{Var}[x_i] \quad (6)$$

we see that

$$\text{Var}[V(d)] = \frac{1}{d^2} \sum_{i=1}^N \text{Var}[x_i] = \frac{N}{d^2} \text{Var}[x]. \quad (7)$$

When again considering $N \sim 2\pi d\epsilon\rho$,

$$\text{Var}[V(d)] \sim \text{Var}[x]\epsilon\rho/d. \quad (8)$$

Hence, the standard deviation of the rings vanishes as $d \rightarrow \infty$; far away rings do contribute to the electrode, but they do not add to the variance of the signal. During the avalanche detection, the start or end of an avalanche is

given by a threshold crossing. In a signal with more variance, more threshold crossing will occur, possibly leading to different avalanche statistics. As we showed, far-away neurons that are uncorrelated increase the mean, but they do not increase the variance, and, thus, do not lead to more (or less) threshold crossings. Notwithstanding, this reasoning only holds for uncorrelated neurons. If x_i are correlated, also far-away neurons could contribute to the variance. Although we think that is not the main cause for the coarse-sampling effect (cf. Fig B), we want to stress the limited range of electrodes for future work.

For a population of neurons receiving (un-) correlated synaptic input, the distance dependence of the LFP signal is studied in much more detail in Ref. [2]. Together with the above reasoning, this work highlights another possible source of sampling bias (which also affects our model electrodes): Because closer-to-critical dynamic states typically feature more correlated activity than subcritical states, the effective distance-dependence of an electrode is also affected by the dynamic state that is being recorded.

To conclude this section, we want to sketch an idealized experimental set-up: in order to determine criticality under coarse-sampling, the set-up should combine i) a large distance between electrodes d_E , ii) a narrow electrode field-of-view (large γ) and, ideally, iii) systems to calibrate with, which feature different dynamic states. This could potentially be used to qualitatively compare the distance to criticality between the systems. However, not only is this much more limited than what is possible with spike data [5–7], but the cut-off is a characteristic and ubiquitous feature commonly observed in experimental data of coarse-sampled recordings [8, 9]. This indicates that electrodes typically have a large field-of-view, and motivated our modeling assumption of $\gamma = 1$.

1.3 Neuron density

As the coarse sampling effect is sensitive to the field of view of electrodes, it may similarly depend on the amount of neurons any electrode captures, and, thus, the density of the neuron population. Hence, we performed a basic test of the robustness of our results with respect to the density of neurons (Fig D). To that end, we kept most parameters of the model as in the main manuscript: The culture extended over 4 cm substrate and neurons were hard-wired to their ≈ 1000 closest neighbors. A change in density impacts how far these neighbors are distributed, but we kept the effective projection range constant ($\sigma = 300 \mu\text{m}$), so that our “local” topology and the connectivity profile remain unchanged. We kept electrode contributions at $1/d$ and placed electrodes at a large distance ($400 \mu\text{m}$), so that every electrode samples many neurons and changes in density can become clear.

Compared to $\rho = 100/\text{mm}^2$ of the main manuscript, we considered lower ($\rho = 25/\text{mm}^2$) and higher densities ($\rho = 400/\text{mm}^2$). Surprisingly, a change of neuron density only has a minor impact on the coarse sampling effect: Overall, the overlap of distributions and the cut-off remain for all considered densities (Fig D). Nonetheless, subtle differences are visible. Firstly, the slopes of the distributions seem to

Coarse-sampling at different neuron densities

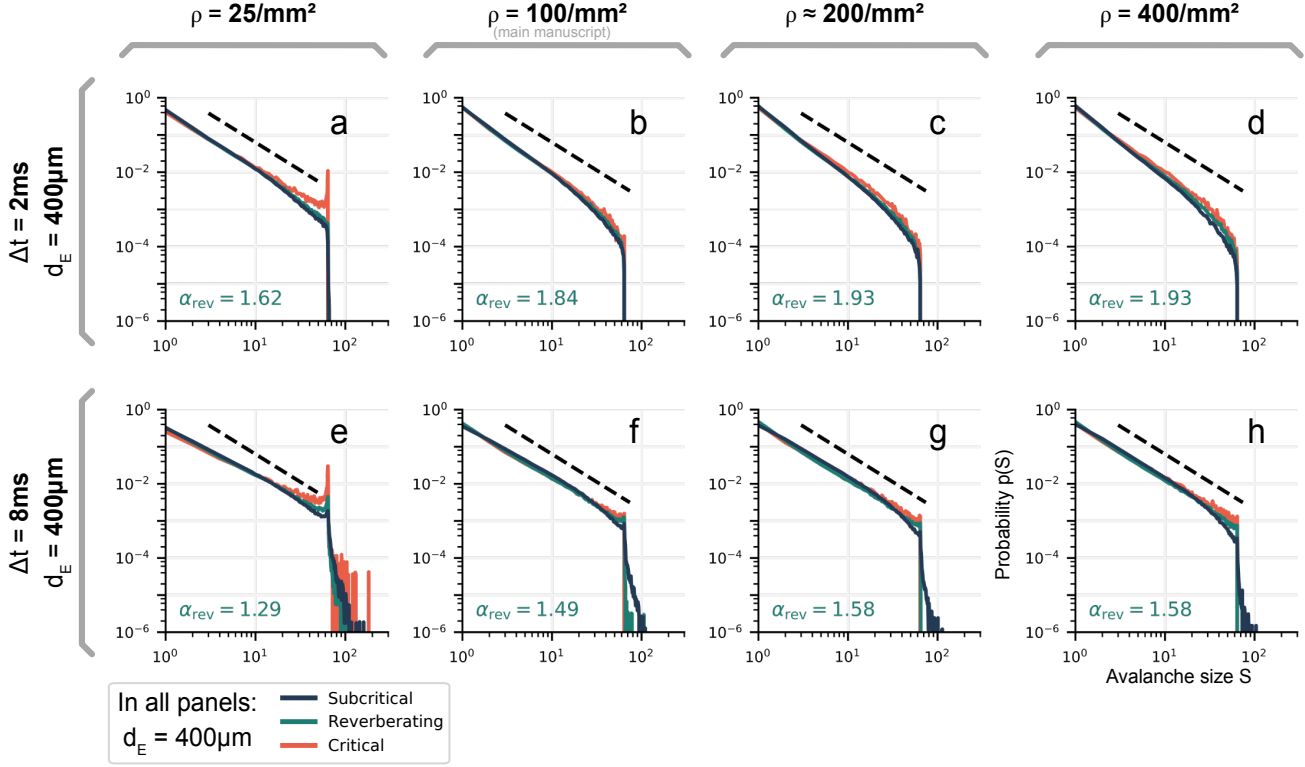


Fig D: Varying neuron densities. Simulations with parameters as in the main manuscript, with matching spatial extend of the substrate, connectivity profile of the neurons and field of view of the electrodes ($\gamma = 1$). As a guide to the eye, black dashed lines indicate $p(S) \sim S^{-1.5}$, and the fitted α for the reverberating state are indicated in the lower corner of every panel. Our main result that measurement overlap can render dynamic states indistinguishable is confirmed.

change, but this is shadowed by the dependence of the slope on the time-bin size. Secondly, for higher densities $\rho \geq 100/\text{mm}^2$ distributions appear critical or slight subcritical, but for the low density, they also resemble super-critical distributions with a pronounced peak near the cut-off.

In conclusion, our main results concerning overlapping avalanche distributions for different dynamic states seem to be fairly invariant when increasing neuron density.

1.4 Low-pass filtering

A relevant question that we have not addressed in the main manuscript is how mechanisms that come into effect *before* the sampling hardware could impact avalanche statistics. Many studies are concerned with low-pass frequency filtering and how measurements of neuronal activity are affected. Such a temporal filtering may arise from the intrinsic neuronal morphology [2, 4, 10] or the surrounding extracellular tissue [11–13].

As a simple test that mimics natural low-pass filtering, we convolved the raw time series of every electrode with an exponentially decaying kernel (Fig E). Thus, the filtering was applied before the remaining analysis pipeline. The decay of the kernel (and the strength of the filtering) is parametrized through the decay time of the exponential.

We considered decay times τ_f between 2 ms and 128 ms (ranging from 1 to 128 time steps of the simulation). The kernel was created using `scipy.signal.exponential` with a window size of 1000 time steps. The remaining analysis pipeline remained unchanged, and, in particular, included the frequency filtering to $0.1 \text{ Hz} < f < 200 \text{ Hz}$ that we assumed as part of the recording hardware.

Whereas the overlap of distributions largely remains when low-pass filtering is applied, the shape of the distributions depends on the strength of the filter. As a general trend, all distributions tend to form “super-critical” peaks as filtering becomes stronger. We associated these peaks with multiple electrodes picking up the same event (boosting the amount of large avalanches, up to the number of electrodes). This goes along with a decreased number of total avalanches that are detected (lower left corner in all panels). Note that the same raw time series with the same duration were used along every row of Fig E.

Together, this is consistent with the expecting “smoothing” of the raw time series due to low-pass filtering: Deflections of a time series around its mean get attenuated, and small excursions (at high frequency) become rare. Because these excursions potentially trigger the start of a new avalanche, fewer avalanches (or events) are detected when filtering becomes stronger. Intriguingly, the change of the

Coarse-sampling with exponential low-pass filter

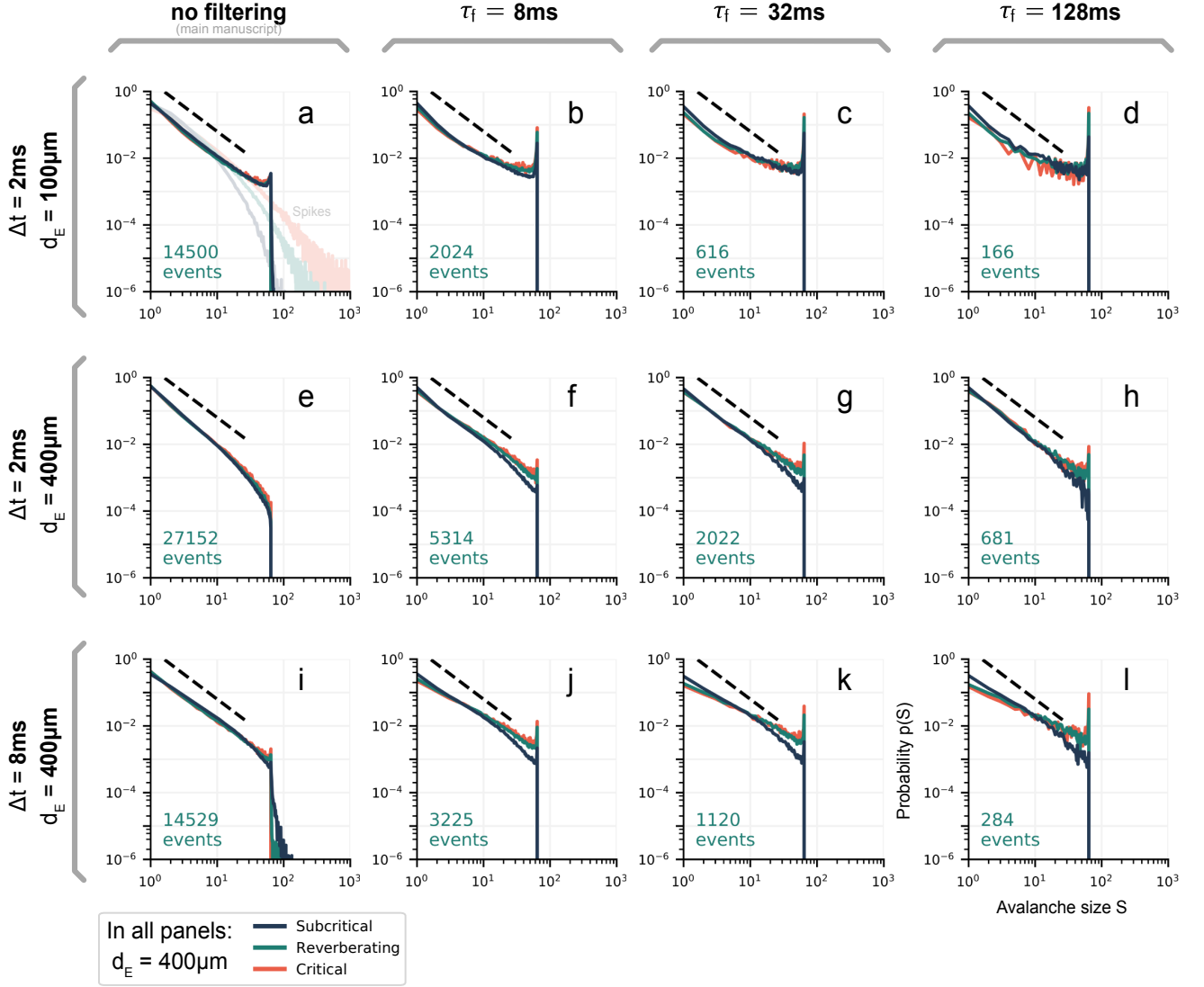


Fig E: Low-pass filtering using an exponential kernel. To mimic low-pass filtering as possibly caused by extracellular tissue or neuron morphology, an exponential kernel with decay time τ_f was applied to the raw signal before applying the analysis pipeline of the main manuscript (which includes frequency filtering to $0.1 \text{ Hz} < f < 200 \text{ Hz}$). As a guide to the eye, black dashed lines indicate $p(S) \sim S^{-1.5}$, and the number of events that contributed to the distribution for reverberating dynamics are indicated in the lower corner of every panel.

distribution shape due to filtering seems to affect critical and reverberating dynamics more severely than subcritical dynamics (especially visible in the bottom row).

However, note that the filtering employed here only serves as an example for a low-pass filter. Experimentally, power-spectra are often found to show $1/f^\beta$ scaling, with $0 < \beta < 4$, which limits the functional form a more realistic filtering kernel might have [12, 14–16].

1.5 Scaling laws may fail under coarse-sampling

The most used indication of criticality in neuronal dynamics is the avalanche-size distribution $p(S)$. However, at crit-

icality, the *avalanche duration distribution* $p(D)$ and the *average avalanche size* for a given duration, $\langle S \rangle(D)$, should also follow power-laws, each with a respective *critical exponent* [17]:

$$p(S) \sim S^{-\alpha} \quad (9)$$

$$p(D) \sim D^{-\beta} \quad (10)$$

$$\langle S \rangle(D) \sim D^\gamma \quad (11)$$

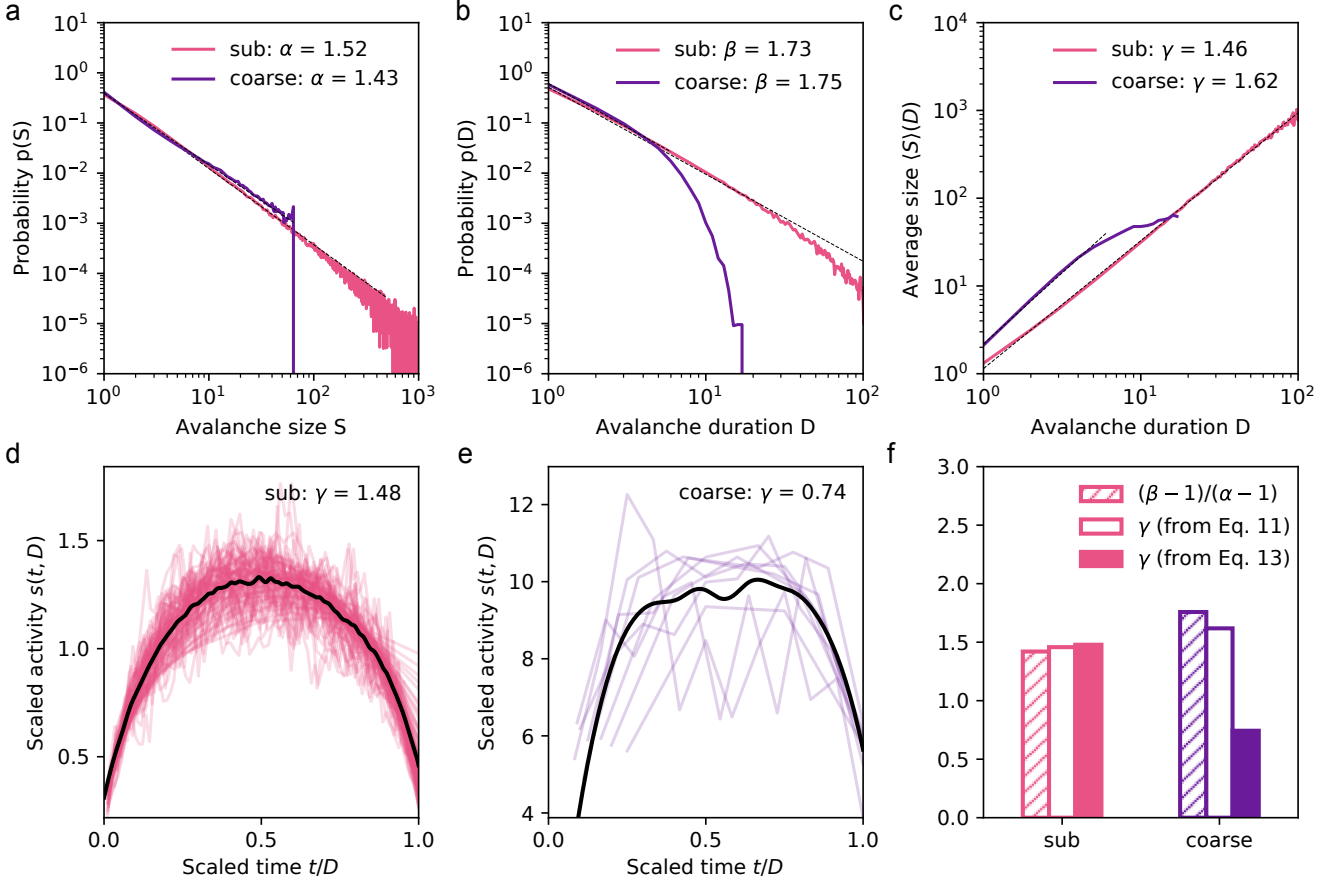


Fig F: Scaling laws of a system with critical dynamics under coarse- and sub-sampling. **a–c:** Avalanche-size distribution $p(S) \sim S^{-\alpha}$, avalanche-duration distribution $p(D) \sim D^{-\beta}$, and average size for a given duration $\langle S \rangle(D) \sim D^\gamma$, respectively, for sub-sampled (“sub”) and coarse-sampled (“coarse”) simulations. Distributions under sub-sampling easily span more than one order of magnitude, while coarse-sampled distributions suffer from an early cut-off (which hinders power-law fits). **d, e:** Shape collapse of $s(t, D) \sim D^{\gamma-1} \mathcal{F}(t/D)$ for sub-sampled and coarse-sampled data, respectively. Under coarse-sampling, the early duration cut-off results in few unique shapes for the collapse (corresponding to unique D -values). **f:** Comparison of the critical exponents obtained independently from Eqs. (11)–(13). Exponents are consistent only under sub-sampling. **Parameters:** $d_E = 400 \mu\text{m}$ and $\Delta t = 8 \text{ms}$.

The exponents are related to one another by the scaling relationship*

$$\frac{\beta - 1}{\alpha - 1} = \gamma. \quad (12)$$

For a pure branching process—or any process in the mean-field directed percolation universality class [18, 19]—they take the values $\alpha = 3/2$, $\beta = 2$ and $\gamma = 2$.

Lastly, at criticality, avalanches of vastly different duration still have the same *average shape*: The activity $s(t, D)$ at any given time t (within the avalanche’s lifetime D) is described by a universal scaling function \mathcal{F} , so that

$$s(t, D) \sim D^{\gamma-1} \mathcal{F}(t/D). \quad (13)$$

In other words, changing $s(t, D) \rightarrow s(t, D)/D^{\gamma-1}$ and $t \rightarrow t/D$ should result in a data collapse for the average avalanche shapes of all durations.

The shape collapse of Eq. 13 is done following the algorithm described in [20]. Briefly, the avalanche profiles

*In this subsection, γ exclusively denotes the scaling exponent and the decay exponent (which is denoted with γ in the rest of the manuscript) equals 1 for all results presented here.

$s(t, D)$ of all avalanches with the same duration D are averaged, and the resulting curve is scaled to t/D and interpolated on 1000 points in the $[0, 1]$ range. Avalanches with $D < 4$, or with less than 20 realizations are removed. The chosen collapse exponent γ is the one that minimizes the error function:

$$E = \frac{\langle \text{Var}(X_D/D^{\gamma-1}) \rangle}{\Delta X^2} \quad (14)$$

where $X_D(t/D)$ is the interpolated average shape of avalanches with size D , and $\Delta X = \max_{t,D}(X_D/D^{\gamma-1}) - \min_{t,D}(X_D/D^{\gamma-1})$. The variance $\text{Var}(\cdot)$ is calculated over all valid D , and the mean $\langle \cdot \rangle$ is taken over the scaled duration t/D . For interpolation and minimization we use the `scipy` [21] functions `interpolate.InterpolatedUnivariateSpline` and `optimize.minimize`, respectively.

From Eqs. (11)–(13), we have three independent ways to determine the exponent γ . Consistency between the three is a further test of criticality. However, to the best of our knowledge, experimental evidence with the full set of

scaling laws is mainly observed under sub-sampling: from spikes of in vitro recordings [†] [23, 24], but see Ref. [22].

The absence of scaling laws in coarse-sampled data can be explained by how coarse-sampling biases the average shape: the cut-off in $p(S)$ near the number of electrodes $S = N_E$ implies that $\langle S \rangle(D) < N_E$. From Eq. (11) we have $D < N_E^{1/\gamma}$. If $\gamma > 1$ the cut-off in $p(S)$ causes a much earlier cut-off in both $p(D)$ and $\langle S \rangle(D)$.

Given that experiments typically have $N_E \sim 10^2$ electrodes, $p(D)$ of a pure branching process (with $\gamma = 2$) would span a power-law for less than one order of magnitude. However, the typical standard to reliably fit a power-law is at least two orders of magnitude [25]. While this is problematic under coarse-sampling (Fig 6), we have shown that the hard cut-off is not present under sub-sampling (Fig 7).

When we apply the independent measurements of γ to our model (with critical dynamics) under sub-sampling, we find consistent exponents for all measurements (Fig Ff). Moreover, the exponents we find under sub-sampling are compatible with experimental values, e.g. $\gamma_{\text{exp}} = 1.3 \pm 0.05$ reported in Ref. [23] and $1.3 \leq \gamma_{\text{exp}} \leq 1.5$ reported in Ref. [24]. Notably, the exponents found in our model and experimentally differ from those expected for a pure branching process ($\gamma = 2$). While not the focus here, we believe this deviation to derive from topological properties of the network, which was also observed in Ref. [23]; distance-dependent weights of local topologies affect avalanche duration and size and yield different exponents than a branching process (which does not face any topological constraints).

When we apply the independent measurements of γ to our model (with critical dynamics) under coarse-sampling, exponents differ from measurement to measurement: The exponent obtained from the shape collapse ($\gamma \approx 0.74$) greatly differs from the other two ($\gamma \approx 1.74$, $\gamma \approx 1.62$), Fig Ff. Moreover, the extremely short range available to fit $p(D)$ and $\langle S \rangle(D)$ with power-laws ($1 \leq D \leq 6$) makes the estimated exponents unreliable.

To conclude, the full set of critical exponents revealed criticality only under sub-sampling. Only in this case we observed both, a match between all the measurements of the exponent γ , and a power-law behavior extending over a range large enough to reliably fit them.

1.6 Coarse Graining the Ising Model

To demonstrate how general the impact of measurement overlap is, we study the two-dimensional Ising model. The Ising model is well understood and often serves as a textbook example for renormalization group (RG) theory in Statistical Physics [26]. In this framework, the system is *coarse grained* by merging multiple parts (spins) into one. An intuitive way to think of it is by zooming out of a photograph on a computer screen; a pixel can only show one color although there might be more details hidden underneath. Coarse graining is also known as the real-space block-spin renormalization and it can be used to assess criticality.

[†]An exception can be found in Ref. [22], where scaling relations were found to hold in vivo. However, in this study, fluorescence imaging was coupled with very large time bins $\Delta t \geq 0.47$ s, the effect of which remains to be understood in full.

Please note that *coarse graining* is different from *coarse-sampling*. Conventionally, coarse-graining perfectly tiles the space without any measurement-overlap (see Fig G).

The two-dimensional Ising model consists of $N = L^2$ spins with states $s_i = \pm 1$, arranged on a square lattice of length L . In its simplest form, it is given by the Hamiltonian $H(\vec{s}) = \sum_{\langle i,j \rangle} s_i s_j$, where $\langle i,j \rangle$ denotes all pairs of nearest neighboring spins. The probability of observing \vec{s} is given by the Boltzmann distribution

$$P(\vec{s}, T) = \frac{1}{Z_T} e^{-H(\vec{s})/k_B T} \quad (15)$$

where T is the temperature of the system, k_B is the Boltzmann constant (here, $k_B = 1$) and Z_T is the partition function that normalizes the distribution. As the temperature $T \rightarrow T_c = 2/\ln(1 + \sqrt{2})$, the system undergoes a second-order phase transition between a disordered spin configuration ($T > T_c$) and an ordered state of aligned spin orientations ($T < T_c$). Many observables diverge at $T = T_c$ for $L \rightarrow \infty$, such as correlation length, specific heat and susceptibility [18, 26].

We perform Monte Carlo simulations of the 2D Ising model using the massively parallel multicanonical method [27, 28]. The multicanonical method offers numerous advantages over conventional Monte Carlo approaches. For instance, instead of simulating at a single temperature, one simulation covers the whole energy space. High-precision canonical expectation values of observables are recovered for any desired temperature during a post-production step. Thereby, we obtain the normalized absolute magnetization as a function of temperature $m(T) = \frac{1}{N} |\sum_i s_i|$.

1.7 Block-Spin Transformation

Measurement overlap causes individual sources to contribute multiple times to a signal. For the Ising model, a similar process takes place when coarse graining is applied. In the process, spins are grouped into blocks of size $b \times b$, here $b = 4$ and every block only takes a single value. The value of each block can be obtained in different ways.

- Most commonly, the majority rule [26] is employed, where the block is assigned +1 (−1) if the majority of spins has value +1 (−1). In this case, the contribution of multiple sources is integrated. Hence we compare this rule to the effects observed when neuronal systems are coarse-sampled.
- Alternatively, one can use the decimation rule [26]. In this case, all except a single spin value within a block are discarded. The block value is assigned from the single spin that is kept. Hence we compare this rule to the effects observed when neuronal systems are sub-sampled.

This block-spin transformation rescales the number of spins by a factor of $1/b^2$, effectively reducing system size (which will cause finite-size effects). It is well known, that when studying the magnetization, the effective size of the compared systems (after rescaling) has to match.

1.8 Overlap

To mimic the measurement overlap, we now introduce an overlap between the blocks of the Ising model coarse graining (Fig G). In the native block-spin transformation, blocks do not overlap. Then, in terms of spins, the linear distance d between two blocks matches the block size $b = d = 4$ (Fig Ga). When the distance between blocks is smaller than the block size, $d < b$ (Fig Gb), measurement overlap is created, while when $d > b$ parts of the system are not sampled. Clearly, the changes that such an overlap will cause on rescaled observables should depend on the rule used to perform the block-spin transformation.

Here, we look at combinations of block size $b = 4$ with distance between blocks of $d = 2$, $d = 4$ and $d = 8$. In order to preserve the effective system size ($L = 16$), we thus perform simulations for $L = 32$, $L = 64$ and $L = 128$, respectively.

Using the majority rule and no overlap—which is the default real-space renormalization-group approach—the procedure moves m away from $m(T_c)$ (Fig Gc, $d = b$): For $T < T_c$, m is increased; For $T > T_c$, m is decreased. Ordinarily, T_c can be obtained by finding the crossing of m between an unblocked ($L = 16$) and a blocked ($L = 64$, $b = 4$) system—only at T_c is the measured m invariant under block rescaling transformations.

1.9 Majority Rule “coarse”

What is the impact of the overlap for the majority rule? For increasing overlap ($d < b$), the crossing occurs at $T > T_c$ (Fig Gc). This is because sharing spins increases the correlations between blocks (pairwise and higher-order), making it more likely that the rescaled spins point into the same direction. In other words, it biases the measurement of m towards order, increasing our estimated critical temperature.

For absent overlap ($d > b$), only every other block is measured. This decorrelates the spins near the borders of each block and, therefore, decreases the correlation between blocks. As a consequence, the spin orientation of the blocked system moves towards disorder, decreasing the measured magnetization m .

1.10 Decimation Rule “sub”

If instead of the majority rule the decimation rule is used, the blocking procedure does not alter the correlation between spins before and after the transformation (Fig Gd). As a consequence, the magnetization remains unaltered in general. However, in the disordered phase, we still notice a systematic deviation from the unblocked system (with $L = 64$). This deviation can be fully attributed to finite-size effects: The distribution of realizable magnetizations in the disordered phase follows a Gaussian with mean zero and variance proportional to the (effective) number of spins. Due to the definition of the magnetization with absolute value, the expectation value of the magnetization for $T \rightarrow \infty$ is determined by the (effective) system size.

As was the case when sub-sampling neuronal systems, the increase in correlation that ultimately leads to biased observables is caused by integrating weighted contributions from various sources. This is not the case when the decimation rule is applied. Note that the impact of different block-transformation rules on $m(T)$ will not hold for all other canonical observables such as the energy $E(T)$ [26].

References

1. Orlandi, J. G. *et al.* Noise focusing and the emergence of coherent activity in neuronal cultures. *Nature Physics* **9**, 582–590 (2013).
2. Linden, H. *et al.* Modeling the spatial reach of the LFP. *Neuron* **72**, 859–872 (2011).
3. Pettersen, K. H. & Einevoll, G. T. Amplitude Variability and Extracellular Low-Pass Filtering of Neuronal Spikes. *Biophysical Journal* **94**, 784–802 (2008).
4. Einevoll, G. T. *et al.* Modelling and analysis of local field potentials for studying the function of cortical circuits. *Nature Reviews Neuroscience* **14**, 770–785 (2013).
5. Wilting, J. & Priesemann, V. Inferring collective dynamical states from widely unobserved systems. *Nature Communications* **9**, 2325 (2018).
6. Wilting, J. & Priesemann, V. Between Perfectly Critical and Fully Irregular: A Reverberating Model Captures and Predicts Cortical Spike Propagation. *Cerebral Cortex* **29**, 2759–2770 (2019).
7. Levina, A. & Priesemann, V. Subsampling scaling. *Nature Communications* **8**, 15140 (2017).
8. Beggs, J. M. & Plenz, D. Neuronal Avalanches in Neocortical Circuits. *Journal of Neuroscience* **23**, 11167–11177 (2003).
9. Gireesh, E. D. & Plenz, D. Neuronal avalanches organize as nested theta- and beta/gamma-oscillations during development of cortical layer 2/3. *Proceedings of the National Academy of Sciences* **105**, 7576–7581 (2008).
10. Buzsáki, G. *et al.* The origin of extracellular fields and currents — EEG, ECoG, LFP and spikes. *Nature Reviews Neuroscience* **13**, 407–420 (2012).
11. Gabriel, S. *et al.* The dielectric properties of biological tissues: II. Measurements in the frequency range 10Hz to 20GHz. *Physics in Medicine and Biology* **41**, 2251–2269 (1996).
12. Bédard, C. *et al.* Does the 1/f Frequency Scaling of Brain Signals Reflect Self-Organized Critical States? *Physical Review Letters* **97**, 118102 (2006).
13. Bédard, C. & Destexhe, A. Macroscopic models of local field potentials and the apparent 1/f noise in brain activity. *Biophysical Journal* **96**, 2589–2603 (2009).
14. Miller, K. J. *et al.* Power-law scaling in the brain surface electric potential. *PLoS Computational Biology* **5** (2009).
15. Milstein, J. *et al.* Neuronal shot noise and Brownian 1/f² behavior in the local field potential. *PLoS one* **4**, e4338 (2009).
16. Donoghue, T. *et al.* Parameterizing Neural Power Spectra into Periodic and Aperiodic Components. *Nat Neurosci* **23**, 1655–1665 (2020).

Table A: Compilation of experimental findings of neuronal avalanches [29]. For cultures, “region” corresponds to the brain region neurons were extracted from. Range of $p(S)$ was either given in the text, or estimated visually. Exponents with “ \approx ” are not explicitly fitted but instead visually compared. Notably, most studies reporting power-law distributions in-vivo built on coarse-sampled measures, or imaging (in which case the effect of the low sampling-frequency on avalanche distributions is not clear). We found only one reference in the literature where in-vivo spiking data were used *and* power-law distributions occurred, although over a very limited range [30].

authors	technique	region	system	exponent α	range of $p(S)$
Beggs <i>et al.</i> , 2003 [8]	LFP	cortex	culture	≈ 1.5	1-60
Gireesh <i>et al.</i> , 2008 [9]	LFP	cortex	culture	1.53 ± 0.02	1-32
Petermann <i>et al.</i> , 2009 [31]	LFP	cortex	monkey	≈ 1.5	1-32
Klaus <i>et al.</i> , 2011 [32]	LFP	cortex	monkey	≈ 1.5	1-96
Priesemann <i>et al.</i> , 2013 [33]	LFP	varied	human	1.58 ± 0.06	1-50
Shew <i>et al.</i> , 2015 [34]	LFP	cortex (visual)	turtle	1.6-2.6	3-200
Clawson <i>et al.</i> , 2017 [35]	LFP	cortex (visual)	turtle	1.8 ± 0.3	2-500
Meisel <i>et al.</i> , 2013 [36]	MEEG	whole head	human	≈ 1.5	1-27
Palva <i>et al.</i> , 2013 [37]	MEEG	whole head	human	1.31	1-66
Shriki <i>et al.</i> , 2013 [38]	MEEG	whole head	human	≈ 1.5	1-100
Arviv <i>et al.</i> , 2015 [39]	MEEG	whole head	human	1.50	1-100
Scott <i>et al.</i> , 2014 [40]	imaging	cortex	rat	≈ 1.5	1-1000
Bellay <i>et al.</i> , 2015 [41]	imaging	cortex	rat	1.63 ± 0.13	0.01-10
Fagerholm <i>et al.</i> , 2015 [42]	imaging	cortex	rat	≈ 1.5	1-1000
Yaghoubi <i>et al.</i> , 2018 [43]	imaging	hippocampus	culture	1.65 ± 0.1	1-500
Ponce-Alvarez <i>et al.</i> , 2018 [22]	imaging	whole brain	zebrafish	2.01 ± 0.03	1-10000
Bocaccio <i>et al.</i> , 2019 [44]	imaging	whole head	human	≈ 2	1-1000
Friedman <i>et al.</i> , 2012 [23]	spikes	cortex	culture	1.7	1-30
Massobrio <i>et al.</i> , 2015 [45]	spikes	cortex	culture	1.48-1.52	1-500
Hahn <i>et al.</i> , 2017 [30]	spikes	cortex (visual)	monkey	1.58 ± 0.03	1-20
Levina <i>et al.</i> , 2017 [7]	spikes	cortex	culture	≈ 2	1-5900
Kanders <i>et al.</i> , 2020 [24]	spikes	hippocampus	culture	2.18 ± 0.05	1-60

17. Sethna, J. P. *et al.* Crackling noise. *Nature* **410**, 242–250 (2001).
18. Sethna, J. P. *Statistical Mechanics: Entropy, Order Parameters, and Complexity* 1st (Oxford University Press, New York, 2006).
19. Janssen, H. K. & Täuber, U. C. The field theory approach to percolation processes. *Annals of Physics* **315**, 147–192 (2005).
20. Marshall, N. *et al.* Analysis of Power Laws, Shape Collapses, and Neural Complexity: New Techniques and MATLAB Support via the NCC Toolbox. *Frontiers in Physiology* **7**, 1–18 (2016).
21. Virtanen, P. *et al.* SciPy 1.0: fundamental algorithms for scientific computing in Python. *Nature methods* (2020).
22. Ponce-Alvarez, A. *et al.* Whole-Brain Neuronal Activity Displays Crackling Noise Dynamics. *Neuron* **100**, 1446–1459 (2018).
23. Friedman, N. *et al.* Universal critical dynamics in high resolution neuronal avalanche data. *Physical Review Letters* **108**, 1–5 (2012).
24. Kandera, K. *et al.* Fingerprints of a second order critical line in developing neural networks. *Communications Physics* **3**, 13 (2020).
25. Stumpf, M. P. H. & Porter, M. A. Critical Truths About Power Laws. *Science* **335**, 665–666 (2012).
26. Newman, M. E. J. & G. T. Barkema. *Monte Carlo Methods in Statistical Physics* 1st, 490 (Oxford University Press, New York, 1999).
27. Zierenberg, J. *et al.* Scaling properties of a parallel implementation of the multicanonical algorithm. *Computer Physics Communications* **184**, 1155–1160 (2013).
28. Gross, J. *et al.* Massively parallel multicanonical simulations. *Computer Physics Communications* **224**, 387–395 (2018).
29. Neto, J. P. *Criticality and Sampling in Neural Networks* PhD thesis (University of Göttingen, 2020).
30. Hahn, G. *et al.* Spontaneous cortical activity is transiently poised close to criticality. *PLOS Computational Biology* **13**, e1005543 (2017).
31. Petermann, T. *et al.* Spontaneous cortical activity in awake monkeys composed of neuronal avalanches. *Proceedings of the National Academy of Sciences* **106**, 15921–15926 (2009).
32. Klaus, A. *et al.* Statistical analyses support power law distributions found in neuronal avalanches. *PLoS ONE* **6** (2011).
33. Priesemann, V. *et al.* Neuronal Avalanches Differ from Wakefulness to Deep Sleep – Evidence from Intracranial Depth Recordings in Humans. *PLoS Computational Biology* **9**, e1002985 (2013).
34. Shew, W. L. *et al.* Adaptation to sensory input tunes visual cortex to criticality. *Nature Physics* **11**, 659–663 (2015).
35. Clawson, W. P. *et al.* Adaptation towards scale-free dynamics improves cortical stimulus discrimination at the cost of reduced detection. *PLOS Computational Biology* **13**, e1005574 (2017).
36. Meisel, C. *et al.* Fading Signatures of Critical Brain Dynamics during Sustained Wakefulness in Humans. *Journal of Neuroscience* **33**, 17363–17372 (2013).
37. Palva, J. M. *et al.* Neuronal long-range temporal correlations and avalanche dynamics are correlated with behavioral scaling laws. *Proceedings of the National Academy of Sciences* **110**, 3585–3590 (2013).
38. Shriki, O. *et al.* Neuronal Avalanches in the Resting MEG of the Human Brain. *Journal of Neuroscience* **33**, 7079–7090 (2013).
39. Arviv, O. *et al.* Near-Critical Dynamics in Stimulus-Evoked Activity of the Human Brain and Its Relation to Spontaneous Resting-State Activity. *Journal of Neuroscience* **35**, 13927–13942 (2015).
40. Scott, G. *et al.* Voltage Imaging of Waking Mouse Cortex Reveals Emergence of Critical Neuronal Dynamics. *Journal of Neuroscience* **34**, 16611–16620 (2014).
41. Bellay, T. *et al.* Irregular spiking of pyramidal neurons organizes as scale-invariant neuronal avalanches in the awake state. *eLife* **4**, 1–25 (2015).
42. Fagerholm, E. D. *et al.* Cascades and Cognitive State: Focused Attention Incurs Subcritical Dynamics. *Journal of Neuroscience* **35**, 4626–4634 (2015).
43. Yaghoubi, M. *et al.* Neuronal avalanche dynamics indicates different universality classes in neuronal cultures. *Scientific Reports* **8**, 3417 (2018).
44. Bocaccio, H. *et al.* The avalanche-like behaviour of large-scale haemodynamic activity from wakefulness to deep sleep. *Journal of the Royal Society Interface* **16** (2019).
45. Massobrio, P. *et al.* Self-organized criticality in cortical assemblies occurs in concurrent scale-free and small-world networks. *Scientific Reports* **5**, 1–16 (2015).

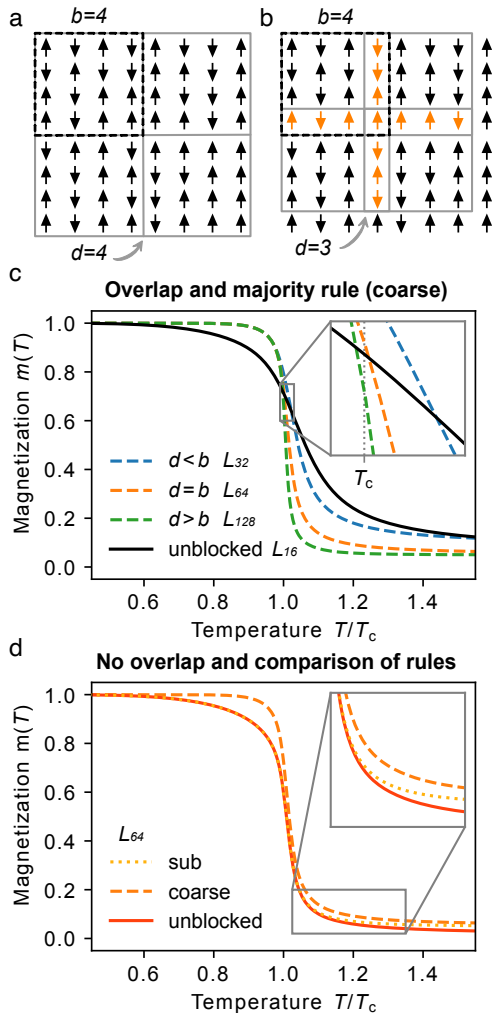


Fig G: Coarse graining the Ising model. **a:** Representation of the standard coarse graining where block size matches the distance between blocks ($d = b = 4$). No overlap is created. **b:** Coarse graining with block size $b = 4$ and a distance between blocks of $d = 3$. Overlapping spins (orange) are shared by two or more blocks. **c:** With the “coarse” majority rule, overlap impacts the spontaneous magnetization $m(T)$. Only the crossing between the unblocked ($L = 16$) and non-overlapping blocked system ($d = b$, $L = 64$) happens at $T = T_C$, as would be expected. Intriguingly, the overlap ($d < b$, $L = 32$) pushes the system towards higher magnetization where spins appear more aligned. On the other hand, the absence of overlap ($d > b$, $L = 128$) causes smaller magnetization where spins appear more random. (Note that, in order to avoid finite-size effects, the target size after coarse graining has to match, here $L = 16$. Consequently, depending on the ratio between d and b , simulations have different system sizes.) **d:** Comparison between the fully-sampled, unblocked system and blocked systems using the majority rule (“coarse”) and the decimation rule (“sub”) for $d = b = 4$. All simulations and curves for $L = 64$. In the ordered, low-temperature phase, the sub curve matches the fully sampled system. Only for the high-temperature phase deviations occur due to finite-size effects (the magnetization for $T \rightarrow \infty$ approaches the value expected for the rescaled $L = 16$ system). The coarse curve is systematically biased towards more ordered states.

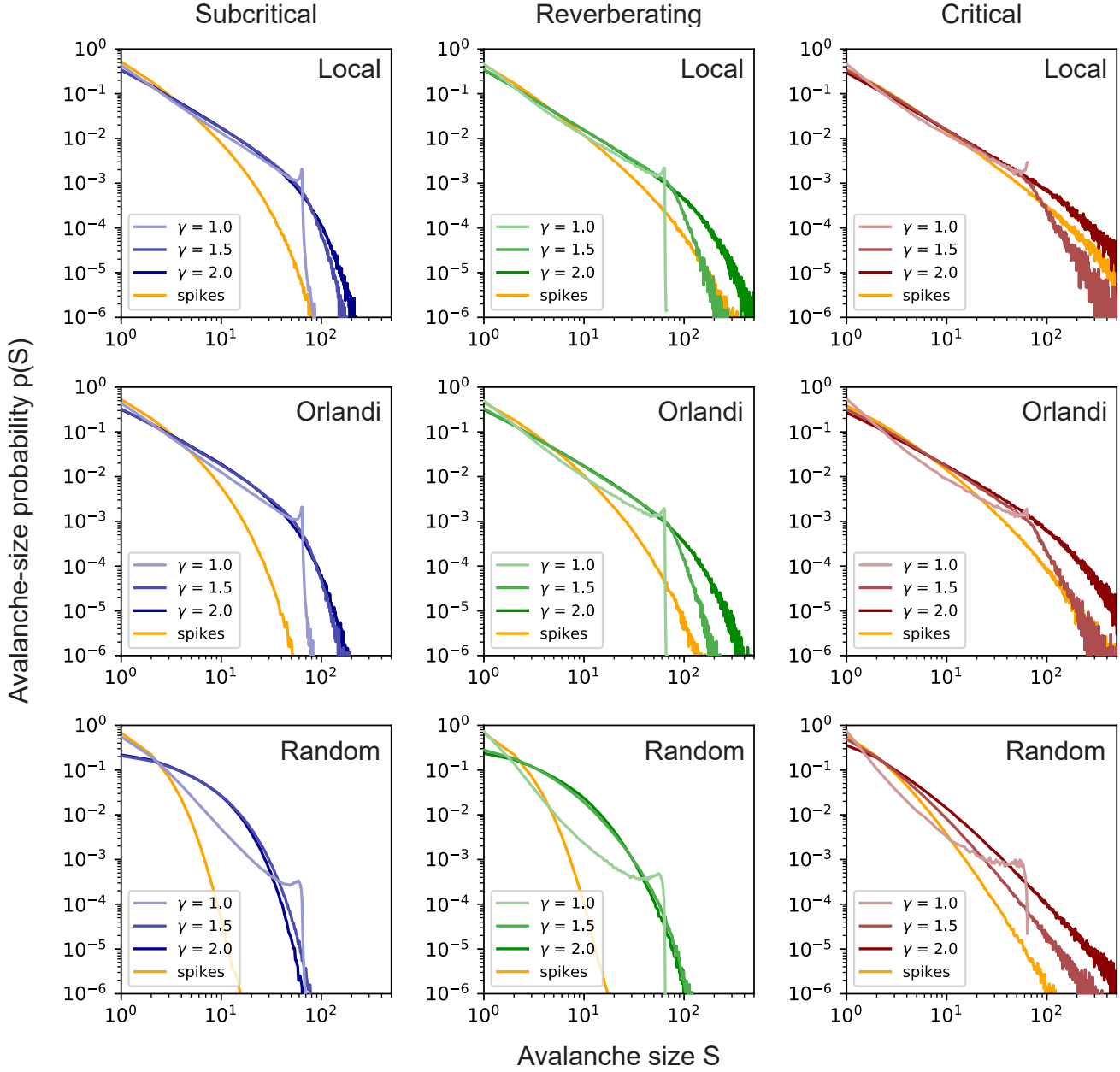


Fig H: Effect of changing the electrode contribution $\sim 1/d^\gamma$ of a spiking neuron at distance d , for different network topologies and $d_E = 200 \mu\text{m}$. Dynamic states are Subcritical (**left**), Reverberating (**center**) and Critical (**right**). Topologies are Local (**top**), Orlandi (**middle**) and Random (**bottom**). Local corresponds to the topology used in the main paper, Orlandi corresponds to the model described in [1], and Random corresponds to a completely random topology. Increasing γ (decreasing electrode FOV) results in a loss of the cut-off for $p(S) \sim N_E$ as the coarse-sampling becomes more spike-like. Bin-size for all distributions is $\Delta t = 4 \text{ ms}$.

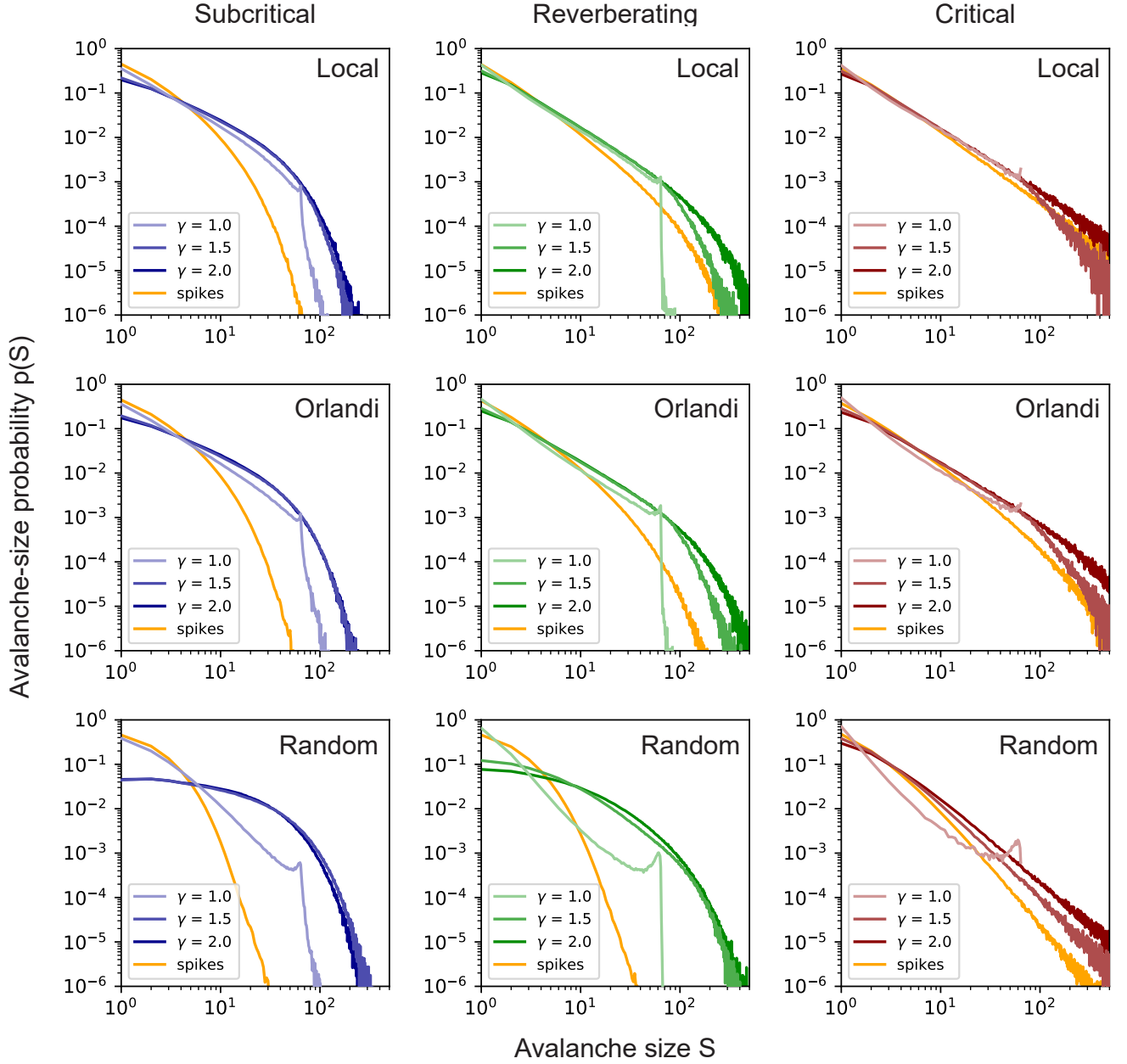


Fig I: Effect of changing the electrode contribution $\sim 1/d^\gamma$ of a spiking neuron at distance d , for different network topologies and $d_E = 400 \mu\text{m}$. Dynamic states are Subcritical (**left**), Reverberating (**center**) and Critical (**right**). Topologies are Local (**top**), Orlandi (**middle**) and Random (**bottom**). Local corresponds to the topology used in the main paper, Orlandi corresponds to the model described in [1], and Random corresponds to a completely random topology. Increasing γ (decreasing electrode FOV) results in a loss of the cut-off for $p(S) \sim N_E$ as the coarse-sampling becomes more spike-like. Bin-size for all distributions is $\Delta t = 8 \text{ ms}$.

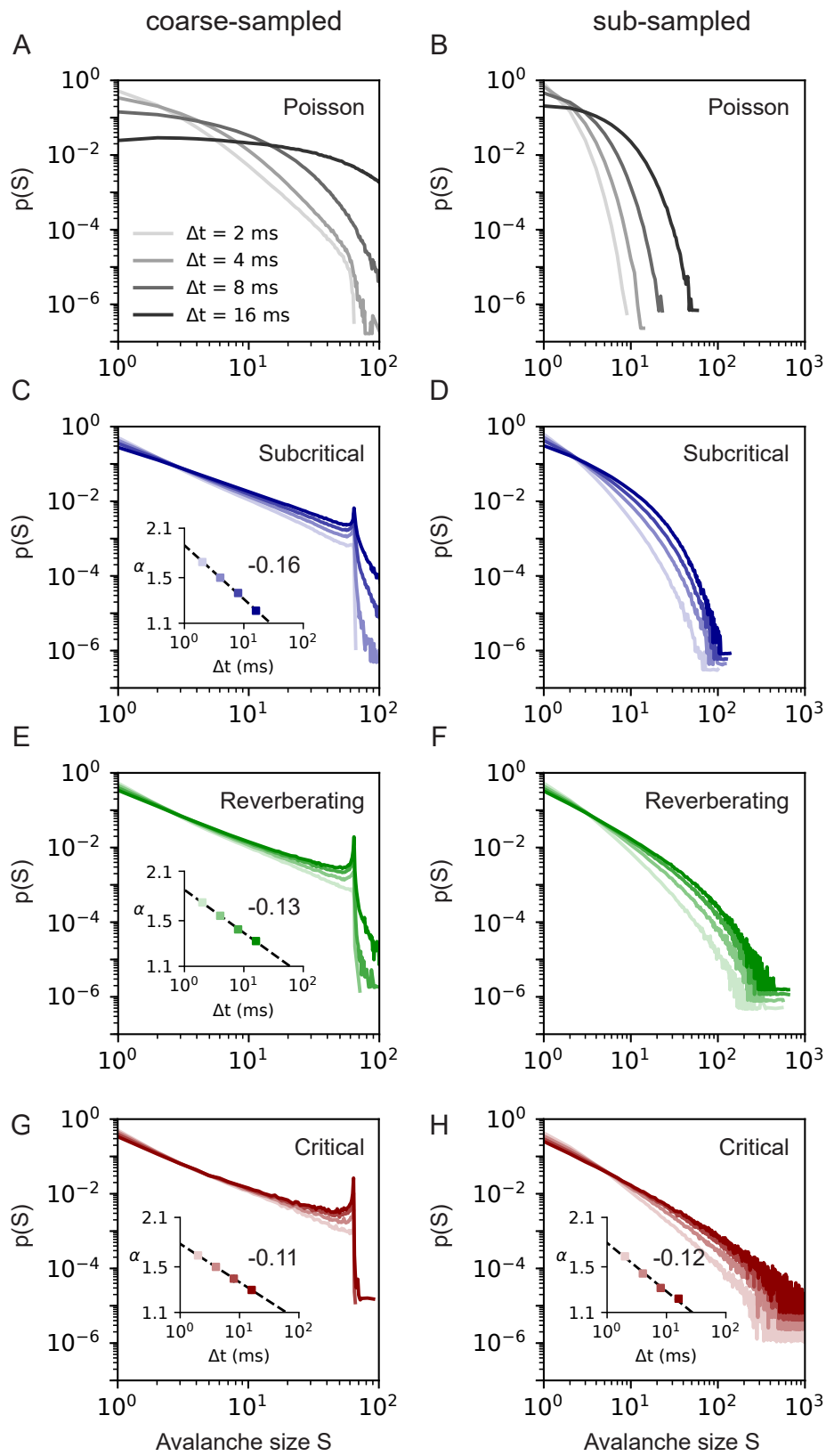


Fig J: Avalanche-size distributions $p(S)$ dependence on time-bin size Δt for $d_E = 200 \mu\text{m}$. Coarse-sampled (left) and sub-sampled (right) results from an array of 64 virtual electrodes with time bin sizes between $2 \text{ ms} \leq \Delta t \leq 16 \text{ ms}$. Dynamics states are Poisson (a-b), Subcritical (c-d), Reverberating (e-f) and Critical (g-h). Distributions are fitted to $p(S) \sim S^\alpha$. **Insets:** Dependence of α on Δt , fitted as $\alpha \sim \Delta t^{-\beta}$. Fit values are shown in Table. 3.

B Supplementary material for “*Modular architecture facilitates noise-driven control of synchrony in neuronal networks*”

Supplementary Materials for
Modular architecture facilitates noise-driven control of synchrony in neuronal networks

Hideaki Yamamoto *et al.*

Corresponding author: Hideaki Yamamoto, hideaki.yamamoto.e3@tohoku.ac.jp;
Jordi Soriano, jordi.soriano@ub.edu

Sci. Adv. **9**, eade1755 (2023)
DOI: 10.1126/sciadv.ade1755

The PDF file includes:

Supplementary Text
Figs. S1 to S12
Tables S1 to S7
Legends for movies S1 to S8
References

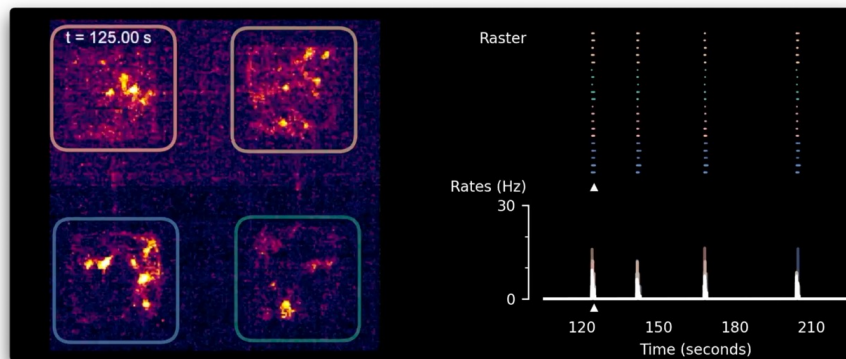
Other Supplementary Material for this manuscript includes the following:

Movies S1 to S8

1. SUPPLEMENTARY VIDEOS AND EXTENDED EXPERIMENTAL RESULTS

A. Supplementary Videos

Videos encompass both experimental recordings and numerical simulations of networks of spiking neurons. The videos corresponding to experimental recordings are played at $20\times$ speed. The left-hand side of the videos shows the recording, while the right-hand side shows the raster plot derived from its analysis. The original image sequences were obtained in greyscale format and here are presented as a blue–red–yellow color scheme to enhance the visualization of activity. The brighter the color, the stronger the activity of the neurons. For modular networks, each of the 4 modules is highlighted with a faint colored outline, where the color matches the grouping of spikes and module rates on the right.



Video 1. Single–bond network during spontaneous activity.

These recordings and their raster plots are the same ones shown in Figs. 1D–G of the main manuscript.

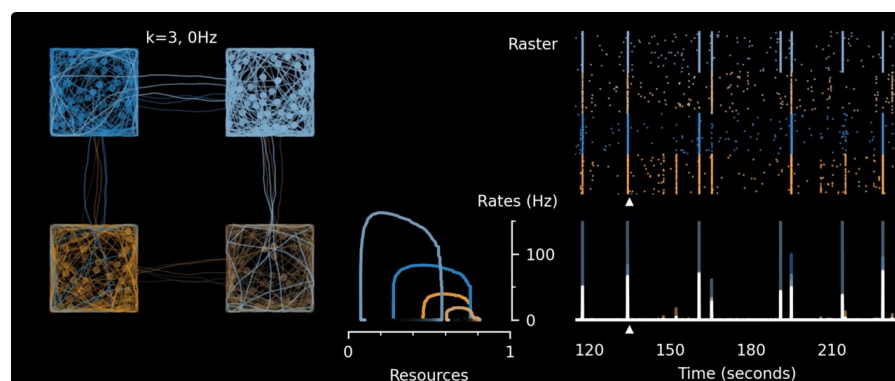
Video 2. Same network as in Video 1 but under optogenetic stimulation.

Video 3. Single–bond network during spontaneous activity before chemical stimulation with potassium. The raster plots correspond to the data shown in Figs. 1H–I of the main manuscript.

Video 4. Same as network as Video 3 but after chemical stimulation with high potassium.

Video 5. Single–bond network during spontaneous activity while exposed to bicuculline.

Video 6. Single–bond network exposed to bicuculline under optogenetic stimulation.



Video 7. Simulations, model of spiking neurons with modules connected by $k = 3$ axons, with neurons receiving only baseline noise.

Video 8. Same network and random number seed as Video 7 but neurons in the lower two modules receive 20 Hz additional noise beyond baseline.

B. Comparison of Different Optogenetic Stimulation Paradigms

In the following, we describe two control experiments to investigate i) the role of how many modules are targeted (partial vs global stimulation) and ii) the impact of asynchronous vs synchronous stimulation (Fig. S1). We focus on modular, single-bond topologies. Note that for these new control experiments, substrates differ from the main manuscript: Cultured cortical neurons were patterned using *microfluidic devices* [83], which we found to provide more reproducible results. The four modules again consist of $200\ \mu\text{m} \times 200\ \mu\text{m}$ squares that are connected by microchannels of three different sizes to adjust the degree of modularity (S: $4\ \mu\text{m}$ width \times $2\ \mu\text{m}$ height, M: $7 \times 2\ \mu\text{m}$, L: $7 \times 4\ \mu\text{m}$). All experiments were conducted at 10–11 DIV, as in the other experiments. For each channel size, we considered three stimulation protocols:

- **stim2** is the protocol described in the main manuscript. The lower two modules are targeted by asynchronous optogenetic stimulation, where ten individual neurons are preselected candidates to be targeted (during each 400 ms time bin, every candidate has a probability $p = 0.4$ to be stimulated).
- **stim4** is similar to the protocol of the main manuscript, but two to three candidates are selected from each of the four modules (ten in total). Note that, due to an experimental constraint, the area from which neurons can be selected is limited, so that candidates do not cover the whole culture.
- **stim1** is a synchronous stimulation protocol, where the entire area of one of the four modules was targeted with a square light pulse of 400 ms. The pulses were delivered at a mean interval of 10 s with a standard deviation of 2 s.

Partial stimulation: We first confirmed the reproducibility of the experiments reported in the main manuscript by applying protocol **stim2**. As shown in the example raster plots (Fig. S1A), collective activity events present in the spontaneous activity (**pre**) were disrupted during stimulation, which decreased the overall neuron correlation and event size (Fig. S1B) and recovered during **post** (not shown). The decrease in correlation was also observed when the optogenetic stimulation was delivered locally, to one of the four modules (**stim1**, Fig. S1B). However, note that the typical response of the cultures to the **stim1** differed to **stim2**: The synchronous stimulation reliably triggered bursting activity, causing an event that started in the targeted module and probabilistically propagated to neighbouring modules, potentially spanning the whole system. This observation is in line with the gating mechanism that we abstractly model in the mesoscopic description (Section 3, below). The asynchronous stimulation, on the other hand, did not trigger events deterministically at pre-defined times. This can be seen as a confirmation of our proposed resource mechanism. Reconsidering the recharge dynamics (main Fig. 4A–C), the perturbing effect of the **stim1** protocol should vanish if the delivery of the pulse is timed to match the intrinsic, natural timing of events each culture has. In this case, the duration of charge-discharge cycles would not be altered, merely the onset-times of events. On the other hand, if pulses are delivered at a higher frequency, resources would be depleted more often. To confirm this intuition, we color-coded the lines representing each culture according to its (natural) IEI during the **pre** condition (Fig. S1). For **stim1**, and channel size M in particular, this intuition seems confirmed: Those realizations where the IEI was already short before the stimulation at $1/10$ s (yellow and red) tend to show smaller changes.

Global stimulation: As presented in Fig. 1 of the main manuscript, a global increase in neuronal excitability induced by chemical stimulation did not break synchrony in modular networks. To address the question whether global but asynchronous stimulation does break synchrony, we applied the protocol **stim4**. Overall, the results for this protocol show the same trends as for **stim2**, with decreased event sizes and neuron correlations, and a strong dependence on the topology.

Channel size: The most consistent trend in the results of these new control experiments is the dependence on channel size. In particular, for large channels (L), where presumably connections between modules are strong and modularity low, the effect size of all stimulation protocols tends to be smallest. This supports our main conclusion, that the modularity of the topology is the key ingredient to facilitate the desynchronizing effect of stimulation.

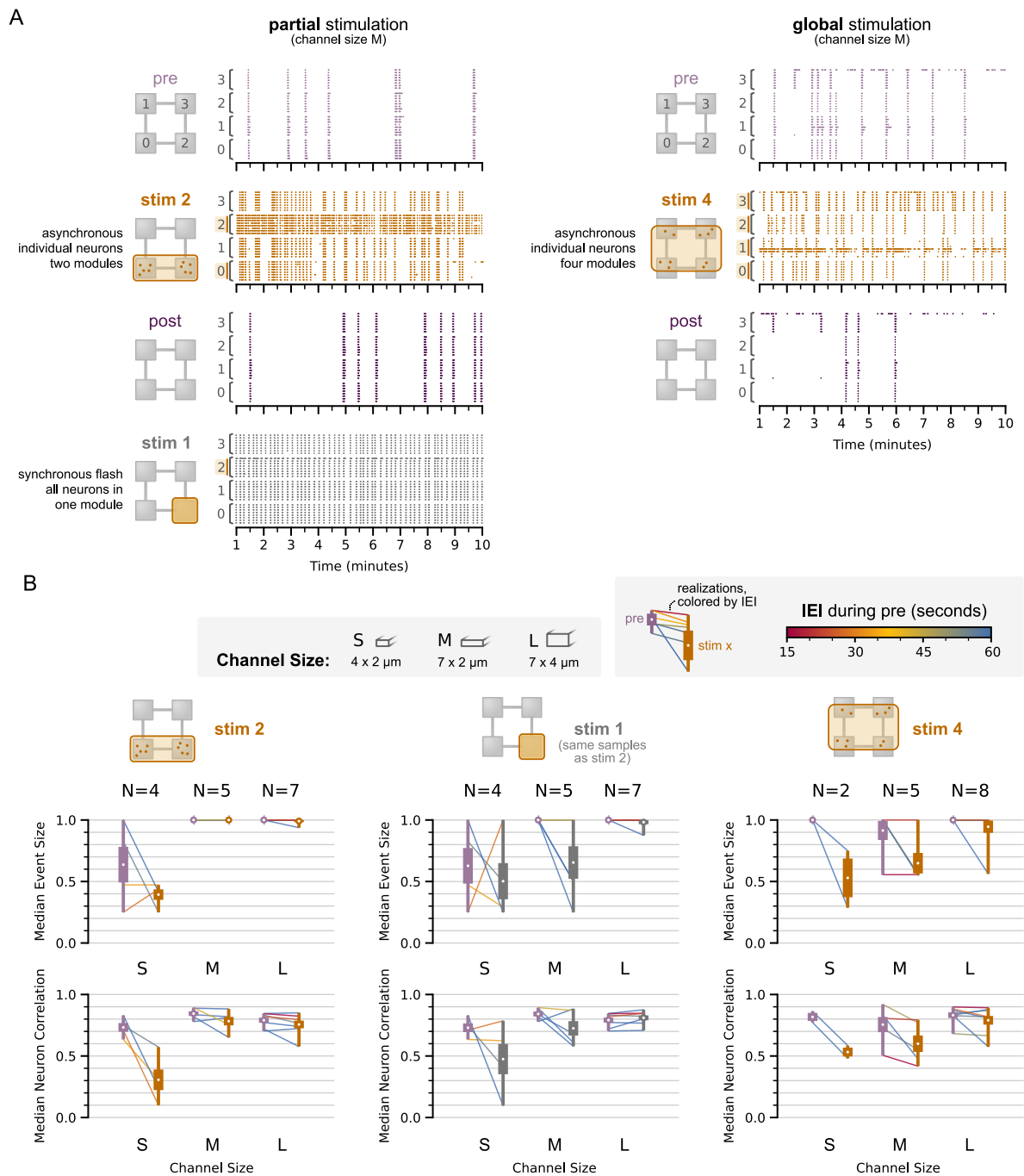


Figure S1. **Comparison of different optogenetic stimulation paradigms.** **A:** Raster plots. As controls of the asynchronous stimulation in two modules **stim2** (main manuscript), we considered two other stimulation paradigms. In **stim1**, a single module was targeted with a flash covering the whole module every ~ 10 s. Thus, the stimulation was *synchronous* (to all neurons of this module) and *partial*, as only a subset of the modules was targeted. Notably, flashes reliably cause events that span at least the targeted module. In **stim4**, individual neurons from all modules were targeted *asynchronously*, similar to **stim2** but extending the stimulation region to the full system (*global*). However, note a constraint of the experimental setup that limited the location of neurons that could be targeted to parts of each module. **B:** For these stimulation paradigms, we compare the **pre** condition with the respective **stim** condition, for three different channel sizes, S, M, and L. Note that the samples for partial stimulation (**stim2** and **stim1**) are correlated, as they were recorded in sequence, from the same cultures. For each realization, the line connecting **pre** and **stim** is color-coded by the mean inter-event-interval (IEI, measured during the **pre** condition). This serves as a proxy for the strength of the perturbation caused by **stim1**: In this paradigm, the impact of stimulation on the recharge dynamics is presumably small when the frequency of the flash (every ~ 10 s) is close to the intrinsic IEI (red for 15 s, blue for 60 s). Because asynchronous stimulation (**stim2**, **stim4**) targets individual neurons, and does not trigger events that span a whole module, this dependence seems less pronounced. Independent of the stimulation protocol, note the dependence on channel size (as an indicator for modularity): With increasing channel size, the effect from all considered forms of stimulation decreases.

C. Effect of the Blockade of Inhibition on Dynamics

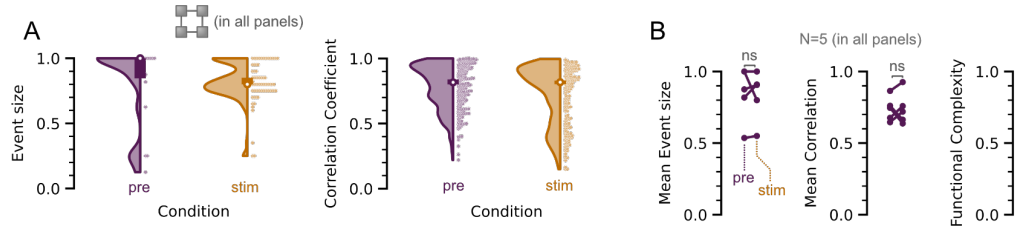


Figure S2. **The desynchronizing effect of optogenetic stimulation relies on GABAergic balancing.** Data collected on 1-b modular networks ($N = 5$ trials) in the presence of $20 \mu\text{M}$ bicuculline, a GABA_A receptor antagonist. The data for this assay was collected using 1-b modular networks grown in both microcontact printed substrates and microfluidic devices (Ref. [83], different samples from those analyzed in the previous section). **A:** Aggregated distributions of network-wide events (left) and pairwise correlation coefficients (right). **B:** Trial-to-trial estimates of the mean event size, mean correlation, and functional complexity. ns, no significance (two-sided, paired-sample t-test). We note that administration of bicuculline at $20 \mu\text{M}$ may seize or substantially decrease the rate of spontaneous activity in small-scale neuronal networks, such as those used in the present work, at 10–11 DIV. In such a case, similar effects could be observed at a concentration of $\sim 5 \mu\text{M}$.

D. Statistics across Experimental Repetitions

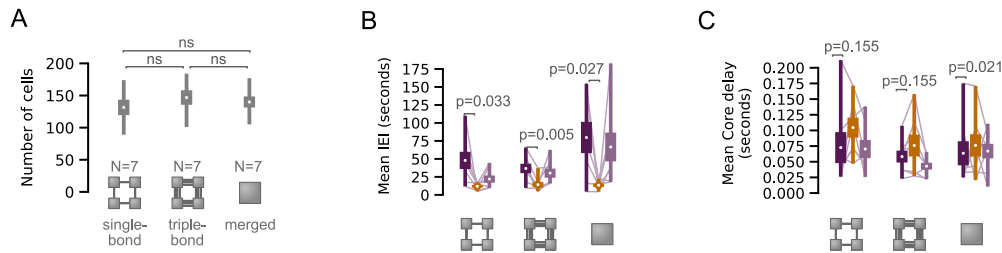


Figure S3. **Trial-level estimates**, related to main Fig. 2. **A:** Mean number of cells per network. The differences between the means of the three topologies are statistically not significant. Two-sided, unpaired t-test. **B, C:** Every faint line corresponds to the estimate of a quantity within one trial and its change across conditions (pre, stim and post). Error bars (thick vertical lines) are obtained from bootstrapping the within-trial estimates (500 samples). The white dot denotes the mean of the bootstrap samples, and the extended thin vertical line indicates the maximal and minimal value observed in a trial. The indicated statistical significance (pre to stim) is calculated from two-sided, paired-sample t-tests. For p-values of all combinations, see Table S1.

Layout	Comparison	Rate	Event size	Neuron correlation	Functional complexity	IEI	Core delay
1b ($N = 7$ trials)	pre-stim	0.8411	0.0067	0.0084	0.0524	0.0338	0.1557
	stim-post	0.6910	0.0130	0.0071	0.0037	0.1033	0.0719
	pre-post	0.9685	0.1749	0.9631	0.5391	0.1219	0.8875
3b ($N = 7$ trials)	pre-stim	0.2072	0.0513	0.0335	0.0384	0.0057	0.1556
	stim-post	0.2957	0.0617	0.0103	0.0170	0.0428	0.0647
	pre-post	0.3505	0.6590	0.9678	0.0666	0.4373	0.0898
merged ($N = 7$ trials)	pre-stim	0.0284	0.0463	0.0195	0.0469	0.0278	0.5641
	stim-post	0.1773	0.0542	0.0181	0.0560	0.0678	0.6848
	pre-post	0.6078	0.4167	0.3847	0.9992	0.7199	0.8951

Table S1. Overview of p-values for Main Fig. 2 and Suppl. Fig. S3. Two-sided, paired-sample t-test.

2. DETAILS OF THE MICROSCOPIC MODEL OF SPIKING NEURONS

A. Topology

To create the 2D topology, we model axonal growth as proposed by Orlandi et al. [18] (cf. Table S3). Neurons are spread out uniformly over a 2D surface where somas are modeled as hard, non-overlapping discs with radius $r_s = 7.5 \mu\text{m}$ from which axons grow on a semi flexible path with mean length $l_a \approx 1000 \mu\text{m}$. The path is constructed from several concatenated axonal segments of unit length $\delta_a = 10 \mu\text{m}$. The variance of the mean bending angle $\sigma(\theta)$ along neighboring segments determines the overall stiffness. If an axon intersects the dendritic tree of another neuron (modeled as soft disks with mean radius $r_d \approx 150 \mu\text{m}$), then each overlapping segment has probability α to establish the connection. (Note, this is a different convention than Ref. [18], where the probability to form the connection is independent of the number of intersecting segments.) Because dynamics are heavily dependent on the in-degree, we adjust α so that $k_{\text{in}} \approx 30$ incoming connections per neuron [82] for all topologies, independent of their modularity. Once the connections are set (as a binary matrix), additional details of the topology can be discarded. The types of neurons (inhibitory GABAergic or excitatory AMPA-glutamatergic) are not distinguished topologically.

In order to create the modular topology, soma, axon segments, and dendritic trees are only placed on the substrate, which consists either of one $400 \times 400 \mu\text{m}^2$ rectangle (merged) or four $200 \times 200 \mu\text{m}^2$ rectangles (modular). To avoid axons growing out of the substrate, larger bending angles (with increased variance $\sigma(\theta') = 5\sigma(\theta)$) are allowed near the domain walls, which effectively deflect the axons back into the module (main Fig. 3A). To connect neighboring modules with a given number of axons, every module acts once as a “source module”. Then, for every adjacent neighboring module, k neurons are selected and forced to first grow their axons towards the center of the target module (neglecting the substrate) before the growth continues randomly within the target, again confined to the substrate. The in-degree distributions for the different topologies are summarized in Fig. S5.

We found this controlled approach to produce more consistent topologies than an algorithm where we would add a given number of bridges as an actual part of the substrate (as in the experiments) and axons had to grow through the bridges by chance. For the latter case, it frequently occurred that modules were only connected in one direction or not connected at all. As the topological structure is the backbone of the observed dynamics, a much larger number of repetitions would have been needed to find reliable ensemble estimates of observables.

B. Modularity

In the following, we show analytically how the modularity index Q depends on the number of axons crossing between modules (\mathbf{k}) and the in-degree per neuron (k_{in})¹. The straightforward mathematical way of measuring how well a partition splits the graph into modules is computing the *modularity*—the fraction of the edges that fall within the given groups minus the expected fraction if edges were distributed at random [84]. While using this measure to find community division is criticized [85], in our case, communities are already defined (as modules) per the experimental or theoretical construction, and we evaluate the modularity for this partitioning.

Modularity is formally defined as:

$$Q = \frac{1}{2m} \sum_{ij} \left(A_{ij} - \gamma \frac{k_i k_j}{2m} \right) \delta(c_i, c_j), \quad (1)$$

where m is the total number of edges, A_{ij} is the adjacency matrix of the graph, k_i is the degree of node i , γ is the resolution parameter that we take, $\gamma = 1$, and $\delta(c_i, c_j)$ is 1 if nodes i and j belong to the same community and 0 otherwise. The summation is performed over all pairs of nodes in the network. The simplified formula for Q reads:

$$Q = \sum_{c=1}^n \left[\frac{L_c}{m} - \gamma \left(\frac{k_c}{m} \right)^2 \right], \quad (2)$$

where summation is performed over all modules c , L_c is number of links within a module, and k_c is the sum of the degrees of all nodes of the module.

When growing the networks with axons crossing over between modules, we control the mean in-degree per neuron. To do so, we need to adjust the expected density of connections per unit length α . Let us compute the number of

¹ Note that the number of axons that cross to neighbouring modules is denoted by k in the rest of the material. In this section, we denote it as \mathbf{k} to differentiate from other degree-related variables.

connections, assuming N neurons in the module and \mathbf{k} neurons that would form a cross-module axon per neighbour. In this case, the total number of connections between neurons of the same module (L_c) is a sum of connections due to axons not crossing modules plus connections due to the parts of crossing axons that are still within the same module. With our model parameters (200 μm module size / separation and $l_a \approx 1000 \mu\text{m}$ axon length) a crossing axon spends $\sim 100 \mu\text{m}$ in the source module, $\sim 200 \mu\text{m}$ between modules, and $\sim 700 \mu\text{m}$ in the target module. Thus, the number of connections within the same module L_c is given by

$$L_c = (N - 2\mathbf{k})\alpha \cdot l_a + 0.1 \cdot 2\mathbf{k} \cdot \alpha \cdot l_a = (N - 1.8\mathbf{k})\alpha \cdot l_a. \quad (3)$$

The number of connections coming from the two other neighbouring modules is proportional to the axon parts they have within the target module, $0.7l_a$:

$$L_o = 0.7 \cdot 2\mathbf{k} \cdot \alpha \cdot l_a = 1.4\mathbf{k} \cdot \alpha \cdot l_a. \quad (4)$$

Combining Eq. 3 and Eq. 4, we get the average in-degree per neuron

$$k_{in} = (L_c + L_o)/N = \alpha l_a (N - 0.4\mathbf{k})/N, \quad (5)$$

which, taking, without loss of generality, $l_a = 1$, gives us

$$\alpha = \frac{k_{in}N}{N - 0.4\mathbf{k}}. \quad (6)$$

The total number of edges in the network is given by $m = 4k_{in}N$ (note that, here, N denoted the number of neurons per module). Inserting the computed m , L_c , and α into Eq. 2 we get

$$Q = \sum_{c=1}^4 \left(\frac{L_c}{4k_{in}N} - \left(\frac{k_{in}N}{4k_{in}N} \right)^2 \right) = 4 \left(\frac{(N - 1.8\mathbf{k})k_{in}N}{4(N - 0.4\mathbf{k})k_{in}N} - \frac{1}{16} \right) = \frac{N - 1.8\mathbf{k}}{N - 0.4\mathbf{k}} - \frac{1}{4}. \quad (7)$$

Interestingly, the final result does not depend on the choice of k_{in} —which gives us some degree of freedom to select a reasonable value for it in simulations (we took $k_{in} = 30$). The computed modularity closely matches the observations from network generation (minor discrepancies are expected due to variable degrees and actual numbers of synapses in every simulation. cf. Table S2).

	analytic	simulations, for different k_{in}			
		$k_{in} = 15$	20	25	30
$k=0$	0.750	0.748	0.749	0.749	0.749
$k=1$	0.715	0.706	0.706	0.705	0.705
$k=3$	0.642	0.621	0.619	0.618	0.616
$k=5$	0.566	0.535	0.533	0.532	0.530
$k=10$	0.361	0.322	0.322	0.322	0.324
$k=20$	-0.125	-0.102	-0.089	-0.074	-0.057
merged	0	0.018	0.018	0.019	0.019

Table S2. Modularity Q for different k vs. k_{in} combinations. Analytically, Q is independent from k_{in} , which is closely matched by the values measured in simulations.

C. Dynamics

To model neuronal behaviour, we use quadratic integrate-and-fire dynamics [80] with synaptic depression [86], which is implemented in a reduced form as in Ref. [18]. The neuron population consists of 20% inhibitory and 80% excitatory neurons, where inhibitory currents are modeled to have a higher amplitude and a slower decay time than excitatory ones [49, 87], cf. Table S3. Dynamic parameters of the model were chosen so that the network resembles regular spiking neurons [80] and the frequency of network-wide events was between 3 to 12 per minute, as observed in the experiments. Note that the parameter combination that was ultimately used is not unique and other combinations could yield the same burst frequency [88].

Independent of the neuron type, membrane dynamics are described through two coupled differential equations² for the membrane potential v and the recovery variable u :

$$\tau_v \dot{v} = a(v - v_{\text{ref}})(v - v_{\text{thr}}) - u + I_{\text{AMPA}} - I_{\text{GABA}}, \quad (8)$$

$$\tau_u \dot{u} = b(v - v_{\text{ref}}) - u, \quad (9)$$

$$\text{if } v \geq v_{\text{peak}} : \begin{cases} v \rightarrow v_{\text{reset}}, \\ u \rightarrow u + u_{\text{incr}}. \end{cases} \quad (10)$$

The first term in Eq. (8) describes the basic behavior of the membrane potential. Below threshold, $v < v_{\text{thr}}$, the membrane potential slowly decays to the resting value v_{ref} depending on the characteristic time constant τ_v and leak factor a . Once the threshold is exceeded by repeated stimulation, the membrane potential rises quickly until the peak potential v_{peak} is reached, a spike is triggered, and the potential is reset to v_{reset} . The membrane potential is decreased through the recovery variable u , which is driven by the activation of K^+ currents and the inactivation of Na^+ currents [80]. In practice, the coupling of Eqs. (8) and (9) determines the inter-spike interval and implements an effective refractory period.

The coupling of neurons is realized through excitatory and inhibitory current terms in Eq. 8: I_{AMPA} and I_{GABA} consist respectively of all excitatory and inhibitory currents arriving from the rest of the network. Each spike from a presynaptic neuron instantaneously increments the current term of the postsynaptic neuron. Note that in Ref. [18] small membrane fluctuations were implemented through an additional term, which we here omit to control the level of noisy input through a single control parameter.

Whenever an excitatory (inhibitory) pre-synaptic neuron spikes, it emits a current I that increments (decrements) the membrane potential of the post-synaptic neuron. The strength of the current depends on the amount of pre-synaptic resources (associated with the available neurotransmitters). To model the synaptic currents I and the level of synaptic resources ($R = 1$ for full available resources, $R = 0$ for full depletion), every neuron has three additional dynamic variables:

$$\tau_{\text{AMPA}} \dot{I}_{\text{AMPA}} = -I_{\text{AMPA}}, \quad (11)$$

$$\tau_{\text{GABA}} \dot{I}_{\text{GABA}} = -I_{\text{GABA}}, \quad (12)$$

$$\tau_R \dot{R} = 1 - R, \quad (13)$$

$$\text{if } v \geq v_{\text{peak}} : R \rightarrow \beta R. \quad (14)$$

Note that I respectively describes all excitatory and inhibitory currents that arrive at the neuron, whereas R scales the outgoing current ($0 \leq \beta \leq 1$). Whenever a pre-synaptic neuron of type x spikes, the respective post-synaptic current term (AMPA or GABA) is incremented instantaneously:

$$I_{x,\text{post}} \rightarrow I_{x,\text{post}} + j_{x,\text{pre}} R_{\text{pre}}, \quad (15)$$

where $j_{x,\text{pre}}$ is a constant to describe the current strength that depends on the type of the pre-synaptic neuron. From Eqs. (11)–(13), we see that I_x decay to 0 with a characteristic time τ_x and R slowly recovers to 1 with τ_R . In general, τ_R is much longer than the other time constants (see Table S3).

D. Stimulation

To incorporate optogenetic stimulation, the model features a controlled source of noise. The excitatory current arriving at each neuron is increased by small spikes of amplitude j_m generated randomly by a Poisson process

$$I_{\text{AMPA}} \rightarrow I_{\text{AMPA}} + j_m \quad \text{at rate } h, \quad (16)$$

where h denotes the ‘‘synaptic noise rate’’ that serves as our control parameter when investigating the interplay of modularity and stimulation (main Figs. 3, 4 and Fig. S4).

In the main manuscript, we consider a baseline noise level to all neurons at $h = 80$ Hz, which accounts for miniature synaptic potentials (‘‘minis’’) even in the absence of stimulation [18]. To mimic the experimental stimulation within two modules, additional Poisson noise at 20 Hz is applied to the neurons in those modules. Note that, because Poisson noise is additive, a local increase of the baseline input to 100 Hz would be equivalent.

² We express the equations in reduced form, and, for readability, omit the resistance R by denoting $I := RI^*$.

Parameter	Description	References
Topology		[18]
$N = 160$	Number of neurons, out of which 20% inhibitory	[49, 87]
$200 \mu\text{m} \times 200 \mu\text{m}$	Substrate area per module (4 modules)	
$\rho = 1000 \text{mm}^{-2}$	Density of plated neurons	
$r_s = 7.5 \mu\text{m}$	Radius of somas (hard discs)	
$r_d \approx 150 \mu\text{m}$	Radius of dendritic trees (soft discs), drawn from Normal dist. ($\mu = 150 \mu\text{m}$, $\sigma = 20 \mu\text{m}$)	
$l_a \approx 1000 \mu\text{m}$	Length of axons, drawn from Rayleigh dist. ($\sigma = 800 \mu\text{m}$)	
$\delta_a = 10 \mu\text{m}$	Length of axon segments	
$\theta \approx 0^\circ$	Bending angle between segments, drawn from Normal dist. ($\mu = 0^\circ$, $\sigma = 57^\circ$)	
$\alpha \approx 0.3 - 2.7\%$	Probability to form a connection, per intersecting axon segment. Adjusted to realize k_{in} .	
$k_{\text{in}} \approx 30$	Average in-degree per neuron (all substrates)	[82]
Dynamic variables		
v	Membrane potential	
u	Recovery variable	
I_{AMPA}	Excitatory current	
I_{GABA}	Inhibitory current	
R	Synaptic resources	
Time scales		
$\tau_v = 50 \text{ms}$	Time scale of the membrane potential v	
$\tau_u = 50 \text{ms}$	Time scale of the recovery variable u	
$\tau_R = 20 \text{s}$	Time scale of recovery of synaptic resources R	
$\tau_{\text{AMPA}} = 10 \text{ms}$	Decay time of post-synaptic excitatory current	
$\tau_{\text{GABA}} = 20 \text{ms}$	Decay time of post-synaptic inhibitory current	
Dynamic constants		[18, 80]
$v_{\text{ref}} = -60 \text{mV}$	Resting potential	
$v_{\text{thr}} = -45 \text{mV}$	Threshold potential	
$v_{\text{peak}} = 35 \text{mV}$	Peak potential, after v_{thr} is passed, rapid growth towards v_{peak}	
$v_{\text{reset}} = -50 \text{mV}$	After-spike reset value of the membrane potential v	
$u_{\text{incr}} = 50 \text{mV}$	After-spike increment value of recovery variable u	
$a = 0.5 \text{mV}^{-1}$	Leak factor	
$b = 0.5$	Sensitivity of u to sub-threshold fluctuations of v	
$j_{\text{AMPA}} = 45 \text{mV}$	AMPA current strength	
$j_{\text{GABA}} = 50 \text{mV}$	GABA current strength	
$\beta = 0.8$	$R \rightarrow \beta R$ after spike, here synaptic depletion, thus $\beta < 1$	
$h = 80 - 115 \text{Hz}$	Rate for Poisson noise (80 Hz baseline, 0 – 35 Hz stimulation)	
$j_m = 15 \text{mV}$	Strength of Poisson noise (stimulation), applied on I_{AMPA}	
Simulation settings		[89]
$T = 30 \text{min}$	Simulation time (after 5 min thermalisation)	
$\delta t = 0.05 \text{ms}$	Time-step of numeric time integration (Euler)	
$\approx 30 \text{min}$	Wall-clock runtime per simulation	
50	Number of repetitions	

Table S3. Overview of parameters and variables of the microscopic model.

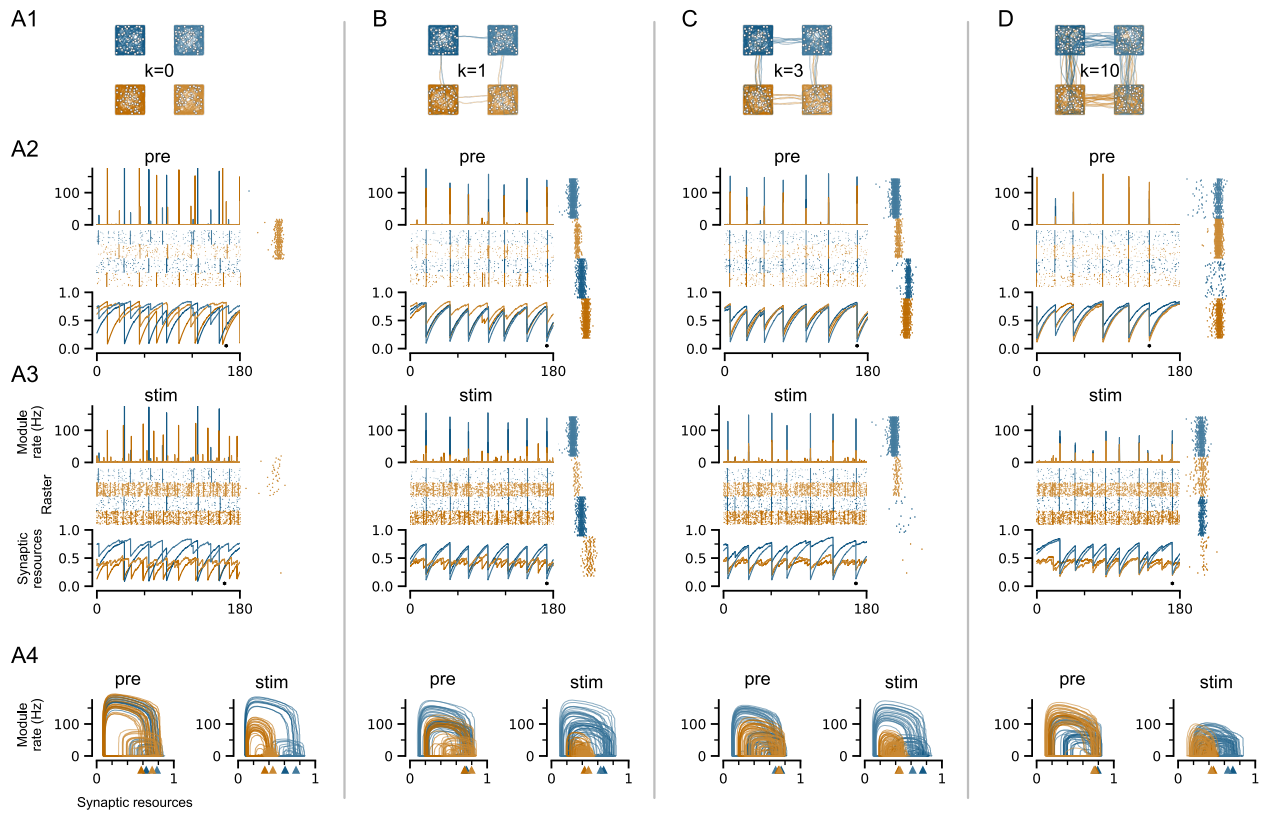


Figure S4. **Extended simulation details.** **A:** Overview of topology and dynamics for $k = 0$, corresponding to four independent modules. The dynamics plotted below (A2–A4) share this topology (and the RNG seed), and differ only in the stimulation rate. **A1:** Representation of the topology, featuring soma (white circles) and axons (colored lines). **A2, A3:** Module-level firing rate, raster plot and synaptic resources for a 180 s time window at 80 Hz baseline input (pre), and with an additional 20 Hz stimulation to the orange modules (stim). Synaptic resources are averaged across all neurons in a particular module and color-coded accordingly. The black dot denotes a 250 ms long zoom into the raster plot to illustrate a single event. **A4:** Charge-discharge cycles are illustrated in the resource-rate plane. Both synaptic resources and firing rates are calculated on the module level. 80 traces are shown (20 per module) where each trace lasts from end-time to end-time of two consecutive events (system-level bursting). The triangles on the x -axis indicate the average level of resources when an event starts. **B–D:** like A, but for $k = 1$, $k = 3$ and $k = 10$. **Summary:** In general, stimulation causes bursts to fire at lower rates (circle size) and to start at lower resource levels (triangles near x -axis). When modules are disconnected ($k = 0$), cycles reflect single-module properties independent of the stimulation. For intermediate connections ($k = 3$), the fluctuation in the trajectories of the non-targeted modules is strongest, but still retains module-dependent sizes. When intermodular connection is further increased ($k = 10$), cycles of non-targeted modules also decrease, as they activate together with targeted modules—while synchrony is maintained due to strong connections.

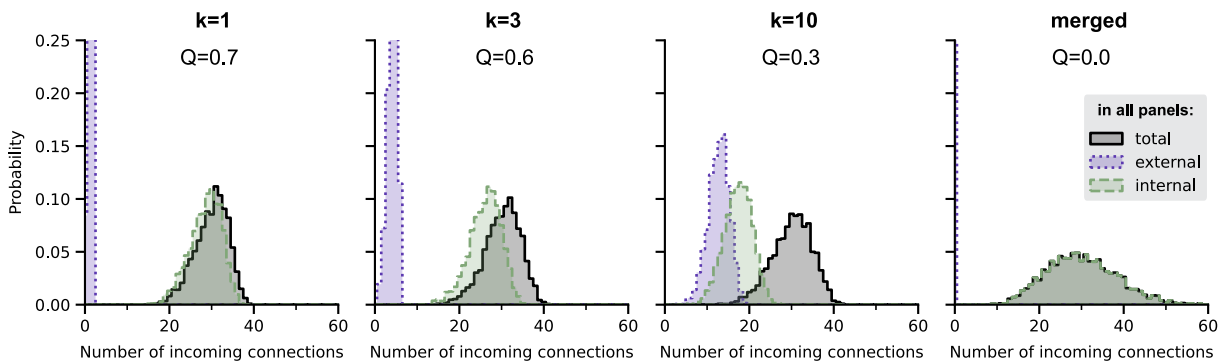


Figure S5. **In-degree distributions for different topologies.** For all topologies, the growth was adjusted to match an expected in-degree of $k_{in} \approx 30$. In simulations, modular cultures synchronize less strongly when average synaptic resources get depleted. This effect depends on the the number of incoming connections, which, determined by the topology, may greatly differ between *internal* connections (originating in the same module) and *external* connections spanning across modules. Distributions obtained from 20 independent realizations of each topology.

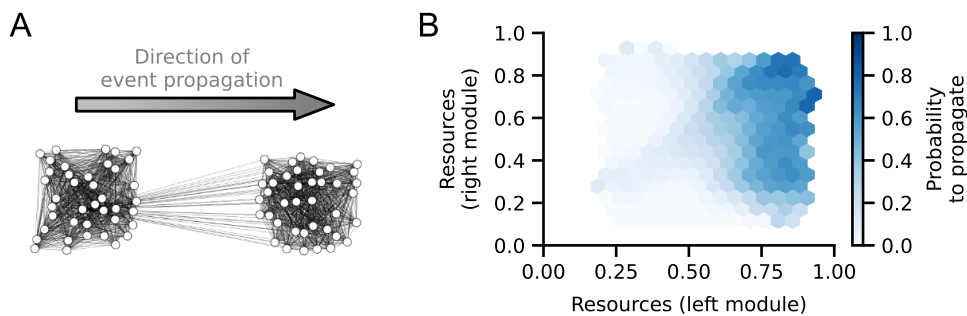


Figure S6. **Probability of event propagation.** We investigated the stochastic inter-modular connections, and in particular, how the probability of burst propagation depends on available resources. We performed simulations of two-module networks, where a single axon projected one-way from the left to the right module ($k = 1$, $\bar{k}_{in} = 30$). **A:** Sketch of the resulting connectivity. Causally, events can only propagate from the left to the right module. **B:** Probability that an event propagates from the source module (left) to the target module (right) as a function of the respective resource levels (module-average). To record events, 500 network realizations were sampled for a simulated duration of 5 min. Each simulation was repeated with different noise levels targeting the left, right or both modules. Noise frequency was varied from 0 to 35 Hz in steps of 5 Hz. Events were mostly detected as for the main manuscript, but the system-wide rate threshold was fixed to 3 Hz to account for the altered topology. Events were classified as “successfully propagated” if both modules participated (module-level threshold crossing separated at most 100 ms). Coincidental events, where the right module fired alone, or by chance, just before the other module, were discarded. Thus, all considered events originate in the left module. For each of the remaining events, we extracted the average resources present in the source and target module, at the time of the event start. For all resulting (and binned) combinations of resources in the source- and target-module, we then calculated the propagation probability as the fraction of events that did indeed propagate. Note that we cannot set the combinations of resources directly (but, rather, we have to measure after adjusting them indirectly by setting the provided noise), which limits the accessible regions in the plotted phase plane. However, overall, the propagation probability is more sensitive to a depletion of resources in the originating module (x -axis) compared to depletion in the target module (y -axis).

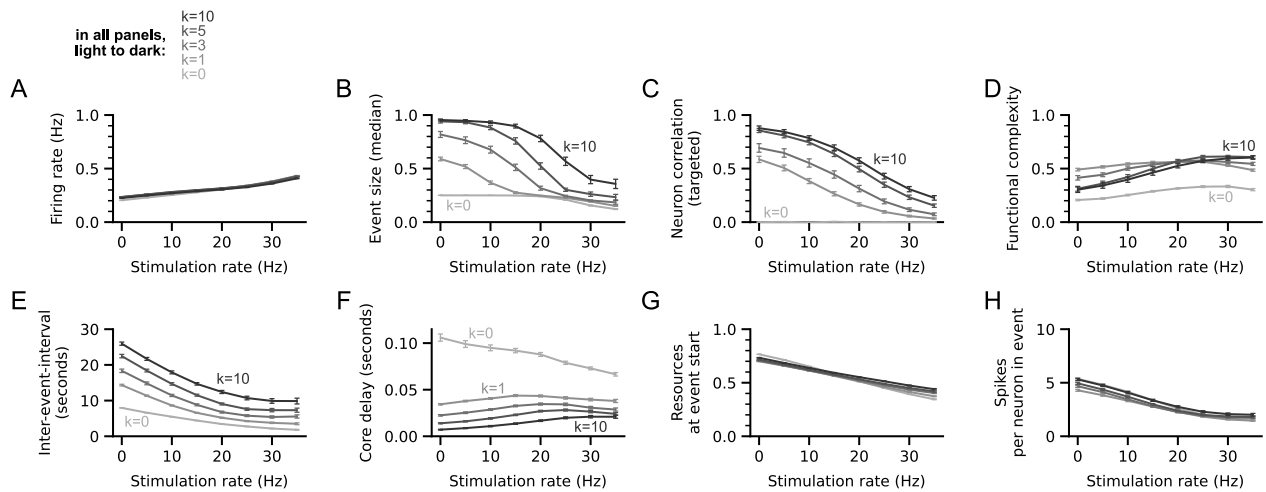


Figure S7. **In simulations, increasing noise decreases the intensity of network-wide events.** Dynamics depend on stimulation rate and the number of axons connecting modules, k . $k = 0$ is included as a control, indicating chance-level synchronization. **A:** Stimulation slightly increases the mean firing rate. **B:** Event size describes the fraction of neurons that fire at least one spike during a detected event (the chance-level event size that corresponds to one module is 0.25). Event sizes are larger for higher k but decrease under stimulation. **C:** Correlation of neuron pairs where both neurons are in modules targeted by stimulation (corresponding to main Fig. 4D, where the correlation of module-level firing rates is shown). **D:** Functional complexity is maximal at different stimulus intensity, depending on k . **E:** Inter-event-intervals decrease under stimulation. **F:** Core delays describe the time between the respective highest-firing rate time-points when multiple modules contribute to an event. It serves as a proxy of the multi-module burst-duration. Note that $k = 0$ corresponds to chance-level. **G:** Consistent with the observed changes of charge-discharge cycles, the average module-level resources at the time point when an event starts decrease with increased stimulation rate. **H:** For every detected event we calculate the number of spikes each neuron contributed. Besides the decrease in the number of neurons that contribute (panel B), the decrease in spikes is a second mechanism to conserve (module-level) resources.

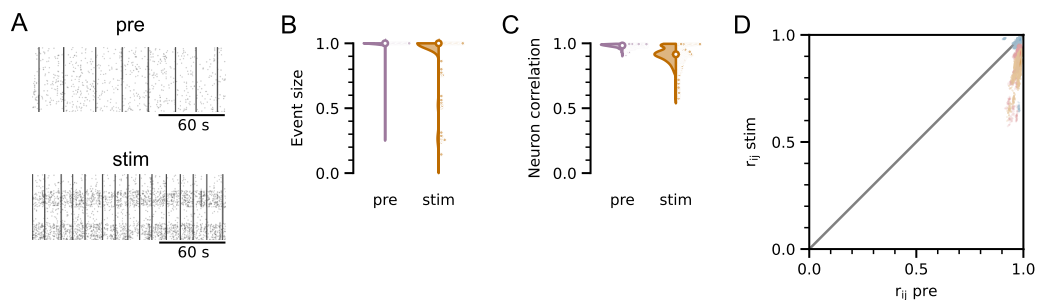


Figure S8. **Blocking inhibition in simulations weakens the desynchronizing effect of input.** Same as main Fig. 3, but with the current strength of inhibitory neurons set to $j_{GABA} = 0$. Parameters: $k = 3$, $k_{in} \approx 30$.

E. Optical Recordings and Spike Detection

The raster plots from simulations that we presented in the main manuscript seem to differ from the experimental rasters, at first glance. In the following we explore that these differences are likely rooted in the sampling. Optical recordings are known to miss some spiking events, whereas simulations provide perfect sampling. In order to assess how these missing spikes affect the statistics of rates and bursting, we here considered a “virtual optical recording”, in which some events are removed from simulated data, and then the statistics are compared.

Recently, Huang *et al.* [90] performed simultaneous patch-clamp recordings of spiking activity with fluorescence imaging, and computed the fraction of missing events. They found that isolated spikes are more likely to go undetected by fluorescence analyses, while consecutive spikes are detected more reliably. In order to mimic this phenomenology, we consider a probability $p_{\text{miss}}(n)$ of missing a single event when n spikes are presented in a time window of 250 ms, as reported in [90]. Then, the probability of missing m out of n spikes in a given time bin is given by a binomial distribution, $B(m, n, p_{\text{miss}}(n))$. The result of this process can be seen in Fig. S9. One can see that the raster gets “cleaner”, since many of the asynchronous, isolated spikes are removed, thus giving a picture closer to that of the experiments. Notably, the burst-like events appear unaltered. We computed some core observables before and after applying the filter: the number of modules involved in events, the fraction of neurons involved (event size), inter-event-intervals, neuron correlations. Although detected firing rates decrease (not shown), and correlation distributions do not cover the low tail (corresponding to uncorrelated activity in-between events), the statistics of events and (median) correlations remain mostly the same. Thus, we conclude that results of simulations can be directly compared with those coming from the experiments, despite the fact that fluorescence misses some events. Since most missed events are isolated, bursting and synchronization statistics are not affected.

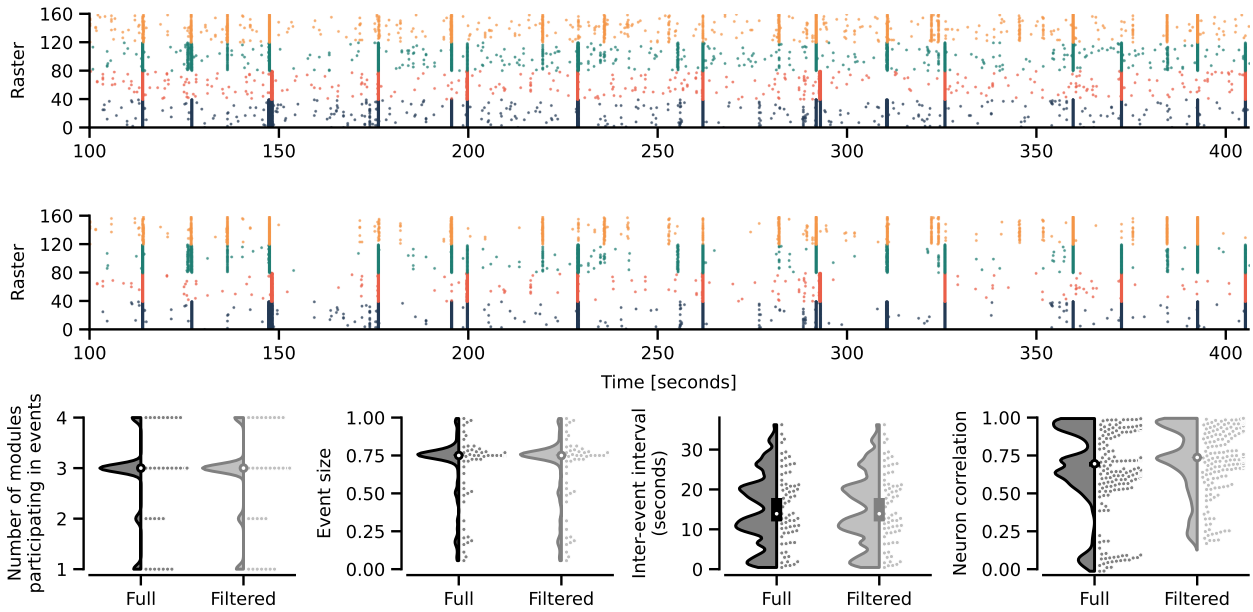


Figure S9. **Effect of missed spikes due to fluorescence in measured statistics.** Optical measurements predominantly miss isolated spikes from the recording. However, especially event-related observables are hardly affected. **A:** Original spike train at reference conditions ($k = 3$, pre). **B:** Filtered raster plot, after virtual optical recording. Note that we picked a realization that shows rather segregated activity, beyond the monotonic four-module synchrony. **C:** Observables employed in the main manuscript remain mostly unaffected when filtered. However, neuron-level correlations tend to be slightly higher when filtered. This is expected, as the missing of spikes occurs dominantly in the low-activity regime outside of synchronized events—which corresponds to uncorrelated firing of individual neurons.

3. DETAILS OF THE MESOSCOPIC MODEL WITH GATING MECHANISM

A. Mean-field Description of Module Dynamics

In order to link the mechanisms that we uncovered based on single-neuron dynamics and their impact on large-scale behavior, we developed a mesoscopic description that bridges local, finite-size aspects with conventional mean-field ideas to describe large populations of neurons through coarse-grained variables. In particular, the smallest spatial unit we consider in the following is a module. Each module i is characterized by only two stochastic variables: the module firing rate, $\rho_i(t)$, and the amount of available synaptic resources, $R_i(t)$. Notice that in a mean-field description individual neurons are assumed to be fully connected, meaning that the variables $\rho_i(t)$ and $R_i(t)$ do not present any dependence on space. The dynamics of an isolated module follows a rate model, which are a common choice to represent the activity of neuronal masses [75, 91–93]:

$$\dot{\rho}_i(t) = \underbrace{-\frac{1}{\tau_\rho}\rho_i(t)}_{\text{Decay}} + \underbrace{F[I_i(t)]}_{\text{Input}} + \underbrace{\sigma\xi_i(t)}_{\text{Noise}}, \quad (17a)$$

$$\dot{R}_i(t) = \underbrace{-\frac{1}{\tau_d}\rho_i(t)R_i(t)}_{\text{Discharge}} + \underbrace{\frac{1}{\tau_c}(R_0 - R_i(t))}_{\text{Charge}}. \quad (17b)$$

Here, we also include short-term synaptic plasticity, Eq. (17b), to describe through one variable the average depletion and recovery of neurotransmitters of all neurons in the module, following Tsodyks and Markram [94, 95]. See Table S4 for a full description of all parameters.

At any given time t , module i receives a total input

$$I_i(t) = \underbrace{\rho_i(t)R_i(t)}_{\text{Self}} + \underbrace{h}_{\text{External}} + w \underbrace{\sum_{j \neq i} A_{ij} g_{ij}(t) \rho_j(t) R_j(t)}_{\text{Neighbours}}. \quad (18)$$

Input can stem from three sources: recurrent input from the module itself, external input accounting for, e.g., stimulation, and input from neighbouring modules (which depends on the state of the neighbour $\rho_j(t)R_j(t)$, the connections between modules $w A_{ij}$ and a novel gating variable $g_{ij}(t)$, see Section 3C, below). The effect of inputs is implemented through a sigmoidal transfer function F , which maps the input to a change of the target-modules' rate:

$$F(I; \theta, a, b) = \begin{cases} b \frac{1 - e^{-a(I - \theta)}}{1 + e^{a\theta} e^{-a(I - \theta)}} & I > \theta, \\ 0 & I \leq \theta, \end{cases} \quad (19)$$

where θ , a , and b are constant parameters that determine the shape of the transfer function (Fig. S10A). The sigmoidal is selected such that $F(I = 0; \theta, a, b) = 0$, as is customarily done to ensure continuity of the function at zero input [91].

The dynamics of a single module are as follows: whenever the total input stays below the threshold [$I_i(t) < \theta$], the transfer of inputs is suppressed, and the firing rate decays [$\rho_i(t) \rightarrow 0$] with the (relatively short) time scale τ_ρ . During such times of low activity, synaptic resources are rarely used and slowly charge with time scale τ_c , until reaching the upper reference [$R_j(t) \rightarrow R_0$]. Notice that the amount of resources modulates the recurrent input [Eq. (18)], so that an isolated module without resources cannot increase its firing rate. On the other hand, once resources are charged and available, input from any source can trigger a feedback loop; a once-heightened firing rate causes the recurrent inputs to exceed the threshold, which again causes an increase in firing rate. Such self-accelerating episodes of high activity are commonly called bursts, and they will only terminate once the resources are depleted. For an isolated module, the noise term in Eq. (17a) ensures that such bursts occur from time to time, which reproduces well the behavior of in vitro systems (without enriched topologies), where large bursting events occur stochastically.

Here, depending on model parameters, an isolated module can also undergo stochastic burst cycles, where it alternates between states of high and low firing rates. Cycles tend to appear independently of parameters if the charging and discharging timescales are well separated and the maximum resources are enough to trigger the modules' feedback loop with a small fluctuation. The periods of cycles (and the burst duration) are determined by the timescales of resource charging (τ_c) and discharging (τ_d). This has been previously demonstrated in detail in Refs. [12, 96].

B. The Role of External Input

In the mesoscopic model, our experimental optogenetic stimulation is accounted for by the amplitude of module-level fluctuations σ , and the external input h in Eq. (18). In particular, this input is supplied to all modules at constant rate³; it is independent of the gate state, firing rate and resources. Consistent with the SNN-simulations, we find that an increase in external input decreases the amplitude of charge-discharge cycles in the resource-rate plane (Fig. S10C), and, if the gating mechanism is enabled, it helps to desynchronize modules (Fig. S11). This raises the question: how does external input decrease the amplitude of charge-discharge cycles?

Let us consider an isolated module at different values of h , without input from neighbours, and without fluctuations ($\sigma = 0$, Fig. S10B). For small h , no matter how we initialize the system, it will always end up in the charged state with zero firing rate and fully charged resources. For sufficiently large h , the system is in an input-driven regime that is characterized by high firing rates and low synaptic resources. The transition into this regime is discontinuous (Fig. S10B), and can be explained by the non-linear activation function (Eq. 19, Fig. S10A): only once all collected inputs exceed θ , does a rate change occur — and for the considered case of no neighbours, the only possible sources are h and the modules' recurrent input ($\rho_i R_i$). Once the system is in the input-driven regime, the total input always overcomes the decay, leading to the stationary dynamics with $\rho_i(t) > 0$. In neither of the above cases does the system undergo full (and repeated) charge-discharge cycles.

Parameter	Description
Dynamic variables	
$\rho_i(t)$	Firing rate (or activity) of module i
$R_i(t)$	Available synaptic resources in module i
$I_i(t)$	Total input arriving at module i
$\xi_i(t)$	Gaussian noise (mean 0, variance 1)
Dynamic constants	
$R_0 = 1$	Baseline synaptic resources
$\sigma = 0.1$	Intensity of (additive) background noise
$h = 0.0 - 0.3$	External input (rate), supplied to all modules
Time scales	
$\tau_\rho = 1$	Time scale of module rates (decay back to baseline)
$\tau_d = 5$	Time scale of discharging synaptic resources
$\tau_c = 40$	Time scale of charging synaptic resources
$\tau_{gd} = 1$	Time scale of disconnecting gates
$\tau_{gc} = 20$	Time scale of (re-)connecting gates
Input transfer sigmoid	
$\theta = 0.2$	Activation threshold, for input below θ no transfer
$a = 1.6$	Knee (abruptness of change) mapping module input to rate change
$b = 20.0$	Input gain of the function
Gates and module coupling	
$g_{ij}(t)$	Gate states. 1 if connected (transmitting activity), 0 else
Ω_{ij}	Rates at which gates connect/disconnect
A_{ij}	Adjacency matrix of modules. 1 if coupled/neighbouring, 0 else
$w = 0 - 0.15$	Coupling strength between modules
$a_g = 10$	Knee of sigmoid mapping $R_j(t) \rightarrow \Omega_{ij}$
$\theta_g = R_0/2$	Threshold of resources below which gates start to disconnect
Simulation settings	

Table S4. Overview of parameters and variables of the mesoscopic model.

³ The constant rate in the mean-field picture is motivated microscopically by the Poisson spiking of every neuron in the population.

Next, let us next consider the isolated module, but with fluctuations ($\sigma \neq 0$, Fig. S10C). From Eq. (18), we note that h contributes as a linear term in the exponents ($I - \theta$) of the transfer function Eq. (19). Thus, increasing h is equivalent to lowering the threshold θ , which determines how easily a burst can start due to fluctuations of a given amplitude σ . Thus, when the external input is increased $h \rightarrow \theta$, the module bursts more frequently and the average amount of available resources decreases. Due to the effectively lower threshold, even at the decreased resources, fluctuations can start a (less intense) burst. Together, this manifests in smaller charge-discharge cycles.

How do h and σ relate to the optogenetic stimulation in the experiments? As h describes the *average* external input to the underlying neuron population, the random optogenetic stimulation of individual neurons corresponds to an increased h . Consistently, increasing h causes higher activity in the mesoscopic model, as we also observed in experiments during stimulation. Because the targets of optogenetic stimulation are random, stimulation also corresponds to an increase of the module-level noise (an increase in σ). Reconsidering Fig. S10C, we see that increasing σ also decreases the size of charge-discharge cycles (as long as $h < \theta$). When fluctuations have a larger amplitude, they are more likely to push the module away from the stable point at high resources, triggering a burst. Thus, the average amount of resources at which bursts occur is lowered — just as in the case when increasing h . Thus, h and σ have a similar effect. In the following, we keep $\sigma = 0.1$ fixed and focus on systematically varying h .

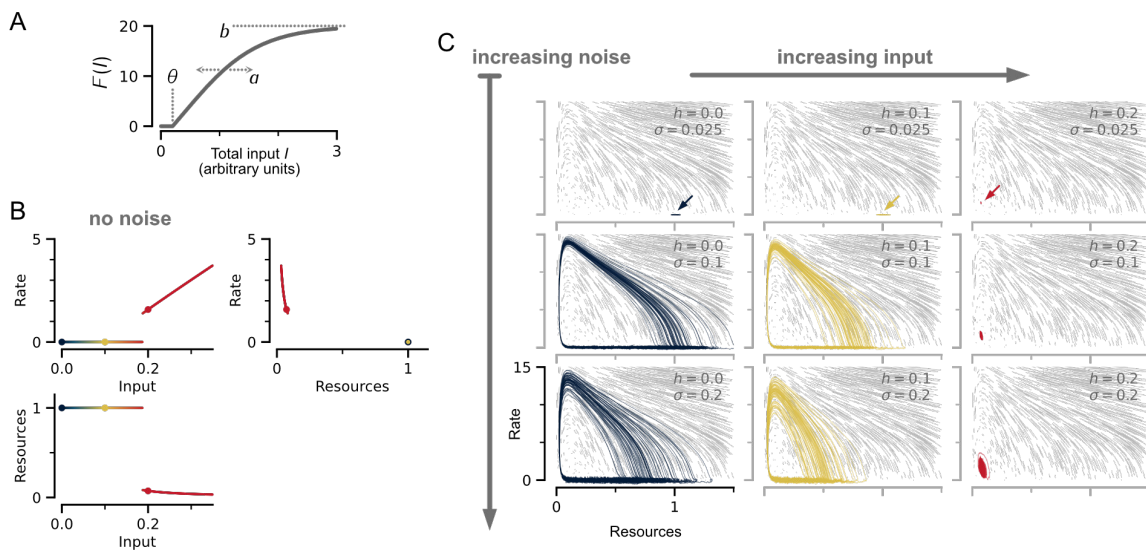


Figure S10. **Interplay of noise and external input for individual modules.** In the absence of fluctuations (“no noise”, $\sigma = 0$), an isolated module will always end up at a stable fixed point. Charge-discharge cycles can only be triggered by sufficiently large fluctuations. **A:** Sketch of the transfer function $F(I; \theta, a, b)$ mapping the total input arriving at a module to a rate change. **B:** The position of the fixed point depends on the external input h . Colors scale from blue (low input) to red (high input) and match across panels to show how the fixed point moves in different representations. Bigger dots correspond to the values of h shown in panel C. As h is increased, the system undergoes a discontinuous transition to the input-driven (up) state, near $h \approx \theta = 0.2$, see accompanying text. **C:** Charge-discharge cycles in the Resource-Rate plane for simulations that include noise. Gray background lines indicate the deterministic flow field and derive from short, equally long time-integrations of Eqs. 17b and 17a (excluding the noise term and inputs from other modules). Long gray lines indicate fast dynamics and short lines indicate slow dynamics. The colored lines are example trajectories of the full model for a single module, including noise but without interacting neighbors. **C, top to bottom:** Increasing σ . Independent of external input h , only fluctuations can trigger a discharge by perturbing the module sufficiently far from the fixed point. **C, left to right:** Increasing h . For small $h \ll \theta = 0.2$, fluctuations trigger a fast discharge (bursting at high rates, depleting resources). Once resources are depleted, the module slowly recovers resources at rates near zero. For larger $h \geq \theta$, the system is in the input-driven regime of continuous firing at medium rates and low resources (right column). In this regime, fluctuations cannot start a burst (and the characteristic large cycles), because no resources are available.

C. Stochastic Gates as Connections between Mesoscopic Modules

In a mean-field formulation, one assumes that connectivity in the neuron population is all-to-all — an assumption which we here clearly violate when neurons are predominantly confined to grow connections within modules. As

we illustrate in the following, this manifests in the way modules synchronize and necessitates the introduction of a stochastic gating mechanism.

In the experimental cultures, modules connect because individual neurons grow an axon into a neighboring, coupled module. Thus, the total input projected from module j to i should depend on the average firing rate within the source module $\rho_j(t)$ and the number of connecting axons. Describing the average number of connecting axons through a continuous variable (the coupling strength w), and considering all coupled modules, then the total input to i would be $I_i(t) \sim w \sum_{j \neq i} A_{ij} \rho_j(t)$, where A_{ij} is the adjacency matrix describing links from j to i (1 if modules are coupled, 0 otherwise).

Clearly, in our experimental setup (and the simulations of LIF-neurons), the local topology plays a key role when coupling different modules, because only few individual neurons project to neighboring clusters ($1 \leq k \leq 10$). In particular, if $k = 1$ and the projecting neuron is already in a refractory state when a module-level burst occurs (or, by chance, it fails to release an action potential) then activity cannot spread between modules, preventing synchronization. Thus, the mean-field coupling strength (w) only partly captures the mechanism of the microscopic number of connecting axons (k): It accounts for the scaling of the input due to more connections but not for the increased probability of a successful transmission of activity. To account for this, we introduce a novel gating mechanism that incorporates the probabilistic nature of the connections between modules through a discrete gate variable. This allows us to maintain the advantages of the mean-field description (such as better analytic tractability) by accounting for the effects of low-level spatial structure while avoiding the necessity to explicitly incorporate it. As such, our model combines continuous and discrete variables and is an example of *hybrid stochastic systems*, which have also been employed to successfully describe single-cell dynamics [97].

A gate from module j to i is a discrete (Boolean) variable $g_{ij}(t)$ with two possible states: connected (1, activity can pass) or disconnected (0, activity cannot pass). Gates are not symmetric; g_{ij} can be connected while g_{ji} is disconnected, so that activity can spread in an inhomogeneous manner. Microscopically, disconnected gates represent a state in which the presynaptic neurons are exhausted. We have already included the state of the gates in the input to each module [Eq. (18)]. Input is projected from j to i only if both modules are coupled ($A_{ij} = 1$) and the gate is currently connected [$g_{ij}(t) = 1$]. The gates transition between states as follows: They (re-)connect at a constant rate, so that a disconnected gate recovers after a typical time τ_{gc} , and gates become more likely to disconnect as resources of the source-module are depleted. The stochastic transition-rates are:

$$\Omega_{ij} (0 \rightarrow 1) = \frac{1}{\tau_{gc}}, \quad (20a)$$

$$\Omega_{ij} (1 \rightarrow 0) = \frac{1}{\tau_{gd}} \left[1 - \frac{1}{1 + e^{-a_g(R_j(t) - \theta_g)}} \right], \quad (20b)$$

where a_g , and θ_g are parameters that control the (sigmoidal) response of the gate to the amount of available resources (cf. Fig. 4E in the main manuscript). For sufficiently small time steps δt , these rates directly correspond to the probability that a gate connects or disconnects, $P_{ij} \approx \Omega_{ij} \delta t$.

D. Gates Desynchronize Modules

How does the gating mechanism affect the interaction of multiple modules? Let us first consider how modules synchronize while gates are connected. In this case, the input from one module to another has the same effect that we saw for stochastic fluctuations and isolated modules. If a module is charged, a sufficiently strong perturbation can trigger a module-level burst. In addition, because bursts feature a high firing rate, they also cause severe input to all neighboring modules [Eq. (18)], which again acts as an initial perturbation, triggering subsequent bursts in those modules. Note that, because time scales are separated, the time of discharge during the burst is much quicker than the charging, so that all modules that participated in the system-level burst start recharging at what can be considered the “same time”. Thus, they are also ready to burst again, and the system synchronizes. A crucial detail is that pairs of modules enter a recurrent feedback loop, just as we described for a single module; with constantly connected gates [$g_{ij} = 1$ in Eq. (18)], a change in ρ_j is very similar to a change of ρ_i . Of course, the recurrent feedback loop does not occur for vanishing coupling $w \rightarrow 0$, in which case modules become independent and could only synchronize by chance.

Our stochastic gating mechanism can disrupt the inter-module feedback loop for non-vanishing coupling: When a module starts bursting, its available resources are rapidly consumed, so that its outgoing gates will deactivate quickly ($\sim \tau_{gd}$). Once a gate is disconnected, it will remain disconnected for a relatively long time ($\sim \tau_{gc}$). In this period, if the module bursts again, activity cannot spread to the neighboring modules. Hence, if modules tend to burst with

a time scale faster than τ_{gc} , the recurrent feedback loop between modules is hindered, because the crucial initiating inputs cannot pass through the disconnected gates, and therefore the system cannot synchronize.

Finally, let us reconsider the external input h , an increase of which caused smaller charge-discharge cycles for isolated modules, by effectively lowering the threshold θ . Importantly, the smaller charge-discharge cycles correspond to more frequent bursts on the module level and lower average resources. For multiple modules connected by the gating mechanism, the lower resources cause the gates to be disconnected more often, and the fraction of bursts occurring in times of disconnected gates increases. Thus, it becomes less likely for a module-level burst to trigger a system-wide burst, because either gates are not ready or the target modules are not in the state of sufficiently charged resources.

To summarize, in order to desynchronize the modules of the mesoscopic model for non-vanishing coupling strengths, two ingredients are needed: i) a sufficiently strong amplitude of fluctuations to cause charge-discharge cycles, and ii) an inhomogeneous as well as stochastic coupling between modules, implemented through our novel gating mechanism. If both conditions are met, then the desynchronization can be facilitated by increasing the external input h to all modules (cf. Figs. S11 and S12).

4. CODE AVAILABILITY

Our source code for analysis and simulation is available via Github:

- Github: https://github.com/Prieseemann-Group/stimulating_modular_cultures
- DOI: 10.5281/zenodo.7962283

Experimental data and processed analysis results are available via G-Node GIN:

- https://gin.g-node.org/pspitzner/stimulating_modular_cultures
- DOI: 10.12751/g-node.t77b3p

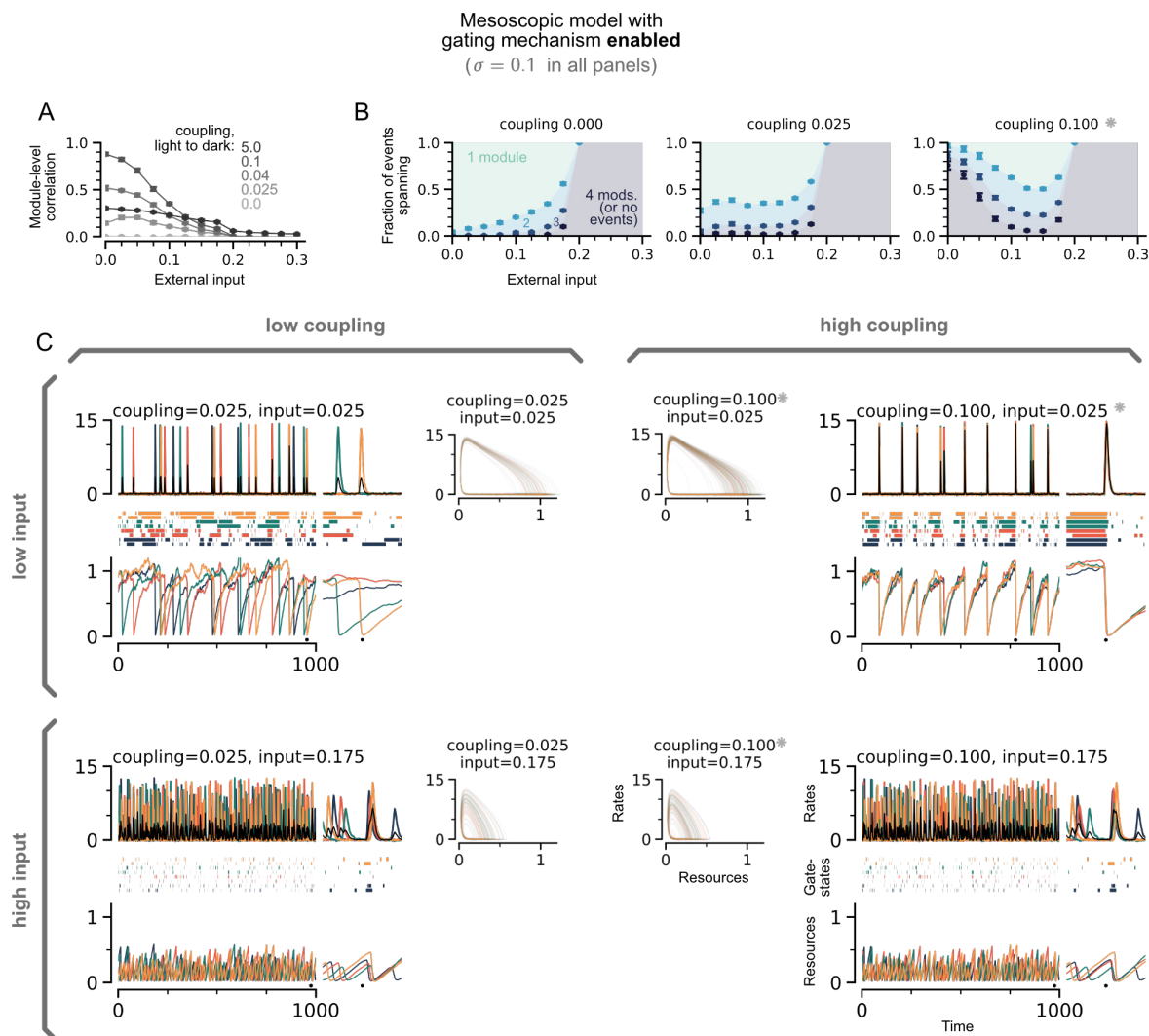


Figure S11. **Mesoscopic model with gating mechanism enabled, and varying stimulation to *all* modules.** With the gating mechanism, modules desynchronize when the coupling between modules is removed, or the external input is increased. Correlations between modules gradually decrease with increasing external input, until reaching the transition to the up state at $h \approx \theta = 0.2$. Note that very strong coupling (e.g. $w = 5.0$) leads to a saturation of the gating mechanism so that gates are always disconnected and modules can no longer synchronize, despite the strong coupling. Panels with a gray star are also presented in the main manuscript.

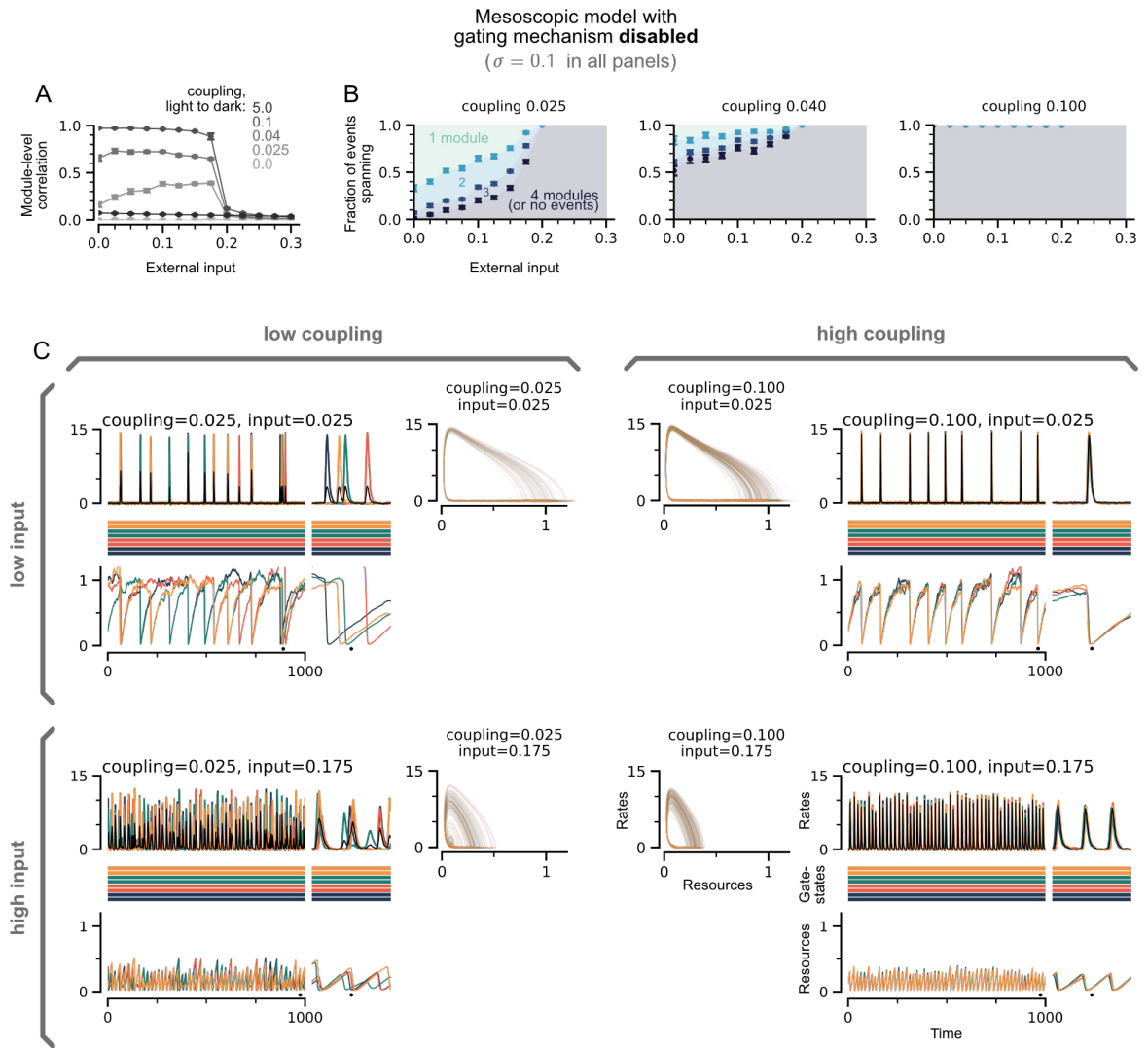


Figure S12. Mesoscopic model with gates permanently connected, and varying stimulation to *all* modules. Without the gating mechanism, modules only desynchronize for vanishing coupling. An increase of external input cannot desynchronize the modules. Correlations between modules drop abruptly as the system enters the input-driven up state $h \geq \theta = 0.2$.

5. DATA TABLES

Layout	Condition		targeted modules	across	non- targeted	all
single-bond	pre	median	0.72	0.76	0.81	0.76
		2.5	0.66	0.69	0.75	0.74
		97.5	0.81	0.82	0.85	0.82
	stim	median	0.22	0.31	0.73	0.41
		2.5	0.05	0.16	0.51	0.21
		97.5	0.31	0.41	0.74	0.44
	post	median	0.74	0.79	0.81	0.81
		2.5	0.56	0.61	0.80	0.73
		97.5	0.78	0.80	0.84	0.81
tripe-bond	pre	median	0.82	0.80	0.84	0.81
		2.5	0.80	0.68	0.78	0.78
		97.5	0.90	0.88	0.88	0.88
	stim	median	0.72	0.71	0.75	0.73
		2.5	0.27	0.31	0.71	0.46
		97.5	0.81	0.74	0.81	0.76
	post	median	0.81	0.84	0.86	0.85
		2.5	0.68	0.68	0.75	0.72
		97.5	0.90	0.89	0.89	0.89
merged	pre	median	0.92	0.89	0.91	0.91
		2.5	0.73	0.81	0.72	0.79
		97.5	0.95	0.92	0.93	0.92
	stim	median	0.59	0.51	0.74	0.62
		2.5	0.26	0.30	0.36	0.28
		97.5	0.84	0.85	0.89	0.87
	post	median	0.92	0.88	0.93	0.91
		2.5	0.87	0.83	0.82	0.85
		97.5	0.95	0.92	0.94	0.93
simulation (two modules targeted, $k = 3$)	pre (0.0 Hz)	median	0.83	0.81	0.82	0.82
		2.5	0.77	0.76	0.78	0.80
		97.5	0.86	0.84	0.85	0.84
	post (20.0 Hz)	median	0.33	0.50	0.80	0.58
		2.5	0.28	0.46	0.74	0.53
		97.5	0.44	0.53	0.84	0.63

Table S5. **Pairwise correlation sorted according to stimulation targets.** The data shown in the barplots (main Fig. 2D) compares neuron correlation and their dependence on the neuron’s positions. For every neuron pair, both neurons could reside in the “targeted modules”, both could reside in “non-targeted” modules, or “across”, where one neuron is within a targeted module and the other one is not. The last column contains the ensemble of all pairs, irrespective of position. Note that for merged topologies, no modules exist but categorization is still possible, depending on whether a neuron is a potential stimulation target. The median corresponds the single-realization estimate (median neuron correlation), 2.5% and 97.5% are percentiles of the bootstrap distribution.

Layout	Condition	Percentile	Event size	Neuron correlation	IEI (seconds)	Core delays (ms)
single-bond	pre	50	1.00	0.77	18.97	39.17
		2.5	0.96	0.76	16.15	32.83
		97.5	1.00	0.78	21.35	45.26
	stim	50	0.46	0.40	6.23	70.00
		2.5	0.42	0.38	5.60	65.83
		97.5	0.50	0.42	6.92	77.83
	post	50	0.83	0.78	12.43	46.67
		2.5	0.81	0.77	11.43	42.24
		97.5	0.88	0.78	13.94	53.89
tripe-bond	pre	50	0.95	0.86	16.13	31.17
		2.5	0.95	0.86	12.96	27.91
		97.5	0.95	0.87	20.20	35.67
	stim	50	0.75	0.75	7.04	46.67
		2.5	0.73	0.74	6.33	39.92
		97.5	0.80	0.75	7.55	53.58
	post	50	0.95	0.88	17.13	34.83
		2.5	0.95	0.87	15.35	29.03
		97.5	0.95	0.88	19.69	41.25
merged	pre	50	1.00	0.89	19.85	35.83
		2.5	1.00	0.89	17.75	32.67
		97.5	1.00	0.90	23.67	40.42
	stim	50	0.75	0.72	5.35	37.67
		2.5	0.68	0.71	4.89	34.75
		97.5	0.79	0.75	5.87	40.00
	post	50	1.00	0.92	20.78	31.33
		2.5	1.00	0.91	15.73	28.17
		97.5	1.00	0.92	25.82	35.09
chemical	KCl =0 mM	50	0.81	0.72	42.40	59.25
		2.5	0.75	0.71	20.39	37.24
		97.5	0.88	0.74	48.64	100.00
	KCl =2 mM	50	0.94	0.76	20.01	104.50
		2.5	0.88	0.73	17.15	67.67
		97.5	0.94	0.78	22.34	153.33
bicuculline	0 μ M	50	1.00	0.82	73.90	173.58
		2.5	0.85	0.80	56.74	129.58
		97.5	1.00	0.84	100.15	177.17
	20 μ M	50	0.80	0.82	6.31	29.92
		2.5	0.80	0.80	4.97	26.87
		97.5	0.85	0.83	8.34	34.21
simulation (two modules targeted, $k = 3$)	pre (0.0 Hz)	50	0.81	0.84	18.76	18.00
		2.5	0.79	0.84	18.46	17.67
		97.5	0.81	0.85	19.06	18.17
	stim (20.0 Hz)	50	0.27	0.58	5.50	28.31
		2.5	0.26	0.57	5.38	27.75
		97.5	0.27	0.58	5.64	28.79

Table S6. **Statistics aggregated across trials.** For all the violins (main Figs. 2A,B and 3E) we plot aggregated observations (activity events, IEI or a pair of neurons contributing a correlation coefficient) that are collected across all trials. To get uncertainty estimates, we bootstrap the observations (a large number) and calculate the median for each of the 500 bootstrap samples. Then, considering all bootstrap samples, we get a distribution of where these medians fall. The percentiles of this distribution are plotted as the error sticks in the violins: the error bar from the 2.5% to the 97.5% and the white dot is located at the 50% (corresponding to the median of all bootstrap samples). Here, we use the median as we expect these distributions to be non-Gaussian, and skewed (for instance, the median event size of non-stimulated single-bond is 1, because the distribution is skewed — this would not be captured so well if we used the mean instead of the median).

Layout	Condition		Event size	Correlation coefficient	Functional complexity	IEI (seconds)	Core delays (ms)
single-bond ($N = 7$ realizations)	pre	mean	0.98	0.77	0.47	41.13	0.05
		sem	0.05	0.03	0.06	12.86	0.03
		max	1.00	0.85	0.75	109.98	0.24
		min	0.69	0.49	0.39	9.64	0.03
	stim	mean	0.52	0.39	0.68	9.45	0.07
		sem	0.11	0.06	0.07	2.91	0.02
		max	0.88	0.73	0.77	16.52	0.16
		min	0.25	0.21	0.47	4.41	0.04
	post	mean	0.93	0.79	0.47	18.57	0.05
		sem	0.05	0.04	0.04	8.14	0.02
		max	1.00	0.82	0.69	49.46	0.14
		min	0.75	0.47	0.38	9.60	0.02
triple-bond ($N = 7$ realizations)	pre	mean	0.96	0.82	0.39	34.41	0.05
		sem	0.04	0.04	0.06	9.76	0.01
		max	1.00	0.92	0.55	56.53	0.10
		min	0.75	0.72	0.24	7.06	0.02
	stim	mean	0.85	0.70	0.52	9.89	0.05
		sem	0.11	0.09	0.05	4.29	0.02
		max	1.00	0.90	0.67	41.80	0.11
		min	0.33	0.27	0.29	4.55	0.02
	post	mean	0.97	0.85	0.33	25.25	0.04
		sem	0.07	0.05	0.07	12.93	0.01
		max	1.00	0.91	0.55	47.84	0.06
		min	0.75	0.68	0.22	13.12	0.02
merged ($N = 7$ realizations)	pre	mean	0.99	0.90	0.30	61.41	0.05
		sem	0.02	0.05	0.07	24.62	0.03
		max	1.00	0.95	0.46	154.61	0.16
		min	0.94	0.69	0.16	3.14	0.02
	stim	mean	0.72	0.62	0.49	9.04	0.04
		sem	0.28	0.16	0.10	2.77	0.02
		max	1.00	0.94	0.70	16.11	0.14
		min	0.30	0.27	0.24	3.76	0.02
	post	mean	0.98	0.90	0.31	48.17	0.06
		sem	0.03	0.03	0.06	25.23	0.02
		max	1.00	0.93	0.48	158.83	0.09
		min	0.88	0.81	0.16	5.64	0.01
chemical ($N = 4$ realizations)	KCl =0 mM	mean	0.79	0.72	0.58	63.01	0.12
		sem	0.08	0.01	0.02	39.26	0.08
		max	1.00	0.75	0.62	177.93	0.34
		min	0.69	0.69	0.54	19.52	0.04
	KCl =2 mM	mean	0.92	0.75	0.48	34.50	0.15
		sem	0.05	0.09	0.09	12.55	0.09
		max	1.00	0.93	0.57	63.82	0.36
		min	0.78	0.53	0.21	17.38	0.03
bicuculline ($N = 5$ realizations)	0 μ M	mean	0.90	0.76	0.49	90.78	0.15
		sem	0.16	0.05	0.06	13.84	0.03
		max	1.00	0.91	0.63	126.47	0.18
		min	0.25	0.65	0.38	55.56	0.07
	20 μ M	mean	0.88	0.76	0.47	49.69	0.08
		sem	0.16	0.05	0.11	32.90	0.06
		max	1.00	0.94	0.65	134.48	0.30
		min	0.25	0.70	0.16	4.91	0.03

Table S7. **Trial-wise statistics.** For all the trial-level plots (main Fig. 1J and Figs. 2E–H) we consider observables of individual trials (realizations). Thus, the observable is calculated once for each realization (for example, functional complexity, the median neuron correlation in a trial, or the median event size in a trial). We then bootstrap these trials and get a distribution from the bootstrap samples. The white dot is the mean of the samples, the error bar indicates the mean plus/minus the bs-sample standard error and the extended thin line indicates that maximal/minimal value observed in any realization. Here, we use the mean because we expect these distributions to be normal.

REFERENCES AND NOTES

1. W. R. Softky, C. Koch, The highly irregular firing of cortical cells is inconsistent with temporal integration of random EPSPs. *J. Neurosci.* **13**, 334–350 (1993).
2. A. Arieli, A. Sterkin, A. Grinvald, A. D. Aertsen, Dynamics of ongoing activity: Explanation of the large variability in evoked cortical responses. *Science* **273**, 1868–1871 (1996).
3. M. E. Raichle, The restless brain. *Brain Connect.* **1**, 3–12 (2011).
4. J. Aru, J. Aru, V. Priesemann, M. Wibral, L. Lana, G. Pipa, W. Singer, R. Vicente, Untangling cross-frequency coupling in neuroscience. *Curr. Opin. Neurobiol.* **31**, 51–61 (2015).
5. A. Fornito, A. Zalesky, E. Bullmore, Fundamentals of brain network analysis. Academic Press (2016).
6. R. M. Hutchison, T. Womelsdorf, E. A. Allen, P. A. Bandettini, V. D. Calhoun, M. Corbetta, S. Penna, J. H. Duyn, G. H. Glover, J. Gonzalez-Castillo, D. A. Handwerker, S. Keilholz, V. Kiviniemi, D. A. Leopold, F. Pasquale, O. Sporns, M. Walter, C. Chang, Dynamic functional connectivity: Promise, issues, and interpretations. *Neuroimage* **80**, 360–378 (2013).
7. T. Matsui, T. Q. Pham, K. Jimura, J. Chikazoe, On co-activation pattern analysis and non-stationarity of resting brain activity. *Neuroimage* **249**, 118904 (2022).
8. J. M. Beggs, D. Plenz, Neuronal avalanches in neocortical circuits. *J. Neurosci.* **23**, 11167–11177 (2003).
9. R. Legenstein, W. Maass, Edge of chaos and prediction of computational performance for neural circuit models. *Neural Netw.* **20**, 323–334 (2007).
10. D. R. Chialvo, Emergent complex neural dynamics. *Nat. Phys.* **6**, 744–750 (2010).
11. L. Cocchi, L. L. Gollo, A. Zalesky, M. Breakspear, Criticality in the brain: A synthesis of neurobiology, models and cognition. *Prog. Neurobiol.* **158**, 132–152 (2017).
12. S. di Santo, P. Villegas, R. Burioni, M. A. Muñoz, Landau-Ginzburg theory of cortex dynamics: Scale-

- free avalanches emerge at the edge of synchronization. *Proc. Natl. Acad. Sci. U.S.A.* **115**, E1356 (2018).
13. M. A. Muñoz, *Colloquium: Criticality and dynamical scaling in living systems*. *Rev. Mod. Phys.* **90**, 031001 (2018).
 14. B. Cramer, D. Stöckel, M. Kreft, M. Wibral, J. Schemmel, K. Meier, V. Priesemann, Control of criticality and computation in spiking neuromorphic networks with plasticity. *Nat. Commun.* **11**, 2853 (2020).
 15. D. Plenz, T. L. Ribeiro, S. R. Miller, P. A. Kells, A. Vakili, Self-organized criticality in the brain. *Front. Phys.* **9**, 639389 (2021).
 16. N. Brunel, Dynamics of sparsely connected networks of excitatory and inhibitory spiking neurons. *J. Comput. Neurosci.* **8**, 183–208 (2000).
 17. A. Renart, J. de la Rocha, P. Bartho, L. Hollender, N. Parga, A. Reyes, K. D. Harris, The asynchronous state in cortical circuits. *Science* **327**, 587–590 (2010).
 18. J. G. Orlandi, J. Soriano, E. Alvarez-Lacalle, S. Teller, J. Casademunt, Noise focusing and the emergence of coherent activity in neuronal cultures. *Nat. Phys.* **9**, 582–590 (2013).
 19. P. Fries, Rhythms for cognition: Communication through coherence. *Neuron* **88**, 220–235 (2015).
 20. P. Villegas, P. Moretti, M. A. Muñoz, Frustrated hierarchical synchronization and emergent complexity in the human connectome network. *Sci. Rep.* **4**, 5990 (2014).
 21. M. I. Rabinovich, P. Varona, A. Selverston, H. D. I. Abarbanel, Dynamical principles in neuroscience. *Rev. Mod. Phys.* **78**, 1213–1265 (2006).
 22. E. Tognoli, J. A. S. Kelso, The metastable brain. *Neuron* **81**, 35–48 (2014).
 23. O. Weinberger, P. Ashwin, From coupled networks of systems to networks of states in phase space. *Discrete Continuous Dyn. Syst. Ser. B* **23**, 2043–2063 (2018).
 24. L. Donetti, P. I. Hurtado, M. A. Muñoz, Entangled networks, synchronization, and optimal network

- topology. *Phys. Rev. Lett.* **95**, 188701 (2005).
25. A. Arenas, A. Diaz-Guilera, J. Kurths, Y. Moreno, C. Zhou, Synchronization in complex networks. *Phys. Rep.* **469**, 93–153 (2008).
26. Y. M. Lai, M. A. Porter, Noise-induced synchronization, desynchronization, and clustering in globally coupled nonidentical oscillators. *Phys. Rev. E* **88**, 012905 (2013).
27. M. Dazza, S. Métens, P. Monceau, S. Bottani, A novel methodology to describe neuronal networks activity reveals spatiotemporal recruitment dynamics of synchronous bursting states. *J. Comput. Neurosci.* **49**, 375–394 (2021).
28. A. Y. Y. Tan, Y. Chen, B. Scholl, E. Seidemann, N. J. Priebe, Sensory stimulation shifts visual cortex from synchronous to asynchronous states. *Nature* **509**, 226–229 (2014).
29. J. Zierenberg, J. Wilting, V. Priesemann, Homeostatic plasticity and external input shape neural network dynamics. *Phys. Rev. X* **8**, 031018 (2018).
30. R. M. Bruno, B. Sakmann, Cortex is driven by weak but synchronously active thalamocortical synapses. *Science* **312**, 1622–1627 (2006).
31. K. C.-K. Malina, B. Mohar, A. N. Rappaport, I. Lampl, Local and thalamic origins of correlated ongoing and sensory-evoked cortical activities. *Nat. Commun.* **7**, 12740 (2016).
32. H. Mizuno, K. Ikezoe, S. Nakazawa, T. Sato, K. Kitamura, T. Iwasato, Patchwork-type spontaneous activity in neonatal barrel cortex layer 4 transmitted via thalamocortical projections. *Cell Rep.* **22**, 123–135 (2018).
33. M. H. Friedberg, S. M. Lee, F. F. Ebner, Modulation of receptive field properties of thalamic somatosensory neurons by the depth of anesthesia. *J. Neurophysiol.* **81**, 2243–2252 (1999).
34. D. S. Greenberg, A. R. Houweling, J. D. Kerr, Population imaging of ongoing neuronal activity in the visual cortex of awake rats. *Nat. Neurosci.* **11**, 749–751 (2008).
35. W.-P. Chang, J.-S. Wu, C.-M. Lee, B. A. Vogt, B.-C. Shyu, Spatiotemporal organization and thalamic

- modulation of seizures in the mouse medial thalamic-anterior cingulate slice. *Epilepsia* **52**, 2344–2355 (2011).
36. Ł. Kuśmierz, S. Ogawa, T. Toyozumi, Edge of chaos and avalanches in neural networks with heavy-tailed synaptic weight distribution. *Phys. Rev. Lett.* **125**, 028101 (2020).
37. C. W. Lynn, D. S. Bassett, The physics of brain network structure, function and control. *Nat. Rev. Phys.* **1**, 318–332 (2019).
38. J. W. Scannell, M. P. Young, The connectional organization of neural systems in the cat cerebral cortex. *Curr. Biol.* **3**, 191–200 (1993).
39. J. W. Scannell, G. A. P. C. Burns, C. C. Hilgetag, M. A. O’Neil, M. P. Young, The connectional organization of the cortico-thalamic system of the cat. *Cereb. Cortex* **9**, 277–299 (1999).
40. C.-C. Hilgetag, G. A. P. C. Burns, M. A. O’Neill, J. W. Scannell, M. P. Young, Anatomical connectivity defines the organization of clusters of cortical areas in the macaque monkey and the cat. *Phil. Trans. R. Soc. Lond. B* **355**, 91–110 (2000).
41. D. Meunier, R. Lambiotte, E. T. Bullmore, Modular and hierarchically modular organization of brain networks. *Front. Neurosci.* **4**, 200 (2010).
42. M. P. van den Heuvel, E. T. Bullmore, O. Sporns, Comparative connectomics. *Trends Cogn. Sci.* **20**, 345–361 (2016).
43. W.-C. A. Lee, V. Bonin, M. Reed, B. J. Graham, G. Hood, K. Glattfelder, R. C. Reid, Anatomy and function of an excitatory network in the visual cortex. *Nature* **532**, 370–374 (2016).
44. H. Yamamoto, S. Moriya, K. Ide, T. Hayakawa, H. Akima, S. Sato, S. Kubota, T. Tanii, M. Niwano, S. Teller, J. Soriano, A. Hirano-Iwata, Impact of modular organization on dynamical richness in cortical networks. *Sci. Adv.* **4**, eaau4914 (2018).
45. J. L. Nathanson, Y. Yanagawa, K. Obata, E. M. Callaway, Preferential labeling of inhibitory and excitatory cortical neurons by endogenous tropism of adeno-associated virus and lentivirus vectors.

Neuroscience **161**, 441–450 (2009).

46. N. C. Klapoetke, Y. Murata, S. S. Kim, S. R. Pulver, A. Birdsey-Benson, Y. K. Cho, T. K. Morimoto, A. S. Chuong, E. J. Carpenter, Z. J. Tian, J. Wang, Y. L. Xie, Z. X. Yan, Y. Zhang, B. Y. Chow, B. Surek, M. Melkonian, V. Jayaraman, M. Constantine-Paton, G. K. S. Wong, E. S. Boyden, Independent optical excitation of distinct neural populations. *Nat. Methods* **11**, 338–346 (2014).
47. Y. Penn, M. Segal, E. Moses, Network synchronization in hippocampal neurons. *Proc. Natl. Acad. Sci. U.S.A.* **113**, 3341–3346 (2016).
48. G. Zamora-López, Y. Chen, G. Deco, M. L. Kringelbach, C. Zhou, Functional complexity emerging from anatomical constraints in the brain: The significance of network modularity and rich-clubs. *Sci. Rep.* **6**, 38424 (2016).
49. N. Sukenik, O. Vinogradov, E. Weinreb, M. Segal, A. Levina, E. Moses, Neuronal circuits overcome imbalance in excitation and inhibition by adjusting connection numbers. *Proc. Natl. Acad. Sci. U.S.A.* **118**, e2018459118 (2021).
50. S. Sadeh, C. Clopath, Inhibitory stabilization and cortical computation. *Nat. Rev. Neurosci.* **22**, 21–37 (2021).
51. D. Cohen, M. Segal, Network bursts in hippocampal microcultures are terminated by exhaustion of vesicle pools. *J. Neurophysiol.* **106**, 2314–2321 (2011).
52. E. Tibau, M. Valencia, J. Soriano, Identification of neuronal network properties from the spectral analysis of calcium imaging signals in neuronal cultures. *Front. Neural Circuits* **7**, 199 (2013).
53. E. A. Leicht, M. E. J. Newman, Community structure in directed networks. *Phys. Rev. Lett.* **100**, 118703 (2008).
54. S. Teller, C. Granell, M. De Domenico, J. Soriano, S. Gómez, A. Arenas, Emergence of assortative mixing between clusters of cultured neurons. *PLOS Comput. Biol.* **10**, e1003796 (2014).
55. M. A. Rabadan, E. D. De La Cruz, S. B. Rao, Y. Chen, C. Gong, G. Crabtree, B. Zu, S. Markx, J. A.

- Gogos, R. Yuste, R. Tomer, An in vitro model of neuronal ensembles. *Nat. Commun.* **13**, 3340 (2022).
56. B. Pietras, V. Schmutz, T. Schwalger. Mesoscopic description of hippocampal replay and metastability in spiking neural networks with short-term plasticity, *PLOS Comput. Biol.* **18**, e1010809 (2022).
57. J. P. Neto, F. P. Spitzner, V. Priesemann, Sampling effects and measurement overlap can bias the inference of neuronal avalanches. *PLOS Comput. Biol.* **18**, e1010678 (2022).
58. E. Montbrió, D. Pazó, A. Roxin, Macroscopic description for networks of spiking neurons. *Phys. Rev. X* **5**, 021028 (2015).
59. Á. Byrne, R. D. O’Dea, M. Forrester, J. Ross, S. Coombes, Next-generation neural mass and field modeling. *J. Neurophysiol.* **123**, 726–742 (2020).
60. C. Bick, M. Goodfellow, C. R. Laing, E. A. Martens, Understanding the dynamics of biological and neural oscillator networks through exact mean-field reductions: A review. *J. Math. Neurosci.* **10**, 9 (2020).
61. I. V. Tyulkina, D. S. Goldobin, L. S. Klimenko, A. Pikovsky, Dynamics of noisy oscillator populations beyond the Ott-Antonsen ansatz. *Phys. Rev. Lett.* **120**, 264101 (2018).
62. S. M. Sherman, R. W. Guillery, The role of the thalamus in the flow of information to the cortex. *Phil. Trans. R. Soc. Lond. B* **357**, 1695–1708 (2002).
63. M. D. McDonnell and L. M. Ward, The benefits of noise in neural systems: Bridging theory and experiment. *Nat. Rev. Neurosci.* **12**, 415–425 (2011).
64. G. Shahaf and S. Marom, Learning in networks of cortical neurons. *J. Neurosci.* **21**, 8782–8788 (2001).
65. D. A. Wagenaar, R. Madhavan, J. Pine, S. M. Potter, Controlling bursting in cortical cultures with closed-loop multi-electrode stimulation. *J. Neurosci.* **25**, 680–688 (2005).
66. M. Chiappalone, P. Massobrio, S. Martinoia, Network plasticity in cortical assemblies. *Eur. J. Neurosci.* **28**, 221–237 (2008).

67. X. Zhang, F.-C. Yeh, H. Ju, Y. Jiang, G. F. W. Quan, A. M. J. VanDongen, Familiarity detection and memory consolidation in cortical assemblies. *eNeuro* **7**, ENEURO.0006–19.2020 (2020).
68. Y. Inglebert, J. Aljadeff, N. Brunel, D. Debanne, Synaptic plasticity rules with physiological calcium levels. *Proc. Natl. Acad. Sci. U.S.A.* **117**, 33639–33648 (2020).
69. S. Okujeni, U. Egert, Self-organization of modular network architecture by activity-dependent neuronal migration and outgrowth. *eLife* **8**, e47996 (2019).
70. S. Okujeni, U. Egert, Structural modularity tunes mesoscale criticality in biological neuronal networks. *J. Neurosci.* **43**, 2515–2526 (2023).
71. F. M. Krienen, M. Goldman, Q. Zhang, R. C. H. del Rosario, M. Florio, R. Machold, A. Saunders, K. Levandowski, H. Zaniewski, B. Schuman, C. Wu, A. Lutservitz, C. D. Mullally, N. Reed, E. Bien, L. Bortolin, M. Fernandez-Otero, J. D. Lin, A. Wysoker, J. Nemesh, D. Kulp, M. Burns, V. Tkachev, R. Smith, C. A. Walsh, J. Dimidschstein, B. Rudy, L. S. Kean, S. Berretta, G. Fishell, G. Feng, S. A. McCarroll, Innovations present in the primate interneuron repertoire. *Nature* **586**, 262–269 (2020).
72. S. Loomba, J. Straehle, V. Gangadharan, N. Heike, A. Khalifa, A. Motta, N. Ju, M. Sievers, J. Gempt, H. S. Meyer, M. Helmstaedter, Connectomic comparison of mouse and human cortex. *Science* **377**, eabo0924 (2022).
73. G. Tononi, O. Sporns, G. M. Edelman, A measure for brain complexity: Relating functional segregation and integration in the nervous system. *Proc. Natl. Acad. Sci. U.S.A.* **91**, 5033–5037 (1994).
74. L.-D. Lord, A. B. Stevner, G. Deco, M. L. Kringelbach, Understanding principles of integration and segregation using whole-brain computational connectomics: Implications for neuropsychiatric disorders. *Philos. Trans. A Math. Phys. Eng. Sci.* **375**, 20160283 (2017).
75. G. Deco, V. K. Jirsa, P. A. Robinson, M. Breakspear, K. Friston, The dynamic brain: From spiking neurons to neural masses and cortical fields. *PLOS Comput. Biol.* **4**, e1000092 (2008).
76. Y. Xu, M. Takai, T. Konno, K. Ishihara, Microfluidic flow control on charged phospholipidpolymer interface. *Lab Chip* **7**, 199–206 (2007).

77. H. Yamamoto, S. Kubota, Y. Chida, M. Morita, S. Moriya, H. Akima, S. Sato, A. Hirano-Iwata, T. Tanii, M. Niwano, Size-dependent regulation of synchronized activity in living neuronal networks. *Phys. Rev. E* **94**, 012407 (2016).
78. C. M. Hales, J. D. Rolston, S. M. Potter, How to culture, record and stimulate neuronal networks on micro-electrode arrays (MEAs). *J. Vis. Exp.* **39**, 2056 (2010).
79. T. Deneux, A. Kaszas, G. Szalay, G. Katona, T. Lakner, A. Grinvald, B. Rózsa, I. Vanzetta, Accurate spike estimation from noisy calcium signals for ultrafast three-dimensional imaging of large neuronal populations in vivo. *Nat. Commun.* **7**, 12190 (2016).
80. E. M. Izhikevich, Simple model of spiking neurons. *IEEE Trans. Neural Netw.* **14**, 1569–1572 (2003).
81. S. Sahara, Y. Yanagawa, D. D. M. O’Leary, C. F. Stevens, The fraction of cortical GABAergic neurons is constant from near the start of cortical neurogenesis to adulthood. *J. Neurosci.* **32**, 4755–4761 (2012).
82. J. Soriano, M. R. Martínez, T. Tlustý, E. Moses, Development of input connections in neural cultures. *Proc. Natl. Acad. Sci. U.S.A.* **105**, 13758–13763 (2008).
83. T. Takemuro, H. Yamamoto, S. Sato, A. Hirano-Iwata, Polydimethylsiloxane microfluidic films for in vitro engineering of small-scale neuronal networks. *Jpn. J. Appl. Phys.* **59**, 117001 (2020).
84. M. Newman, in *Networks* (Oxford University Press, ed. 2, 2018).
85. R. Guimerà, M. Sales-Pardo, and L. A. Nunes Amaral, Modularity from fluctuations in random graphs and complex networks. *Phys. Rev. E* **70**, 025101(R) (2004).
86. E. Alvarez-Lacalle and E. Moses, Slow and fast pulses in 1-D cultures of excitatory neurons. *J. Comput. Neurosci.* **26**, 475–493 (2009).
87. J. S. Isaacson, M. Scanziani, How inhibition shapes cortical activity. *Neuron* **72**, 231–243 (2011).
88. K. A. Ferguson, F. Njap, W. Nicola, F. K. Skinner, S. A. Campbell, Examining the limits of cellular adaptation bursting mechanisms in biologically-based excitatory networks of the hippocampus. *J. Comput. Neurosci.* **39**, 289–309 (2015).

89. M. Stimberg, R. Brette, D. F. Goodman, Brian 2, an intuitive and efficient neural simulator. *eLife* **8**, e47314 (2019).
90. L. Huang, P. Ledochowitsch, U. Knoblich, J. Lecoq, G. J. Murphy, R. C. Reid, S. E. J. de Vries, C. Koch, H. Zeng, M. A. Buice, J. Waters, L. Li, Relationship between simultaneously recorded spiking activity and fluorescence signal in GCaMP6 transgenic mice. *eLife* **10**, e51675 (2021).
91. H. R. Wilson, J. D. Cowan, Excitatory and inhibitory interactions in localized populations of model neurons. *Biophys. J.* **12**, 1–24 (1972).
92. M. Jedynak, Collective excitability in a mesoscopic neuronal model of epileptic activity. *Phys. Rev. E* **97**, 012204 (2018).
93. W. Gerstner, W. M. Kistler, R. Naud, L. Paninski, in *Neuronal dynamics: From single neurons to networks and models of cognition* (Cambridge Univ. Press, 2014).
94. M. V. Tsodyks, H. Markram, The neural code between neocortical pyramidal neurons depends on neurotransmitter release probability. *Proc. Natl. Acad. Sci. U.S.A.* **94**, 719–723 (1997).
95. D. Holcman, M. Tsodyks, The emergence of Up and Down states in cortical networks. *PLOS Comput. Biol.* **2**, e23 (2006).
96. V. Buendía, P. Villegas, R. Burioni, M. A. Muñoz, Hybrid-type synchronization transitions: Where incipient oscillations, scale-free avalanches, and bistability live together. *Phys. Rev. Research* **3**, 023224 (2021).
97. P. C. Bressloff, J. N. Maclaurin, Stochastic hybrid systems in cellular neuroscience. *J. Math. Neurosci.* **8**, 12 (2018).

C Supplementary material for “*How contact patterns destabilize and modulate epidemic outbreaks*”

Supplementary Material for How contact patterns destabilize and modulate epidemic outbreaks

Johannes Zierenberg,¹ F. Paul Spitzner,¹ Jonas Dehning,¹
Viola Priesemann,^{1,2} Martin Weigel,³ and Michael Wilczek^{1,4}

¹Max Planck Institute for Dynamics and Self-Organization, 37077 Göttingen, Germany

²Institute for the Dynamics of Complex Systems, University of Göttingen, 37077 Göttingen, Germany

³Institut für Physik, Technische Universität Chemnitz, 09107 Chemnitz, Germany

⁴Theoretical Physics I, University of Bayreuth, 95440 Bayreuth, Germany

In the Supplementary material, we provide additional controls to verify the robustness of our results in the main manuscript.

A. Non-deterministic disease progression

In the main manuscript, we have focused on deterministic disease progression, where latent and infectious periods had a precise duration. For a more realistic view, we want to allow for the latent and infectious periods to vary from case to case (Fig. S1). However, if we draw random periods then we can no longer enumerate the statistics of $P(n_{\text{inf}})$ but have to sample it instead. Specifically, we sample 10^6 disease realizations, where we first draw a random realization of the disease progression $(T_{\text{lat},i}, T_{\text{inf},i})$, to then draw disease start times s_i from the ensemble of all encounters until we find an s_i such that the disease progression is within the remaining duration of the experiment, i.e., $s_i + T_{\text{lat},i} + T_{\text{inf},i} \leq T_{\text{exp}}$. Only once we have a valid disease start time s_i , we count the number of subsequent encounters within the infectious period as above. If, for any disease realization, we need to draw more than 1000 disease start times until we find a valid one, we abort the estimation for the set of parameters $(T_{\text{lat}}, T_{\text{inf}}, k)$. By this procedure to first draw and fix a random realization of the disease progression, we avoid a bias towards small periods that would occur due to the finite period of the experimental data.

Here, we chose to draw the periods T_{lat} and T_{inf} from a gamma distribution, where we fix the mean $\langle T_i \rangle$ by choosing

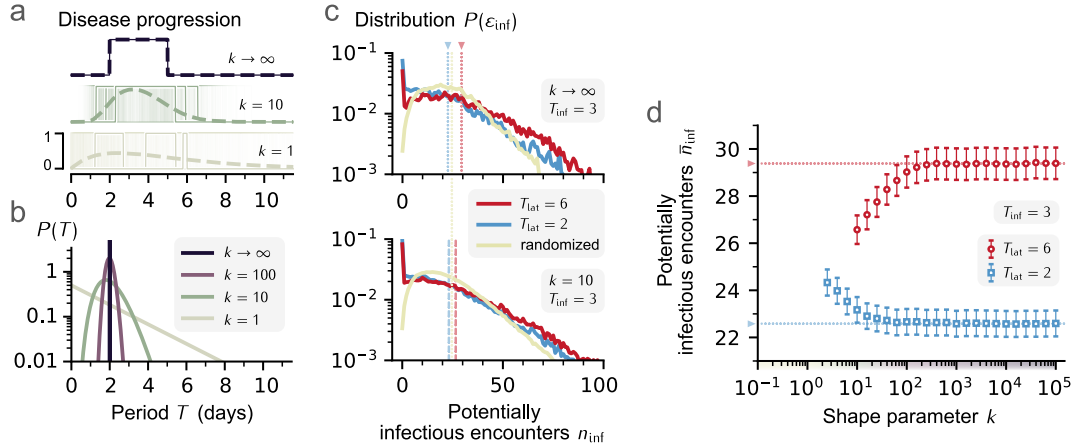


FIG. S1. Increased variability of disease-stage periods does not affect conclusions on robustness of outbreaks but weakens the modulation of spreading pace. **a, b:** To include person-to-person variability, we draw both latent and infectious periods from gamma distributions characterized by the shape parameter k , which interpolates between exponential ($k = 1$) and delta ($k \rightarrow \infty$) distributions. For small k , T_{lat} and T_{inf} differ in duration from realization to realization — across individuals, the probability to be infectious at a given time is smeared out. As k increases, the periods vary less around their expected value and the disease progression eventually becomes deterministic. **c:** Probability distributions of potentially infectious encounters n_{inf} for $k \rightarrow \infty$ (top) and $k = 10$ (bottom). When randomizing trains, the probability of zero-infectious encounters is suppressed. **d:** Mean number of potentially infectious encounters \bar{n}_{inf} as a function of k for the two examples from the main manuscript ($T_{\text{inf}} = 3$ days and $T_{\text{lat}} = 2$ or 6 days). For $k \rightarrow \infty$, we recover the result for deterministic disease progression (dashed lines), where the latent period induces a notable difference between the two examples. For smaller k , the resonance effects remain relevant but the difference decreases, see also Fig. S2.

the scale $\theta = \langle T_i \rangle / k$ such that $P_k(T_i) = T_i^{k-1} e^{-T_i/\theta} / [\Gamma(k)\theta^k]$. Hence, the shape parameter k parameterizes the case-to-case variability (Fig. S1a) and allows us to interpolate between a delta distribution ($k \rightarrow \infty$) and the exponential distribution ($k = 1$) that is commonly assumed in computational epidemiology for mathematical tractability [1]. Clinically observed distributions are neither delta distributed nor exponential distributed and may be best described by distributions with a clear peak but vanishing probability at zero, such as log-normal distributions or gamma distributions with shape parameters in between $(1, \infty)$. On the one hand, delta-distributed periods seem like a convenient but unrealistic simplification. On the other hand, exponentially distributed periods may appear more realistic, however, they imply an artificially high probability of short durations, which in turn leads to realizations where the infectious period either starts shortly upon infection or has close-to-zero duration (example traces in Fig. S1a). In fact, it has been argued already in the past that gamma distributions are more realistic [2–4], see for example empirical distributions of latent periods for COVID-19 [5], such that more realistic shape parameters could be in the range $h \in [5, 20]$ which is between delta and exponential. To investigate how case-to-case variability affects the number of potentially infectious encounters n_{inf} , we again consider the probability distribution $P(n_{\text{inf}})$ (Fig. S1c), and revisit the two examples ($T_{\text{inf}} = 3$ days with either $T_{\text{lat}} = 2$ days or $T_{\text{lat}} = 6$ days).

For the delta-disease ($k \rightarrow \infty$, top), the red ($T_{\text{lat}} = 6$ days) and blue ($T_{\text{lat}} = 2$ days) distributions exhibit a peak at zero, they are broad, and have a long tail. Comparing red and blue, we find that the latent period determines the height of the peak at zero as well as the position of the bulk distribution, and, thereby, determines the mean number of potentially infectious encounters (dashed vertical lines). The mean values clearly differ. Again comparing with the randomized encounter trains (yellow line), we find no peak at zero, a shorter tail, and no dependence on the latent period (the respective randomized lines fall on top of each other). Importantly, a peak at zero implies that the infected individual does not pass on the infection, so that the disease becomes more likely to die out if case numbers are low.

Employing a non-deterministic disease progression ($k = 10$, Fig. S1c bottom), the distribution from randomized data is barely affected. However, the red and blue distributions are more similar to each other, but also broader and smoother than for the delta-disease. This can be explained by gamma-distributed periods acting as a smoothing kernel along both dimensions of Fig. S1f, where variability in the infectious period directly affects \bar{n}_{inf} , while variability in the latent period affects \bar{n}_{inf} through the resonance effect. Consequently, we expect that with decreasing shape parameter k , the mean number of potentially infectious encounters becomes independent of the mean latent period. Indeed, when considering \bar{n}_{inf} as a function of k , we find that the estimates for our two examples approach each other, as k decreases (Fig. S1d).

Note that our analysis has a lower bound in k once realizations of disease progression (latent + infectious period) cannot find sufficiently many initial encounters to fit into the finite duration of the experiment (4 weeks for Copenhagen Networks Study). However, using other examples with smaller latent and infectious periods (where we can acquire enough statistics), we show that the two extreme cases meet for $k \approx 1$ (see Fig. S2).

B. Non-deterministic disease progression with fast disease stages

With the parameters of the main text, we were not able to sample for small k values (more variability across disease realizations) because the 28-day duration of the data becomes too short once the periods of disease progression are close-to exponentially distributed ($k \rightarrow 1$).

To avoid this issue and to illustrate shorter timescale, we here compare with another hypothetical example of a “faster” disease progression, where $T_{\text{inf}} = 0.5$ days and T_{lat} is either 1 or 1.5 days (Fig. S2). In this case, expected periods are very short so that even realizations with periods that severely exceed their expected value fit into the 28-day duration.

We find a few noteworthy aspects: First, the absolute value of potentially infectious encounters n_{inf} is much lower for faster disease progression. This is due to the much shorter infectious period. However, the relative deviation from the randomized surrogate data is consistent between the two examples. Second, we now find that the longer latent period (1.5 vs 1.0 days) leads to fewer potentially infectious encounters (red vs blue). This is just a result of the chosen latent periods: choosing an even longer latent period would result in a respective decrease of n_{inf} (e.g. 2.0 vs 1.5 contacts). Third, as expected, as $k \rightarrow 1$, the estimates of n_{inf} overlap for different latent periods, because individual disease realizations become very variable (cf. Fig. S1a).

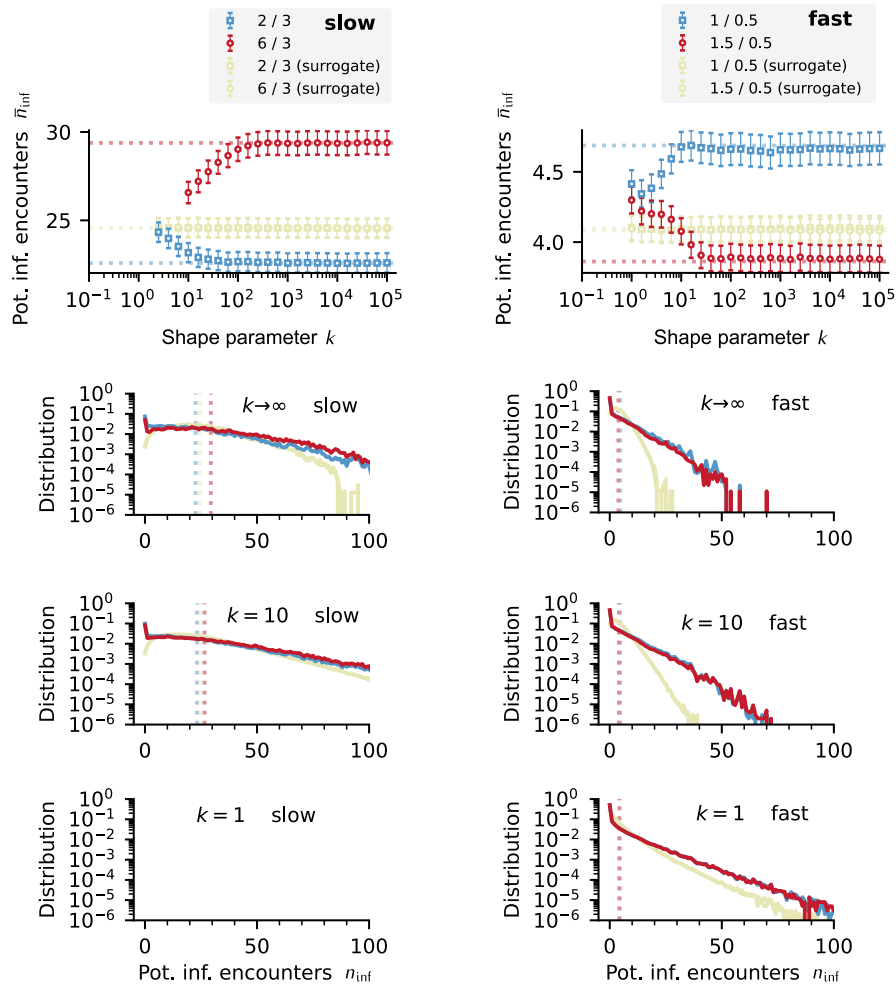


FIG. S2. **Example with smaller latent and infectious periods provides additional insight on low- k regime of non-deterministic disease progression.** Here, we compare the example from the main manuscript (“slow”, $T_{inf} = 3$ days and T_{lat} either 2 or 6 days) with a hypothetical “fast” disease progression ($T_{inf} = 0.5$ days and T_{lat} either 1 or 1.5 days) and show both the mean number of potentially infectious encounters as a function of the shape parameter k of the gamma-distributed latent and infectious period (top) as well as their distributions for selected k . Due to the finite duration of the recording, the accessible low- k regime is determined by the mean latent and infectious period, because for low k large periods quickly exceed the finite duration. For faster disease progression (smaller latent and infectious period), we observe modulations on smaller timescales and, in addition, reach the low- k regime of exponentially distributed periods ($k = 1$) commonly assumed in epidemiological simulations. As one can see more clearly for faster disease progression, the mean number of potentially infectious encounters approach each other in this low- k regime, which can only be anticipated from the results for slower disease progression. This implies that modulations will not be present for exponentially distributed latent and infectious periods but only for more realistic non-exponentially distributed ones with higher k .

C. Simple point processes cannot fully reproduce temporal features

As we noted in the main text, each of the considered simple generative models is insufficient to reproduce the full set of observed temporal features of contact patterns. Here, we provide a more complete overview of processes and the features they reproduce (Fig. S3). We identified three relevant features:

- i)** a time-varying, cyclostationary encounter rate $\rho(t)$ (first column)
- ii)** a heavy-tailed inter-encounter-interval distribution $P(\delta t)$ (second column)
- iii)** encounter rates vary between individuals (third column)

Feature i) is responsible for modulation of the conditional encounter rate $\Psi(\tau)$ (fourth column). Combined with disease progression, this causes modulations of \bar{n}_{inf} and distributions $P(n_{\text{inf}})$ that vary with T_{lat} and T_{inf} (last two columns). Feature ii) is responsible for zero-spreading events, which destabilize epidemic outbreaks and manifest in the peak of $P(n_{\text{inf}})$ for $n_{\text{inf}} \approx 0$ (last column). Feature iii) is responsible for super-spreading events, which correspond to the tail of $P(n_{\text{inf}})$ and, thus, can cause a systematic shift of \bar{n}_{inf} .

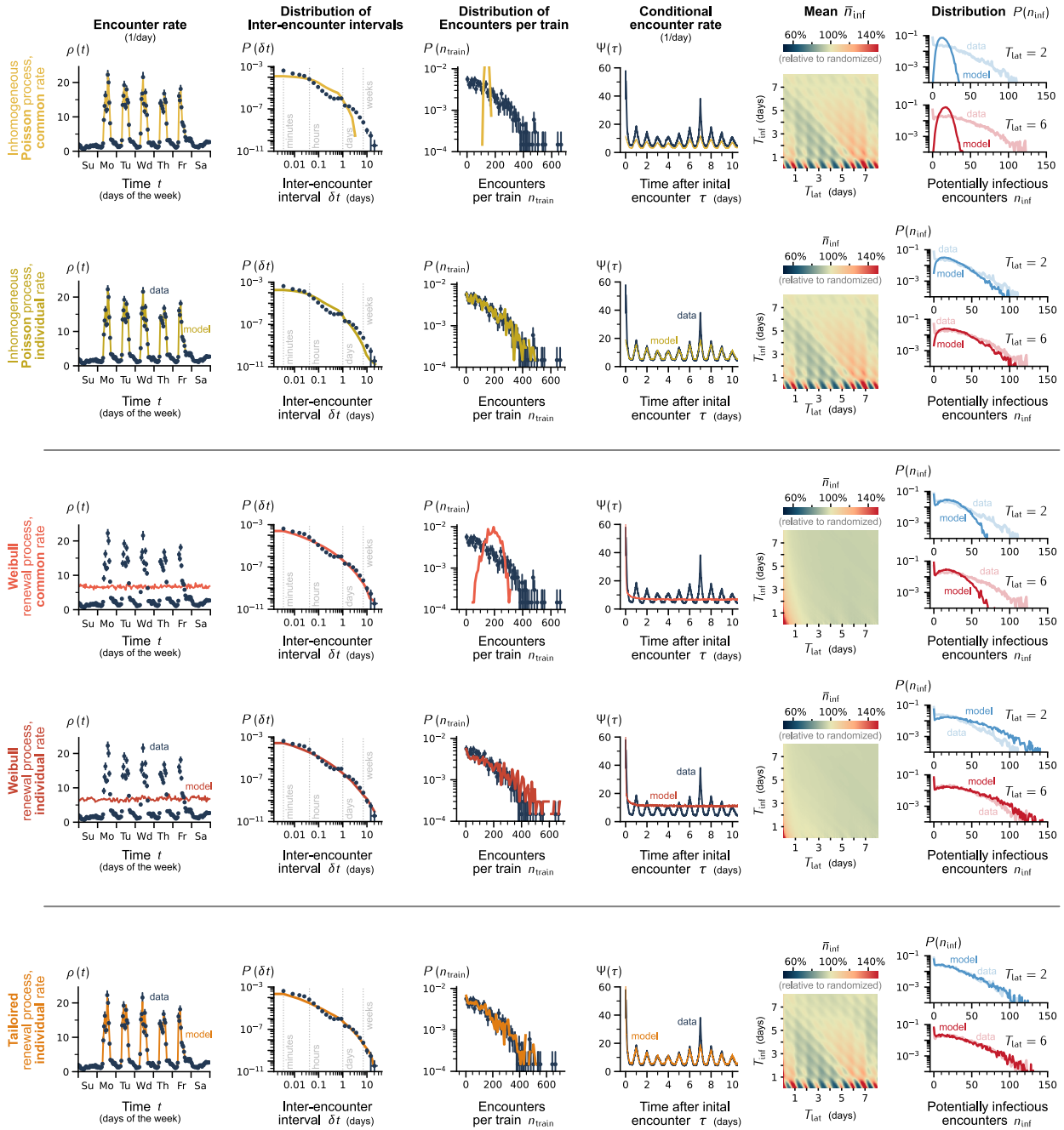


FIG. S3. **Simple generative processes are not capable of reproducing all aspects of the full real-world contact statistics.** An inhomogeneous Poisson process can reproduce cyclostationary $\rho(t)$ but fails to reproduce sufficiently heavy-tailed $P(\delta t)$. A Weibull-renewal process reproduces heavy-tailed $P(\delta t)$ but fails to reproduce the cyclostationary $\rho(t)$. Generative processes need to reproduce variability between individuals $P(n_{\text{train}})$ to produce long-tailed distributions $P(n_{\text{inf}})$. In order to reproduce the data in all the considered aspects, we designed a tailored Weibull-renewal process with heterogeneous rates.

D. Control regarding continuous contribution of participants

In the main manuscript, we use the full published data set of the Copenhagen Networks Study [6], covering the physical proximity data of 675 participants. Upon closer inspection, there are periods both at the beginning and the end of the experiment without entries for some of these 675 participants. Since entries also occur for Bluetooth signals with unknown devices, this may indicate irregularities in the contact behavior of some of the participants, e.g., incomplete participation of individuals.

In order to make sure that our results are not affected by such boundary effects, we reanalyzed the data and included only the contact trains of those individuals for which any Bluetooth signal was recorded on both the first and last day of the study (Fig. S4). Technically, we achieved this easily by restricting our analysis to those IDs for which timestamps were recorded within the first day (timestamp $< 1 \cdot 24 \cdot 60 \cdot 60$ s) and the last day (timestamp $> 27 \cdot 24 \cdot 60 \cdot 60$ s), reducing the data set to 533 contact trains.

This control analysis fully supports our quantitative results from the main manuscript (Fig. S4) such that we can rule out artifacts from boundary effects of incomplete participation. In particular, we observe a matching weekly structure of the encounter rate (Fig. S4a), a matching distribution of inter-encounter intervals that can be fitted with a Weibull distribution (Fig. S4b), and a matching conditional encounter rate (Fig. S4c). Consequently, both mean potentially infectious encounters for deterministic disease progression (Fig. S4d and f) as well as for non-deterministic disease progression (Fig. S4e and g) match our main results.

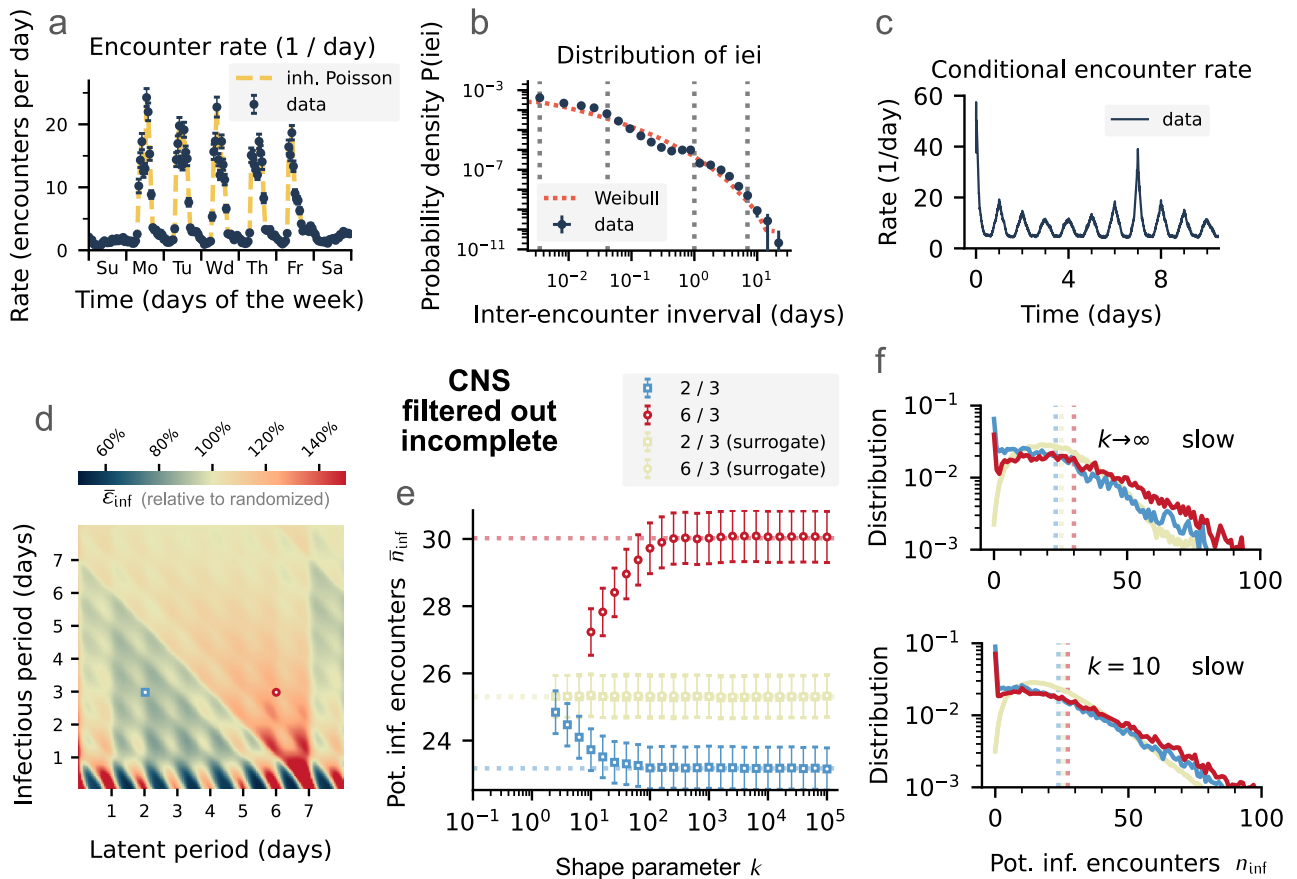


FIG. S4. **Control regarding continuous contribution of participants.** Here, we excluded those trains that did not have any encounters during the first or last day. This results in 533 instead of 675 trains. Panels match key figures from the main manuscript. Results are consistent. The fitted Weibull distribution has shape parameter 0.3739 and scale parameter 3161.

E. Analysis of an alternative data set

To further test the robustness of our results, we repeated our analysis on an independent data set. Here, we consider contact data recorded at one of the office buildings of the French Institute for Public Health Surveillance “InVS” [7, 8]. This data is recorded with a different technique, namely so-called near-field chips that only record signals in close proximity ($\lesssim 5$ m) and avoid to threshold the Bluetooth signal. Moreover, the temporal resolution of contacts is 20s as opposed to 5min in the main manuscript. In addition, the data is recorded for a different social group, namely employees within an office building. Last, the data is recorded in another country (France) by a different collaboration (SocioPatterns). The data set spans 2 weeks of recording 145 participants (two thirds of the staff agreed to participate).

The analysis of this completely independent data set provides completely consistent results to those presented in the main manuscript (Fig. S5). When comparing the results, we have to highlight that the available statistics for this data set are much smaller due to smaller duration and smaller number of participants. However, we clearly see the expected weekly structure in the encounter rate (which is here again dominated by working days because of office hours), the distribution of inter-encounter intervals that is well described by a Weibull distribution, as well as the typical conditional encounter rate with a peak at 7 days. Consequently, the results for (Δ) disease progression are also consistent with our main findings on the modulation of potential secondary infections (Fig. S5d). Results on non-deterministic disease progression are confined to shorter latent and infectious periods due to the shorter experimental duration. We conclude that the additional data set fully supports our results in the main manuscript.

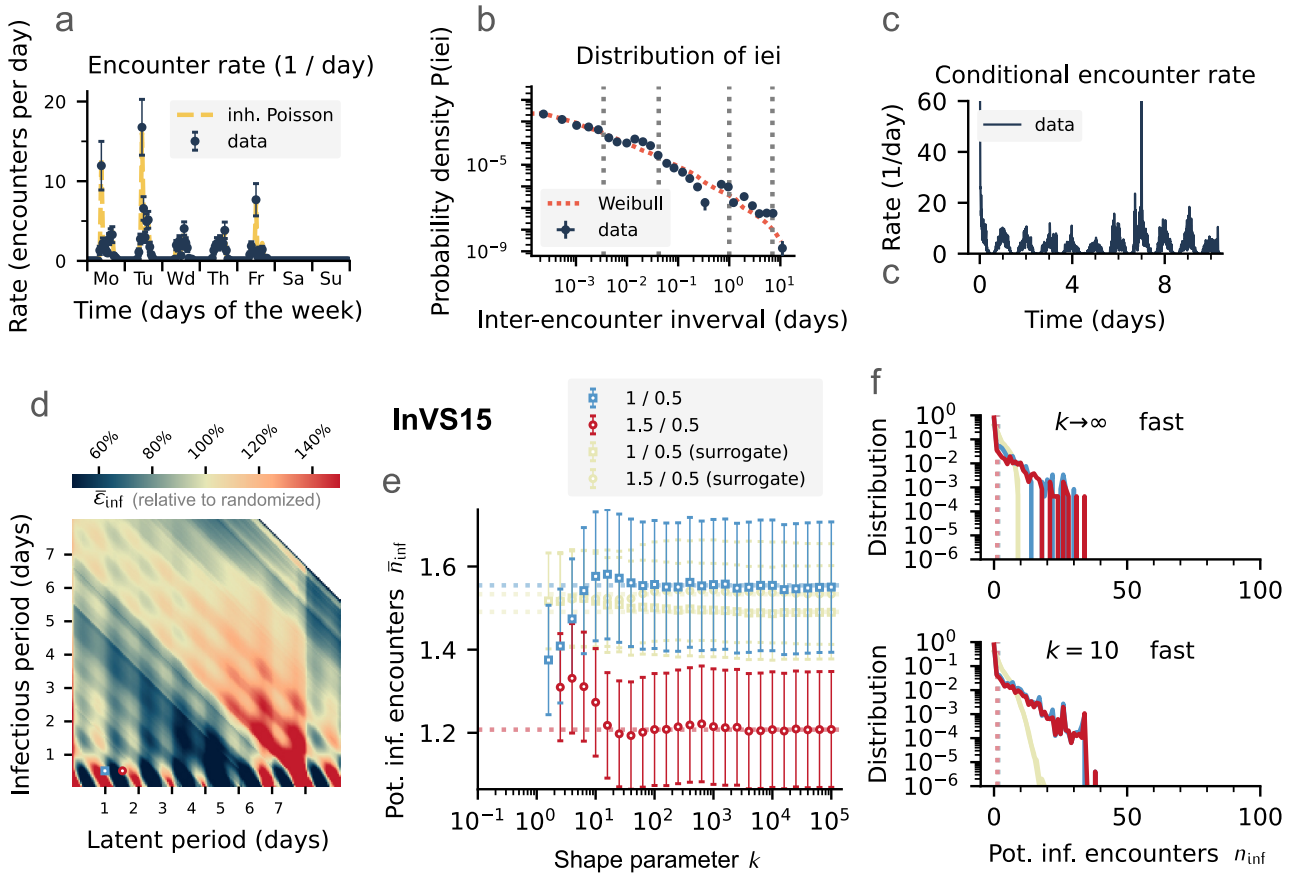


FIG. S5. **Main results for other data set.** Because the recording lasted “only” two weeks, the duration of disease that can be sampled were limited to the fast disease progression. The fitted Weibull distribution has shape parameter 0.225 and scale parameter 675.

F. Infections from outside the study group

To check the effect of contacts that could take place with people who were not part of the study, we investigate disease onsets that do not directly follow the contact patterns observed in the data (Fig. S6). In our analysis of the main manuscript, an infection could only originate from an encounter with another participant in the data set. Here, we keep the original encounter trains (to evaluate potentially infectious encounters) but the disease onset can occur at any time, due to a hypothetical contact with an external person. We focus on the resulting distribution and the mean of potentially infectious encounters n_{inf} (Fig. S6).

We distinguish the following different possibilities of disease onset:

- internal:** Onsets occur as in the main manuscript only at encounters recorded in the data set. This naturally incorporates the spatio-temporal structure of encounters, in particular their temporal inhomogeneity and their variability across participants.
- external i:** Onsets occur completely randomly, at random times for random participants. This neglects both temporal inhomogeneity of encounters and their variability across individuals.
- external ii:** Onsets occur at random times with a probability proportional to the encounter rate for random participants with a probability proportional to their total number of encounters. This incorporates both the (averaged) temporal inhomogeneity of encounters and the variability across individuals.
- external iii:** Onsets occur at random times with a probability proportional to the encounter rate but uniformly across random participants. This incorporates the (averaged) temporal inhomogeneity of encounters but neglects the variability across individuals.
- external iv:** Onsets occur at uniformly random times for random participants with a probability proportional their total number of encounters. This neglects the temporal inhomogeneity of encounters but incorporates the variability across individuals.

Once an onset has been chosen, the disease progression is modeled as in the main manuscript. We focus on the usual examples but use gamma-distributed latent and infectious periods with $k = 10$ to evaluate potentially infectious encounters ($k = 10$ aims to strike a balance between completely deterministic and exponential disease stages [2–4]).

Comparing the different versions of disease onset (Fig. S6), we can attribute clear effects to both the temporal inhomogeneity of the onset time as well as the variability of onset times across individuals. Please note that in all cases the encounter statistics of the actual encounter trains did not change — all we change is the statistics of the disease onset time. Please note further that the results for different versions of disease onset represent the extreme scenario where all disease onsets originate from external sources.

Comparing the distributions of n_{inf} for fixed T_{lat} (Fig. S6a and Fig. S6c), we notice that those distributions that best resemble the shape of internal disease onset are those where external disease onset statistics incorporate the variability across individuals (external ii and iv). This can be explained by the fact that also for internal disease onset more onsets occur for contact trains with more encounters, which in turn increases the probability of higher n_{inf} and thereby also the mean n_{inf} . It appears that for the overall shape of the distribution, as well as the leading order of its mean value, it is not necessary that disease onsets occur with the same temporal inhomogeneity as true encounters for the chosen infectious periods (this may change for very small infectious periods though).

Comparing further the results of specific disease onsets for different T_{lat} (Fig. S6b comparing solid vs opaque symbols), we notice that incorporating the temporal inhomogeneity into the disease onset (external disease ii and iii) seems relevant for the modulation that causes differences in \bar{n}_{inf} due to latent periods. This can be explained by reoccurring contact patterns: if infections are not more likely to occur during times of many contacts (as for external i and iv), then differences in the number of potential infections are smeared out when averaging over multiple realizations.

Concluding, the results for the extreme scenarios of external infections fully support our conclusions from the main manuscript.

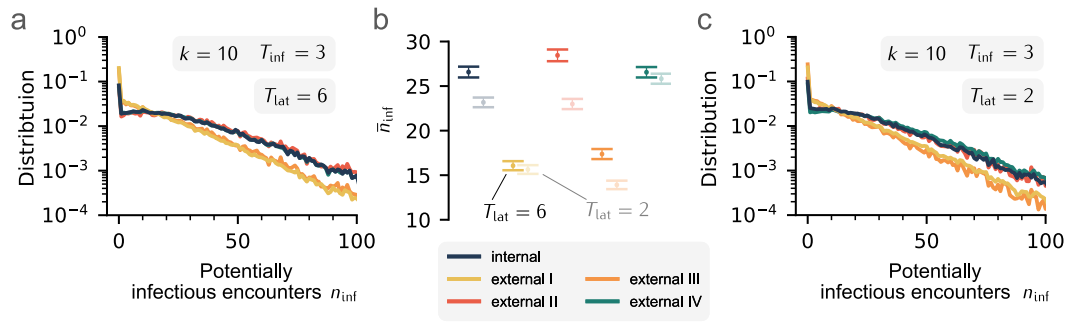


FIG. S6. **Infectious encounters for external infections.** In our analysis in the main manuscript, we preserved the temporal features by constraining disease onsets to available encounters. **a:** Distribution of potentially infectious encounters for non-deterministic disease progression ($k = 10$). 6 days latent period. **b:** Comparison of the mean \bar{n}_{inf} between 6 days latent period (dark) and 2 days latent period (light). **c:** Same as a), but 2 days latent period.

G. Impact of the distance threshold for considered contacts

In the main manuscript, we filtered the physical proximity data to only include contacts with a minimal Bluetooth signal strength (RSSI $\gtrsim -80$ dBm) as a proxy for contact distances below 2 m [9]. This choice was motivated in the main manuscript and moreover corresponds to a value that optimizes the ratio between strong and weak links [9]. Here we show that our results are robust under changes in the cut-off signal strength which sets a scale, but does not alter the patterns observed. In particular, we consider two cases of lower (RSSI $\gtrsim -75$ dBm) and higher (RSSI $\gtrsim -95$ dBm) threshold. As can be seen from Fig. S7, this threshold changes the scale of the encounter rate (Fig. S7a) but does not alter the resonance effect compared to random encounters (Fig. S7b).

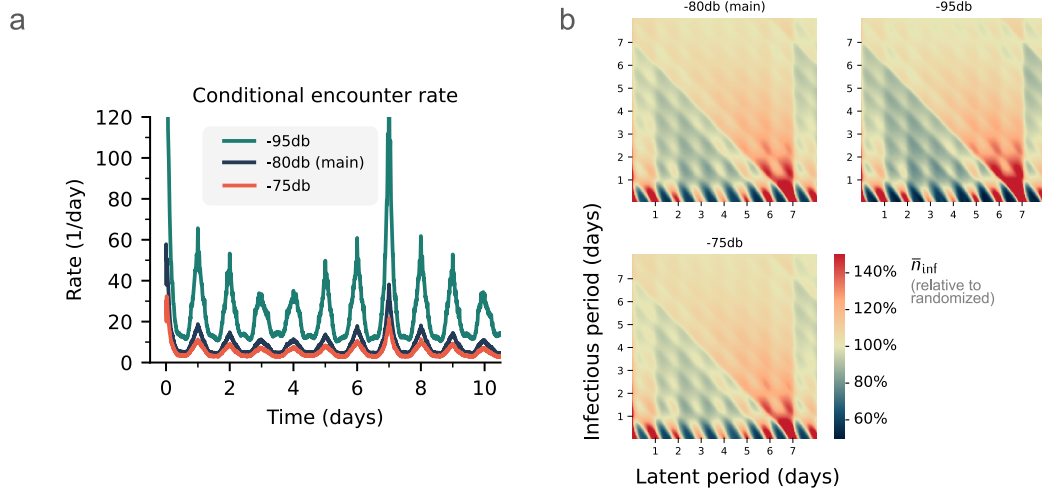


FIG. S7. **Effect of threshold distance.** To test which impact the distance at which a contact becomes potentially infectious has on our results, we varied the RSSI threshold in the preprocessing step. A higher threshold (RSSI $\gtrsim -95$ dBm) corresponds to including more contacts (which previously were considered too far away), thus resulting in a higher number of potentially infectious encounters, and (in absolute numbers) to a higher conditional encounter rate. Vice versa, a lower threshold (RSSI $\gtrsim -75$ dBm, corresponding to about 1 meter distance) leads to a lower conditional encounter rate. In both cases, the overall functional shape of the conditional encounter rate (featuring valleys at night, peaks at daytime and pronounced peaks at seven days) remains intact. Consequently, also the number of potentially infectious encounters *relative to randomized* remain mostly unaltered.

H. Impact of the contact duration for considered contacts

In the main manuscript, we filtered contacts to only include those with a sufficient duration of at least 15 minutes. This choice was motivated in the main manuscript, and it is particularly suitable to avoid transient contacts that arise in passing. Still, different choices are possible. Here, we show for shorter and longer minimum durations that this choice only affects the scale of the encounter rate but does not affect any results relating to the modulation of potentially infectious encounters (Fig. S8).

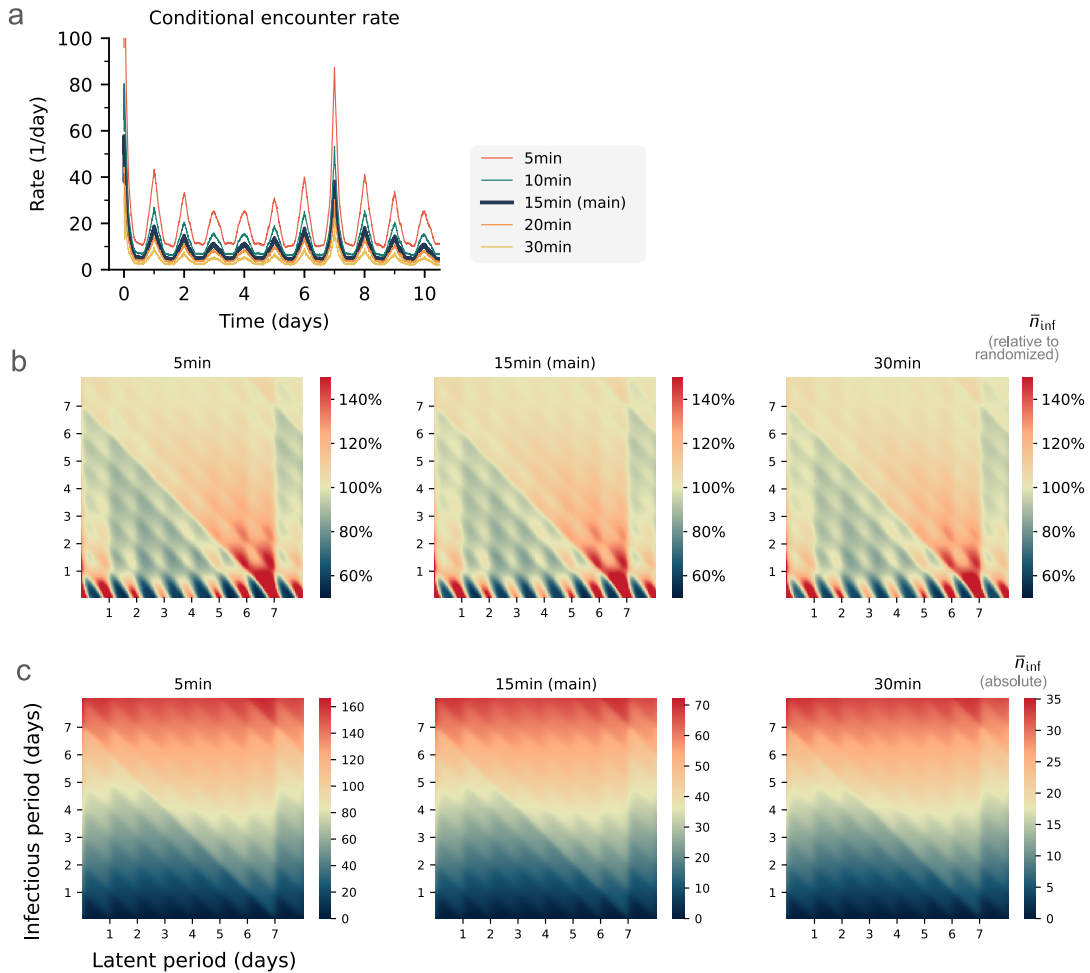


FIG. S8. **Effect of threshold duration.** To test which impact the minimum duration after which a contact becomes potentially infectious has on our results, we varied the required duration for qualifying contacts during the preprocessing step. A shorter required duration (e.g. 5 minutes vs 15 minutes in the main manuscript) leads to more contacts qualifying and a higher conditional encounter rate. Vice versa, a longer required duration (e.g. 30 minutes) leads to a lower conditional encounter rate. In both cases, the overall functional form of the conditional encounter rate remains intact. Again, although we see a higher absolute number of potentially infectious encounters, the change relative to randomized encounter trains is mostly unaltered.

-
- [1] R. Pastor-Satorras, C. Castellano, P. Van Mieghem, and A. Vespignani, Epidemic processes in complex networks, *Rev. Mod. Phys.* **87**, 925 (2015).
 [2] N. T. J. Bailey, Some Stochastic Models for Small Epidemics in Large Populations, *Appl. Stat.* **13**, 9 (1964), 2985218.

- [3] D. Anderson and R. Watson, On the spread of a disease with gamma distributed latent and infectious periods, *Biometrika* **67**, 191 (1980).
- [4] A. L. Lloyd, Destabilization of epidemic models with the inclusion of realistic distributions of infectious periods, *Proc. R. Soc. Lond. B Biol. Sci.* **268**, 985 (2001).
- [5] H. Xin, Y. Li, P. Wu, Z. Li, E. H. Y. Lau, Y. Qin, L. Wang, B. J. Cowling, T. K. Tsang, and Z. Li, Estimating the Latent Period of Coronavirus Disease 2019 (COVID-19), *Clin. Infect. Dis.* **74**, 1678 (2022).
- [6] P. Sapiezynski, A. Stopczynski, D. D. Lassen, and S. Lehmann, Interaction data from the Copenhagen Networks Study, *Sci. Data* **6**, 1 (2019).
- [7] M. Géniois, C. L. Vestergaard, J. Fournet, A. Panisson, I. Bonmarin, and A. Barrat, Data on face-to-face contacts in an office building suggest a low-cost vaccination strategy based on community linkers, *Netw. Sci.* **3**, 326 (2015).
- [8] M. Géniois and A. Barrat, Can co-location be used as a proxy for face-to-face contacts?, *EPJ Data Sci.* **7**, 1 (2018).
- [9] V. Sekara and S. Lehmann, The Strength of Friendship Ties in Proximity Sensor Data, *PLOS ONE* **9**, e100915 (2014).